Probing the Three Gauge-boson Couplings in 14 TeV Proton-Proton Collisions

by

Matthew Dobbs

B.Sc., McGill University, 1997.

A Dissertation Submitted in Partial Fulfillment of the
Requirements for the Degree of

DOCTOR OF PHILOSOPHY

in the Department of Physics and Astronomy,
University of Victoria.

We accept this thesis as conforming
to the required standard.

Dr. M. Lefebvre, Supervisor (Department of Physics and Astronomy)

Dr. R. Keeler, Departmental Member (Department of Physics and Astronomy)

Dr. M. Roney, Departmental Member (Department of Physics and Astronomy)

Dr. D. Harrington, Outside Member (Department of Chemistry)

Dr. U. Baur, External Examiner
(Department of Physics, State University of New York at Buffalo)

Supervisor: Dr. M. Lefebvre

Abstract

The potential for probing the Standard Model of elementary particle physics by measuring the interactions of $W^{\pm}$-bosons with Z^0-bosons and photons ($WW\gamma$ and WWZ triple gauge-boson couplings) using TeV-scale proton-proton collisions is described in the context of the ATLAS detector at the 14 TeV Large Hadron Collider (LHC). The ATLAS detector and LHC are currently under construction at the European Organization for Nuclear Research (CERN), with the first data expected in 2006.

New analysis techniques are presented in this thesis: (1) A new strategy for placing limits on the consistency of measured anomalous triple gauge-boson coupling parameters with the Standard Model is presented. The strategy removes the ambiguities of form factors, by reporting the limits as a function of a cutoff operating on the diboson system invariant mass. (2) The 'optimal observables' analysis strategy is investigated in the context of hadron colliders, and found to be not competitive, as compared to other strategies. (3) Techniques for measuring the energy dependence of anomalous couplings are presented.

Assuming the triple gauge-boson couplings are consistent with the Standard Model, the expected 95% confidence intervals for anomalous couplings are

$$
\begin{array}{rrrrr}
-0.0033_{\text{stat.}}, & -0.0012_{\text{syst.}} & < \lambda_\gamma < & +0.0033_{\text{stat.}}, & +0.0012_{\text{syst.}} \\
-0.0065_{\text{stat.}}, & -0.0032_{\text{syst.}} & < \lambda_Z < & +0.0066_{\text{stat.}}, & +0.0031_{\text{syst.}} \\
-0.073_{\text{stat.}}, & -0.015_{\text{syst.}} & < \Delta\kappa_\gamma < & +0.076_{\text{stat.}}, & +0.0076_{\text{syst.}} \\
-0.10_{\text{stat.}}, & -0.024_{\text{syst.}} & < \Delta\kappa_Z < & +0.12_{\text{stat.}}, & +0.024_{\text{syst.}} \\
-0.0064_{\text{stat.}}, & -0.0058_{\text{syst.}} & < \Delta g_Z^1 < & +0.010_{\text{stat.}}, & +0.0058_{\text{syst.}}
\end{array}
$$

for 30 fb^{-1} (about 3 years) of integrated low luminosity LHC data.

In addition, a new phenomenological method for simulating higher order quantum chromodynamics corrections to hadronic processes using Monte Carlo techniques, called the *phase space veto method*, is presented. The method allows for the incorporation of next-to-leading order (NLO) matrix elements into showering and hadronization event generators, while avoiding double-counting and providing unweighted event generation. To demonstrate the method, an event generator using the phase space veto method for the process $p\overset{(-)}{p} \to Z + X \to l^+l^- + X$ at NLO is constructed and

interfaced consistently to a general purpose showering and hadronization simulation package.

Examiners:

Dr. M. Lefebvre, Supervisor (Department of Physics and Astronomy)

Dr. R. Keeler, Departmental Member (Department of Physics and Astronomy)

Dr. M. Roney, Departmental Member (Department of Physics and Astronomy)

Dr. D. Harrington, Outside Member (Department of Chemistry)

Dr. U. Baur, External Examiner
(Department of Physics, State University of New York at Buffalo)

Contents

List of Tables

List of Figures

Acknowledgments

The highlight of my post-graduate studies is having had the opportunity to work with many excellent scientists and admirable people. In many respects, the high energy physics group at the University of Victoria has made this possible. First, by including me in their group of highly motivated, talented, and closely interacting physicists; and second by facilitating my attendance at a broad range of international workshops, conferences, and to be resident at the European Organization for Nuclear Research (CERN)—which in turn has allowed me to foster my own collaborations. The importance of these opportunities for my education cannot be understated.

Michel Lefebvre helped guide and direct my studies and research from the onset—to him I am indebted. His enthusiasm is un-stoppable and highly contagious. Besides being an outstanding graduate adviser, he is an excellent communicator in private physics discussions, the class room, and while delivering talks. If just a fraction of his talents have rubbed off on me, then I regard my experience at Victoria as a success.

Richard Keeler invested considerable effort in reading the manuscript of this thesis at an early stage, and I thank him for that and all the help along the way. I spent a great deal of time collaborating with, and learning from, Dugan O'Neil while working on the Hadronic Endcap Calorimeter (HEC). Besides being an excellent physicist, Dugan is my role model for the perfect collaborator—and I hope we have the opportunity to work together again soon. Throughout my time in Victoria, I benefited immensely from informal discussions with other graduate students including Dominique Fortin, Kevin Graham, and in particular Brigitte Vachon. In addition to those already mentioned, I thank Alan Astbury, Margret Fincke-Keeler, Naoko Kanaya, Bob Kowalewski, Mike Roney and Randy Sobie for numerous lunch-time discussions, which are a notable part of the HEP group culture at Victoria—and contributes in a big way to the graduate student education experience.

During my stay at CERN, two people stood out as role models because of their ability to instantly understand, discuss, and evaluate a broad scope of physics and its implication for experimental observations: Ian Hinchliffe and Fabiola Gianotti. Like many students, I aspire to some day have the same grasp of the field. Also, like many students, I benefited from their ability to instantly shift down to my level and talk about the concepts in plain language.

I am grateful to Jorgen Beck Hansen—with whom I collaborated fruitfully on software and diboson physics, and learned a great deal—particularly in the early stages of my research. I thank R.D. Schaffer for provided me with the foundations of software engineering—and probably saving me from some small disasters. I am grateful to Horst Oberlack, Peter Schacht, and Hasko Stenzel for providing an excellent group atmosphere in the Hadronic Endcap community, and helping me to learn so much during the HEC beam tests. It has been a real pleasure to work with Stefan Tapprogge as co-convener of the ATLAS Standard Model Working Group. In the context of Monte Carlo studies and related workshops I benefited from numerous discussions with Törbjorn Sjöstrand, Joey Huston, Stefano Frixione, and Walter Giele.

I thank Ulrich Baur for many informative (and fun) discussions over the years. Besides learning a great deal of physics, I have learned a lot from watching the way he

interacts with physicists—particularly students—including myself. He rarely leaves an email unanswered for more than a few hours. Most important, he succeeds in conveying to students that discussing physics issues or providing answers to their questions is a priority and pleasure for him. He is able to isolate the foundation elements of these questions and provide answers or suggest directions for discovering solutions. His willingness to read and provide insightful at-a-distance comments on my Monte Carlo phenomenology paper manuscripts was a big boost for me.

This research has been supported by the Natural Sciences and Engineering Research Council of Canada (NSERC) in the form of post-graduate scholarships and ATLAS research funding. The role of NSERC in developing and supporting young researchers in Canada is indispensable.

Dedicated to Brigitte,
who has traveled along-side me down the same beautiful paths;
and to my brother Jason,
whose original insights continue to inspire me.

Chapter 1

Introduction

Particle physics is the study of the fundamental constituents of matter and their interactions. The ordinary matter which surrounds us and makes up most of the visible universe is made up almost exclusively of the lightest generation of particles: the electron, up, and down quarks. It is only at extremely high energy scales—such as the first fractions of a second after the Big Bang, or at the interaction point where the beams of particle accelerators collide—that the other generations of matter are resolved. High energy collisions provide physicists with the opportunity to study the rich physics which is so important to the development of our universe in its earliest stages.

The Large Hadron Collider (LHC) is currently under construction at the European Organization for Nuclear Research (CERN) laboratory near Geneva, Switzerland. When it achieves its first collisions in 2006, it will become the accelerator based high energy frontier for the world, pushing forward by almost an order of magnitude the energy scales probed by the currently operating Fermilab Tevatron collider. ATLAS is a multi-purpose detector which will capture and record the signatures of the particles participating in the collision induced reactions. The ATLAS experiment will provide the ideal environment to test our current understanding of nature, contained in a very successful theory known as the Standard Model (SM).

The SM predicts the *gauge-boson* particles, which propogate the electroweak force, interact not only with matter particles, but also with one another. The photon (electromagnetic radiation such as ordinary sunlight) is one example of a gauge-

boson, the other gauge-bosons are the $W^{\pm}$-bosons and Z^0-boson. These interactions manifest themselves as a coupling between three gauge-bosons, such as a WWZ or $WW\gamma$ coupling, referred to as triple gauge-boson couplings (TGC's). The existence of these couplings has been beautifully verified at the Large Electron Positron Collider (LEP) [Ale99, Del99a, L3 98, Opa98]. TGC's are tightly connected with the symmetry properties of the model and reflect the full mathematical (gauge) group structure of the fundamental interactions. Any deviation from the SM prediction would indicate the presence of new, i.e. previously unobserved, physics.

The production of gauge-boson pairs in hadronic collisions is sensitive to triple gauge-boson couplings, providing a direct test of these interactions. The thrust of this thesis is a study of how the TGC vertex can be best measured at the LHC. The study can be divided into two main areas: development of new techniques for the computer modeling of gauge-boson production with higher order quantum chromodynamics (QCD, the strong nuclear force theory) corrections, and an examination of the analysis techniques which may be used to measure TGC's in the LHC environment.

Since the author's contributions to computer simulations of high energy physics collisions are well documented in the literature [Dob01a, Dob01b, Dob01c, Dob01d, Boo01], this thesis will focus primarily on the analysis techniques for measuring gauge-boson self interactions at the LHC.

The remainder of this chapter introduces the Standard Model, the LHC collider, and the ATLAS experiment. New computer modeling techniques for simulating gauge-boson production with QCD corrections in the framework of a Monte Carlo event generator are presented in Chapter 2. Chapter 3 reviews the theory and phenomenology of TGC's and diboson production. In Chapter 4 the simulation and selection of the signals and backgrounds used for this study are presented. Several methods for measuring the TGC vertex are described, evaluated, and compared in Chapter 5 before summarizing the study in the concluding chapter.

1.1 The Standard Model

Glashow [Gla61], Weinberg [Wei67], and Salam [Sal69] succeeded in unifying electromagnetism with the weak nuclear force using a model that proposes the massive gauge-bosons as the mediators of the weak currents. This *electroweak* model evolved into the theory that is now known as the Standard Model (SM). The SM encompasses our knowledge of the fundamental particles and their interactions. The model has withstood three decades of experimental testing—confirming it at a level that was certainly unexpected from the onset.

There are two fundamental types of particles in the SM: fermions and bosons. Fermions have half-integer spin, obey the Pauli exclusion principle, and always have anti-symmetric quantum mechanical wave functions. Bosons are particles with integer spin, for which the wave function is always symmetric. The fundamental particles are summarized[1] in Table 1.1. Fermions are further subdivided into two classes, leptons and quarks, each of which is composed of three generations. Leptons have integer charge, and are governed by the electroweak force. Quarks, carrying one-third-integer charge, are subject to the strong force in addition to the electroweak force. Each quark has an associated color 'charge', of which there are three varieties, traditionally labeled as red, green, and blue. Color is the quantum number to which the strong force couples. For each fermion, there is a corresponding anti-fermion with identical mass, opposite electric charge, and opposite color. Thus in the quark sector, there are 6 different *flavors* of quarks u, d, c, s, t, b each of which comes in 3 colors and each having a corresponding anti-quark partner $\bar{u}, \bar{d}, \bar{c}, \bar{s}, \bar{t}, \bar{b}$ which comes in 3 anticolors.

The fundamental forces are mediated (propagated) by the exchange of vector-bosons. The strong force is propagated by gluons, and will be described below. The photon, $W^{\pm}$-boson, and Z^0-boson—collectively called gauge-bosons—propagate the electroweak force. The $W^{\pm}$ and Z^0 particles are very different from the photon,

[1] In particle physics, units with $\hbar = c = 1$ are normally used. $\hbar$ is the Planck constant divided by 2π and c is the speed of light. In this prescription energy, momentum, and mass all have the same units, and are usually expressed in electron volts (eV).

Leptons, Spin=$\frac{1}{2}$

e $M \simeq 0.5 \times 10^{-3}$ GeV, $Q = -1$	μ $M \simeq 0.105$ GeV, $Q = -1$	τ $M \simeq 1.777$ GeV, $Q = -1$
ν_e $M < 10^{-8}$ GeV, $Q = 0$	ν_μ $M < 10^{-4}$ GeV, $Q = 0$	ν_τ $M < 0.018$ GeV, $Q = 0$

Quarks, Spin=$\frac{1}{2}$

u $M \simeq 0.003$ GeV, $Q = \frac{2}{3}$, color $= r, g, b$	c $M \simeq 1.2$ GeV, $Q = \frac{2}{3}$, color $= r, g, b$	t $M \simeq 175$ GeV, $Q = \frac{2}{3}$, color $= r, g, b$
d $M \simeq 0.006$ GeV, $Q = -\frac{1}{3}$, color $= r, g, b$	s $M \simeq 0.1$ GeV, $Q = -\frac{1}{3}$, color $= r, g, b$	b $M \simeq 4$ GeV, $Q = -\frac{1}{3}$, color $= r, g, b$

Vector-bosons, Spin=1

Electroweak Force Propagators

γ $M = 0$ GeV, $Q = 0$	$W^\pm$ $M \simeq 80.4$ GeV, $Q = \pm 1$	Z^0 $M \simeq 91$ GeV, $Q = 0$

Strong Force Propagators

g $M = 0$ GeV, $Q = 0$, 8 color varieties

Scalar-boson, Spin=0

Higgs $M =?$ GeV, $Q = 0$

Table 1.1: Summary of the fundamental particles which make up the Standard Model of particle physics. The electric charge Q is in units of positron charge, M is the particle mass, and the three colors are labeled red (r), green (g), and blue (b).

because they have large masses—about 10^5 times larger than the electron mass. This accounts for the substantial difference in the strengths of the electromagnetic and weak forces.

The $W^{\pm}$ and Z^0 masses are a problem for the SM, which is a theory that obeys a local gauge invariance symmetry. This symmetry lies at the very foundation of the model. However, gauge invariance works only if the associated gauge-bosons are massless. Thus the electroweak symmetry must be hidden or 'broken'. This "mass problem" is different from the other mass problem in the Standard Model, which is the problem of accounting for the origin and broad distribution of fermion masses. The first requires a knowledge of electroweak symmetry breaking, while the second also requires an understanding of the Yukawa couplings which set the scale for the fermion masses.

In the Standard Model, the Higgs mechanism [Hig64] accounts for (but does not predict) both the gauge-boson and the fermion masses. The mechanism introduces a new complex scalar (spin=0) doublet field, which provides 4 extra degrees of freedom for the model. Three of these degrees of freedom are 'eaten' by the electroweak gauge-bosons and manifest themselves as the $W^{\pm}$ and Z^0 particle masses. The fourth degree of freedom appears as the scalar Higgs particle, for which the mass is also not predicted. The fermions also couple with the Higgs field to acquire mass. This mechanism is successful at providing for the gauge-boson masses while maintaining gauge invariance.

At large distance scales, the photon (γ) is the only SM force propagator which is noticeable. It is only at sub-atomic distances that the other forces become important. Probing small distance scales is equivalent to probing large energy scales—the quantities are related by the De Broglie wavelength—and so the interaction point of colliding beam accelerators provides a powerful probe for investigating the fundamental structure of nature in a domain where all of the particles of Table 1.1 are relevant.

Gravity is not part of the Standard Model, and its absence is the clearest indication that the SM is a low energy approximation to a more fundamental underlying theory.

Gravity is so feeble in comparison to the other forces that it can be completely ignored at the energy scales relevant for high energy physics. Nevertheless, the quest for a theory that incorporates gravity, and unifies it with the other forces to produce a Grand Unified Theory (GUT), is considered the 'holy grail' of the field.

Quantum Chromodynamics

The strong force, propagated by gluons, is governed by Quantum Chromodynamics (QCD) which is based on the $SU(3)_C$ gauge symmetry. Gluons are the propagators of QCD. They are massless and carry no electric charge, but carry both color and anti-color 'charge'. They come in 8 varieties corresponding to the $SU(3)_C$ color octet states. Color is the QCD analogue of charge in electromagnetism. However, since in QCD the gluons carry color charge, they may participate in 'self-interactions'—whereas photons do not carry electric charge, and so they do not couple to other photons. Thus gluon-gluon couplings are allowed in the SM, whereas photon-photon couplings are not.

One of the properties of QCD is *asymptotic freedom*, wherein the strong coupling constant α_S becomes small at high energy or short distance scales (i.e. $\alpha_S \to 0$ as the energy scale $\to \infty$). It is only in this high energy domain that a valid description of QCD can be obtained with perturbative mathematics.

The strong force potential between a quark-antiquark pair takes the form $-\frac{4}{3}\frac{\alpha_S}{r} + kr$, where k is a constant and r is the distance separating the two quarks. The second term gives rise to a property known as *color confinement*. As a direct result of this confinement, quarks and gluons can never be observed in isolation. Instead, they appear in nature as color-singlet (i.e. color neutral) mesons or baryons which are combinations of two or three quarks respectively.

As a (color connected) quark-antiquark pair is pulled apart, the color confinement term in the potential dictates that the energy grows linearly, until eventually there is enough energy to produce a new quark-antiquark pair from the vacuum. This results in the phenomenon of *jets* at high energy. When a quark is recoiling against an antiquark, the energy stored in the potential is transformed into more quark-

antiquark pairs, the net result being two collimated streams of hadrons called jets.

The unification of QCD with electroweak theory into a single quantum theory is one of the fundamental goals of theoretical particle physics. Several promising avenues exist for this unification, Supersymmetry being a favored candidate at present.

Electroweak interaction

Electroweak theory is based on the $\mathrm{SU}(2)_L \times \mathrm{U}(1)_Y$ gauge symmetry, which is briefly sketched in this section. $\mathrm{SU}(2)_L$ is a non-Abelian group containing three generators $W^1_\mu, W^2_\mu, W^3_\mu$ to which three massless gauge-bosons are associated. The subscript L means that the associated gauge symmetry only applies to the chiral left component of fermions. The $\mathrm{SU}(2)_L$ symmetry manifests itself as weak isospin invariance. The Abelian $\mathrm{U}(1)_Y$ group is associated with another massless gauge-boson, with B_μ as its generator. The conserved quantum number associated with the $\mathrm{U}(1)_Y$ symmetry is weak hypercharge, $Y = 2(Q - T_3)$, where Q is the electric charge and T_3 the weak isospin.

The fermions are grouped into left-handed (i.e. chiral left) weak isospin doublet fields, and right handed singlets. For the quarks, these fields may be represented,

$$\begin{pmatrix} u_i \\ d'_i \end{pmatrix}_L, \; u_{iR}, \; d_{iR} \tag{1.1}$$

where i denotes the quark generations and d' denotes the weak eigenstate of the quark mixing matrix, which is related to the mass eigenstates through the Cabibbo-Kobayashi-Maskawa matrix V_{ij} by $d'_i = \sum_j V_{ij} d_j$.

At this stage both the gauge-bosons and fermions are massless, a necessary condition for gauge invariance in this (as yet incomplete) model. The Higgs field is represented by a complex doublet

$$\begin{pmatrix} \phi^+ \\ \phi^0 \end{pmatrix} = \begin{pmatrix} \frac{\phi_1 + i\phi_2}{\sqrt{2}} \\ \frac{\phi_3 + i\phi_4}{\sqrt{2}} \end{pmatrix}. \tag{1.2}$$

By minimizing the Higgs potential, the 4 degrees of freedom associated with the Higgs doublet are reparametrized such that 3 of them undergo a phase transformation [Hig64], introducing 'spontaneous symmetry breaking' to the model and providing three of the gauge-bosons with mass and leaving one massive scaler Higgs

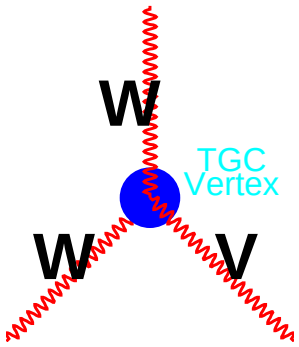

Figure 1.1: The three gauge-boson vertex is the interaction between the particles which propagate the electroweak force. In this cartoon, a W-boson is interacting with a V-boson (where V denotes either a photon γ or a Z^0-boson).

particle. After symmetry breaking, the physical gauge fields representing the photon, W^+, W^-, and Z^0 emerge, and are related to the massless fields by

$$\begin{pmatrix} W_\mu^+ \\ W_\mu^- \\ Z_\mu^0 \\ A_\mu \end{pmatrix} = \begin{pmatrix} 1 & -i & 0 & 0 \\ 1 & +i & 0 & 0 \\ 0 & 0 & \cos\theta_W & -\sin\theta_W \\ 0 & 0 & \sin\theta_W & \cos\theta_W \end{pmatrix} \begin{pmatrix} W_\mu^1 \\ W_\mu^2 \\ W_\mu^3 \\ B_\mu \end{pmatrix} \tag{1.3}$$

where $W_\mu^\pm$ are the massive $W^\pm$-boson fields, Z_μ^0 is the massive Z^0-boson field, A_μ is the massless photon field, and θ_W is the Weinberg electroweak mixing angle.

Neglecting the fermion masses and mixings, the electroweak sector of the Standard Model has four free parameters: the coupling constant $\alpha_{\rm QED}$, the gauge-boson masses M_Z, M_W and the Higgs mass M_H. QCD introduces another parameter,[2] the strong coupling $\alpha_{\rm S}$, for a total of 5 free parameters in the bosonic sector of the Standard Model.

In the Standard Model (SM), only the $W^\pm$ couples to other gauge-bosons. These interactions are often referred to (rather loosely) as 'self-interactions', because they involve interactions between gauge-bosons. The simplest manifestation of these gauge-boson 'self-couplings' is the WWZ and $WW\gamma$ interaction vertices, shown in Figure 1.1. ZZZ, $ZZ\gamma$, $Z\gamma\gamma$, and $\gamma\gamma\gamma$ vertices are not allowed in the model, because neither the Z nor the γ carries charge or weak isospin which are the quantum numbers to which the gauge-bosons couple. Vertices containing an odd number of W-bosons (WZZ, $W\gamma\gamma$, $WZ\gamma$, WWW) are excluded by charge conservation.

[2] A second parameter, $\theta_{\rm QCD}$, is allowed in QCD theory and gives rise to strong CP violation. The term can be neglected in the context of perturbation theory [Ell96], and so does not enter into the Feynman rules. From measurements of the dipole moment of the neutron [Che88], $\theta_{\rm QCD}$ is constrained to be smaller than 10^{-9} and so it is plausible to assume it is exactly zero. The seemingly fine tuned smallness of the parameter is referred to as the strong CP problem.

Phenomenology relevant to triple gauge-boson couplings will be discussed further in Chapter 3. This thesis focuses on how the properties of the WWZ and $WW\gamma$ couplings can best be measured in TeV scale proton-proton collisions.

1.2 The Large Hadron Collider at CERN

High energy hadronic collisions provide an excellent probe for studying fundamental interactions like the triple gauge-boson vertices discussed above. At sufficiently high energy, the constituent elementary partons inside the protons are resolved, and participate directly in reactions. The center-of-mass energy of these partonic collisions occurs over a broad range. In this manner, using fixed energy proton beams, one can probe a broad spectrum of energy regimes. The basic structure of proton-proton collisions is illustrated in the cartoon of Figure 1.2, which shows the production of a $W\gamma$ gauge-boson pair, as an example of one proton-proton collision reaction or *event*. The diagram is time ordered from left to right. Initially two groups (or *bunches*) of protons are approaching one another. A constituent quark from one proton interacts with a constituent antiquark from another proton. The reaction produces a photon (γ) and a W^--boson. The photon is stable, but the W^- is not—it decays to an electron and antineutrino. The physics which is of primary interest for the study presented here is depicted as a small explosion in the center of the figure—our focus is in the study of this physics with a high energy hadron collider.

The Large Hadron Collider (LHC) [LHC95] is a 14 TeV proton-proton collider designed to push the energy of the constituent parton collisions forward to the Tera-electronvolt (TeV) scale. The accelerator is currently being constructed at the European Organization for Nuclear Research (CERN) laboratory near Geneva, Switzerland. In this section the LHC accelerator complex and physics environment are described.

1.2.1 Injection complex

Before entering the LHC itself, particles pass through a chain of injector machines shown in Figure 1.3. This chain re-uses upgraded versions of existing CERN acceler-

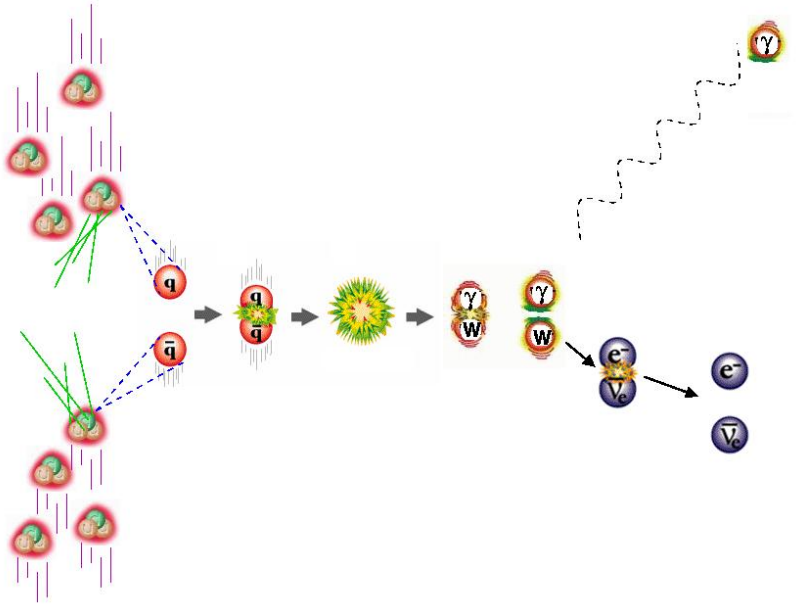

Figure 1.2: The basic features of a proton-proton collision are illustrated. In this figure time progresses from left to right. Initially two groups (or *bunches*) of protons are approaching one another. A constituent quark from one proton interacts with a constituent antiquark from a proton moving in the opposite direction. The reaction produces a photon (γ) and a W^--boson. The photon is stable, but the W^- is not—in this example it decays to an electron and antineutrino.

ators and particle sources. The journey starts at the Proton Linac2, a 50 MeV linear accelerator which injects the particles into the 50 m diameter Proton Synchrotron Booster (PSB).

The Linac2 began operation in 1978, and employs the traditional linac design. It is fueled by a continuous hydrogen ion (i.e. proton) source, called the duoplasmatron. The linac itself consists of a series of drift tubes charged which alternating currents to provide electric fields, as shown in Figure 1.4. The drift tube spacing varies in length, getting progressively longer further away from the ion source. Each length is chosen such that as the protons travel down the linac attaining ever greater velocity, they spend an equal amount of time between each set of drift tubes. The protons from the source which are in sync with the radio frequency (RF) timing are accelerated down the linac, remaining in-time with the electric field and receiving a kick at each drift tube. Thus each RF cycle produces a group—or *bunch*—of protons.

Every second the Linac2 produces a pulsed beam of 50 MeV protons about 20-150 μs long. The original design provided currents up to 150 mA, which is insufficient for the high LHC luminosity. The output has been upgraded to 180 mA, an intensity which was achieved in November 1999.

In the PSB, protons are accelerated by RF cavities as they travel in a circular path being bent and focused by dipole and quadrupole magnets. The PSB is a synchrotron accelerator, which means the ring of magnets is at a fixed radius (25 m for the PSB), and the magnetic field strength is increased proportional to the particle momentum as the protons are accelerated. The RF frequencies are timed such that they keep pace with the particles as they circle the ring. At injection time, the RF operates at 0.6 MHz, which increases to 1.7 MHz when the protons are ejected with 1.4 GeV momentum to continue their journey on to the Proton Synchrotron (PS).

The 200 m diameter Proton Synchrotron (PS) was built in 1954 in parallel with CERN's first operating accelerator, the Synchro-Cyclotron. The PS has two important roles. The first is simple acceleration, bringing the protons up to 25 GeV from their injection energy of 1.4 GeV. The PS has provided over 40 years of service in this role. While circulating at top energy, the beam will be allowed to debunch, and

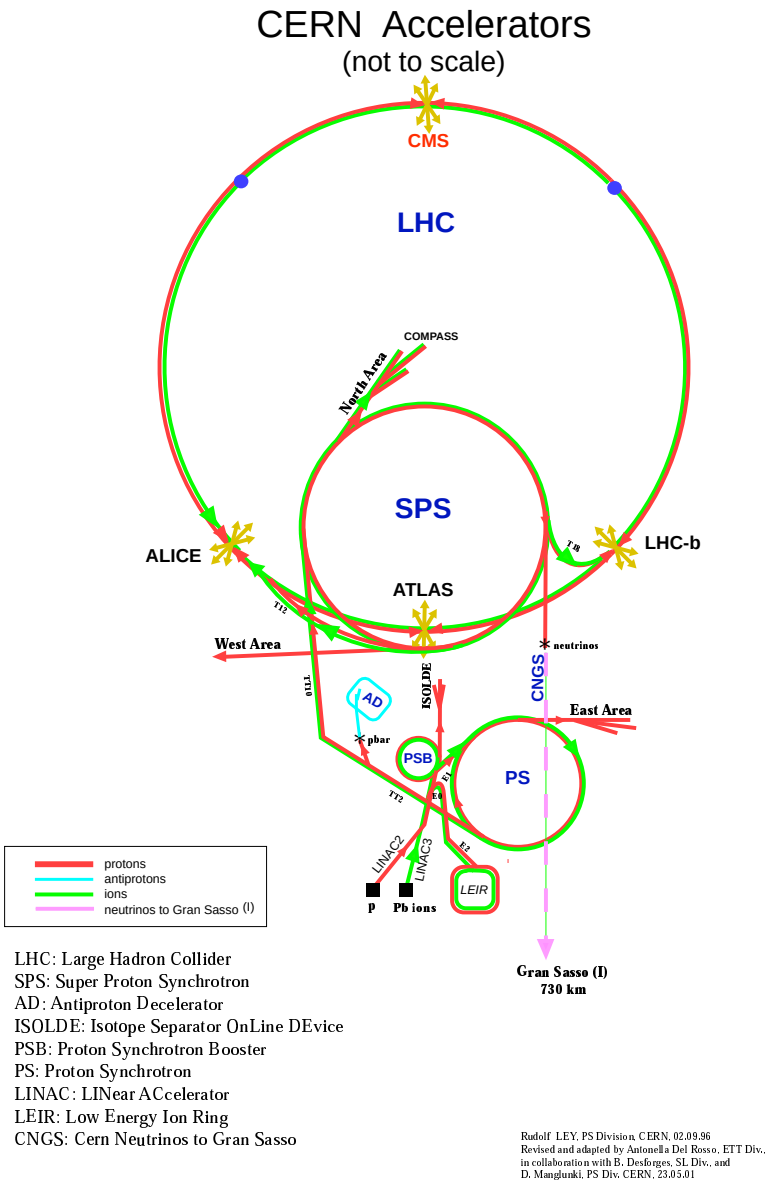

Figure 1.3: The accelerator complex at CERN is shown with the locations of the four LHC experiments ATLAS, CMS, LHCb, and ALICE indicated. The circumference of the LHC ring is 26.7 km.

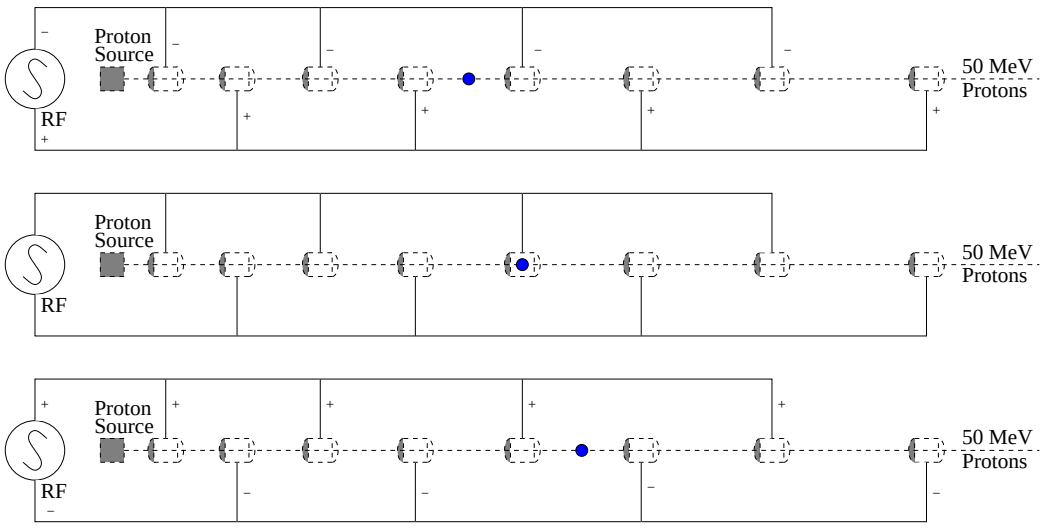

Figure 1.4: Schematic diagram of a proton being accelerated in a linac at three subsequent stages of a single RF cycle. The electric fields are timed such that when the proton (indicated by a small solid dot, which more accurately represents a 'bunch' of protons) is between drift tubes, it is being pushed by a positive charged drift tube from behind and pulled by a negatively charged one from in front (top and bottom). The charge on the drift tubes is neutral when the protons pass through them (middle).

will be subsequently recaptured using new 40 and 80 MHz RF cavities (the 40 MHz system adiabatically captures the beam with the correct bunch spacing, while the 80 MHz system system compresses the bunches longitudinally). This achieves the second function of the PS, producing the 25 ns bunch spacing required by the LHC.

At this energy the protons are highly relativistic, traveling at about 0.999 times the speed of light. Matter is limited to travel at speeds below that of light, and so the protons will remain at essentially constant velocity even when they are 'accelerated' to higher energy. As such, the RF timing can be kept approximately constant, and the 25 ns (40 MHz) bunch spacing can be maintained through subsequent stages of acceleration.

The protons receive their next stage of acceleration at the Super Proton Synchrotron (SPS) where they are boosted up to 450 GeV in a 6.9 km circumference ring. In the 1980's the SPS was used to accelerate and collide protons with antiprotons which allowed the UA1 and UA2 collaborations to confirm the unification of the electromagnetic and weak forces through the 1983 discovery of the $W^{\pm}$ and Z^0

gauge-bosons [UA1 83b, UA2 83a, UA1 83c, UA2 83b]. Since the SPS is limited by the total amount of particles it can accelerate, 12 separate SPS pulses will be used to fill each LHC ring. Each acceleration cycle takes 2.4 seconds and in this time the protons travel a distance inside the SPS equal to about 17 rotations around the earth. The total time required to fill both LHC rings is about seven minutes, including the rise and fall times of the various magnets.

1.2.2 The main accelerator

The LHC will be housed in the 26.7 km tunnel which was excavated for its predecessor, the Large Electron Positron (LEP) Collider. The machine consists of two colliding proton synchrotrons capable of accelerating protons from their injection energy of 450 GeV up to the design energy of 7 TeV. The beams will circulate and intersect for about 10 hours, before the number of protons in the beam is reduced enough to justify starting the injection and acceleration process again.

The magnetic field B (in T) required to bend a charged particle with momentum p (in GeV) in a circular orbit of radius R (in m), is $B = \frac{P}{0.3R}$. For a 7 TeV proton beam, this implies a magnetic field of 5.4 T applied everywhere along the particle's path—in practice space needs to be reserved for other purposes (RF accelerating cavities, cleaning insertions, quadrupole magnets, etc.) and so the bending field needs to be about 50% higher. Conventional iron-cored magnets are limited to magnetic fields of about 2 T, so superconducting[3] technology is necessary for the LHC magnets.

Anti-parallel magnetic fields in two separate evacuated channels are required to bend the counter-rotating proton beams along their circular path. Traditionally, this would be accomplished with two separate strings of magnets installed side-by-side in their own cryostats. The LHC employs a novel twin-aperature design, shown in Figure 1.5, wherein both beam channels are contained in a single yoke and cryostat. Combining two sets of windings in a common magnetic and mechanical structure is compact and efficient, because the field in one aperature is increased by the return

[3]Superconducting materials, which usually operate at very low temperatures, conduct electric current without resistance or power loss.

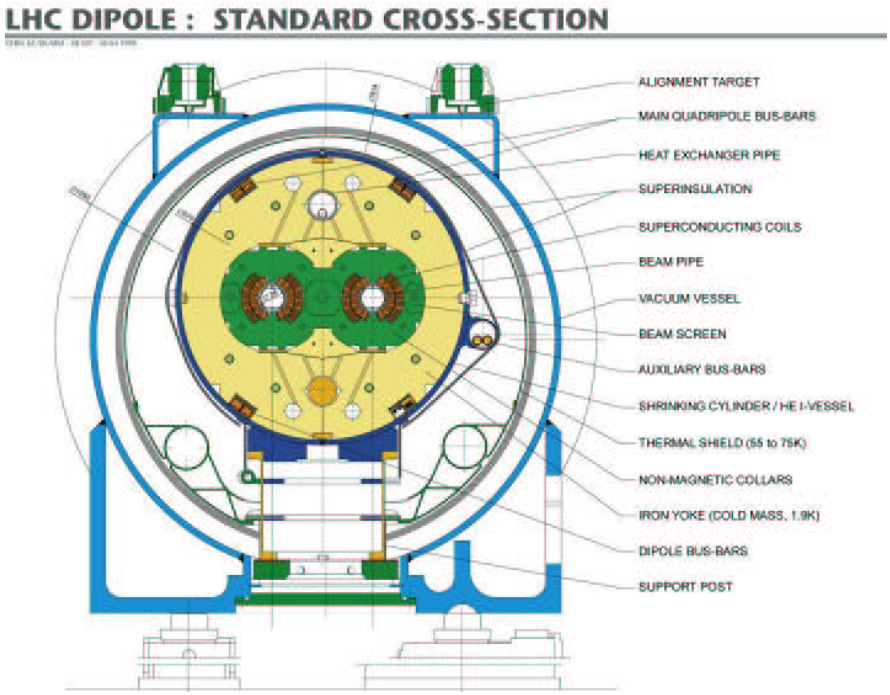

Figure 1.5: Transverse cross-section of the LHC twin-aperature 8.33 T superconducting dipoles. [LHC95]

flux of the other.

The magnets represent the forefront of superconducting magnet technology, operating at cryogenic temperatures over many kilometers and producing a magnetic field of 8.33 T. The coils are constructed of copper-clad niobium-titanium cables in a bath of 1.9 K superfluid helium. The bending power for the LHC is provided by 1232 main dipole magnets. The beam will be focused using 400 main superconducting quadrupole magnets with a gradient of 223 T/m, and many thousands of other superconducting magnets for steering the beams, colliding, and correcting multipole errors. The magnets are being constructed by industry in Europe, Japan, India, and the USA.

The particle acceleration in the LHC will be accomplished with eight superconducting 400 MHz RF cavities per beam. The RF cavities replenish the energy (about 6.7 KeV per revolution) which the protons lose to synchrotron radiation.[4] The cav-

[4]Charged particles radiate photons when they are bent in a magnetic field, a process known as synchrotron radiation. The amount of energy lost is inversely proportional to the particle mass to the fourth power (M^{-4}). This makes it considerably easier to accelerate protons (mass $\simeq$ 1 GeV)

ities operate at a rate 10 times faster than the bunch spacing, which serves to keep the longitudinal spread of the bunches to a minimum (the bunch length will be about 75 cm).

An immense amount of energy, about 334 MJ, will be stored in each proton beam as they circulate in the ring.[5] Surrounding the beam-pipes will be the 1.9 K superfluid helium. The beams have to be very well collimated, because losing a tiny fraction of the beam particles into the magnets would deposit enough energy to raise the superfluid helium above its critical temperature, quenching the magnets. To achieve this, there will be two cleaning insertions in the ring, located equidistant between the ATLAS and CMS experiments. The cleaning insertions consist of 500 m straight sections where the halo of the beam is peeled off with collimators. Because of the heat this creates when the halo protons shower, the magnets will be traditional warm iron core dipoles and quadrupoles. The warm twin aperature quadrupoles are one of the Canadian contributions to the accelerator.[6]

1.2.3 The LHC environment

The two superconducting channels of the accelerator will be filled with 2835 bunches of 10^{11} protons each. The bunches are spaced at intervals of 25 ns, and will be made to cross 40 million times per second at the center of the LHC detectors. Each time the bunches cross, an average of about 25 proton-proton interactions will occur at a center-of-mass energy of 14 TeV. This amounts to a total inelastic event rate of approximately one billion proton-proton interactions per second at each interaction point when the LHC is operating at its design luminosity[7] of $10^{34}\text{cm}^{-2}\text{s}^{-1}$. These conditions are referred to as 'high luminosity running'. Initially when the collisions

to very high energy than it is to accelerate electrons (mass $\simeq$ 0.0005 GeV), since electrons would loose a factor 10^{13} more energy per revolution than protons assuming equivalent particle energy and bending radius.

[5]This is roughly equivalent to the kinetic energy of a freight train traveling at full speed.

[6]When CERN physicist Gijs de Rijk showed the author the warm twin aperature quadrupoles he said, "beautiful aren't they? ... but we didn't know that until two weeks after they arrived because we had to order a Robertson's screw driver from Canada to open the crates they were shipped in". A Robertson's screw driver has a square tip, and is (apparently) only used in Canada.

[7]The event rate is given by the cross section times the luminosity, thus the number of events for a given process is directly proportional to the integrated luminosity.

Process	Events per LHC Low Luminosity Year
total inelastic event rate	10^{15}
$pp \to t\bar{t} + X$	6.1×10^{6}
$pp \to b\bar{b} + X$	7.0×10^{12}
$pp \to Z^0/\gamma + X$ with $\sqrt{\hat{s}} > 10$ GeV	1.1×10^{9}
$pp \to W^{\pm} + X$	1.8×10^{9}
$pp \to W^{+}W^{-} + X$	7.7×10^{5}
$pp \to W^{\pm}Z^0 + X$	2.9×10^{5}
$pp \to Z^0Z^0 + X$	1.2×10^{5}
$pp \to Z^0\gamma + X$ with $P_{\gamma}^{T} > 10$ GeV	1.4×10^{6}
$pp \to W^{\pm}\gamma + X$ with $P_{\gamma}^{T} > 10$ GeV	1.8×10^{6}

Table 1.2: Inclusive event rates are presented for some of the processes of interest at the LHC. The event rates are for one year of low luminosity LHC running, which corresponds to an integrated luminosity of 10 fb^{-1}. The cross sections are calculated at leading order with the general purpose event generator Pythia 6.152 [Sjö01a] using the program's default parameters.

begin in 2006, the LHC will operate for a 'low luminosity' period at $10^{33}\text{cm}^{-2}\text{s}^{-1}$.

At this energy scale, the fundamental constituents of the proton—quarks and gluons—will be resolved. The protons are composed of three valence quarks *uud* and a sea of other quarks, anti-quarks, and gluons which are constantly being created and annihilated. Each of these constituents will carry a fraction of the proton's momentum, and it is these fundamental particles which will be initiating the high transverse momentum physics which will be studied at the LHC. The interactions will occur over a broad range of energy scales, and the energy of individual interactions will not be dictated by the machine parameters. This provides the ideal conditions to search for a broad range of new phenomena.

Among the multitude of interactions will be the events which represent the physics of interest. They typically occur at rates many orders of magnitude below the total inelastic event rate. Table 1.2 shows the event rates for a few of the processes which will be studied at the LHC. The processes of interest for this study are $W\gamma$ and WZ diboson production, which occurs once every billion or so events. This is the primary challenge of a high luminosity hadron collider like the LHC: building a detector which is capable of providing accurate 'images' of the interesting events

among the multitude of other ordinary events, many of which will be occurring simultaneously. Though the interesting events will be rare in comparison to the total event rate, they are nevertheless extremely abundant in the absolute sense which allows for precision studies of the physics they embody. These huge event rates constitute the strongest asset for the LHC. The production of a top-quark pair, for example, will occur approximately once every second at the LHC—which should be compared to the handful of top events at Tevatron Run I which allowed for the discovery of this particle in 1995 [CDF95, D0 95].

Four experiments have been approved for operation at the LHC, and will produce images of the reactions which occur at the four points on the LHC ring where the beams cross (Figure 1.3). ATLAS [Atl94a] and CMS [CMS94] are multi-purpose experiments whose primary goal is to discover the origin of electroweak symmetry breaking and to probe for new physics which may emerge at the TeV energy scale. The present study is conducted in the context of the ATLAS experiment. LHCb [LHCb95] is a dedicated B-physics detector optimized for measurements of CP violation in beauty-meson decays, which is relevant for an understanding of the matter-antimatter asymmetry in the universe. Both CMS and ATLAS will also be pursuing beauty-physics programmes. The LHC is capable of accelerating and colliding heavy ions as well as protons. The ALICE [Ali95] experiment is a dedicated heavy ion detector designed to study ion-ion and ion-proton collisions, providing information about strongly interacting matter at extreme energy density. This should allow the creation and exploration of the quark-gluon plasma, a phase transition wherein quarks and gluons are deconfined. This transition *to* the plasma is the inverse of the plasma to hadronic matter transition that is believed to have happened 10 μs after the big bang. CMS will also operate when LHC is in heavy ion mode. ATLAS is currently exploring the possibilities of using its detector for heavy ion physics, but has not submitted a proposal to the CERN management at this time.

1.2.4 LHC Schedule

The commissioning of the LHC is currently scheduled to begin in January 2006. An initial pilot run in April 2006 is expected to produce the first collisions. The first physics run is scheduled for August 2006. Initially the accelerator will run in low luminosity (10^{33} cm^{-2}s^{-1}) mode, providing the experimental collaborations time to understand their detectors, and extract the precision physics measurements for which systematic errors dominate. On the scale of one to three years, as the accelerator division learns how to control and optimize the machine, the LHC will be ramped up to its design luminosity, 10^{34} cm^{-2}s^{-1}. This high luminosity environment provides the best opportunities to search for new exotic physics processes, but is particularly challenging for the detectors. The TGC analysis presented in this thesis is optimized for low luminosity LHC conditions.

1.3 The ATLAS Detector

The signal and background modeling for the research presented in this thesis have been simulated in the context of the ATLAS detector. In this section the detector's general design and performance is reviewed.

ATLAS is one of two multi-purpose detectors designed to exploit the physics potential of the LHC. The ATLAS detector, like the LHC, is currently under construction. The detector is being built by an international collaboration of about 1850 physicists, engineers, and technicians from 34 countries. The Canadian particle physics community is heavily involved with the ATLAS project, with about 90 people from 9 institutions[8] contributing.

ATLAS has been optimized for the physics processes expected to appear as the TeV energy frontier is explored. Foremost among the possibilities is the search for the origin of electroweak symmetry breaking which is expected to manifest itself as the Higgs boson or Higgs-like particles. The Higgs mass is not predicted by the Standard

[8]Canadian institutions involved in the ATLAS collaboration are: the University of Alberta, University of British Columbia, Carleton University, Université de Montréal, Simon Fraser University, University of Toronto, TRIUMF, University of Victoria, and York University.

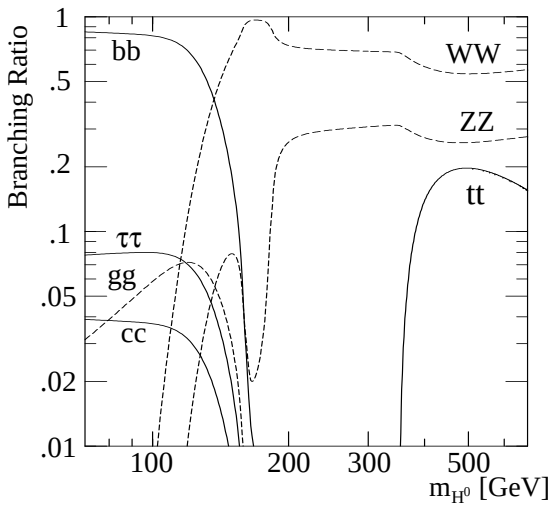

Figure 1.6: The branching ratios of the Standard Model Higgs boson [PDG00b] depend strongly on the Higgs mass, meaning there are a wide variety of Higgs signatures for which the detector needs to be optimized. The $H^0 \to \gamma\gamma$ branching ratio peaks at 0.002 for a Higgs mass of 125 GeV, and is too small to appear on the scale of the figure.

Model, and the branching ratios for its decay products (shown in Figure 1.6) depend strongly on its mass. This means there are a variety of Higgs signatures to prepare for, as well as the broad scope of other new physics—such as supersymmetry—which might appear.

ATLAS is composed of several sub-detectors, each optimized to detect some aspect of the collision event. The overall structure of the detector is cylindrically symmetric and is shown in the cut-away view of Figure 1.7. The inner detector sits closest to the beam and is immersed in the magnetic field of the central solenoid. It is responsible for tracking, particle identification, and locating displaced decay vertices. Around the inner detector are the calorimeters, which absorb electrons, photons, and hadrons providing position and energy measurements. High energy muons deposit very little energy as they pass through dense material, allowing them to escape the detector without being absorbed. The last layer of sub-detectors is the muon system, which measures the trajectories of muons as they move in a curved arc through the detector's magnetic field. The exterior dimensions of the ATLAS detector are defined by the muon spectrometer with a radius of 11 m (making ATLAS about 8 stories high) and a total length of 42 m between the outer-most muon chambers. The complete detector weighs over 7000 tons. A comprehensive description of the detector sub-systems can be found in Ref. [Atl99a] and references therein. In the sections which follow, each of the sub-systems is briefly reviewed. A summary of the systems is presented in

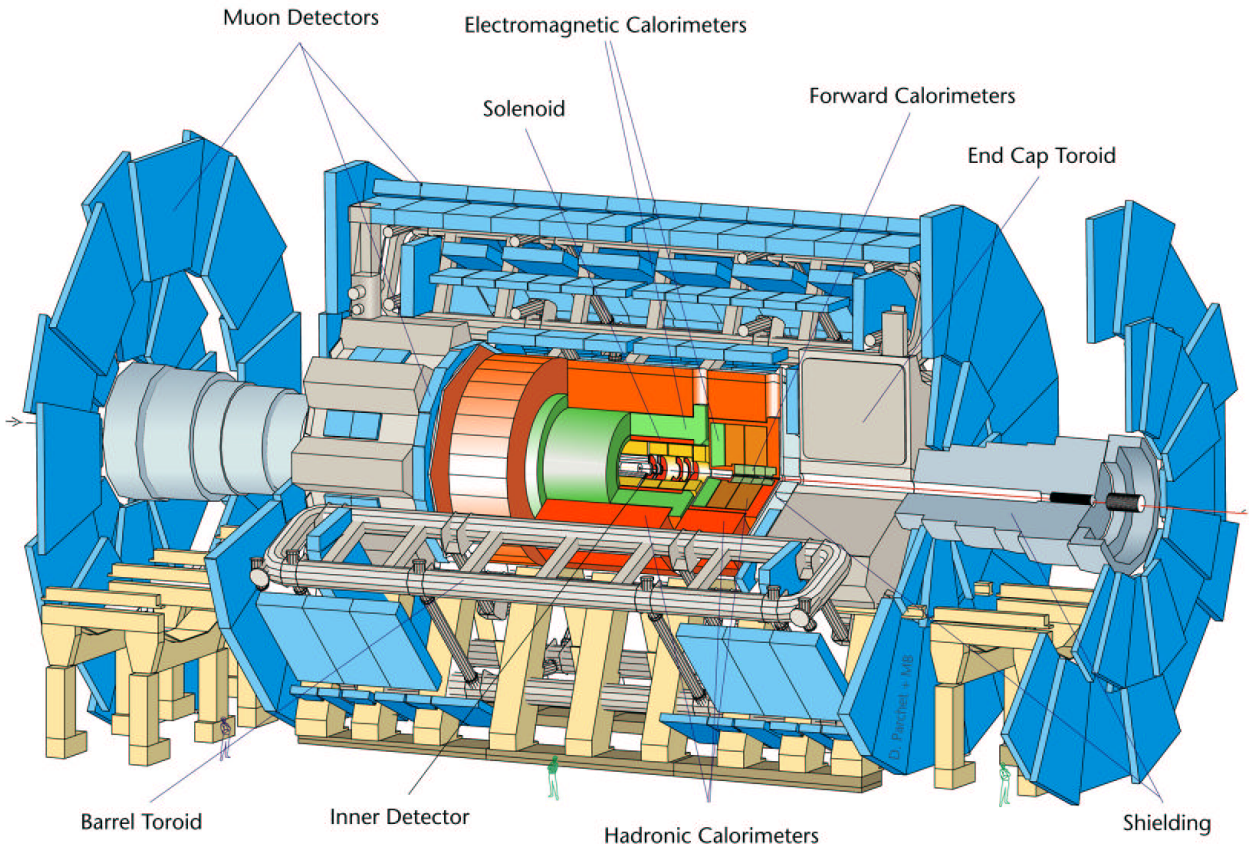

Figure 1.7: A cut-away view of the ATLAS detector is presented with the major sub-systems indicated [Atl99a, Fig. 1-i]. The outer radius of the detector is 11 m.

Table 1.3.

A relatively new development for the ATLAS collaboration has been the possibility of "staging" some components of the detector installation, i.e. delaying the construction and installation of some detector elements beyond the time that the first data is collected. The study presented in this thesis assumes a complete ATLAS detector—the staging of detector components has not been included in the detector simulation. The scenario for a staged ATLAS detector installation is briefly reviewed in the Appendix of this thesis.

System	Description	Performance
Magnets	solenoid surrounding inner detector	2 T
	3 air core toroid magnets for muon system	3.9-4.1 T
Inner Detector	silicon pixels and strips transition radiation tracker with electron/hadron separation capabilities	$\frac{\sigma}{P_T} = \frac{P_T(\text{GeV})}{2000} \oplus 0.01$
EM Calorimeters	lead / liquid argon	$\frac{\sigma}{E} = \frac{10\%}{\sqrt{E(\text{GeV})}}$
Hadron Calorimeters	barrel: iron scintillator forward: copper & tungsten / liquid argon	$\frac{\sigma}{E} = \frac{50\%}{\sqrt{E(\text{GeV})}} \oplus 0.03$
Muon Spectrometer	air core: precision and fast trigger chambers	$\frac{\sigma}{P_T} \simeq 10\%$ at 1 TeV

Table 1.3: The main features and performance parameters of the ATLAS detector are presented. The symbol $\oplus$ indicates the terms are added in quadrature.

1.3.1 Magnet system

The ATLAS magnet system curves the trajectories of charged particles allowing for measurements of particle momenta and charge identification. The direction the particles rotate around the magnetic field indicates the sign of their electric charge, while the radius of curvature is inversely proportional to their momentum. The layout of the ATLAS magnets can be seen in Figure 1.7.

The superconducting central solenoid provides the inner detector with a 2 T magnetic field. The central solenoid is positioned between the inner detector and the electromagnetic calorimeter (EMC), and so has been designed to be as thin as possible so as to minimize its effect on the EMC performance. To further reduce the material in front of the EMC, the central solenoid and EMC share a single cryostat.

The magnetic field for the muon spectrometer is provided by three superconducting air core toroid systems: the barrel and 2 end-caps. The field from these magnets is very different from the one provided by the solenoid. It encircles the beam-line and is perpendicular to it, deflecting muons in the plane defined by the muon position and the beam axis.

The barrel region uses eight 3.9 T peak field toroids arranged azimuthally and symmetrically around the calorimetry. The barrel coils are housed individually in separate cryostats, which absorbs the forces between the coils. Two end-cap toroids, housed in two cryostats, provide a peak magnetic field of 4.1 T. They are inserted in

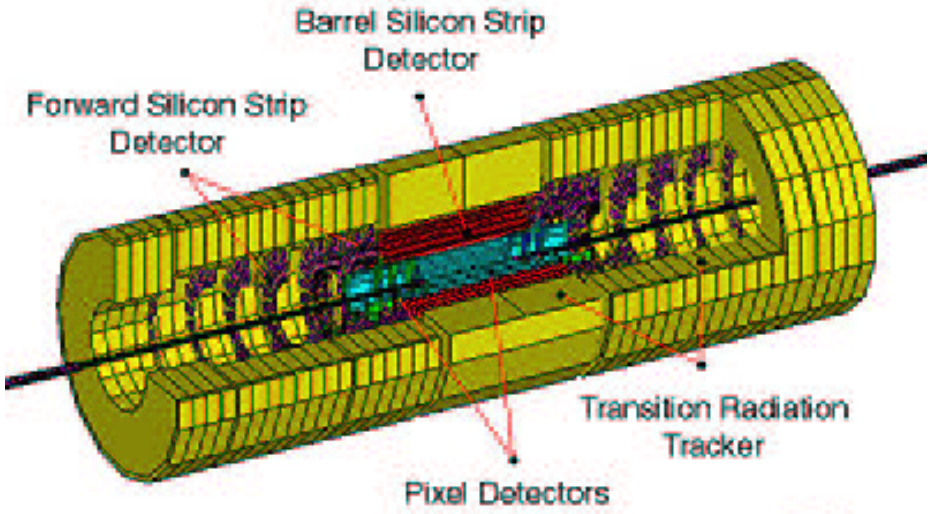

Figure 1.8: A cut-away view of the ATLAS inner detector is shown [Atl97a]. The outer radius of the inner detector is 1.15 m.

the barrel toroids and line up with the central solenoid. The entire magnet system is cooled indirectly by a forced flow of helium at 4.5 K through tubes which are welded on the casing of the coil windings.

1.3.2 Inner detector

The inner detector (ID), shown in Figure 1.8, is located closest to the interaction point in a cylinder of radius 1.15 m and length 6.8 m. The ID performs pattern recognition, momentum and vertex measurements, and enhanced electron identification. It provides coverage over the "region of precision physics" extending across the central pseudo-rapidity[9] region of $-2.5 \leq \eta \leq 2.5$ (i.e. it extends down to an angle of 9.4° from the beam-line on either side). The detector is immersed in the 2 T magnetic field of the central solenoid which is oriented parallel to the beam axis in order to curve the trajectories of charged particles in the plane transverse to the beam.

[9]Pseudo-rapidity, $\eta = -\ln\tan\frac{\theta}{2}$ where $\cos\theta = \frac{P_z}{p}$, is the high energy ($p \gg m$) approximation to rapidity, $y = \frac{1}{2}\ln\frac{E+p_z}{E-p_z}$. Rapidity is a useful kinematic variable for hadron collider physics since the shape of the rapidity distribution $\frac{dN}{dy}$ is invariant under a longitudinal boost. Since pseudo-rapidity has a one-to-one relationship with the polar angle and is a good approximation of rapidity at high energy, it is the natural angular measure for high energy hadron collider detectors.

The ID consists of three different detector systems: a combination of discrete high-resolution pixel and strip detectors in the inner part of the tracking volume and continuous straw-tube tracking detectors with transition radiation capability in the outer part.

The pixel sensors measure displaced vertices and provide the first 'hits' for reconstructing particle tracks. They consist of thin layers of silicon divided into pixels 50×300 microns in size. There are about 140 million pixel channels in total arranged in three cylindrical layers surrounding the beam axis at average radii of 4 cm, 10 cm, and 13 cm, and five disks on either side. The pixel detectors provide the high precision position measurements needed to identify particles which originated from displaced vertices. This is particularly important for identifying the decay products of short lived particles like B-mesons and τ-leptons, which typically travel only a few millimeters before decaying.

The semiconductor tracker (SCT) provides 8 more precision measurements per track at radii ranging from 30 to 52 cm. The integrated surface area of the strips is over 60 m^2, making it an order of magnitude larger than previous generations of silicon microstrip detectors. The layers are composed of narrow stereo strips of silicon 80 microns wide and a few centimeters long. The stereo layers run at an angle of 2.3° relative to each other, allowing for localization of the hits.

Silicon technology is too expensive for coverage at larger radii. The transition radiation tracker (TRT) provides continuous coverage extending 56 to 107 cm from the beam-line. The detector is based on gas-wire drift detectors called straw tubes. Each wire is housed in its own 4 mm diameter tube which is filled with an appropriate gas (70% Xe, 20% CO_2, 10% CF_4), and high voltage is maintained between the metalized tube wall and the wire. The straw tubes are able to operate at very high rates because of the isolation of the sense wires within small individual gas volumes. When a charged particle traverses the tube, it ionizes the gas, producing free electrons which drift to the center wire. By accurately measuring the timing of the current in the wire, the distance of the particle's trajectory from the wire can be inferred.

As its name implies, the TRT has a second role as a transition radiation detec-

tor. Highly relativistic electrons will radiate collimated X-rays as they traverse the interfaces between materials of different dielectric constants. The number of radiated photons is proportional to the particle's relativistic boost γ, and so it can be used to identify particles (electron/hadron discrimination is most effective in the momentum range 1-100 GeV). Foam and foils are used in the TRT to produce the interfaces. The photons from this radiation will be detected by the Xenon in the straw tubes, producing pulses in the straw tube wires which are much larger than the tracking pulses. By identifying these larger pulses, electrons can be identified in the TRT.

Particle tracks typically traverse 3 pixel layers, 4 stereo silicon strip layers, and a large number ($\simeq$36) of straw tube tracking points as they travel from the interaction point through the inner detector. The relative precision of the different ID detector systems is well matched, such that no single measurement dominates the momentum resolution. The lower precision per hit in the TRT is balanced by its larger number of measurements as compared to the silicon systems. This provides very robust pattern recognition and momentum reconstruction. The momentum resolution for the inner detector will be $\frac{\sigma}{P^T} = 5 \times 10^{-4}\text{GeV}^{-1} P^T \oplus 0.01$.

1.3.3 Calorimetry

The calorimetry system, shown in Figure 1.9, sits just outside the central solenoid and plays an important role in ATLAS. It is designed to trigger on and provide energy and directional measurements of electrons, photons, jets, and missing transverse energy.[10]

ATLAS uses two different calorimeter technologies. Liquid argon technology is chosen for the regions of the calorimetry system closest to the beam, mainly due to its fast signal readout capabilities, radiation hardness, and ease of calibration. The

[10]Neutrinos (which are subject only to the weak force) interact very rarely with matter, meaning they are essentially invisible to high energy collider detectors. Rather than observing the neutrinos directly, their momentum is inferred. The momentum of all other particles in an event are measured and conservation of momentum of the whole event is employed to infer the "missing momentum" which is associated primarily with neutrinos. For the case of hadron colliders there is a further complication. The events are boosted longitudinally with respect to the lab frame. This boost cannot be directly measured since many particles escape down the beam-pipe carrying longitudinal momentum, hence conservation is applied to the transverse momentum only, providing a missing transverse momentum measurement. At high energy the mass of most particles is negligible and missing transverse momentum and missing transverse energy become interchangeable.

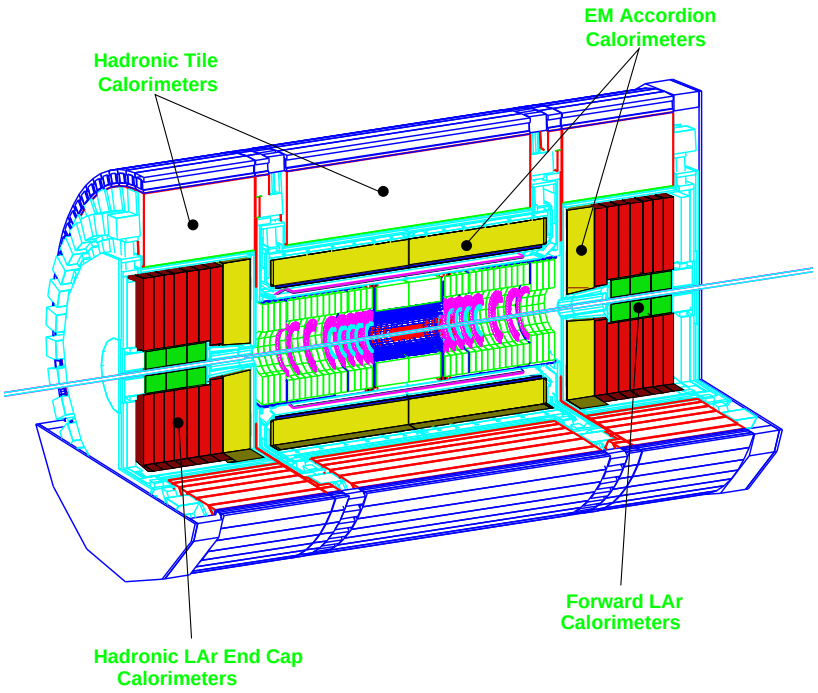

Figure 1.9: A three dimensional view of the ATLAS calorimeter system is presented [Atl99a, Fig. 1-iii]. The outer radius of the calorimetry system is 4.25 m.

liquid argon calorimetry is contained in a cylinder which extends ±6.65 m from the interaction point, has an outer radius of 2.25m, and an inner cavity radius of 1.4 m in the barrel. Further from the beam, scintillating tiles are used for the hadronic tile calorimeter.

The electromagnetic calorimeter (EMC) absorbs electrons and photons, which shower electromagnetically in a cascade of radiated photons and conversions to electron-position pairs. The EMC is further divided into an electromagnetic barrel calorimeter, with cylindrical symmetry providing coverage for $|\eta| < 1.475$, and two electromagnetic end-caps providing coverage for the region $1.375 < |\eta| < 3.2$. The region of overlapped coverage for the EMC and ID, $|\eta| < 2.5$, defines the 'region of precision physics' for ATLAS. The EMC's are highly granular lead/liquid argon sampling calorimeters with "accordion-shaped" electrodes. The accordion geometry provides azimuthal symmetry without any cracks or pad boundaries, while allowing the active regions to be read out from the front and back of the calorimeter. The granularity (typically 0.003×0.1 in $\Delta\eta \times \Delta\phi$) provides for accurate position mea-

surements, and aids in the separation of nearly collinear showers, such as the ones produced by a π^0-meson decaying to two photons. The EMC is 24 radiation lengths[11] (X_0) thick in the barrel and 26 X_0 in the end-caps. The EMC will achieve an energy resolution of $\frac{\sigma}{E} \simeq \frac{10\%}{\sqrt{E(\mathrm{GeV})}}$.

The EMC is preceded by a presampling detector in the region $|\eta| < 1.8$ which serves to correct for the energy lost in the approximately 2 X_0 of material (ID, central solenoid, cryostat) between the EMC and the interaction point.

Hadrons (baryons and mesons composed of quarks) produce larger showers that penetrate more deeply than electromagnetic ones. These showers are contained with the hadron calorimeter system which surrounds the EMC. The hadron calorimeters need not be as granular as electromagnetic calorimeters, on account of the larger shower size. It is more important that they are large, so as to provide good containment for the showers and reduce the probability of particles from hadronic showers punching-though into the muon system. This requires at least 10 interaction lengths[12] (λ_I) of material.

Liquid Argon technology is used for the hadron calorimeters in the end-cap regions where higher radiation tolerance is needed. The Hadronic End-cap calorimeter (HEC) shares a cryostat with the electromagnetic end-cap and the special copper/tungsten/liquid argon forward calorimeter. The HEC is a copper plate sampling calorimeter and provides coverage for the region $1.2< |\eta| <3.2$. Each end-cap is constructed of two independent wheels which sit one behind the other.

An important step in the construction of a complex detector such as ATLAS is the testing and calibration of the subdetectors in particle beams. Since the construction and testing of the HEC has been one of the major focuses of the Canadian ATLAS collaboration and the author has been heavily involved with the beam tests of the HEC during the period 1998-2000, the basic performance results of those tests are discussed briefly here, before continuing with the overview of ATLAS calorimetry.

Each of the two HEC wheels consists of 32 pie-shaped modules. The first HEC

[11] In lead, one radiation length is X_0=0.56 cm, and is the relevant scale for electromagnetic showers.
[12] In iron, one interaction length is λ_I=16.8 cm, and is the relevant scale for hadronic showers.

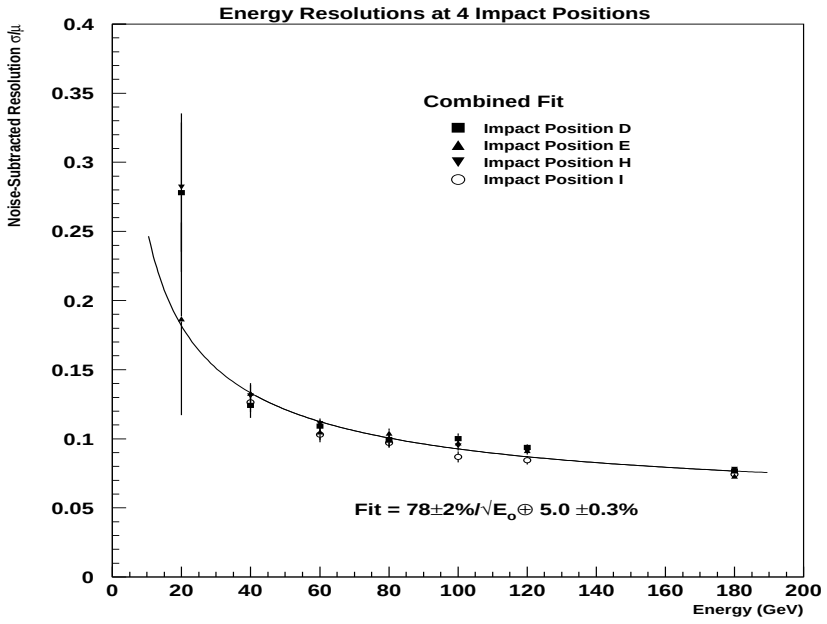

Figure 1.10: The Hadronic End-cap calorimeter energy resolution for charged pions is shown as a function of beam energy [Atl99b]. The impact positions D, E, H, and I correspond to four different spatial locations for the beam striking the front face of the calorimeter.

modules built to the final ATLAS specifications were tested in particle beams at CERN in April 1998. The goal of the beam tests is to measure the basic performance characteristics of the calorimeter, by measuring the energy deposited by beams of particles with known energy and impact position. The author contributed to this (and subsequent) beam tests, and co-authored the analysis presented in Refs. [Atl99b, Dob99a] which forms part of the HEC collaboration publication of Ref. [Atl01d]. The resolution for reconstructing the energy deposited in the calorimeter by pions is energy dependent, and shown in Figure 1.10 over an energy range of 20 to 180 GeV. The intrinsic energy resolution as a function of beam energy E_0 may be parametrized as

$$\frac{\sigma}{E} = \frac{(78\ \pm 2)\%}{\sqrt{E_0\ (GeV)}} \oplus (5.0\ \pm 0.3)\%. \tag{1.4}$$

The full ATLAS detector will have a slightly better response to pions in the endcap region than the HEC does alone. This is because the HEC is positioned behind the electromagnetic endcap calorimeter, which has finer sampling and granularity. The expected resolution for the final ATLAS configuration has been studied with Monte Carlo simulations in Ref. [Atl01d] and is $\frac{(54\ \pm 2)\%}{\sqrt{E_0\ (GeV)}} \oplus (2.6\ \pm 0.1)\%$. A combined HEC/EMC beam test will take place at CERN in August 2002.

The forward calorimeter sits inside the center of the HEC wheels. It extends the η coverage down to $|\eta| < 4.9$, improving the detector's ability to tag, reconstruct, and possibly trigger on very forward jets. The nearly-hermetic coverage afforded by this calorimeter also improves the reconstruction of missing transverse energy, usually associated with neutrinos. Its front face is 4.7 m from the interaction point, and its forward location means it will have to withstand colossal radiation doses (up to about 10^6 Gy per year[13]). It consists of three longitudinal sections. The one closest to the interaction point is made of copper, while the other two are made of tungsten. The nuclear interaction length for copper is about $\lambda_I = 15$ cm, whereas tungsten provides additional stopping power having $\lambda_I = 9.6$ cm. Each section of the calorimeter consists of a matrix of copper or tungsten surrounding concentric rods and tubes. The metal matrix is kept grounded, while the rods inside the tubes are at

[13] 2.5-3.0 Gy is considered a lethal dose for humans [PDG00c].

positive high voltage. The gaps separating the rods from the metal matrix are filled with liquid argon and provide the active medium for the calorimeter.

The hadronic tile calorimeter, with an outer radius of 4.25 m extending ±6.10 m longitudinally, is located at larger radii where the radiation levels are lower and the less expensive iron-scintillator technology is suitable. The tile calorimeter is separated into one large barrel and two extended barrel cylinders on either side. It is a sampling calorimeter with iron absorbers and plastic scintillating tiles as the active medium. Particles hitting the iron shower, producing a large number of secondary particles. When the particles in the shower traverse the scintillator, they produce light which is read out with wavelength shifting fibers using a separate photo-multiplier on either side of each tile. The total amount of light produced in the active medium by the shower is proportional to the energy of the particle which instigated the shower. The readout cells, amounting to over 10 000 channels, are arranged in towers which "pseudo-point" toward the interaction region in a staircase-like manner. The tile calorimeter is 9.2 λ_I thick which, combined with the 1.2 λ_I thickness of the EMC, provides over 10 λ_I of absorption material. The energy resolution for hadronic showers in the barrel region (from the combined EMC and hadron calorimeters) will be $\frac{\sigma}{E} \simeq \frac{50\%}{\sqrt{E(\mathrm{GeV})}} \oplus 0.03$.

1.3.4 Muon spectrometer

The muon spectrometer, which measures the curvature of muon trajectories, surrounds the calorimetry system and consists of three stations of high-precision tracking chambers complemented by fast trigger chambers (Figure 1.11). The light and open structure of the air-core toroid magnet system minimizes multiple scattering effects while providing strong bending power over a large field volume. The field encircles the beam axis and bends muon trajectories in the plane defined by the muon position and the beam axis. The outer chambers of the barrel extend to a radius of 11 m and the outer-most forward muon chambers are mounted on the cavern wall 21 m longitudinally from the interaction point.

Three concentric stations of drift tubes provide precision track coordinate mea-

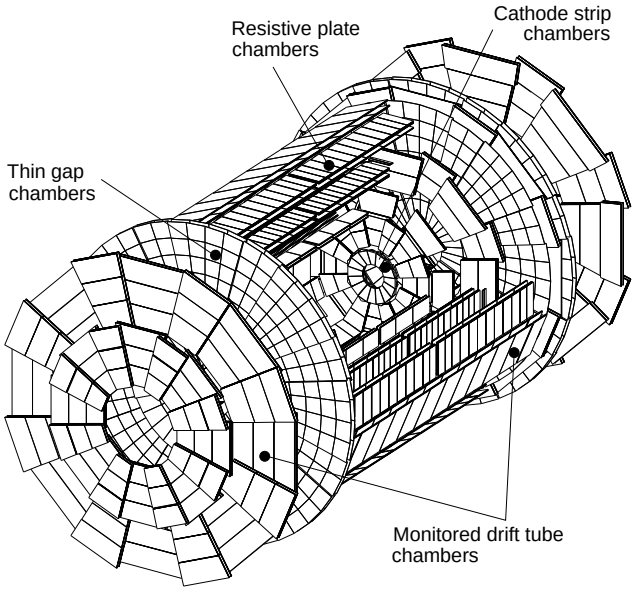

Figure 1.11: A three dimensional cut-away view of the ATLAS muon system is shown. The monitored drift tubes and cathode strip detectors provide high precision tracking measurements, while the resistive plate chambers and thin gap chambers are used primarily for fast triggering [Atl97b, Fig. 4-2]. The muon system has an outer radius of 11 m.

surements over the majority of the muon system coverage and are referred to as monitored drift tubes (MDT). Each of the three stations consists of layers of Ar CO_2 gas filled 3 cm diameter aluminum tubes with readout wires running down their axes. Muons are detected by the ionization charge they produce in the gas. High voltage is applied between the tubes and the wires causing the charge to drift to the wires, where it is read out.

In the first layer of the end-caps and for $|\eta| > 2$, finer granularity is needed to cope with the demanding rate and background conditions. This is provided by the Cathode Strip Chambers (CSC), which use strips to read out the charge induced when an avalanche forms on the anode wire of multiwire proportional chambers.

For triggering purposes, fast readout is essential. Two types of detectors are used for the muon system trigger chambers: resistive plate chambers (RPC) in the barrel $|\eta| < 1.4$ and thin gap chambers in the end-cap region. The RPC's provide 1 ns time resolution using narrow gas gaps formed by two parallel resistive plates

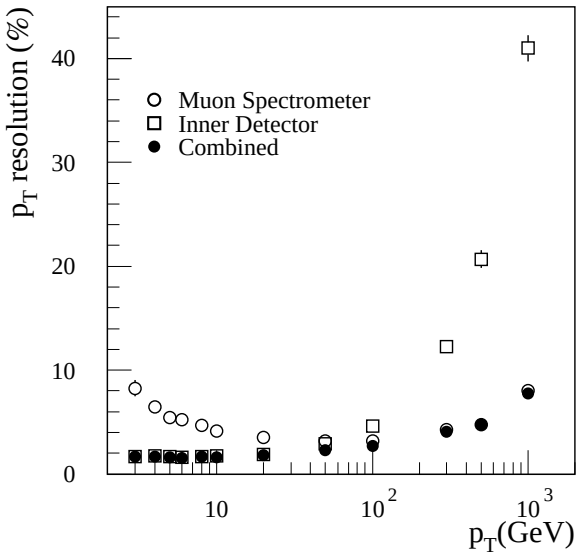

Figure 1.12: The expected muon transverse momentum resolution for the ATLAS muon spectrometer, the ATLAS inner detector, and the two systems combined is shown as a function of transverse momentum [Atl99a].

separated by insulating spacers. The thin gap chambers are similar to multiwire proportional chambers. The thin gap chambers anode wires are arranged parallel to the MDT wires, but its readout strips are arranged in the orthogonal direction. The wires provide the fast triggering, while the orthogonal arrangement of the readout strips provides a second position measurement. Each trigger chamber has at least two detector layers, and the full muon trigger system covers a surface area of over 6550 m^2.

The choice of air core magnet technology allows for good stand-alone muon system performance. The muon spectrometer transverse momentum resolution is shown in Figure 1.12. The muon spectrometer will achieve a stand-alone momentum resolution of $\frac{\sigma}{P^T} \simeq 2-3\%$ over most of the kinematic range, with the exception of very high momenta, where it worsens to $\frac{\sigma}{P^T} \simeq 10\%$ for 1 TeV muons. In the low transverse momentum region, the muon spectrometer resolution is degraded by the effect of the energy lost in the calorimeters, and hence the resolution is not proportional to the muon transverse momentum, as would be expected for a spectrometer with no material in front of it.

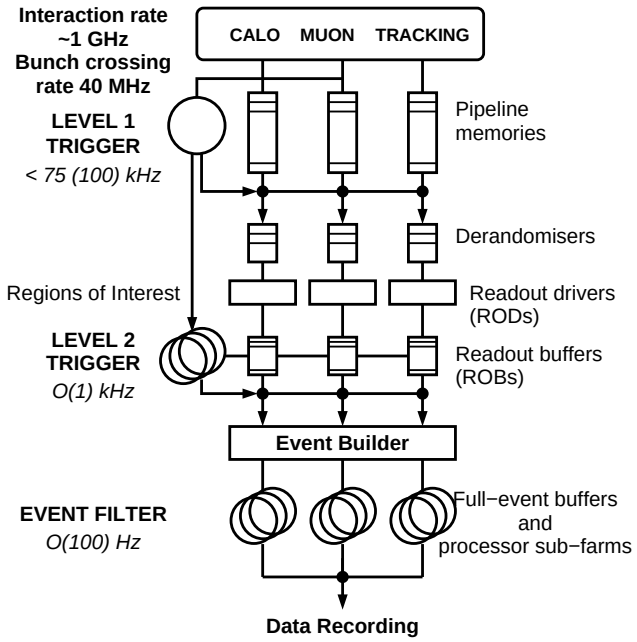

Figure 1.13: Schematic of the ATLAS trigger system is shown [Atl98b, Fig. 1-1].

1.3.5 Triggering

The high LHC event rate provides a challenging environment for ATLAS triggering. The event rate, about 10^9 events/s, must be reduced to an affordable rate for writing the events to computer-disk, which is about 100 events/s. The trigger will be responsible for processing and selecting these events. The trigger decision rate is at the order of 1 μs, whereas the bunch crossing rate of 40 MHz means events will be arriving at the trigger input every 25 ns. While awaiting the trigger decision, events will be stored in analog pipelines.

The trigger system is organized in three levels, shown schematically in Figure 1.13. The first level has the largest input rate, and employs fast signals from the calorimetry and muon system. Level 1 is a hardware trigger with programmable thresholds to allow flexibility. It identifies the high transverse momentum signatures which characterize interesting physics. Level 1 accepts about 1 out of every 10^4 events, reducing the rate to 10^5 Hz. In addition to providing low level trigger decisions, its secondary role is to identify regions of interest for further processing in the high level triggers.

The high level triggers are composed of a level 2 trigger and the Event Builder. As

for level 1, the selection is based on high-P^T signatures. High level event reconstruction is guided by the regions of interest information provided by the level 1 trigger. As a result of this, the level 2 system processes only a few percent of the event fragments stored in the readout buffers. The high level triggers are implemented in software running on commodity computer farms.

The present baseline for the inclusive high-P^T trigger menu at low luminosity is [Atl01b]

$$e25i,\ 2e15i,\ \gamma 60i,\ 2\gamma 20i,\ \mu 20i,\ j360,\ 3j150,\ 4j100,\ j60 + xE60 \qquad (1.5)$$

where the first letter indicates the type of object (e, μ, γ, j, xE for electron, muon, photon, jet, and missing transverse energy), the number following the object gives the transverse momentum threshold in GeV, the letter i implies isolation criteria is imposed, and the initial number (if present) gives the multiplicity of objects. This trigger menu leads to a rate of 100 Hz at low luminosity. The addition of pre-scaled B-physics triggers would increase the rate to 160 Hz.

Chapter 2

New Methods for Simulating QCD Corrections

Given the complexity of the experimental environment and the subtlety of the phenomenological calculations, a mapping of the theoretical predictions onto the experimental expectation is non-trivial. Monte Carlo event generators are normally used for this purpose in High Energy Physics.

The Monte Carlo method is a technique for numerically evaluating integrals, such as cross sections, by sampling the integrand at randomly chosen points (called *phase space points*). It is most useful when an integral is too difficult to evaluate analytically, or when the integral has complex boundaries—such as those which arise in particle physics from detector acceptances and kinematic cuts. In addition, it will be seen that the Monte Carlo method has a very useful feature: the ability to simulate events probabilistically, i.e. as they might be observed in an experiment.

This chapter introduces computer simulations of high energy collision events with an example of a basic Monte Carlo event generator for Drell-Yan lepton pair production. In the section which follows, the two most common methods for modeling QCD corrections using Monte Carlo generators are described: the parton shower approach and numerical integration of next-to-leading order (NLO) matrix elements. The last section of this chapter describes qualitatively a new technique, called the phase space veto [Dob01d], which has been developed by the author to incorporate NLO matrix elements into programs which use the parton shower.

The subject matter of this chapter relates to the study of TGC's at hadron colliders

because everything described here is directly applicable to any electroweak process, including diboson production, at a hadron collider. The phase space veto method has been applied to Drell-Yan lepton pair production [Dob01d], but as yet has not been applied in complete form to diboson processes. The method is built on two previous advances in Monte Carlo methods with NLO matrix elements, both of which were applied to diboson production at hadron colliders. In Ref. [Dob01b], the numerical integration of the NLO matrix elements is arranged in a manner which allows for the generation of unweighted events (a topic which will be discussed further in the following sections). Ref. [Dob01c] extends that formulation to include a parton shower, but does so in a manner that requires the use of a two-stage numerical integration which requires significant computer time. The phase space veto—the focus of this chapter—generalizes these methods in an elegant and simple manner which competes with leading order event generators in terms of efficiency and computer time.

2.1 A Basic Monte Carlo Generator

The goal of an event generator is to produce hypothetical events with the distribution predicted by theory—i.e. the frequency we expect the events to appear in nature. For this thesis, proton-proton collisions producing two gauge-bosons, $pp \to W^{\pm}V$ where V denotes a Z^0 or γ, are of interest. Rather than starting with this complicated case, consider instead the production of a single gauge-boson (e.g. a Z^0 decaying to electrons) at an imaginary accelerator which collides 45 GeV u-quarks with 45 GeV $\bar{u}$-quarks. The process of interest is then $u\bar{u} \to Z^0 \to e^+e^-$ at 90 GeV.

There are two degrees of freedom for the events: the $(\cos\theta,\ \phi)$ decay angles[1] of the Z^0. A Monte Carlo generator for this process is very easy to construct. As physics input, only the matrix element $\mathcal{M}^{u\bar{u}}_{\rm Born}(u\bar{u} \to Z^0 \to e^-e^+)$ is needed. The differential cross section is given by

$$d\sigma^{\rm Born}(u\bar{u} \to Z^0 \to e^-e^+) \ = \ \frac{1}{2\hat{s}}\ |\mathcal{M}^{u\bar{u}}_{\rm Born}(u\bar{u} \to Z^0 \to e^-e^+)|^2\ \frac{d\cos\theta d\phi}{8(2\pi)^2} \qquad (2.1)$$

[1]The rotational symmetry of the $u\bar{u}$ collisions implies the differential cross section is independent of the azimuthal angle ϕ.

where $\hat{s}$ is the center-of-mass energy squared. The next step is to *sample the phase space*. The phase space is the multi-dimensional hypercube which spans all of the degrees of freedom. For this process it is the two dimensional space $-1 < \cos\theta < 1,\ 0 < \phi < 2\pi$. A candidate event is sampled by choosing the $\cos\theta,\ \phi$ variables using a uniformly distributed random number generator. The candidate event's differential cross section (or *event weight*) $d\sigma$ is calculated from Eq. 2.1, and is directly related to the probability of this event occurring. The average of many candidate event weights $\langle d\sigma \rangle$ is an approximation to the integral $\int d\sigma$ and converges to the cross section.

At this point the candidate events are distributed flat in phase space, and there is no physics information in the distributions. Two methods can be used to derive physical predictions from these candidate events: (1) the event weights may be used to create histograms representing physical distributions, or (2) the events may be *unweighted* such that they are distributed according to the physical prediction. The former is very simple. A histogram of some relevant distribution (i.e. the transverse momentum of the e^-) is filled with the event weights from a large number of candidate events. The individual candidate events are meaningless, but in the limit of an infinite number of candidate events, the distribution is exactly the one predicted by Eq. 2.1. The latter method produces events with the frequency predicted by the theory being modeled, and the individual events represent what might be observed in a trial experiment—in this sense unweighted events provide a genuine simulation of an experiment.

The *hit-and-miss* technique (also known as the acceptance-rejection method or the Von Neumann method) is normally used to unweight events. To apply the method, the maximum event weight $d\sigma_{\mathrm{MAX}}$ must be known. For this process, the maximum occurs when one of the leptons is collinear with one of the quarks, so it is easy to calculate $d\sigma_{\mathrm{MAX}}$ by inserting these conditions ($\cos\theta = \pm 1$) into Eq. 2.1. For more complicated processes the maximum event weight can be approximated by randomly scanning the parameter space. For each candidate event, the ratio of event weight over the maximum event weight $\frac{d\sigma}{d\sigma_{\mathrm{MAX}}}$ is compared to a random number g generated

uniformly in the interval (0,1). Events for which the ratio exceeds the random number ($\frac{d\sigma}{d\sigma_{\mathrm{MAX}}} > g$) are accepted, the others are rejected. The accepted events have the frequency and distribution predicted by Eq. 2.1, and represent the physical expectation for the imaginary $u\bar{u}$ collider experiment. The computer program which produces these events is an event generator, whereas a program which produces the weighted candidate events of the other method might better be termed an "event integrator".

The Monte Carlo generator described above is an *exact leading order* generator. This means that it describes the production of $Z^0 \to e^+e^-$ at the $u\bar{u}$ collider using a perturbative expansion in the coupling constant (α_{EM}) including all of the Feynman diagrams[2] at leading order. For this process, the order ${\alpha_{\mathrm{EM}}}^2$ quark-antiquark annihilation diagram (referred to as the *s-channel*) is the only one contributing at leading order. The term 'exact' means that the calculation uses exactly one order, and does not imply that the result is exactly the prediction of the theory (the exact prediction according the SM theory would mean all diagrams contributing at any order are included, and physicists do not know how to perform such a calculation).

2.1.1 Parton model

The basic event generator example is not useful, because color confinement dictates that quarks cannot be produced in isolation—they are forever confined inside color-singlet composite baryons or mesons. If the quarks were to be replaced with electrons, the example would be relevant to e^+e^- colliders—and in fact describes (at Born level) the physics which the LEP 1 programme focused on. For a hadron collider like the LHC, the beams will be composed of protons of fixed energy. The collision energy will be so large that the quarks, antiquarks, and gluons (collectively called partons) which make up the proton will be resolved, and it will be these fundamental particles which undergo the reactions. A reaction like the one described with Eq. 2.1 is termed the *hard subprocess*. Additional information is needed to describe the probability of finding the constituent partons with a particular momentum fraction inside the

[2] A Feynman diagram or graph is symbolic notation representing the mathematical equation for a matrix element, $\mathcal{M}$. The cross section (or event rate) is proportional to the square of the sum of all matrix elements, $\sigma \propto |\mathcal{M}_1 + \ldots + \mathcal{M}_i + \ldots + \mathcal{M}_n|^2$.

protons. The parton model provides this information.

The key ingredient to the parton model is the parton density function (p.d.f.) $f_{\mathrm{P}\to\overset{(-)}{\mathrm{q}}}(x)$ which describes the probability of finding a parton $\overset{(-)}{q}$ inside the proton[3] p carrying a fraction x of the proton's forward momentum (thus for protons with momentum 7 TeV along the z-direction, the z-momentum of the parton is $x\times$7 TeV).

The important feature of the parton model is factorization. The relevant scale for the proton structure is the proton mass, about 1 GeV. For hard subprocesses at a center-of-mass energy $\sqrt{\hat{s}}$ well above this scale, any corrections connecting the proton physics to the hard subprocess is suppressed by a factor $\frac{M^2_{\mathrm{proton}}}{\hat{s}}$. This means the two phenomena can be factorized and treated separately.

Singularities occur when defining the p.d.f.'s. These are absorbed into renormalized p.d.f.'s which, due to the perturbative QCD calculation, acquire a scale dependence, $f(x) \to f(x, Q)$. The factorization theorem [Col87] states that for (inclusive) hard scattering processes in hadron-hadron collisions, all collinear singularities at every order in perturbation theory can be absorbed into p.d.f.'s whose scale dependence is given by the (Dokshitzer)-Gribov-Lipatov-Altarelli-Parisi (GLAP) [GLAP72] evolution equations.

The proton, being a bound state, cannot be described with perturbative mathematics. This makes any calculation in this regime extremely difficult. The p.d.f.'s are thus not calculated, but rather measured by experiment.

The differential cross section for the $u\bar{u} \to e^+e^-$ subprocess of Eq. 2.1 in proton beams is then[4]

$$d\sigma^{\mathrm{Born}}(pp \to u\bar{u} \to Z^0 \to e^-e^+) \;=$$

$$\int f_{\mathrm{p_1}\to\mathrm{u}}(x_1, Q) f_{\mathrm{p_2}\to\bar{\mathrm{u}}}(x_2, Q)\; d\sigma^{\mathrm{Born}}(u\bar{u} \to Z^0 \to e^-e^+)\; dx_1 dx_2 \qquad (2.2)$$

where the factorization scale Q represents the momentum transfer from the proton, and is usually taken to be the subprocess energy $\sqrt{\hat{s}}$. This differential cross section

[3]Parton density functions are not only used to describe the internal structure of a proton, but also may be defined, for example, to describe the probability of a photon emerging from an electron beam $f_{\mathrm{e}\to\gamma}(x)$.

[4]When the $\overset{(-)}{q}$ is resolved inside the proton, beam remnants are left behind, and so $pp \to u\bar{u}$ would be more accurately represented as $pp \to u\bar{u} + X$.

is the probability of the $u\bar{u} \to Z^0 \to e^- e^+$ subprocess being initiated from the two colliding proton beams. It does not, however, give the complete story because there are several other similar processes at the same order which result in identical final states. The subprocess could be initiated by $\bar{u}u$ quarks (i.e. a 'backwards' version of the above), or by any other quark-antiquark combination such as $d\bar{d}, \bar{d}d, c\bar{c}, \bar{c}c$, etc. (the gg initial state can also produce the identical final state, but this process proceeds via a quark-triangle, and so it is suppressed by two powers of $\alpha_{\rm S}$—it is a next-to-next-to-leading order diagram). Thus the differential cross section for $pp \to Z^0 \to e^- e^+$ is given by summing over all quark flavors of initial state partons

$$\begin{aligned} d\sigma^{\rm Born}(pp \to Z^0 \to e^- e^+) \; = \\ \int \sum_{i}^{\text{quark flavors}} \Big[& f_{\rm p_1 \to q_i}(x_1, Q) f_{\rm p_2 \to \bar{q}_i}(x_2, Q) d\sigma^{\rm Born}(q_i \bar{q}_i \to Z^0 \to e^- e^+) \\ & + \; f_{\rm p_1 \to \bar{q}_i}(x_1, Q) f_{\rm p_2 \to q_i}(x_2, Q) d\sigma^{\rm Born}(\bar{q}_i q_i \to Z^0 \to e^- e^+) \Big] \, dx_1 dx_2. \end{aligned} \tag{2.3}$$

where the sum runs over all quark flavors.

A Monte Carlo event generator for this process would be constructed in a manner identical to the basic generator above, with the exception that there are now 4 degrees of freedom: the gauge-boson decay angles $(\cos\theta, \phi)$ and the parton momentum fractions[5] x_1, x_2.

The choice of the lepton pair production process as an example to illustrate Monte Carlo techniques is particularly relevant for hadron collider physics. Calculated in 1970 by Drell and Yan [Dre70], it was the first hadron-hadron process to be calculated in the context of the parton model and was also one of the early next-to-leading order QCD calculations [Alt79]. Two Nobel prizes have been awarded for discoveries

[5]In practice it would be very inefficient to sample flat in x_1, x_2-space, because the cross section is strongly peaked in the region of the Z^0 mass (i.e. when $x_1 x_2 s = M_Z^2$, where $\sqrt{s}$ is the machine energy, 14 TeV for the LHC). It would be more efficient to sample in terms of the subprocess energy squared $\hat{s} = x_1 x_2 s$ and the subprocess rapidity (i.e. boost), $y_{\rm CMS} = \frac{1}{2} \ln \frac{x_1}{x_2}$, with the change of variables compensated by a Jacobian factor. Good efficiency is obtained by sampling $\hat{s}$ from a Breit-Wigner distribution and $y_{\rm CMS}$ flat, since this mimics the shapes of the expected distributions (the best efficiency is obtained by sampling the phase space according to the distribution being modeled, i.e. Eq. 2.3, but if it were known how to do that, it would not be necessary to use the hit-and-miss Monte Carlo method).

of new particles produced by the Drell-Yan mechanism.[6] Experimentally, after 30 years of measurements, it remains an extremely important process. It will be an important tool at TeV scale hadron colliders for probing new physics (e.g. large extra dimensions, extra neutral gauge bosons), performing precision measurements of electroweak parameters, constraining the parton density functions, and calibrating the detector. The latter is perhaps most important to the physics programme, because it means our knowledge of this process will feed into the systematic errors for most physics measurements: the lepton energy and momentum scale may be calibrated *in situ* with $Z^0 \to l^+l^-$ events, the jet energy scale may be determined using events with a Z^0 decaying to leptons recoiling against a high transverse momentum jet, and the Drell-Yan event rate may be used to determine the absolute luminosity.

2.2 Simulation of QCD Corrections

The basic Monte Carlo generator described in the previous section provides a very limited representation of physics events because there are always exactly two particles (the e^-e^+ from the Z^0 decay) in the final state. It is clear that even at leading order there will be other particles present, such as the beam fragments which are left behind when a quark is resolved within the proton from the beam. But these *beam fragments* are not nearly as important as the corrections to the subprocesses due to higher order effects. Since the strong coupling is considerably larger than the electromagnetic one (about 1/10 vs. 1/129 at the energy scales of interest), the QCD corrections give the biggest effect.

The present section focuses on the two methods most commonly used to include higher order quantum chromodynamics (QCD) corrections in the simulation: the parton shower [Sjö85, Mar88] and numerical integration of next-to-leading order (NLO) distributions.

[6] Sam Ting shared the 1976 Nobel prize with Burton Richter for the discovery of the J/Ψ (the $c\bar{c}$ meson which helped to confirm the quark model) through the Drell-Yan mechanism $pN \to J/\Psi + X \to \gamma^\star + X \to \mu^+\mu^- + X$ at Brookhaven (Richter discovered the J/Ψ independently in e^+e^- collisions at the Stanford Linear Accelerator). Carlo Rubbia and Simon van der Meer were awarded the 1984 Nobel prize for the discovery of the $W^\pm$ and Z^0 gauge-bosons through the Drell-Yan mechanism at the CERN Sp$\bar{\text{p}}$S collider.

Both methods have proven extremely useful, but each has a limited—though complementary—region of applicability.

2.2.1 Showering and hadronization event generators

Programs which employ the parton shower approach, such as `PYTHIA` [Sjö01a], `HERWIG` [Cor01], and `ISAJET` [Bae99], have enjoyed widespread use by experimentalists. These programs, referred to as showering and hadronization generators (SHG's), are general purpose tools because they are able to simulate a wide variety of initial and final states. They begin with a leading order hard subprocess such as the one described in the preceding section. Higher order effects are added by evolving the event using the parton shower, which allows partons to branch into pairs of other partons. The resultant partons are then grouped together or *hadronized* into color-singlet hadrons and resonances are decayed. Finally, the underlying structure of the event is generated: beam remnants, interactions from other partons in the protons, and collisions between other protons in the colliding beams (called *pile-up*).

The general structure of an event from an SHG is shown in Figure 2.1. The time evolution of the event goes from bottom to top. Two protons (indicated by three solid lines to denote their valence quark content) collide and a parton is resolved at scale Q and momentum fraction x in each one. The phenomenology of the parton resolution is encoded in the parton density function $f(x, Q^2)$. In this example a valence quark is resolved in the proton shown on the left, while an anti-quark is resolved from the proton on the right's sea quark distribution. The quark and anti-quark annihilate into an s-channel resonance denoted by a wavy line. The resonance then decays into a fermion anti-fermion pair. This part of the event is called the *hard subprocess*. If the resonance is a Z^0 and the fermion anti-fermion pair are e^+e^-, the physics described thus far is exactly that which is contained in the basic event generator of the previous section. Instead, assume the resonance decays to a quark anti-quark pair. The SHG incorporates higher order QCD effects by allowing the (anti)quarks to branch into $\overset{(-)}{q}g$ pairs, while the gluons may branch into $q\bar{q}$ or gg pairs. The resultant partons

may also branch, resulting in a shower or cascade of partons.[7] This part of the event is labeled *parton shower* in the figure. Showering of the initial state partons is also included in the SHG's, but is not shown in the figure for simplicity. The event now consists of a number of elementary particles, including quarks, antiquarks, and gluons which are not allowed to exist in isolation, as dictated by color confinement. Next, the program groups the colored partons into color-singlet composite hadrons using a phenomenological model referred to as hadronization (also called fragmentation). The hadronization scale is in the non-perturbative regime, and the programs use fairly crude phenomenological models which contain several non-physical parameters that are tuned using experimental data. Nevertheless, since the hadronization scale is much smaller than the scales of interest, the impact of the hadronization model choice on the final result is typically small for most physical processes. After hadronization, many short-lived resonances will be present, and are decayed by the program.

The SHG's also add in features of the underlying event. The *beam remnants* are the colored remains of the proton which are left behind when the parton which participates in the hard subprocess is 'pulled out'. The motion of the partons inside the proton results in a small ($\approx$ 1 GeV) *primordial transverse momentum*, against which the beam remnants recoil. The beam remnants are color connected to the hard subprocess, and so should be included in the same hadronization system. Multiple parton-parton interactions, wherein more than one pair of partons from the beam protons interact, are also accounted for. In a final step, pile-up from other proton-proton collisions in the same bunch crossing are added to the event (at the LHC, there will be an average of about 25 such interactions per bunch crossing at design luminosity).

This chapter focuses mainly on higher order QCD corrections and so, having briefly outlined the general structure of event generation using an SHG, only the parton shower—which accounts for higher order QCD corrections—will be described further in the following section. Before so doing, a few comments are in order.

[7]Though the discussion of parton showers presented here is restricted to QCD showers, an identical prescription can be applied to electromagnetic showers, and is used in SHG's to incorporate higher order QED corrections.

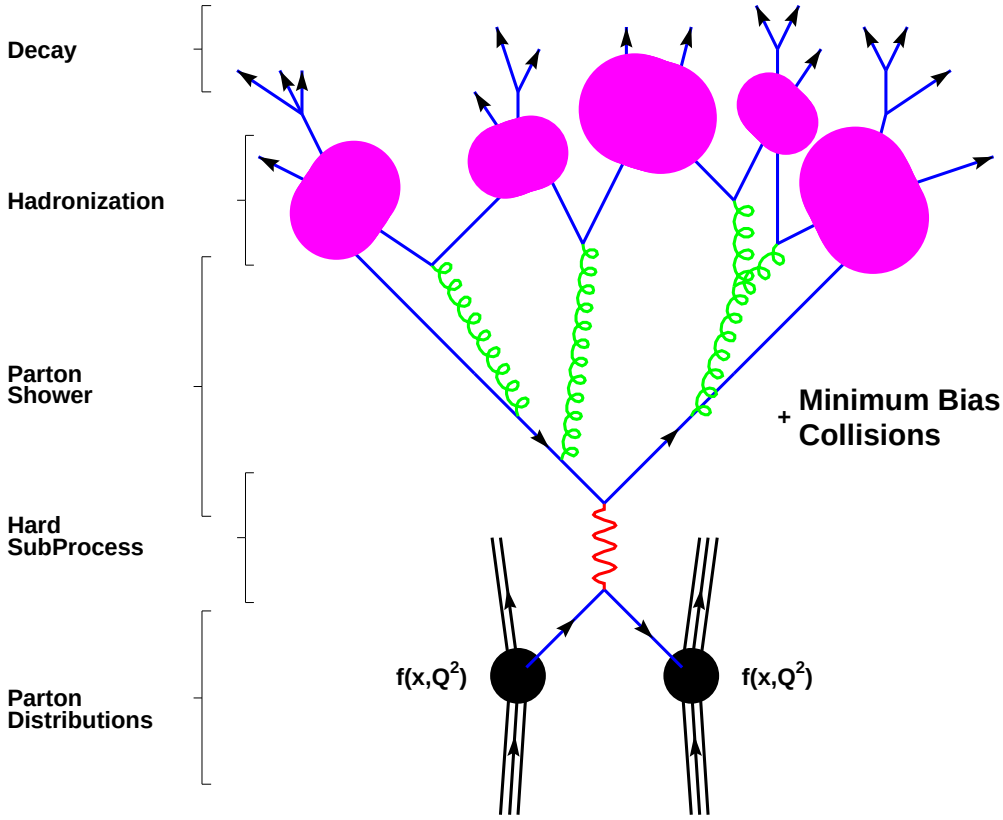

Figure 2.1: The basic structure of a showering and hadronization generator event is shown schematically [Dob01a]. Refer to the text for a detailed description.

SHG's produce events with the frequency predicted by theory, and so they are event generators in the true sense (as opposed to 'event integrators'). One important related point about the generation of an event with the SHG's is that, with a few minor exceptions, the hard subprocess is the only process dependent part. Everything else is (almost) completely generic, and so implementing a new physics process usually only involves implementing the computer code for a new hard subprocess.[8] The SHG's are normally implemented such that the generation of everything except the hard subprocess happens with unit probability—i.e. only the hard subprocess has a weight associated with it. This means (with certain exceptions which are unimportant here) that after selecting a hard subprocess event using the hit-and-miss method, all the other aspects of the generation are added onto the accepted event *without ever rejecting the event.* This is important for the modularization of event generators. Thus when an event generator simulates the hard subprocess a large number of candidate events are attempted, but only a fraction of those candidates are accepted. However, for each hard subprocess event that is chosen and subjected to the subsequent steps of the generation process, one fully simulated event will come out.

Another important aspect of SHG's is that they provide an *exclusive* description of the events. As an example, consider the production of a Z^0-boson as the hard subprocess. For the basic (exactly leading order) event generator which was used to introduce this chapter, the transverse momentum of the Z^0 will always be zero, because there is nothing for the Z^0 to recoil against. The SHG's produce transverse momentum for the Z^0 through the parton shower, against which the hard subprocess must recoil to conserve momentum. This prediction of the transverse momentum is termed *exclusive* because a detailed listing (the event record) of the particles recoiling against the Z^0 is provided. In contrast, a resummed calculation (first proposed in Ref. [Dok80], see Ref. [Ell96, Sec. 6.5] for a brief description) is *inclusive* because it accounts for the leading logarithms in the perturbative expansion to all orders. As such, an (approximate) summation over an infinite number of Feynman diagrams

[8]New physical processes can also affect other parts of the event, but since we are usually interested in new physics operating at large scales, it will usually have a noticeable impact on the hard subprocess only.

has been performed, and no information about what the Z^0 is recoiling against is provided. Exclusive calculations—such as those provided by SHG's—are ideal for the simulation of experiments, because the full event is necessary for detailed detector simulation.

The *event record* is used by the computer programs to keep track of the particles and their relationships within the event—and communicate them to the outside world. The Fortran HEPEVT [Sjö89] event record is the first standard to be widely used, and is successful in transferring the information about a fully generated event to programs for detector simulation. However, it does not contain enough information to act as an intermediary between two steps of the generation process. Recently, this has resulted in renewed attention for event records. As the complexity of event generators grows, it is becoming more common to modularize the programs, allowing different packages to be responsible for specialized aspects of the event. A new event record called HEPUP, developed by Monte Carlo experts (and the author) attending the 2001 Les Houches Physics at TeV Colliders Workshop, has been conceived and implemented in Ref. [Boo01]. It specifies the protocol for arbitrary 'external' hard subprocesses to be inserted into the SHG programs. As the high energy physics community moves towards modularized event generators, it is also moving away from the Fortran programming language and adopting modern object-oriented languages like C++. A new C++ event record called HepMC has been co-developed by the author and J.B. Hansen [Dob01a], incorporating and extending all of the information contained in the Fortran HEPEVT and HEPUP event records, while employing object-oriented patterns. Both of these new tools are already being used extensively by the particle physics community.

Parton Shower

The effort required to perform a QCD calculation to a given fixed order increases approximately factorially with the order of the calculation. Presently many processes are calculated to next-to-leading order, and only a few next-to-next-to-leading order calculations have been completed. The difficulty of the calculations aside, there are

regions of phase space where higher order terms are enhanced and should not be neglected.

The parton shower provides an alternate approach, which does a good job of accounting for the regions where the QCD matrix elements are enhanced, i.e. when a quark splits into two nearly collinear partons, or when a soft gluon is emitted. In these regions the leading logarithmic terms can be identified and summed to all orders.

Consider as an example a final state parton shower for the $pp \to q\bar{q}$ event shown in Figure 2.1. According to the leading order description of the event, the outgoing q and $\bar{q}$ are produced and travel away from each other. This is not a complete description (especially at the much smaller scales which will characterize the particle's interactions with the detector), since QCD color confinement dictates the quarks cannot be observed in isolation. Instead, the outgoing quarks will shower, each producing one or more jets of particles. The SHG accounts for this showering by tracing each of the final state parton lines out from the hard subprocess while evaluating the probability that the parton has branched into two daughter partons. The momentum transfer scale Q is used in the tracing as a measure of "distance" from the hard subprocess. The tracing starts at scale Q_1, for which the resonance mass $M_{q\bar{q}}$ is a reasonable choice. The shower then steps out to some smaller scale, Q_2, and evaluates the probability that the parton has branched into two daughter partons. By repeating this procedure, the scale is *evolved downwards* from the scale Q until a much smaller *cutoff scale* Q_0 is reached which defines the point at which the description becomes non-perturbative, and the parton shower ceases to be a good approximation for the physics.

The basic ingredient for evaluating this probability is the Sudakov form factor

$$\Delta_i(Q^2) \equiv \exp\left[-\sum_{jk}\int_{Q_0^2}^{Q^2}\frac{dq^2}{q^2}\int dz\frac{\alpha_S}{2\pi}\hat{P}_{i\to jk}(z)\right] \tag{2.4}$$

which represents the probability of evolving downwards from scale Q to the cutoff scale Q_0 along parton line i without any branching occurring, summed over all possible branching products j, k. The cutoff scale is chosen to roughly correspond to the scale

at which QCD becomes non-perturbative, and is the transition scale at which the SHG ends the treatment with the perturbative parton shower, and begins describing the physics with the non-perturbative hadronization model. $\hat{P}_{i\to jk}(z)$ is called the regularized splitting function, and represents the probability for a branching of parton type i into jk. z is the energy fraction $z = \frac{E_j}{E_i} = 1 - \frac{E_k}{E_i}$. For example, the splitting function for the emission of a gluon from a quark is

$$\hat{P}_{q\to qg}(z) \;=\; \left(\frac{4}{3}\right)\frac{1+z^2}{1-z}. \tag{2.5}$$

Using this prescription, $\frac{\Delta_i(Q_1^2)}{\Delta_i(Q_2^2)}$ is the probability of evolving downwards from a scale t_1 to a scale t_2 without any branching occurring. This description is readily modeled with the Monte Carlo method. The scale Q_2 of the next branching is generated by solving the equation $\frac{\Delta_i(Q_1^2)}{\Delta_i(Q_2^2)} = g$, where g is a flat random number in the range (0,1). If the scale $Q_2 < Q_0$, then no branching occurs, and the evolution stops. Having selected the scale for the next branching (if there is one), the kinematic variables which define the branching are sampled in a similar manner. The entire procedure is repeated for each outgoing parton in the event, including the ones which have been generated by the parton shower, hence the algorithm's name, since a shower or cascade of colored partons develops.

The procedure for initial state showers is similar, but proceeds in the reverse "direction" via *backwards evolution*, with the momentum transfer $Q^2 < 0$, such that the evolution is space-like, rather than the time-like evolution which occurs for final state showers. Because the incoming parton undergoing the shower must eventually terminate in the proton, ratios of parton density functions must be included in the Sudakov form factor.

The parton shower is successful at modeling the effects of higher order corrections on the shapes of distributions in the regions of soft or collinear parton emissions. However, since the parton shower proceeds with unit probability, it does not address the effect of higher order corrections on the total cross section. The ratio of a higher order QCD cross section calculation to the leading order one is referred to as a k-factor. When comparing SHG simulations with experimental data, the simulated

distributions are commonly normalized to the data, or else a k-factor from a next-to-leading order calculation is applied.

The description of the parton shower presented above is merely a sketch, details about angular ordering, infra-red cutoffs, etc. have been omitted, and the interested reader is referred to the excellent reviews which are presented in Refs. [Ell96, Sjö01b].

2.2.2 Monte Carlo generation at next-to-leading order

NLO Monte Carlo programs provide an extra order beyond the Born level prediction for the cross section. These programs are event integrators—not true event generators—as they are unable to produce events with the frequency predicted by theory. This is because the dimensional regularization scheme which is used to handle inherent divergences in the NLO calculation allows a fraction of the phase space points to have negative probability (or event weight). The usual algorithms for unweighting events, such as the hit-and-miss method discussed above, are unable to handle negative event weights. These programs are used to generate samples of weighted events, which individually have no physical interpretation, but provide accurate predictions of event distributions when many such weighted events are combined into histograms.

Lacking individual events to evolve further, it is difficult to add subsequent event features like hadronization or the underlying event. This has meant that these programs are excellent theoretical tools for predictions of distributions, but limits their usefulness for producing events to be simulated in the detector environment. Because NLO programs provide a good prediction of inclusive cross sections, they are also used for correcting the normalization of distributions from leading order event generators.

The truncation of a perturbative series introduces a renormalization scale dependence (μ_R) for the prediction, which is similar to the factorization scale (μ_F) dependence already discussed for the parton density functions. The choice of the scales is somewhat arbitrary, and the hard subprocess invariant mass is one common choice for both scales, $\mu_R = \mu_F = \sqrt{\hat{s}}$. Because of the arbitrary nature of this choice, the dependence of the prediction on the scale choice is used as a measure of the uncertainty arising from neglected higher order terms. When extra orders are included in a

calculation, the scale dependence normally improves (i.e. decreases). This improved scale dependence is one of the advantages of higher order calculations. If it were possible to perform a calculation to all orders, there would be no scale dependence at all.

NLO programs provide a good description of the physics in the regions of hard and well separated partons, i.e. away from the enhanced soft and collinear regions where contributions from diagrams of all orders are important. Thus the NLO programs provide an accurate prediction in the regions which are complementary to the regions which are well described by the parton shower approach. They also provide a better prediction of the total cross section, since the cross sections provided by SHG programs are strictly leading order.

Phase space slicing method

The NLO cross section receives contributions from the square of the Born graphs, the interference of the Born graphs with the one-loop graphs, and the square of the real emission graphs which contain an extra colored parton in the final state,

$$\mathcal{M}^2_{\rm NLO} \;=\; \mathcal{M}^2_{\rm Born} + \mathcal{M}_{\rm Born} \otimes \mathcal{M}_{\rm one\ loop} + \mathcal{M}^2_{\rm real\ emission}. \tag{2.6}$$

The second and third terms of Eq. 2.6 diverge when treated separately, and so numerical integration calculations employ a regularization scheme which effectively combines pieces of these terms to obtain finite results everywhere in phase space.

Commonly used schemes include the "subtraction method" [Ell81], "dipole method" [Cat97], and "phase space slicing" (PSS) methods [Ber89, Har01, Fab81, Gie92, Gie93]. All of these methods give identical results when used appropriately. For the purposes of what will be presented in the following sections, features of the PSS methods are convenient. Variations of the PSS method include the "two parameter PSS" [Ber89] (see Ref. [Har01] for an accessible review), "one parameter PSS" [Fab81], and "$s_{\rm min}$-slicing" [Gie92, Gie93].

To illustrate the PSS method, consider Drell-Yan production of charged lepton pairs in the region of the Z^0 resonance $p\bar{p}^{(-)} \rightarrow Z^0 + X \rightarrow l^+l^- + X$ at NLO. The

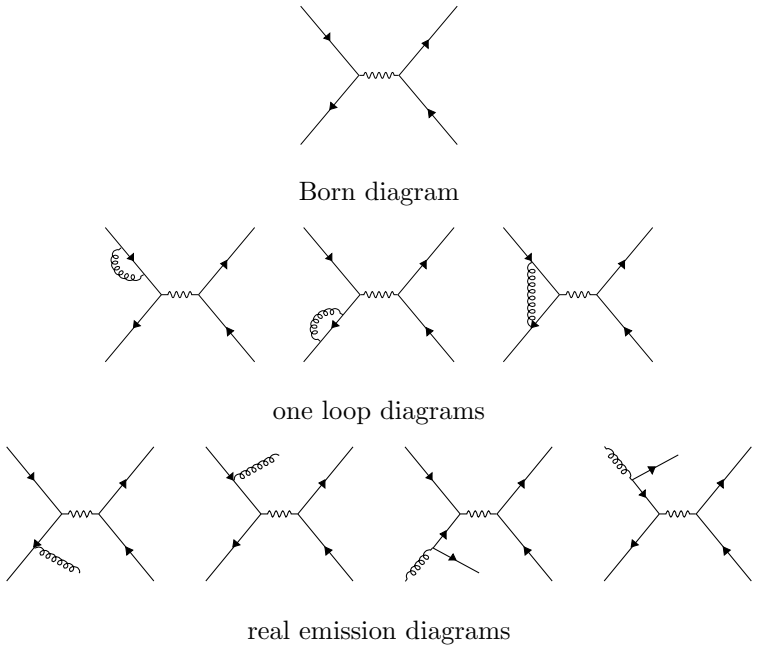

Figure 2.2: Feynman graphs contributing to $p\bar{p}^{(-)} \to Z^0 + X \to l^+l^- + X$ at NLO. The lines incoming from the left are the quarks, the wavy line represents the Z^0 resonance which decays to outgoing leptons, and the curly lines are gluons.

Feynman graphs are presented in Figure 2.2. The first term of Eq. 2.6 is leading order ($\alpha_{\rm QED}$) and contains n particles in the final state. The phase space volume $\Phi_{\rm n}$ which defines the configuration of the four-vectors is referred to as n-body and specified by 4 degrees of freedom: the Z^0 mass, Z^0 boost, and two Z^0 decay angles. The second term of Eq. 2.6 is first order ($\alpha_{\rm QED}\alpha_{\rm S}$) and is also described by n-body kinematics. The third term of Eq. 2.6 is also first order ($\alpha_{\rm QED}\alpha_{\rm S}$) and the final state contains the gauge-boson decay products and a colored parton (e.g. $l^+l^-g,\ l^+l^-q,\ l^+l^-\bar{q}$). The final state is described by (n+1)-body kinematics with 7 degrees of freedom: the system mass, system boost, Z^0 mass, two Z^0 production angles, and two Z^0 decay angles.

For a particular choice of the n-body kinematics, the phase space Φ_{+1} which specifies the kinematics of the real emission is a plane in $\hat{u} = (p_2 - p_j)^2$ vs. $\hat{t} = (p_1 - p_j)^2$ space, shown in Figure 2.3, where p_1 and p_2 are the four-momenta of the massless colliding partons, and p_j is the massless colored emission (the azimuthal degree of freedom is unimportant and not shown). The n-body kinematics occupy a point at

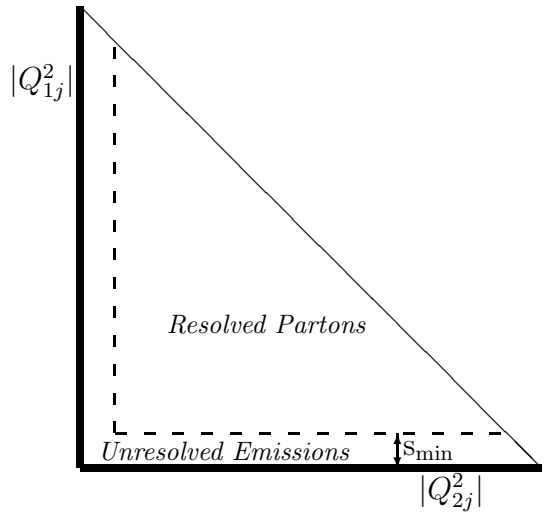

Figure 2.3: A projection of the $p\overset{(-)}{p} \to Z^0 j$ phase space onto the $\hat{u}$ vs. $\hat{t}$ plane is shown, where $\hat{u} = (p_2 - p_j)^2 = -Q^2_{2j}$ and $\hat{t} = (p_1 - p_j)^2 = -Q^2_{1j}$, and $p_1,\ p_2,\ p_j$ are the momenta of the forward colliding parton, backward colliding parton, and real emission. The area above (below) the s_{min} boundary is the region of resolved (unresolved) real emissions.

the origin of this plane. The (n+1)-body kinematics span the $\hat{u}$ vs. $\hat{t}$ plane and the corresponding differential cross section diverges as the origin or either axis of the plane is approached, i.e. when the parton emission becomes soft or collinear.

The PSS methods regulate the singularities by partitioning the phase space into a region of resolved emissions, and a region of unresolved soft and collinear emissions. The resolved part is integrated numerically. The contribution from the unresolved soft and collinear emissions is calculated analytically and included with the n-body squared matrix element such that the net result is finite, though not necessarily positive. For the case of s_{min}-slicing, the boundary of the unresolved region is defined by a single parameter with dimension energy squared. An emission is considered to be unresolved anytime the invariant mass squared s_{ik} of any parton pair is less than the s_{min} resolution parameter

$$|s_{ik}| \ < \ s_{min} \qquad \text{(unresolved region)} \tag{2.7}$$

where the partons $i,\ k$ may be either initial or final state.

The cross section for the entire $\hat{u}$ vs. $\hat{t}$ plane of Figure 2.3—which corresponds to

the cross section for a particular n-body kinematic configuration $\Phi_{\rm n}$, integrated over the extra degrees of freedom which define the real emission—is a constant, schematically

$$\sigma^{\rm n}(\Phi_{\rm n}, {\rm s}_{\rm min}) \; + \; \int_{s_{ik}>{\rm s}_{\rm min}} \sigma^{\rm n+1}(\Phi_{\rm n}, \Phi_{+1}) d\Phi_{+1} \; = \; {\rm Const}(\Phi_{\rm n}). \tag{2.8}$$

This constant is independent of the $\rm s_{min}$ choice.

A Monte Carlo program for this process would typically be broken up into two separate parts. The first would sample the n-body phase space $\Phi_{\rm n}$, integrating over $\sigma^{\rm n}(\Phi_{\rm n}, {\rm s}_{\rm min})$. Each time $\sigma^{\rm n}(\Phi_{\rm n}, {\rm s}_{\rm min})$ is evaluated, it includes an analytical integration over the unresolved emissions. The second part of the program would sample the (n+1)-body phase space $\Phi_{\rm n+1}$ (restricted to the resolved region $|s_{ik}| > {\rm s}_{\rm min}$), integrating over $\sigma^{\rm n+1}(\Phi_{\rm n+1})$. The cross sections from each of the two parts of the program depends explicitly on the $\rm s_{min}$ parameter, but the dependence cancels in the sum of the two cross sections, which is the physical quantity of interest. This effect is demonstrated in Figure 2.4 for the specific case of $p\bar{p} \to Z^0/\gamma^\star + X \to e^+e^- + X$ at 2 TeV. The dependence of the (n+1)-body and n-body contributions to the NLO cross section are shown as the $\rm s_{min}$ parameter is varied over two orders of magnitude. The individual cross section contributions depend strongly on the parameter, but the sum of the contributions is independent of the parameter.

One caveat of this method is that the $\rm s_{min}$ parameter needs to be kept small enough that the unresolved emissions are truly unresolvable at the experimental level. For a complete description of $\rm s_{min}$-slicing refer to [Gie92, Gie93].

2.3 Incorporating NLO Matrix Elements into Showering Event Generators

Having outlined the two types of Monte Carlo programs most commonly used to simulate experiments, the present section is dedicated to describing qualitatively the method which has been implemented in Ref. [Dob01d] to combine the desirable features of the parton shower approach with next-to-leading order hard subprocess matrix elements. The primary aim of this method is to improve the usefulness of NLO

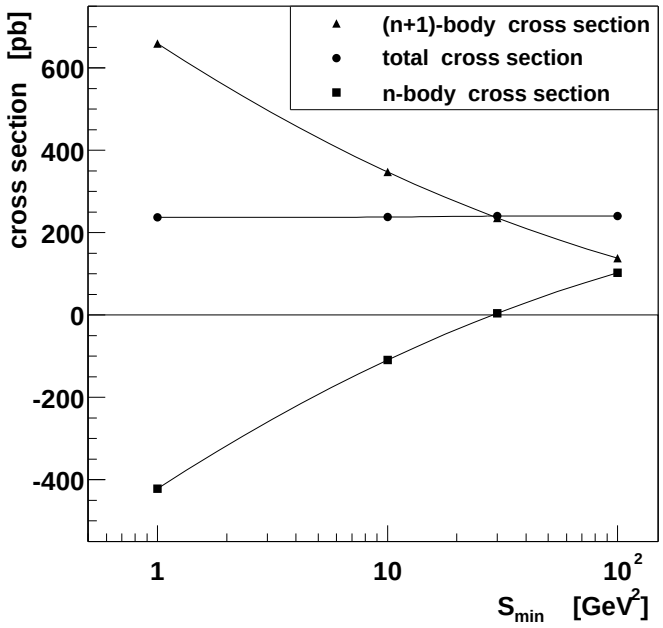

Figure 2.4: The (n+1)-body and n-body contributions to the NLO cross section and the total cross section (sum of (n+1)-body and n-body contributions) are shown as a function of the s_{min} parameter. The calculation is performed with the program of Ref. [Dob01d] and the process is $p\bar{p} \to Z^0/\gamma^\star + X \to e^+e^- + X$ at 2 TeV with the lepton-pair mass is restricted to the region 66-116 GeV.

calculations for experimental applications by interpreting the result in a manner which is well suited for interface to showering and hadronization generators and subsequent detector simulation.

The pursuit of techniques for combining NLO calculations with the parton shower is a natural direction for the evolution of event generators. Two primary challenges stand in the way. The first is the negative weights which are inherent in the traditional treatment of NLO matrix elements and have already been discussed in the previous section. This challenge requires the result to be interpretable in a probabilistic way (probabilities should be everywhere positive definite).

The second challenge is referred to as the double counting problem. NLO calculations normally rely on an integration of two phase space volumes of differing dimensionality. Care must be taken to ensure the contributions from each part are counted exactly once. If a parton shower is applied to an event with a specific configuration in phase space, it mutates the configuration, pushing it towards a different region. When a parton shower is applied to a leading order electroweak configuration, this is of no concern, because the shower is adding QCD features to the event which are never sampled otherwise. However, for the NLO calculations there are two distinct phase spaces, the n-body one and the (n+1)-body one. The application of the parton shower to an n-body configuration, for example, could mutate the event such that the post-shower configuration is in a region of phase space which has already been spanned by the (n+1)-body events. This results in a double counting of some regions of phase space, and spoils the calculation. The double counting challenge requires overlaps between phase space volumes of differing dimensionality to be accounted for in a manner which does not double-count or neglect any region.[9]

2.3.1 The phase space veto method

Consider the $\hat{t}$ vs. $\hat{u}$ space shown Figure 2.3. For each n-body phase space point, there exists a specific value of s_{min}, referred to here as s_{zero}, for which the sum of the n-body

[9]Significant advances towards the resolution of the second challenge have been achieved by Collins [Col01] using a subtractive approach, but this approach does not address the issue of negative probability events.

and unresolved (n+1)-body contributions is zero. Knowing the location of this s_{zero} boundary on an event by event basis, one may calculate the NLO cross section and distributions by sampling only the (n+1)-body phase space, restricted to that region which lies above the s_{zero} boundary (resolved partons). Thus $\sigma^{n}(\Phi_n, s_{zero}) = 0$ and the constant of Eq. 2.8 is

$$\int_{s_{ik}>s_{zero}} \sigma^{n+1}(\Phi_n, \Phi_{+1}) d\Phi_{+1} \;=\; \textsc{Const}(\Phi_n). \tag{2.9}$$

The analytic expression for $\sigma^{n}(\Phi_n, s_{min})$ [Gie93] has been used to derive the analytical expression for s_{zero}, which is presented in the appendix of Ref. [Dob01d].

A variant of this idea was originally proposed by Baer and Reno in Ref. [Bae91]. They approximated the s_{zero} boundary as constant and evaluated it by trial and error for single gauge-boson production in hadronic collisions using the two parameter PSS method. However, the location of the boundary varies event-by-event with the n-body kinematics. This was demonstrated by Pötter [Pöt01a], who formulated techniques for evaluating the s_{zero} boundary dynamically event-by-event and implemented them for jet production in deep inelastic scattering [Pöt01b].

To illustrate the phase space veto (Φ-space Veto) method for hadronic collisions, consider again the Drell-Yan $p\overset{(-)}{p} \rightarrow Z^0 + X \rightarrow l^+l^- + X$ example. As for the PSS methods, the phase space is divided into two distinct volumes. The n-body volume encompasses the phase space with no resolved emission ($p\overset{(-)}{p} \rightarrow Z^0 \rightarrow l^+l^-$ kinematics), while the (n+1)-body volume describes the phase space with an extra parton in the final state, $p\overset{(-)}{p} \rightarrow Z^0 j \rightarrow l^+l^- j$, where j denotes a gluon or (anti)quark. For the PSS method, the two volumes would be integrated separately using numerical techniques, and then added together, as described in Section 2.2.2.

For the Φ-space Veto method, the integration is organized differently. Only the (n+1)-body volume is integrated, and the n-body matrix elements are used to test on which side of the s_{zero} boundary each phase space point lies. An event candidate sampled in the unrestricted (n+1)-body phase space represents a point in the $\hat{u}$ vs. $\hat{t}$ plane shown in Figure 2.3. If the point lies below the s_{zero} boundary, the event is vetoed—because the integrated cross section of all such points is zero by construction.

If it lies above the boundary, it is assigned the event weight from the (n+1)-body differential cross section. Since the location of the s_{zero} boundary depends on both the factorization and renormalization scales, the reduced scale dependence of the NLO calculation is maintained.

The location of the s_{zero} boundary is known analytically as a function of the 4-dimensional n-body phase space Φ_n, whereas the candidate event is a point in the 7 dimension (n+1)-body phase space. Thus, it is necessary to project 7 dimension (n+1)-body kinematics onto the 4 dimension n-body ones. This is accomplished by requiring the lepton-pair mass M_{l+l^-}, and rapidity $Y_{l^+l^-}$, to remain unchanged in the projection.[10] To perform the projection, the center of mass frame lepton momenta are boosted into the gauge-boson rest frame (which is the 'new center of mass frame'), and then boosted longitudinally such that the pair regains its original rapidity, $Y_{l^+l^-}$.

In Figure 2.5 the s_{zero} boundary for the Tevatron and LHC collider energies are shown as a function of the lepton-pair rapidity for several parton center of mass choices. The dependence of the s_{zero} boundary on the choice of renormalization and factorization scales is shown in Figure 2.6.

With the analytical expressions for the s_{zero} function, the tools are in place to address the challenge of unweighted event generation. In the next section, it will be shown that the numerical results from this method are consistent with predictions from the traditional NLO formulation. Following that, the algorithm which incorporates the parton shower will be described.

2.3.2 Numerical results

An event generator for the process $p\overset{(-)}{p} \to l^+l^- + X$ has been constructed by the author and used to generate event distributions relevant to the Fermilab Tevatron Collider and the CERN Large Hadron Collider (LHC). It is implemented using the squared ma-

[10] This projection is somewhat arbitrary, one could equally well choose from a number of other possibilities such as fixing the longitudinal momentum of the lepton-pair $P^z_{l+l^-}$, and the lepton-pair mass. The important feature for the projection is that it must leave the system unchanged in the limiting case $s_{zero} \to 0$ when the (n+1)-body phase space collapses onto the n-body phase space. In this limit, all of the acceptable projections are indistinguishable. The projection which is used for the Φ-space Veto is the one which is used by the parton shower algorithm, which will be discussed in the next sections. This consistency motivates the projection choice.

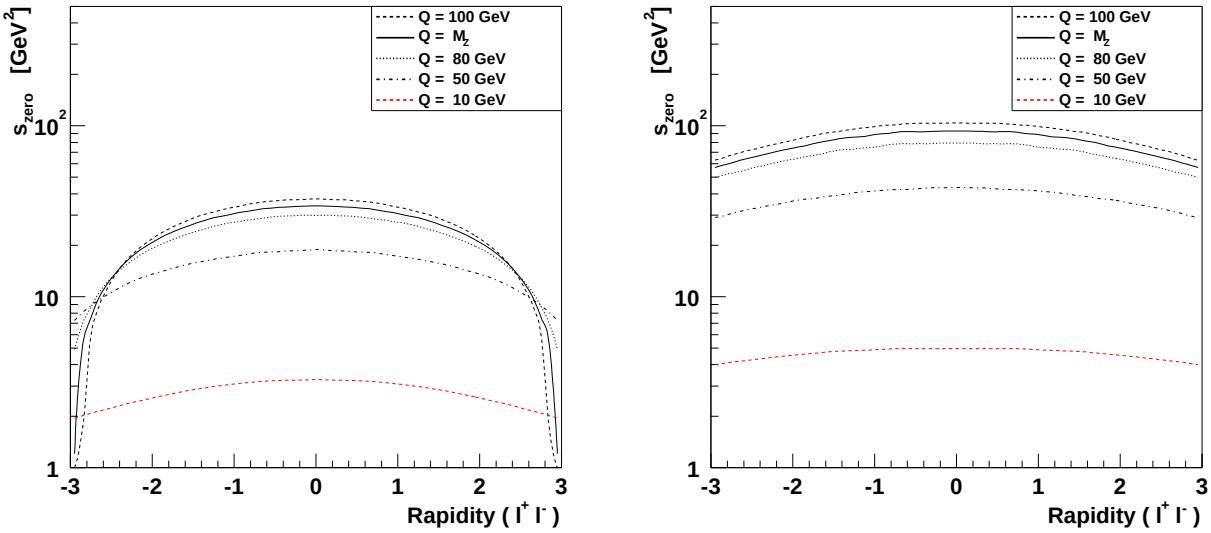

Figure 2.5: The dependence of s_{zero} as a function of lepton-pair rapidity at several choices of parton the center-of-mass energy Q is shown for the $p\bar{p}$ collisions at 2 TeV (Tevatron, left) and for pp collisions at 14 TeV (LHC, right). The s_{zero} function does not depend strongly on the gauge-boson decay angles.

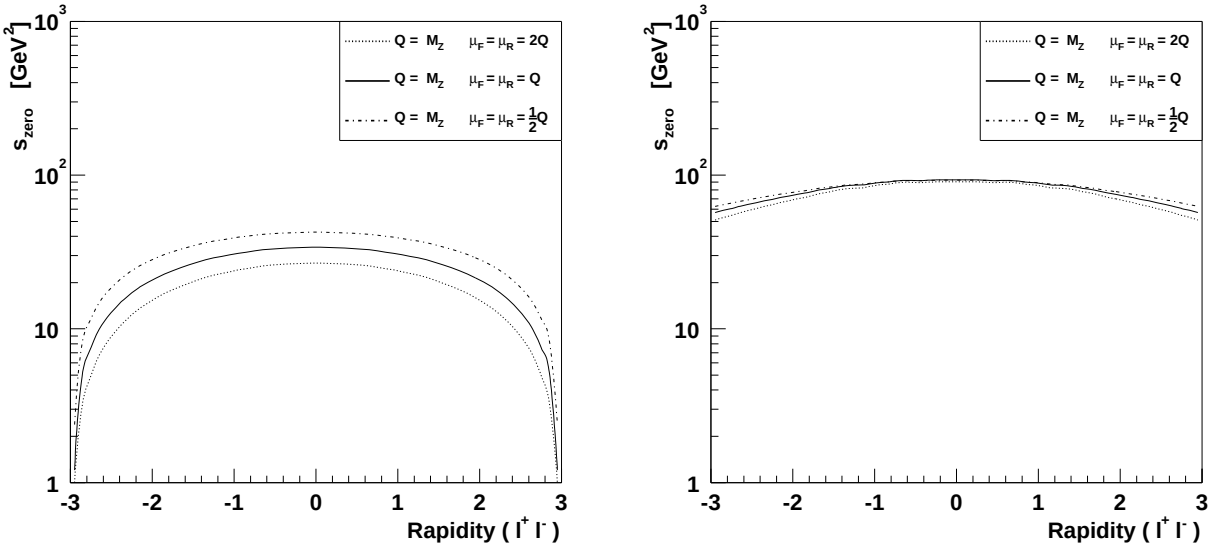

Figure 2.6: The scale variation of the s_{zero} function evaluated at parton center-of-mass energy equal to the Z^0 mass is shown for $p\bar{p}$ collisions at 2 TeV (Tevatron, left) and for pp collisions at 14 TeV (LHC, right). The s_{zero} function encodes information about the factorization and renormalization scale choices into the Φ-space Veto method, preserving the NLO calculation's reduced scale dependence.

trix element expressions of Ref. [Aur81] cast into the s_{min}-slicing method [Gie93]. The matrix elements include both the Z^0 and $\gamma^\star$ diagrams with decay to massless leptons, such that the branching ratio to one lepton flavor is automatically included. This means finite width effects, lepton decay correlations, and forward-backward asymmetries are everywhere taken into account. The generator is written in C++ using modern object-oriented design patterns. A new prototype C++ version of the Bases/Spring program [Kaw95] is used for sampling the phase space and unweighting the events using the hit-and-miss technique. Special care has been taken to make the program user friendly, and it is available upon request from the author.

All of the distributions and cross sections presented in this chapter are for $p\bar{p}$ collisions at 2 TeV (Tevatron Run II) or pp collisions at 14 TeV (LHC), with the Z^0 decaying to e^-e^+ and the lepton-pair mass restricted[11] to the range 66-116 GeV. CTEQ3M [CTEQ94] parton density functions are used. For all calculations the renormalization and factorization scales have been set equal to the lepton pair mass, $\mu_R = \mu_F = M_{l^+l^-}$, and the $\overline{\text{MS}}$ factorization scheme is used. The SHG program `PYTHIA` 6.200 [Sjö01b] will be employed in the following section to provide the parton shower, and so the input parameters for the event generator are chosen to coincide with the ones used in that program: the Z^0 mass and width are $M_Z = 91.188$ GeV and $\Gamma_Z = 2.47813$ GeV, the electroweak mixing angle is $\sin^2\theta_W = 0.232$, and the electroweak coupling is $\alpha_{\text{QED}}(M_Z) = 1/128.8$. The two-loop $\overline{\text{MS}}$ expression for α_S is used with $\Lambda^{4,\overline{\text{MS}}} = 0.239$ GeV.

Using these input parameters, the Φ-space Veto event generator predicts an inclusive cross section of 239.7 ± 0.6 pb for $p\bar{p}$ collisions at 2 TeV. In Figure 2.7 the inclusive cross section prediction from the Φ-space Veto event generator is compared to the predictions from the s_{min}-slicing calculation using several choices of the s_{min} parameter. The results are consistent, indicating the s_{zero} boundary lies within the region where the s_{min}-slicing approximation is valid.

In Figure 2.8 distributions produced with the Φ-space Veto event generator are compared to those derived from numerical integrations using s_{min}-slicing. The Φ-

[11] Hence the gauge-boson is denoted by Z^0, even though the $\gamma^\star$ contribution is included.

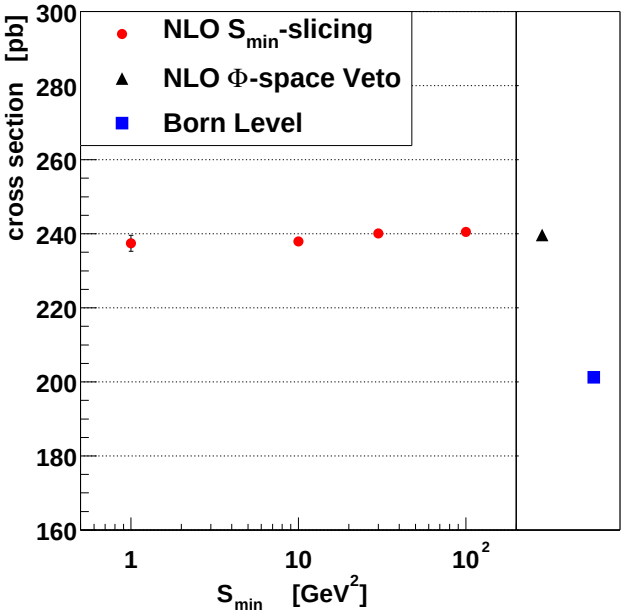

Figure 2.7: The inclusive NLO cross section for $p\bar{p} \to Z^0 + X \to e^+e^- + X$ reactions at 2 TeV with the lepton-pair mass restricted to 66-116 GeV is shown as a function of the s_{min} parameter for the s_{min}-slicing method. The cross section calculated using the Φ-space Veto event generator is superimposed and is in good agreement. The Born-level cross section is also shown.

space Veto method faithfully reproduces the NLO transverse momentum of the electron. The transverse momentum of the gauge-boson also agrees well with the s_{min}-slicing everywhere that the NLO calculation is valid.

In the small P_Z^T region, multiple gluon emission becomes important and fixed order perturbation theory is unreliable. This is evident in the inset of Figure 2.8. In this region the results depend on the specific choice of the s_{min} parameter. This is also the region where the Φ-space Veto method becomes unreliable because the minimum jet scale is coupled to the n-body kinematics. This effect is visible in Figure 2.9, where the kinematics of the vetoed event candidates from the Φ-space Veto method for a typical event generation run are plotted in the P_Z^T vs. s_{min} plane. The largest P_Z^T of a vetoed candidate event is 5.5 GeV, indicating the NLO calculation is unable to provide a useful prediction in the region below ≈ 5.5 GeV. It is worth stressing that this does not make the Φ-space Veto method less useful than s_{min}-slicing since any NLO calculation is unreliable here. This is the region where the distributions are better modeled with the parton shower, and a suitable treatment which removes this minimum jet scale coupling will be provided in the next section. The s_{zero} boundary represents a lower limit to the usefulness of our fixed order perturbative approximation. As such, s_{zero}

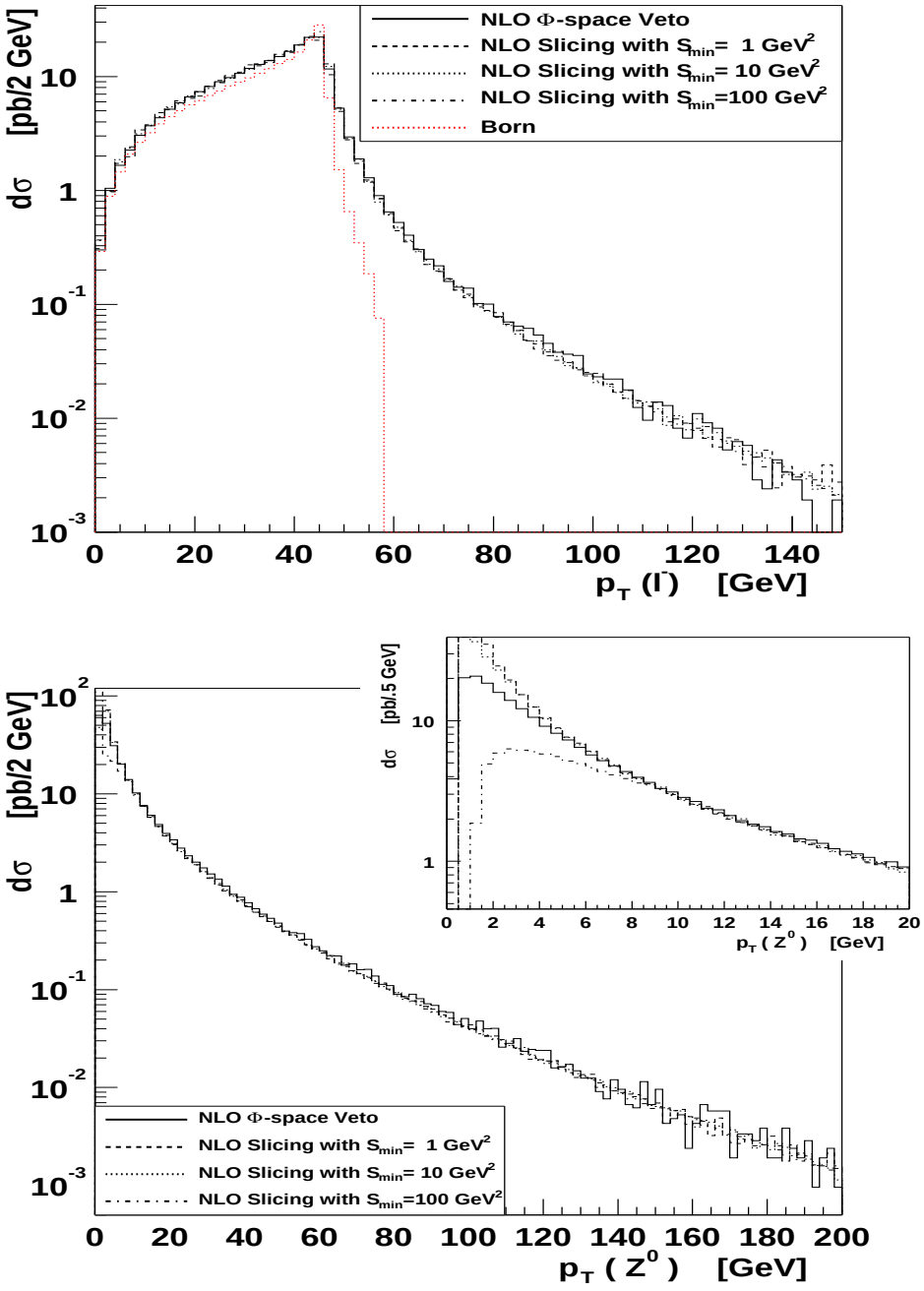

Figure 2.8: The transverse momentum of the electron (top) and gauge-boson (bottom) are shown for the process $p\bar{p} \rightarrow Z^0 + X \rightarrow e^+e^- + X$ at 2 TeV with the lepton-pair mass restricted to 66-116 GeV (no parton showering is used). Distributions derived from numerical integrations at NLO using s_{min}-slicing for various choices of the s_{min} parameter are compared to the distributions from the NLO Φ-space Veto event generator. Agreement is excellent everywhere, except in the low P_Z^T region (bottom, inset) where fixed order perturbative QCD is unreliable. The Born level prediction is also super-imposed for the $P_{e^-}^T$ distribution (top). The Born level prediction for the gauge-boson transverse momentum is a delta function at $P_Z^T = 0$.

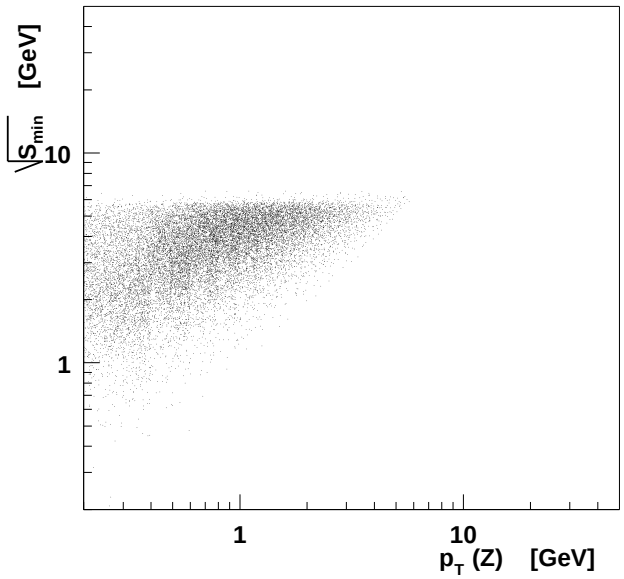

Figure 2.9: The kinematics of Φ-space Veto method event candidates which have been vetoed because they lie below the s_{zero} boundary are plotted in the P_Z^T vs. $\sqrt{s_{min}}$ plane. The largest P_Z^T of a vetoed candidate event is 5.5 GeV. The process is $p\bar{p} \to Z^0 + X \to l^+l^- + X$ at 2 TeV with the lepton-pair mass restricted to 66-116 GeV.

is a useful concept as an approximate measurement of the frontier of the validity of our perturbative calculation.

In Figure 2.10 the factorization and renormalization scale dependence of the transverse momentum distributions of the electron and gauge-boson are shown using the Φ-space Veto method at LHC energy. The scale dependence is identical to that from the s_{min}-slicing method, because the s_{zero} boundary encodes information about the scale choices (Figure 2.6). The change in the distributions resulting from the variation of the scales is an indication of the theoretical error arising from neglected higher order terms. The importance of the reduced scale dependence is demonstrated in Figure 2.11, where the variation in the prediction at Born level and at NLO of the transverse momentum of the electron for $pp \to Z^0 + X \to e^+e^- + X$ at LHC energy is shown. The comparison is restricted to that region where the Born level prediction is meaningful. The same comparison is shown for the lepton-pair mass distribution in Figure 2.12. The change in the scale at Born level results in more than a 25%

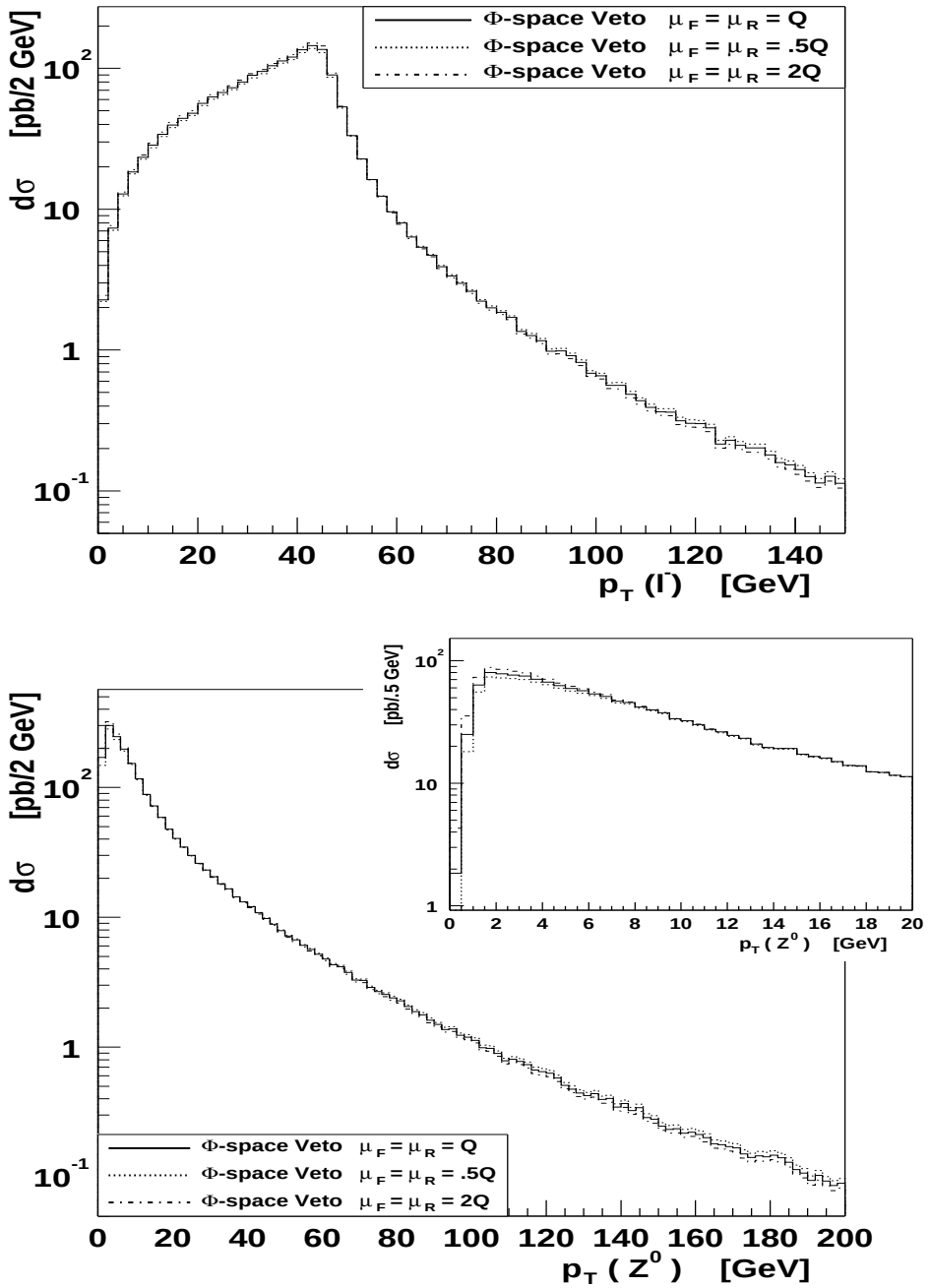

Figure 2.10: The transverse momentum of the electron (top) and gauge-boson (bottom) are shown for the process $p\bar{p} \rightarrow Z^0 + X \rightarrow e^+e^- + X$ at NLO using the Φ-space Veto method (no parton showering is used) for different choices of the renormalization and factorization scales. The spread in the distributions is an indication of the theoretical error from neglected higher order terms. The distributions are for 14 TeV pp collisions at the LHC. The lepton-pair mass is restricted to 66-116 GeV, and the three curves use the same event sample.

variation in the distributions, whereas the prediction from the NLO Φ-space Veto generator reduces this variation to about 7%. The scale dependence arising in predictions from event generators which use leading order subprocesses (like `PYTHIA`, `HERWIG`, and `ISAJET`) will resemble that of the Born level prediction.

2.3.3 Shower evolution

At the present stage, each event consists of the gauge-boson decay products and exactly one colored emission in the final state. The energy scale of the emission (jet energy scale) is at least $\sqrt{s_{zero}}$. Unweighted events are produced, and the normalization is NLO. A coupling between the minimum emission scale $\sqrt{s_{zero}}$ and the kinematic configuration exists in the very small P_Z^T region.

The next step is a consistent interface to a parton shower algorithm. The goal is to have the parton shower dominate the prediction in the soft/collinear region (in particular, it should preserve the parton shower's prediction of Sudakov suppression[12] [Dav85]), and the first order tree level diagrams dominate in the region of hard and well separated partons. This does not compromise the integrity of the prediction, it merely highlights that different approaches are well-suited to different regions.

To accomplish this, a parameter $s_{P.S.}$ is introduced to partition a region of $\hat{t}$ vs. $\hat{u}$ space which is exclusively the domain of the parton shower. This parameter may be thought of as separating the fixed order regime from the all-orders parton shower region, in the same way that an $\mathcal{O}(1\text{ GeV})$ parameter in the showering and hadronization programs defines the scale at which the parton shower is terminated, and the simulation turns to the non-perturbative hadronization model for a description of the physics. This partition is shown in Figure 2.13. Events which lie below the $s_{P.S.}$ boundary are first projected onto n-body kinematics (i.e. the point in $\hat{t}$ vs. $\hat{u}$ space is moved to the origin) and the parton shower is allowed to evolve the event out into the plane. The projection is performed keeping the lepton-pair mass and rapidity fixed,

[12] The transverse momentum distribution of the Z^0 increases as one moves from large to small $P_{Z^0}^T$ until eventually—at a few GeV—it starts to fall off such that it is zero at $P_{Z^0}^T = 0$. This is known as Sudakov suppression, and represents the fact that the probability to produce a massive lepton pair with no addition radiation is zero.

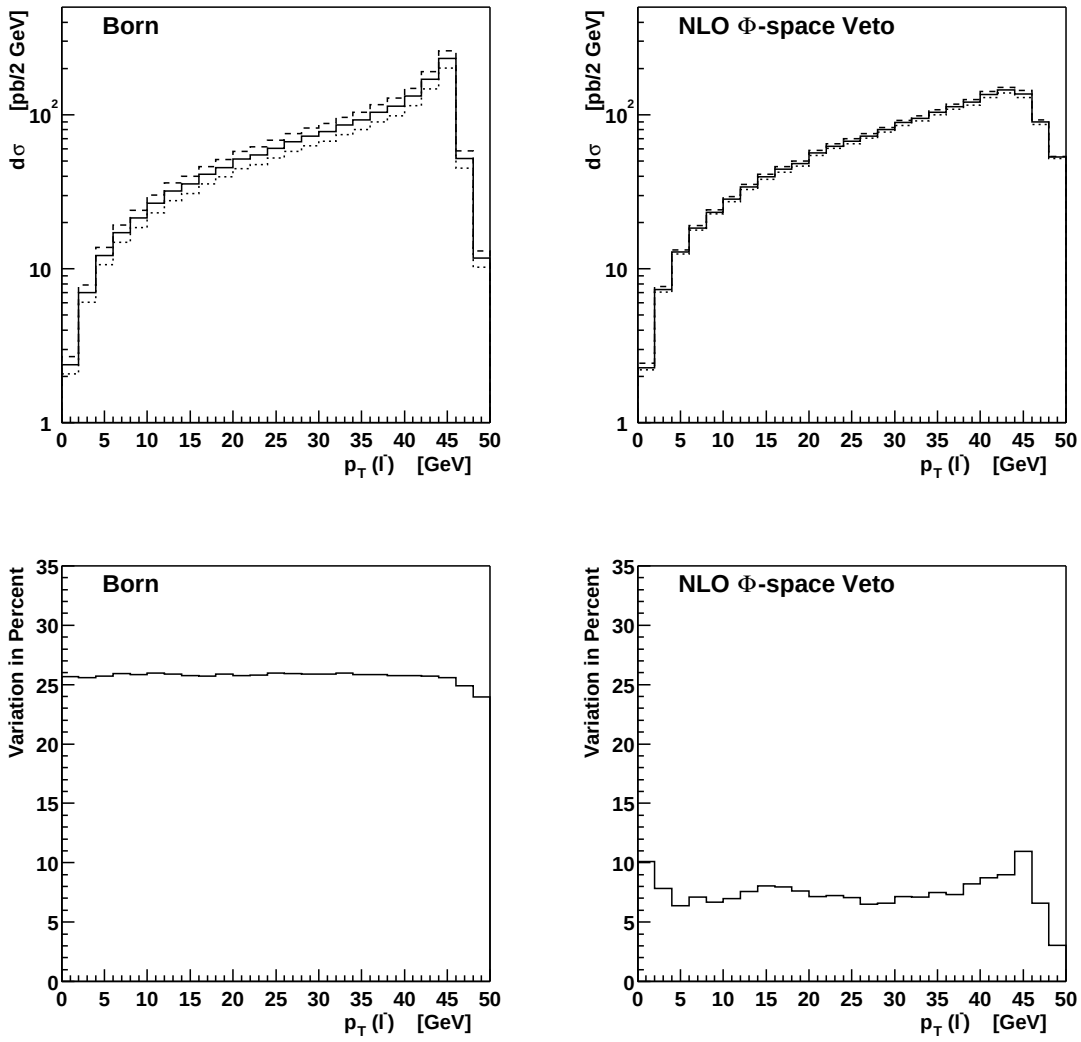

Figure 2.11: The reduced scale dependence of the NLO Φ-space Veto calculation as compared to the Born one is demonstrated. The transverse momentum of the electron (top) for the process $pp \to Z^0 + X \to e^+e^- + X$ with the lepton-pair mass restricted to 66-116 GeV at LHC energy (14 TeV) is shown (the gauge-boson transverse momentum is not shown because the Born level calculation does not provide a prediction for $P_{\rm Z}^T$). The renormalization and factorization scales are varied by a factor two in the Born level calculation (left) and the NLO Φ-space Veto calculation (right). The percent variations of the distributions are shown at bottom. The variation is about a factor 4 smaller for the NLO Φ-space Veto. The effect is smaller at Tevatron energy in this region.

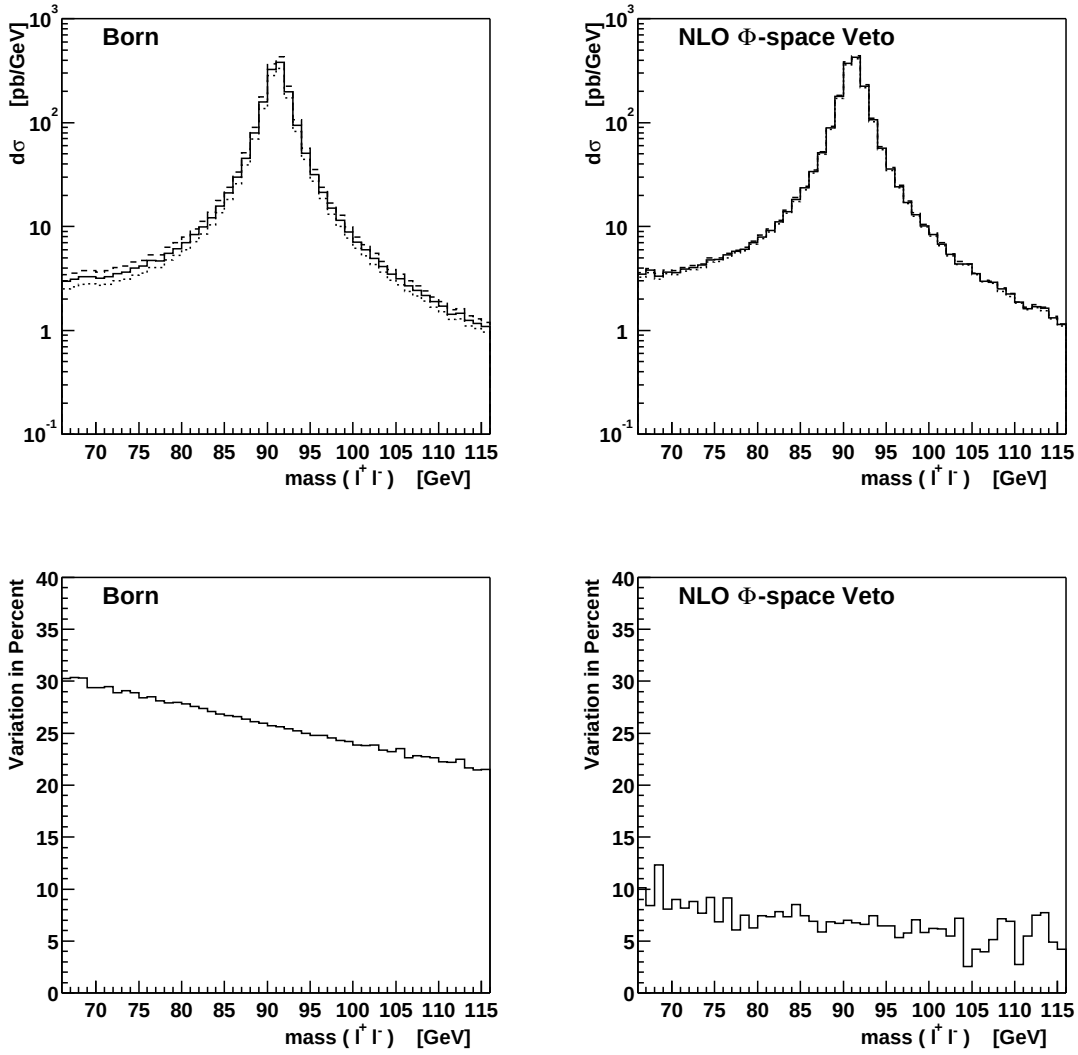

Figure 2.12: The reduced scale dependence of the NLO Φ-space Veto calculation as compared to the Born one is demonstrated. The lepton-pair mass in the vicinity of the Z^0 resonance is shown (top) for the process $pp \to Z^0 + X \to e^+e^- + X$ at LHC energy (14 TeV). The renormalization and factorization scales are varied by a factor two in the Born level calculation (left) and the NLO Φ-space Veto calculation (right). The percent variations of the distributions are shown at bottom. The variation is about a factor 3 smaller for the NLO Φ-space Veto. The effect is smaller at Tevatron energy.

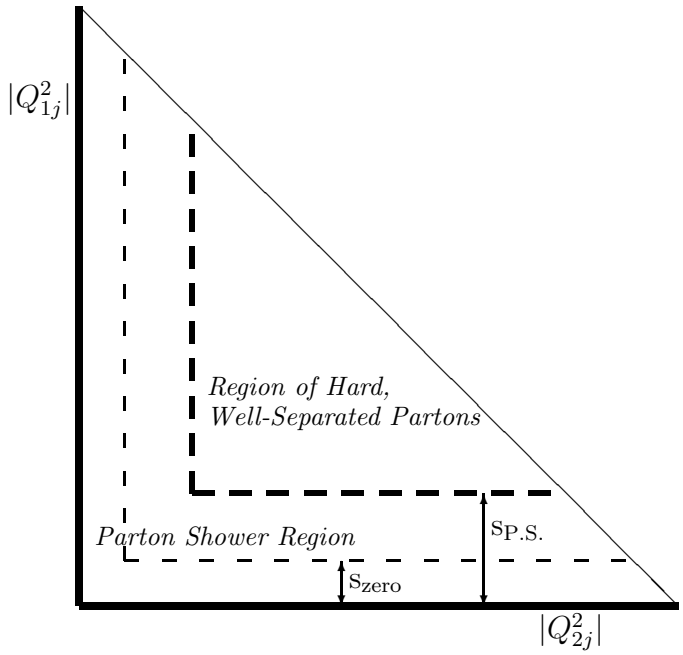

Figure 2.13: A projection of the $p\bar{p}^{(-)} \to Z^0 j$ phase space onto the $\hat{u}$ vs. $\hat{t}$ plane is shown, where $\hat{u} = (p_2 - p_j)^2 = -Q^2_{2j}$ and $\hat{t} = (p_1 - p_j)^2 = -Q^2_{1j}$, and $p_1,\ p_2,\ p_j$ are the momenta of the forward colliding parton, backward colliding parton, and the hardest emission. Events in the region of hard and well separated partons are sampled with the first order matrix element, then evolved further by the parton shower. Events in the region between the s_{zero} and $s_{P.S.}$ boundaries are projected onto n-body kinematics (i.e. onto the origin of the plane) and then evolved with the parton shower to a point which may lie anywhere below the $s_{P.S.}$ boundary. The region below s_{zero} is never sampled, but may be reached by the projected and showered events.

exactly as described in Sec. 2.2.2. This is consistent with the treatment in the parton shower algorithm, which transfers the recoil from the parton shower to the hard subprocess by performing a "conformal boost"[13] on the hard subprocess, keeping the same variables fixed. The parton shower is invoked with the scale set to $\sqrt{s_{\text{P.S.}}}$, which ensures the evolution does not move the event out into a region of phase space which has already been counted using the first order tree level matrix elements.

A reasonable choice for the $\sqrt{s_{\text{P.S.}}}$ parameter is a few times the minimum jet scale, $\sqrt{s_{\text{zero}}}$. This ensures the first order tree level matrix element is reliable above the $s_{\text{P.S.}}$ boundary. The distributions have very little sensitivity to the choice of $s_{\text{P.S.}}$.

For events which lie above the $s_{\text{P.S.}}$ region, the parton shower is also invoked, this time with a scale equal to the minimum invariant mass of any parton-pair

$$\text{parton shower scale} \;=\; \text{minimum}\,[\; Q_{q\bar{q}},\; Q_{qg},\; Q_{\bar{q}g}\;] \tag{2.10}$$

which ensures no double counting can occur by allowing the parton shower to operate only below the scale which defines the fixed order regime.

The effect of the projection and subsequent parton showering is shown in Figure 2.14. Initially the distributions are provided by the Φ-space Veto, solid line. The projection is applied to events that sit below the $s_{\text{P.S.}}$ boundary, which effects only the small P_{Z}^{T} region, and is shown as a dashed line and does not correspond to anything physical. Finally the parton shower is applied (dotted line), and has the largest effect on those events which have been projected.

In Figure 2.15 the Φ-space Veto event distributions (including parton shower evolution) are shown for several choices of the $s_{\text{P.S.}}$ parameter. The dependence on the $s_{\text{P.S.}}$ parameter choice is small, indicating discontinuities which might exist at the $s_{\text{P.S.}}$ boundary are also small.

For the distributions presented here, events from the Φ-space Veto generator have been evolved with the `PYTHIA` 6.200 parton shower. `PYTHIA` is attached using the

[13]The conformal boost is not Lorentz invariant, which serves as a reminder that the parton shower is an approximate model. This sort of approximate treatment of the boost is unavoidable for the shower algorithm, because it receives massless partons as input from the hard subprocess. It then proceeds to split these massless partons, which is in violation of energy and momentum conservation (evident because a massless particle has no rest frame).

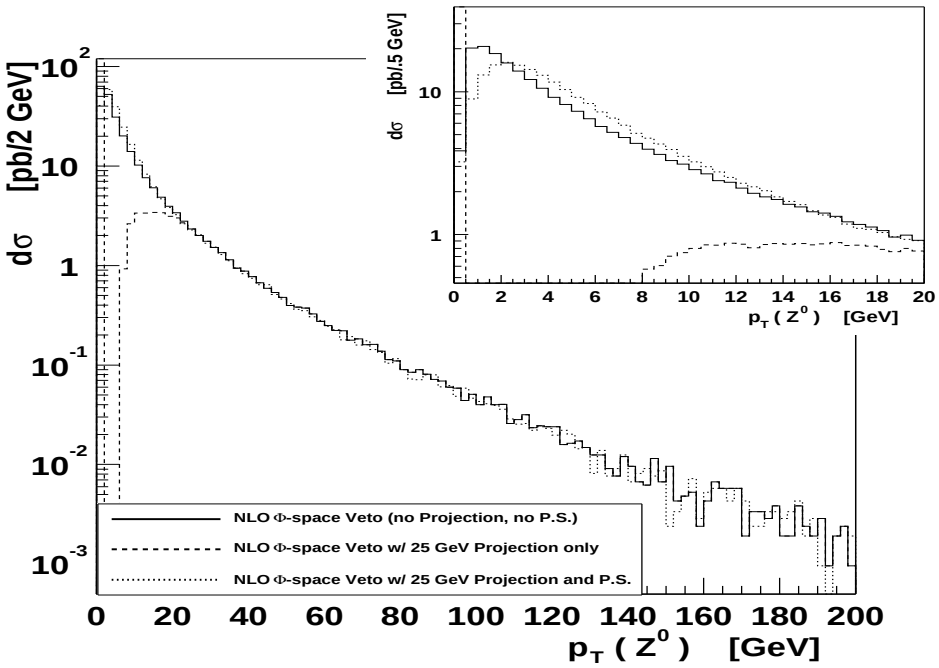

Figure 2.14: The P_Z^T distribution is shown after different stages of the event generation for $p\bar{p} \to Z^0 + X \to e^+e^- + X$ at 2 TeV with the lepton-pair mass restricted to 66-116 GeV. The solid line is the Φ-space Veto NLO distribution without any projection or parton shower. The dashed line is the (nonphysical) distribution for the same event sample, after applying the projection with $\sqrt{s_{\rm P.S.}} = 25$ GeV. The dotted line is the distribution after subsequent evolution through the showering and hadronization program.

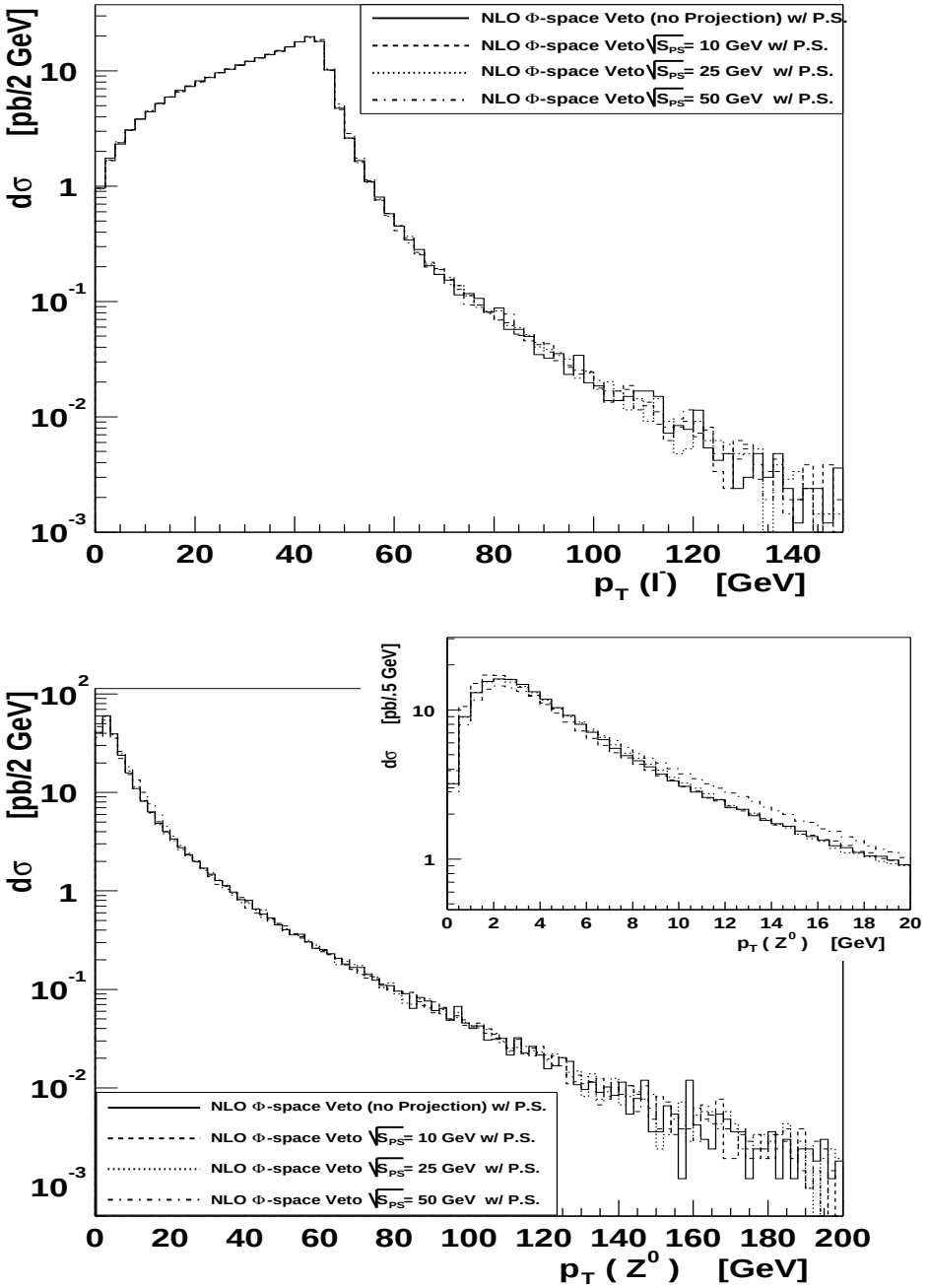

Figure 2.15: The effect of the parton shower on the Φ-space Veto distributions is shown for several choices of the $s_{P.S.}$ parameter which partitions the phase space into the region populated by the parton shower, and the region populated directly by the first order matrix elements. The transverse momentum of the electron (top) and gauge-boson (bottom) are plotted for the process $p\bar{p} \to Z^0 + X \to e^+e^- + X$ at 2 TeV with the lepton-pair mass restricted to 66-116 GeV. There is very little dependence on the specific choice of the $s_{P.S.}$ parameter.

Method	Time for Grid Initialization	Time for 10000 Events	Efficiency
Φ-space Veto	14.0 s	70.3 s	28%
PYTHIA	—	68.6 s	27%

Table 2.1: A comparison of computer processing time for the Φ-space Veto method and for PYTHIA. In each case 10000 events are generated for the process $p\bar{p} \to Z^0 + X \to e^+e^- + X$ at 2 TeV and the events are evolved through the PYTHIA shower and hadronization program. The Φ-space Veto event generator requires some time to initialize the Bases/Spring grids (i.e. "learn the phase space"), whereas no initialization time is required for PYTHIA processes. The processing time per event and efficiency are similar. The computer is a 650 MHz Pentium III.

HEPUP interface [Boo01] (developed in part by the author, see Sec. 2.2.1), which is a generic standard for the communication between event generators. Having evolved the events through the parton shower, PYTHIA provides other features of the event structure such as hadronization, resonance decays, beam remnants, and multiple interactions. The showered event distributions presented in this paper include all of these features. The use of the HEPUP interface allows for the parton shower program to be easily interchanged. The choice of PYTHIA is arbitrary, there is nothing which precludes the use of any other showering program.

The full event generator is now complete. Adaptive integration and phase space generation is provided by BasesSpring. The event weights are evaluated using the Φ-space Veto method, which discards those event candidates lying below the s_{zero} boundary. When the program is executed, the phase space is first mapped onto a grid using an initialization pass with the adaptive integration (performed by the 'Bases' part of the BasesSpring package). The 'Spring' part of the BasesSpring package then provides unweighted events, by sampling candidate events from the adaptive integration grids and accepting events according to the differential cross section using the acceptance-rejection algorithm. After removing the emission from those events which are soft or collinear (as defined by the $s_{P.S.}$ parameter), the events are transferred to the PYTHIA package using the HEPUP interface. PYTHIA performs the parton shower, and subsequent event evolution including hadronization, etc.

A comparison of the computer time for generating the events is presented in Table 2.1. The processing time per event and generation efficiency (percentage of

candidate weighted events which are accepted in the event generation algorithm) for PYTHIA and the Φ-space Veto are similar, indicating the Φ-space Veto method is successful in encoding the extra NLO information without affecting the overall time-performance of event generation.

In Figure 2.16 the Φ-space Veto distributions (solid line, includes evolution with the PYTHIA showering and hadronization package) are compared to the predictions from PYTHIA. In PYTHIA there are two strategies implemented for single gauge-boson production. For both strategies the hard subprocess is chosen according to the Born level matrix element, such that the normalization is always leading order. For the "old" PYTHIA implementation of the process, the event is then evolved with the standard parton shower beginning at a scale equal to the gauge-boson mass. For the new "matrix element (M.E.) corrected" implementation of the process [Miu99], the shower is initiated at a scale equal to the machine energy and is corrected according to the Z^0+jet first order tree level matrix element, which results in a considerable improvement of the high P_Z^T region modeling. The virtual one-loop contribution is not included anywhere in the PYTHIA implementations. The dotted line in Figure 2.16 is from the "old" PYTHIA process, and the dashed line is from the M.E. PYTHIA process. The Φ-space Veto distribution and M.E. corrected PYTHIA shapes are rather similar, indicating the matrix element corrections in PYTHIA are having the desired effect. The Φ-space Veto distributions have the advantage of NLO normalization and a reduced dependence on the factorization and renormalization scales.

While the Drell-Yan production event generator is a useful example for demonstrating many of the benefits of the Φ-space Veto method, it is important to stress that further benefits will be realized when the method is applied to other more complicated processes. In Figure 2.16, it is seen that the PYTHIA matrix element corrections are successful at reproducing the high transverse momentum behavior that has previously only been achieved with next-to-leading order calculations. Matrix element corrections for diboson production were first implemented in Ref. [Dob01c]. For hadronic WZ production, the shapes of the distributions at high transverse momentum are also approximated rather well with matrix element corrections. However, the matrix

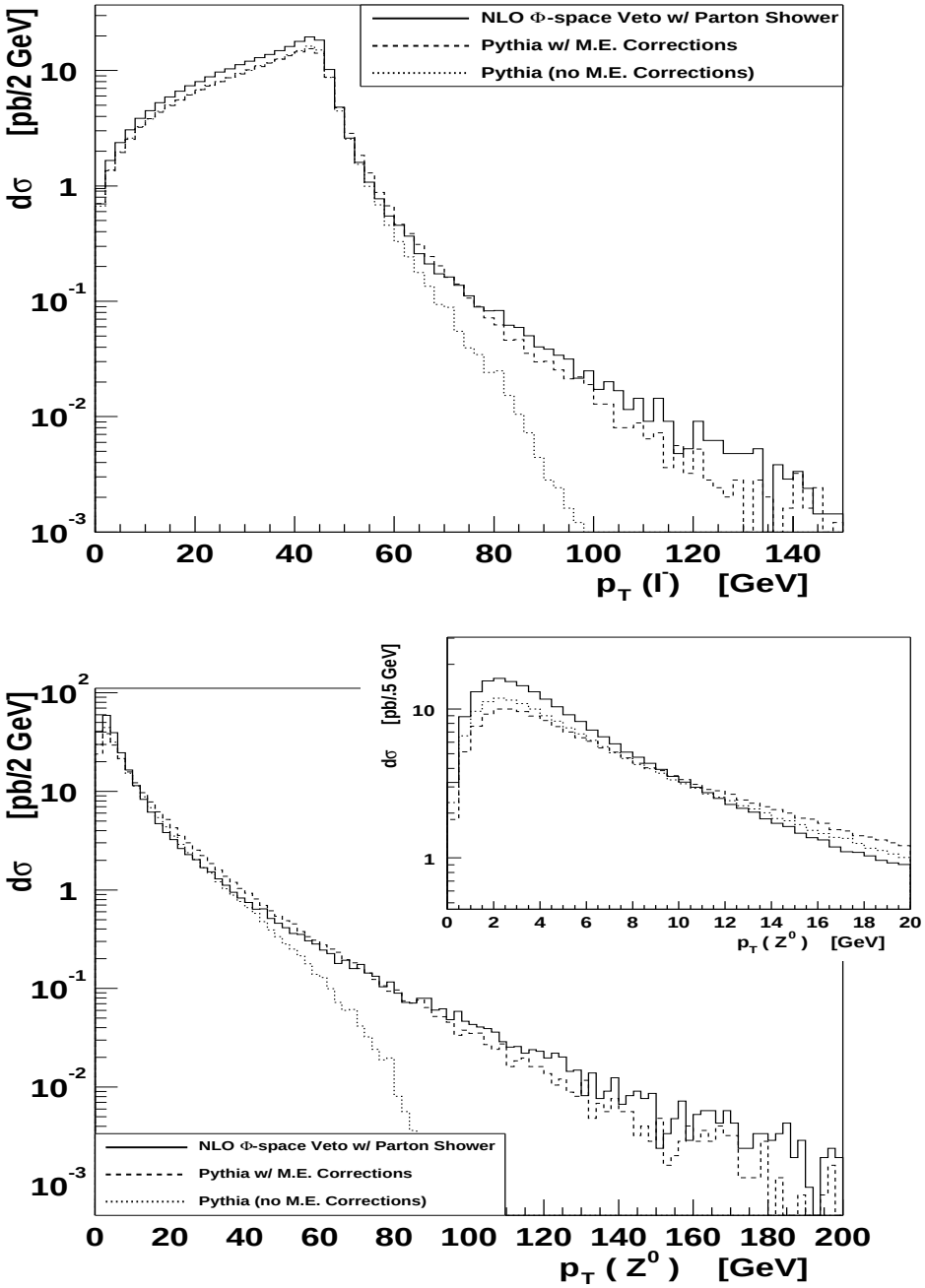

Figure 2.16: Distributions for the process $p\bar{p} \to Z^0 + X \to e^+e^- + X$ at 2 TeV from the Φ-space Veto event generator (solid line, includes evolution through the PYTHIA shower and hadronization program) are compared with the PYTHIA internal process distributions. The dashed line is the "matrix element corrected" PYTHIA prediction and the dotted line is the "old" (no matrix element corrections) PYTHIA prediction. The lepton-pair mass is restricted to 66-116 GeV.

element corrections are less effective at modeling the approximate radiation zero[14] in WZ production. In Ref. [Dob01c], a predecessor to the Φ-space Veto method was also implemented, and it was shown to give good agreement with the NLO radiation zero distribution. As such, it is expected that a Φ-space Veto method event generator for diboson production would not only provide an improved prediction of the cross section and reduced scale dependence, but also a better modeling of distributions than can be achieved with matrix element corrections.

2.3.4 Summary

The methods most commonly used to simulate higher order QCD corrections are the parton shower and the numerical integration of next-to-leading matrix elements. The two methods have complementary regions of applicability. The Φ-space Veto is a new technique which incorporates NLO matrix elements into showering and hadronization generators, effectively combining the two methods. It uses phase space slicing with the slicing parameter determined dynamically event-by-event and employs a veto which enforces the cancellations between virtual and real emission diagrams. In this chapter, the qualitative features of the Φ-space Veto have been presented, more information can be found in Ref. [Dob01d]. The primary motivation for the method is to move numerical NLO calculations beyond the status of "event integrators" to "event generators", making them suitable for interface to showering and hadronization programs and subsequent detector simulation.

The general features of the Φ-space Veto method are:

- event weights are positive definite, meaning the standard methods for event generation can be applied, providing a prediction which is well suited for experimental applications;

- in the soft/collinear region, the results are dominated by the parton shower. In

[14]The approximate radiation zero refers to a particular angle of emission for the Z^0 boson in the center-of-mass frame which is suppressed at Born level by subtle gauge cancellations. The net effect is a suppression of events in the direction transverse to the beam. For $W\gamma$ production, the approximate radiation zero becomes exact at Born level. The radiation zero will be discussed further in the chapters which follow.

particular the low P^T region exhibits Sudakov suppression;

- in the region of hard and well separated partons, the distributions are dominated by the first order matrix element;
- the normalization is NLO and the reduced scale dependence afforded by the NLO calculation is maintained.

The method has been implemented as an event generator (written in object-oriented C++ and available from the author) for $p\overset{(-)}{p} \to Z^0/\gamma^\star + X \to l^+l^- + X$, with showering and hadronization provided by the `PYTHIA` program.

Chapter 3

Vector Boson Interactions

In their simplest form, gauge-boson self interactions refer to an interaction vertex between three gauge-bosons, as shown in Figure 1.1. The self interactions also encompass interactions between four (quartic couplings) or more gauge-bosons. For hadronic diboson production, three Feynman graphs contribute at leading order, as shown in Figure 3.1. Of these three diagrams, only the s-channel diagram contains a triple gauge-boson coupling (TGC).

In this section theory and phenomenology relevant to the TGC vertex is reviewed. The philosophy which has been adopted for energy dependent anomalous TGC parameter form factors is outlined—and differs from the approach which has traditionally been employed for similar studies. In the last part of the chapter current experimental limits on the anomalous TGC parameters are summarized.

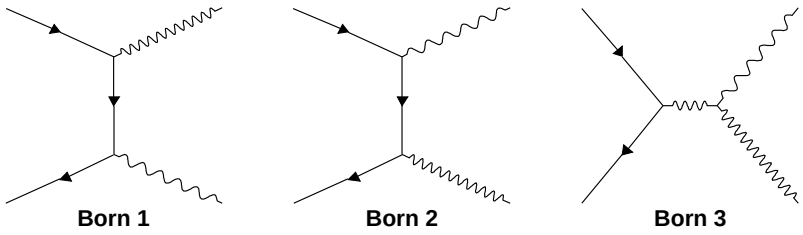

Figure 3.1: The Born-level Feynman graphs for $q\bar{q}' \to W\gamma$ or $q\bar{q}' \to WZ$. The s-channel diagram (right) contains a TGC vertex, whereas the t-channel diagrams (left and middle) do not.

3.1 Parametrisation of the WWV Vertex

In the Standard Model, self interactions of electroweak gauge-bosons are constrained by the non-abelian $\mathrm{SU}(2)_L \times \mathrm{U}(1)_Y$ gauge symmetry. The original motivation for studying (standard) TGC's is to test this constraint, by showing that gauge-bosons couple not only to electric charge but also to weak isospin (i.e. rejecting the possibility of a minimal U(1)-only coupling). This has been beautifully demonstrated at LEP [Ale99, Del99a, L3 98, Opa98] for $e^+e^- \to W^+W^-$, which receives contributions from both the WWZ and $WW\gamma$ vertex.

3.1.1 Effective three gauge-boson Lagrangian

The Standard Model WWV vertex (where V denotes either a Z^0 or γ gauge-boson) is uniquely determined by requiring $\mathrm{SU}(2)_L \times \mathrm{U}(1)_Y$ gauge invariance to be valid at arbitrary energy scales. Deviation from the SM vertex (i.e. anomalous couplings) would signal new physics, which could arise from loop corrections involving propagators of new particles or from unexpected internal structure of the particles which are believed to be fundamental (e.g. composite gauge-bosons). Assuming the new physics occurs at an energy scale significantly larger than that being probed experimentally, it can be integrated out, and expressed as a set of anomalous interaction vertices.

The most general Lorentz and gauge invariant WWV TGC vertex is described by 7 parameters (ignoring any theoretical or experimental constraints) and may be written in terms of an effective Lagrangian [Hag87, Zep88, Bau88b]

$$\begin{aligned}
i\mathcal{L}^{WWV}/g_{WWV} &= [\mathbf{1}+\boldsymbol{\Delta}\mathbf{g_V^1}]V^\mu(W^-_{\mu\nu}W^{+\nu}-W^+_{\mu\nu}W^{-\nu}) \\
&+ [\mathbf{1}+\boldsymbol{\Delta}\kappa_\mathbf{V}]W^+_\mu W^-_\nu V^{\mu\nu} \\
&+ \frac{\lambda_\mathbf{V}}{M_W^2}V^{\mu\nu}W^{+\rho}_\nu W^-_{\rho\mu} \\
&+ i\mathbf{g_V^4}W^-_\mu W^+_\nu(\partial^\mu V^\nu+\partial^\nu V^\mu) \\
&+ i\mathbf{g_V^5}\varepsilon_{\mu\nu\rho\sigma}[(\partial^\rho W^{-\mu})W^{+\nu}-W^{-\mu}(\partial^\rho W^{+\nu})]V^\sigma \\
&- \frac{\tilde{\kappa}_\mathbf{V}}{2}W^-_\mu W^+_\nu\varepsilon^{\mu\nu\rho\sigma}V_{\rho\sigma} \\
&- \frac{\tilde{\lambda}_\mathbf{V}}{2M_W^2}W^-_{\rho\mu}W^{+\mu}_\nu\varepsilon^{\nu\rho\alpha\beta}V_{\alpha\beta}
\end{aligned} \tag{3.1}$$

where M_W is the W-boson mass, V^μ and W^μ are the V and W fields, $W_{\mu\nu} = \partial_\mu W_\nu - \partial_\nu W_\mu$, and $V_{\mu\nu} = \partial_\mu V_\nu - \partial_\nu V_\mu$. The normalization factor is chosen for convenience to be $g_{WW\gamma} = -e$ and $g_{WWZ} = -e\cot\theta_W$.

There are 14 anomalous parameters (referred to here as anomalous TGC's) in total (7 for the WWZ vertex and 7 for the $WW\gamma$ vertex),

$$\Delta g_V^1,\ \Delta\kappa_V,\ \lambda_V,\ g_V^4,\ g_V^5,\ \tilde{\kappa}_V,\ \tilde{\lambda}_V. \tag{3.2}$$

Strictly speaking, these parameters are energy dependent, which will be discussed in Section 3.4.

All anomalous TGC's are zero in the SM.[1] For on-shell photons, electromagnetic gauge invariance requires $\Delta g_\gamma^1 = 0$. g_γ^4 and g_γ^5 are proportional to p_γ^2, and thus vanish for on-shell photons. Δg_Z^1, g_Z^4, and g_Z^5 may differ from their SM values, which is a consequence of the Z^0-boson mass. The operator in the Lagrangian with coefficient g_V^5 is charge (C) and parity (P) odd. The operators with coefficients g_V^4, $\tilde{\kappa}_V$, and $\tilde{\lambda}_V$ parameterize possible CP violation in the bosonic sector because they are CP odd. The properties of the anomalous TGC's are summarized in Table 3.1. For simplicity, most studies assume gauge invariance and separate C and P conservation, which reduces the number of anomalous TGC's for the $WW\gamma$ and WWZ vertices to 5,

$$\Delta g_Z^1,\ \Delta\kappa_Z,\ \lambda_Z,\ \Delta\kappa_\gamma,\ \lambda_\gamma \qquad \text{(gauge invariant C and P conserving anomalous TGC's).} \tag{3.3}$$

Prior to 1998, the LEP collaborations were using a different set of parameters consisting of only three independent coefficients [LEP95] $\alpha_W, \alpha_{W_\phi}, \alpha_{B_\phi}$, where $\lambda_\gamma = \lambda_Z$ and $\Delta\kappa_Z = \Delta g_Z^1 - \Delta\kappa_\gamma \tan^2\theta_W$ has been assumed. The relationships between these coefficients and the ones presented in Eq. 3.1 are

$$\begin{array}{rcl} \Delta g_Z^1 & = & \frac{\alpha_{W_\phi}}{\cos^2\theta_W} \\ \lambda_\gamma = \lambda_Z & = & \alpha_W \\ \Delta\kappa_\gamma & = & \alpha_{W_\phi} + \alpha_{B_\phi} \\ \Delta\kappa_Z & = & \alpha_{W_\phi} - \frac{\sin^2\theta_W}{\cos^2\theta_W}\alpha_{B_\phi}. \end{array} \tag{3.4}$$

[1] Often the anomalous TGC's are written as $g_V^1 = 1 + \Delta g_V^1$ and $\kappa_V = 1 + \Delta\kappa_V$, in which case $g_V^1 = 1$ and $\kappa_V = 1$ in the SM.

anomalous coupling parameter	Operator Dimensionality	Odd Transformations
Δg_V^1	4	
$\Delta\kappa_V$	4	
λ_V	6	
g_V^4	4	C, CP
g_V^5	4	C, P
$\tilde{\kappa}_V$	4	P, CP
$\tilde{\lambda}_V$	6	P, CP

Table 3.1: The dimensionality and transformation properties of the anomalous TGC parameters are summarized. An operator is 'odd' under a transformation if the transformation is equivalent to multiplying the operator by -1.

The HISZ scenario [Hag93] has been used by both the CDF and D0 collaborations and further reduces the number of independent coefficients to two by requiring (somewhat arbitrarily) $\alpha_{W_\phi} = \alpha_{B_\phi}$. Ref. [Opa97] provides a review of the various parameterizations for anomalous TGC's.

The $WW\gamma$ anomalous couplings are directly related to the lowest order terms in a multipole expansion of the $W^\pm$-photon interaction [Hag87, and references therein],

$$\begin{aligned}
q_{W^+} &= e(1+\Delta g_\gamma^1) && \text{is the electric charge} \\
\mu_{W^+} &= \tfrac{e}{2M_W}(2+\Delta\kappa_\gamma+\lambda_\gamma) && \text{is the magnetic dipole moment} \\
Q_{W^+} &= -\tfrac{e}{M_W^2}(1+\Delta\kappa_\gamma-\lambda_\gamma) && \text{is the electric quadrupole moment} \\
d_{W^+} &= \tfrac{e}{2M_W}(\tilde{\kappa}_\gamma+\tilde{\lambda}_\gamma) && \text{is the electric dipole moment} \\
\tilde{Q}_{W^+} &= -\tfrac{e}{M_W^2}(\tilde{\kappa}_\gamma-\tilde{\lambda}_\gamma) && \text{is the magnetic quadrupole moment.}
\end{aligned} \tag{3.5}$$

For a point-like W^+-boson in the Standard Model, the electromagnetic moments are $q = e,\ \mu = \frac{e}{M_W},\ Q = -\frac{e}{M_W^2},\ d = 0$, and $\tilde{Q} = 0$.

3.1.2 Modification to the matrix elements

In order to better understand how the effective Lagrangian relates to kinematic variables, the approximate modifications to the matrix element amplitudes are studied here. In the high energy limit ($\hat{s} >> M_W^2$, where $\sqrt{\hat{s}}$ is the parton center of mass energy) the change in the matrix element $\Delta\mathcal{M}_{H_\gamma,H_W}$ arising from anomalous TGC's

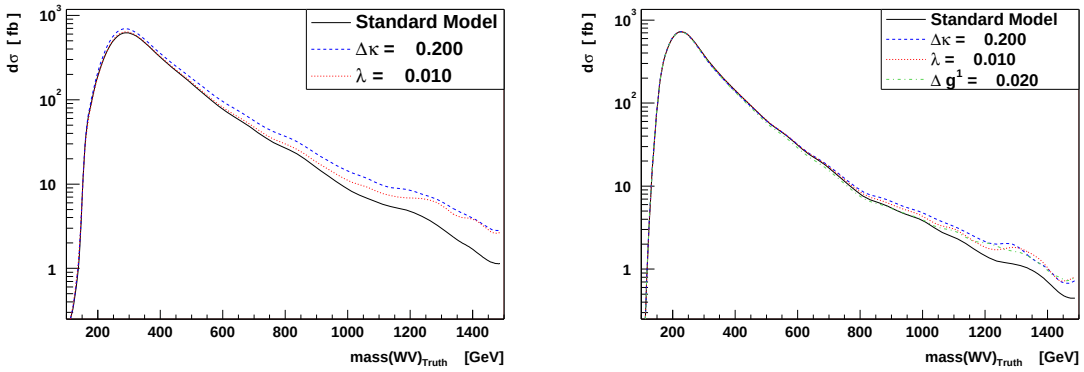

Figure 3.2: The diboson invariant mass distribution is shown for $W\gamma$ (left) and WZ (right) production at the LHC. The distributions are generated at NLO using the parton level generator of Ref. [Bau95] and [Bau93c] (hadronization and detector effects are not included). The kinematic cuts are chosen to coincide with the present analysis, the precise cuts are unimportant (the interested reader may refer to Chapter 4).

for the leading order partonic process $q\bar{q}' \to W\gamma$ is [Bau88b, Sno95]

$$\Delta\mathcal{M}_{\pm,0} \quad \propto \quad \frac{\sqrt{\hat{s}}}{2M_W}[\Delta\kappa_\gamma + \lambda_\gamma]\ \frac{1}{2}(1 \mp \cos\theta^\star_\gamma), \tag{3.6}$$

$$\Delta\mathcal{M}_{\pm,\pm} \quad \propto \quad [\frac{\hat{s}}{2M_W^2}\lambda_\gamma + \frac{1}{2}\Delta\kappa_\gamma]\ \frac{1}{\sqrt{2}}\sin\theta^\star_\gamma\ , \tag{3.7}$$

where H_W, H_γ are the W, γ helicities and $\sin\theta^\star_\gamma$ is the production angle of the photon with respect to the quark direction in the parton center of mass frame. The C or P odd anomalous TGC's have been omitted to simplify the equations. A zero helicity photon ($H_\gamma = 0$) is not allowed because the photon is massless.

The first thing to notice from Eqs. 3.6 and 3.7 is the importance of the dimensionality of the operators in the Lagrangian. The λ-type couplings are the coefficients of dimension six operators. They enhance the cross section by a factor proportional to the parton center of mass energy squared $\hat{s}$. The κ-type couplings are the coefficients of dimension 4 operators, and their enhancement is proportional only to $\sqrt{\hat{s}}$. The diboson invariant mass distribution (which is equal to $\sqrt{\hat{s}}$ at leading order) is shown in Figure 3.2(left) for the Standard Model and two choices of the anomalous couplings (note the $\Delta\kappa_\gamma$ choice is a factor 20 larger than the λ_γ choice). Anomalous couplings of any type enhance the distributions at large invariant mass. The enhancements for

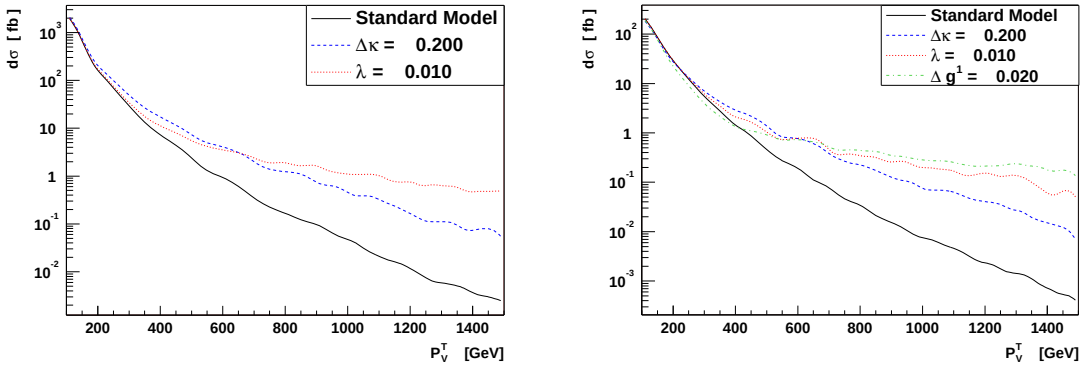

Figure 3.3: The transverse momentum distributon of the photon and Z^0 are shown for $W\gamma$ (left) and WZ (right) production at the LHC. The distributions are generated at NLO using the parton level generator of Ref. [Bau95] and [Bau93c] (hadronization and detector effects are not included). The kinematic cuts are chosen to coincide with the present analysis, the precise cuts are unimportant (the interested reader may refer to Chapter 4).

the κ-type couplings are spread more evenly across the distribution than are those for the λ-type parameter, on account of the operator dimensionality. Because of this energy squared enhancement, the sensitivity to λ-type couplings increases rapidly with increased collider energy. This will provide a distinct advantage for the 14 TeV LHC collider as compared to the 2 TeV Tevatron collider.

Another important factor is the angular term in Eqs. 3.6 and 3.7. The λ-type couplings enjoy an enhancement proportional to $\sin\theta^{\star}_{\gamma}$, which means the effect will be largest in the direction transverse to the quark direction (i.e. transverse to the beam). This corresponds to the central part of a particle detector, where the best measurements are possible. This too, will provide an advantage when probing the λ-type couplings as compared to the κ-type ones. The transverse momentum of the photon is a distribution sensitive to both the energy and angular information, and is shown in Figure 3.3 (left).

Distributions relevant to the decay products of the W-boson are shown in Figure 3.4. The transverse momentum of the charged lepton from the W-decay is shown (top left) and the missing transverse momentum (which relates directly to the neutrino from the W-decay) is shown (bottom left).

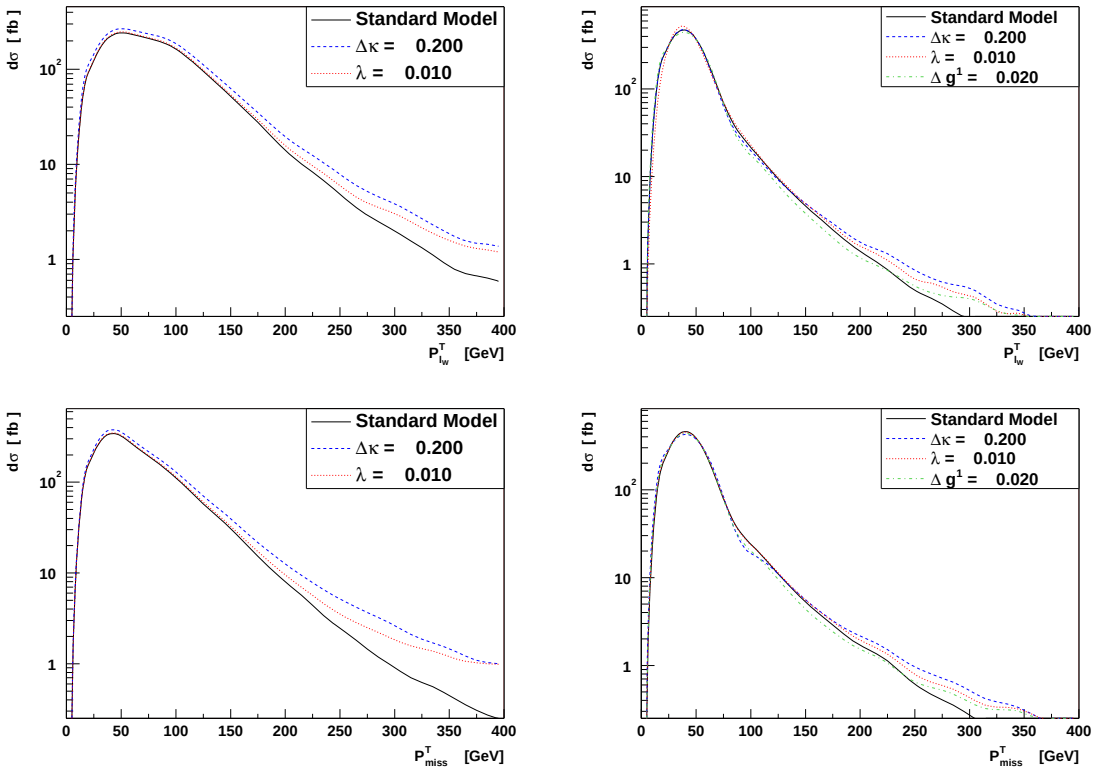

Figure 3.4: The transverse momentum of the charged lepton from the W-decay (top) and the missing transverse momentum (bottom) distributions are shown for $W\gamma$ (left) and WZ (right) production at the LHC. The distributions are generated at NLO using the parton level generator of Ref. [Bau95] and [Bau93c] (hadronization and detector effects are not included). The kinematic cuts are chosen to coincide with the present analysis, the precise cuts are unimportant (the interested reader may refer to Chapter 4).

The change to the matrix element $\Delta\mathcal{M}_{H_Z,H_W}$ arising from anomalous TGC's in WZ production are [Zep88],

$$\Delta\mathcal{M}_{\pm,0} \propto \frac{\sqrt{\hat{s}}}{2M_W}[\Delta g_Z^1 + \Delta\kappa_Z + \lambda_Z]\ \frac{1}{2}(1 \mp \cos\theta_Z^\star), \tag{3.8}$$

$$\Delta\mathcal{M}_{\pm,\pm} \propto \frac{\hat{s}}{2M_W^2}[\lambda_Z]\ \frac{1}{\sqrt{2}}\sin\theta_Z^\star, \tag{3.9}$$

$$\Delta\mathcal{M}_{0,\pm} \propto \frac{\sqrt{\hat{s}}}{2M_W}[2\Delta g_Z^1 + \lambda_Z]\ \frac{1}{2}(1 \pm \cos\theta_Z^\star), \tag{3.10}$$

$$\Delta\mathcal{M}_{0,0} \propto \frac{\hat{s}}{2M_W^2}[\Delta g_Z^1]\ \frac{1}{\sqrt{2}}\sin\theta_Z^\star \tag{3.11}$$

where the effect of C or P odd anomalous TGC's have been omitted and $\frac{\sqrt{\hat{s}}}{2M_W} \approx \frac{\sqrt{\hat{s}}}{2M_Z}$ has been assumed to simplify the equations.

Because the Z^0-boson is a massive particle, $H_Z = 0$ is allowed, and so three more possibilities for the helicity amplitudes $(H_Z, H_W) = (0,+),\ (0,-),\ (0,0)$ exist. The Δg_Z^1 coupling does not spoil electromagnetic gauge invariance for WZ production. For 4 of the 5 amplitudes in which it appears, it is enhanced only by a factor proportional to energy. For the (0,0) amplitude, however, it receives an enhancement proportional to energy squared. This, together with the angular dependence, means the sensitivity to the Δg_Z^1 parameter is expected to be better (worse) than for the $\Delta\kappa_Z$ (λ_Z) parameter at a high energy collider such as the LHC. The distributions which have been discussed for $W\gamma$ production are also shown for WZ production on the right sides of Figures 3.2-3.4.

From the approximate matrix element modifications, it can be seen that several experimental observables can be used to extract information about the anomalous TGC parameters from an ensemble of diboson events:

Event Rate: The cross section, which is proportional to the matrix element squared, is sensitive to the modified matrix elements.

Energy Behavior: The effect of anomalous TGC's increases with diboson invariant mass, meaning non-standard couplings would enhance the cross section most at high parton center of mass energy.

Production Angle: The contribution from the anomalous TGC's depends on the gauge-boson production angle (polar angle with respect to the beam). Since the SM cross section is suppressed in the region of the radiation zero (see Section 3.3), this effect will be of particular importance in the central regions.

Polarization: The gauge-boson helicity has a direct effect on the boson decay angles, which means that the angular distributions (and transverse momentum) of the boson decay products can be used to project out specific helicity states.

In Chapter 5 of this thesis, various techniques for exploiting this information will be explored.

3.2 Higher Order Corrections

An infinite number of Feynman graphs contribute to diboson production at hadron colliders, $p\bar{p}^{(-)} \rightarrow W^{\pm}V + X$. A calculation including all of these graphs is not feasible, and so a truncated perturbative approach is normally adopted wherein all the diagrams up to a particular order in the strong and electroweak coupling constants are included. Because the coupling constants are small numbers at the energy scales of interest ($\alpha_{\mathrm{QED}}(M_Z) \simeq \frac{1}{129}$, $\alpha_{\mathrm{S}}(M_Z) \simeq \frac{1}{10}$), a truncation of the perturbative expansion series at a fixed order is a reasonable approximation for the complete result.

The Born level diagrams (Figure 3.5, top left) constitute the lowest or leading order contribution for WV production. The probability distribution, or differential cross section, of an observable quantity is proportional to the square of the Feynman graphs. The Born graphs contain two electroweak interaction vertices, each of which contributes a factor $\sqrt{\alpha_{\mathrm{QED}}}$ in the calculation, and so the square of these graphs is order ${\alpha_{\mathrm{QED}}}^2$.

Leading order calculations for diboson production are extremely valuable, and are able to predict the basic characteristics of diboson events. The main limitation is that these calculations contain only the two gauge-bosons (or their decay products) in the final state, which is referred to as the n-body final state. A diboson event may have structure which is significantly more complex: other particles may be present

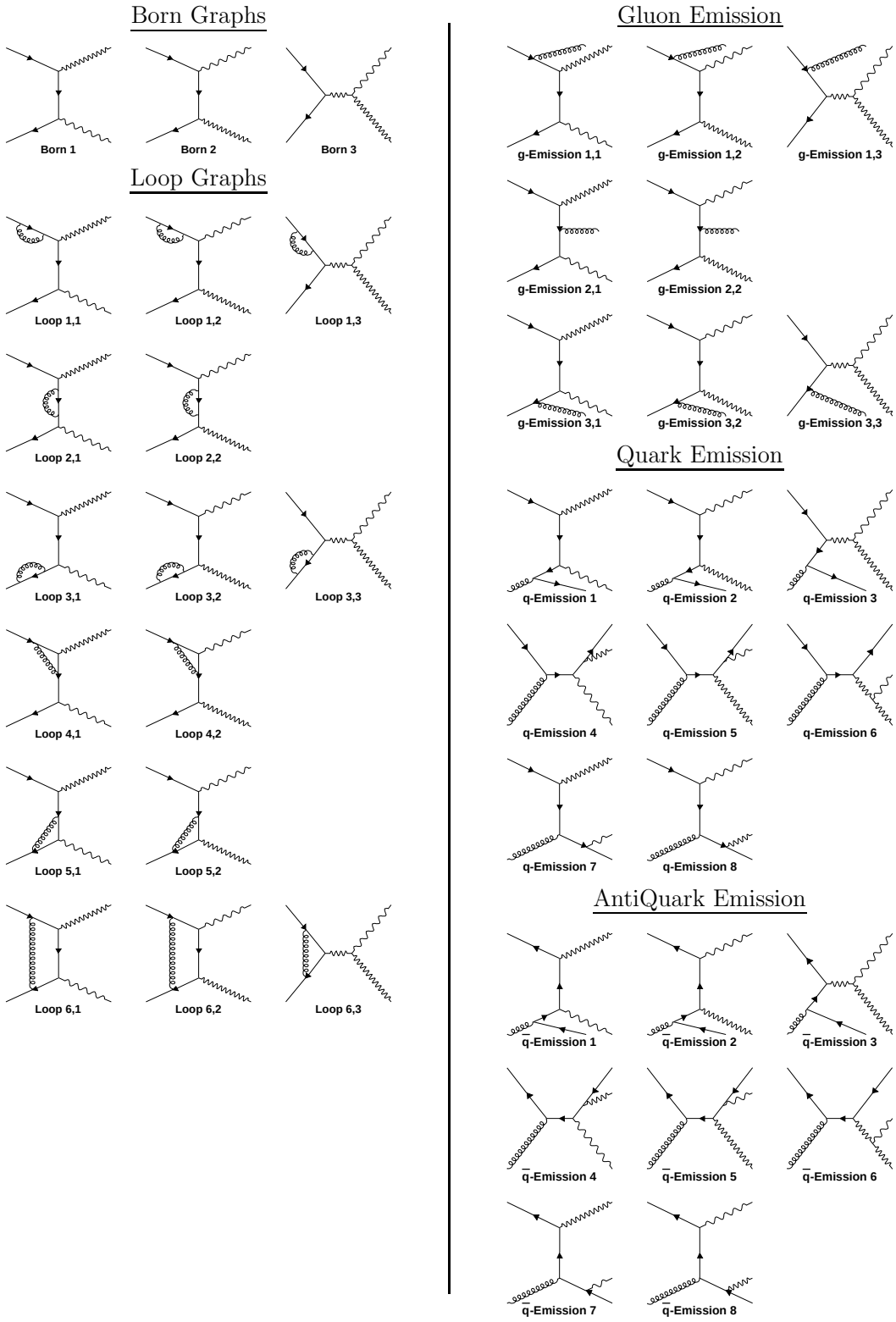

Figure 3.5: The Feynman graphs contributing to diboson production up to next-to-leading order in the strong coupling constant.

within the graph in the form of internal loops, or in the final state in the form of real emissions. Since these graphs with extra particles necessarily contain extra vertices, their probability is diminished by extra coupling constant factors.

The effects of including an extra order in the QCD coupling are more pronounced than for including an extra QED order. The next-to-leading order (NLO) QCD corrections typically increase the inclusive diboson production cross section by about 30% [Bau93c, Bau95], whereas the QED corrections are typically over a factor 10 smaller.[2] The effect of higher order corrections is much larger in the physically interesting region of high transverse momentum gauge-bosons where the QCD corrections can increase the differential cross section by a factor 2-10, and the electroweak corrections typically [Acc01] lower the predictions by about 5-20%. Much effort has been directed at performing next-to-leading order QCD calculations of diboson production.

At NLO, all diagrams contributing up to order $\alpha_{\rm QED}{}^2\alpha_{\rm S}$ must be included. This includes the square of the leading order Born level graphs (Figure 3.5, top left), the interference of the Born graphs with the virtual one-loop graphs (Figure 3.5, bottom left), and the square of the real emission graphs. There are three types of real emission graphs, the annihilation graphs which are initiated by quark-antiquark ($q\bar{q}$) collisions and have an extra gluon (g) in the final state (Figure 3.5, top right), the graphs with qg in the initial state and an extra q in the final state (Figure 3.5, middle right), and the $\bar{q}g$ initial state with an extra $\bar{q}$ in the final state (Figure 3.5, bottom right). The latter two are referred to as Compton diagrams. Because these real emission graphs all have an extra particle in the final state, they are referred to as (n+1)-body final states, and they do not interfere with the n-body Born and one-loop diagrams.

Feynman diagrams without any internal loops are called *tree level*. The evaluation of the associated matrix elements is straightforward, though often times quite lengthy. This procedure has been automated in several computer programs such as Grace [M-T93], madGraph [Ste94], and CompHEP [Puk99].

The matrix elements associated with the virtual one-loop graphs (Figure 3.5,

[2]This expectation is based on the recently completed electroweak next-to-leading order calculations [Bau01] for single gauge-boson production in hadronic collisions, which increases the inclusive cross section by about 1%.

bottom left) are considerably harder to calculate, since an integration over the loop four-momentum must be achieved. Though the n-body diagrams do not interfere with the (n+1)-body ones, the contribution from each—when treated separately—diverges. It is only when the two classes of diagrams are treated together that the result is finite. This has already been discussed in Section 2.2.2.

NLO corrections to hadronic diboson production are large at LHC energies, particularly in the region of high transverse momentum and small rapidity separation (see Figure 3.6) which is the same region of maximum sensitivity to anomalous TGC's. The corrections can amount to more than an order of magnitude and affect the shapes as well as the normalization. The high quark-gluon luminosity at the LHC and a logarithmic enhancement at high transverse momentum in the qg and $\bar{q}g$ real emissions subprocesses (in the region of phase space where a gauge boson recoils against a high P_T jet which radiates a second gauge-boson) are primarily responsible. In the diboson channels which exhibit radiation zero behaviour[3] (i.e. $W\gamma$ and WZ), the Born contribution is suppressed and NLO corrections are even larger [Bau93c, Bau95]. Since the $O(\alpha_s)$ subprocesses responsible for the enhancement at large transverse momentum do not involve the three gauge-boson vertex, the overall effect of NLO corrections is a spoiling of sensitivity to anomalous TGC's.

Distributions obtained by rejecting events with hard jets in the central rapidity region (referred to as a *jet veto*) for one possible choice of jet definition ($P^T_{\text{jet}} > 30$ GeV, $|\eta(\text{jet})| < 3$) are shown in Figure 3.6. The jet veto is effective in recovering the qualitative shape of the LO distributions including the approximate radiation zero in WZ production (Figure 3.6, bottom). The jet veto serves to recover anomalous TGC sensitivity which is otherwise lost when introducing NLO corrections. Ref. [Bau95] reports a 10-30% improvement in anomalous TGC sensitivity limits in WZ production when a jet veto is applied as compared to the inclusive NLO case. These limits are often close to those obtained at LO.

[3]The radiation zero will be discussed in Section 3.3.

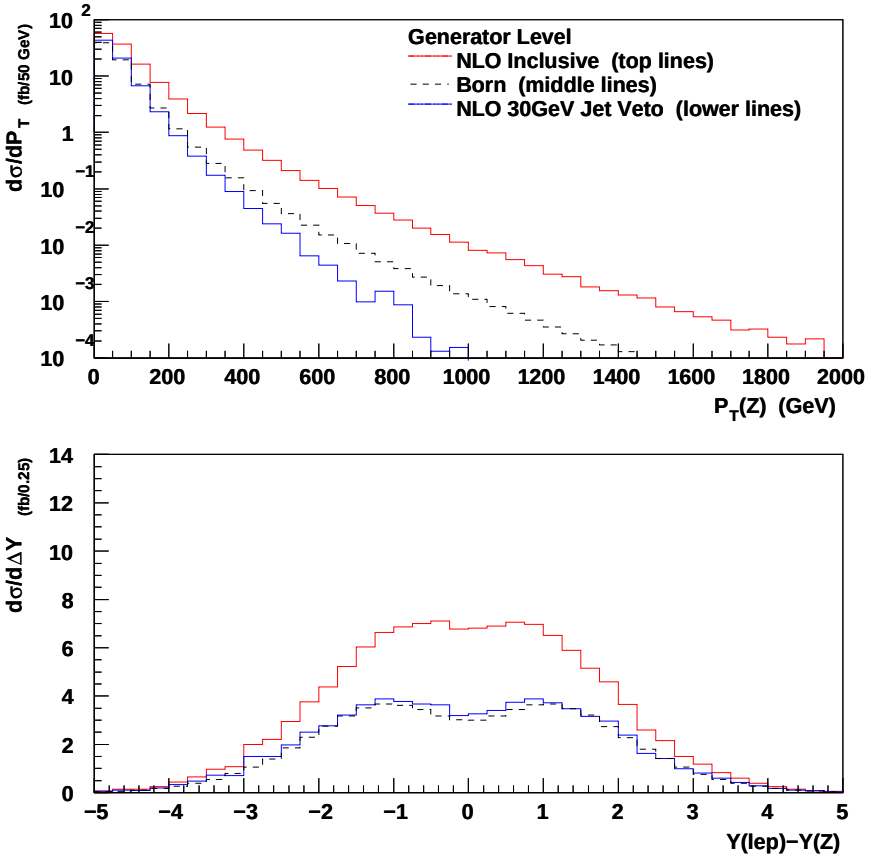

Figure 3.6: The effects of NLO corrections on $pp \to WZ \to l^{\pm}\nu l^{+}l^{-}$ production at LHC are illustrated [Dob99c]. The P_Z^T distribution is shown at top and the rapidity separation of the charged lepton (arising in the W-decay) from the Z^0 ($Y(\text{lep}) - Y(Z)$) is shown at bottom. The three curves are for NLO (upper), Born (dashed middle), and NLO with a 30 GeV jet veto (lower). Kinematic cuts motivated by TGC analyses are chosen. The transverse momentum of all leptons must exceed 25 GeV and the rapidity of all leptons must be less than 3. Missing transverse momentum must be greater than 25 GeV. A jet is defined when the transverse momentum of a parton exceeds 30 GeV in the rapidity interval $|\eta| < 3$.

3.3 Radiation zero

The Born level SM differential cross section for $d\bar{u} \to W^-\gamma$ is [Mik78]

$$\frac{d\hat{\sigma}^{\mathrm{SM}}}{d\cos\theta_{\bar{q},\gamma^\star}} = \textsc{Const}\times\frac{1}{\hat{s}(1-\frac{M_W^2}{\hat{s}})}\frac{(\cos\theta_{\bar{q},\gamma^\star}+1/3)^2\left[(1+\frac{M_W^2}{\hat{s}})^2+(1-\frac{M_W^2}{\hat{s}})^2\cos^2\theta_{\bar{q},\gamma^\star}\right]}{1-\cos^2\theta_{\bar{q},\gamma^\star}}, \tag{3.12}$$

where Const is an unimportant overall factor, $\cos\theta_{\bar{q},\gamma^\star}$ is the scattering angle of the photon relative to the incoming antiquark in the $q\bar{q}$ center-of-mass frame, and $\hat{s}$ is the center-of-mass energy squared. The *radiation zero* refers to the cancellation which occurs at $\cos\theta_{\bar{q},\gamma^\star} = -1/3$ for $W^-\gamma$ production ($\cos\theta_{\bar{q},\gamma^\star} = 1/3$ for $W^+\gamma$). An approximate radiation zero exists for $W^\pm Z^0$ production as well, for which more details can be found in Ref. [Bau94b].

At the present time, the radiation zero has yet to be observed experimentally. The prospects for observing it at the Tevatron from Run II data are good [Tev00, Sec. 4.6.1].

For hadronic collisions, it is not possible to ascertain from which beam the quark or antiquark arises. This makes the distribution for $\cos\theta_{\bar{q},\gamma^\star}$ impossible to observe experimentally. Instead, one may reconstruct the center-of-mass production angle $\cos\theta_{V^\star}$ of the γ or Z^0 with respect to one of the beams. This distribution is shown in Figure 3.7 for $W\gamma$ and WZ production at the LHC. The symmetric proton-proton beams imply that the distributions are also symmetric, and so the effect of the radiation zero is a dip at $\cos\theta_{V^\star} = 0$, rather than a cancellation at $\cos\theta_{\bar{q},\gamma^\star} = \pm 1/3$. At a $p\bar{p}$ collider such as the Tevatron, the quark is statistically most likely to arise from the proton beam valence quark distributions, while the antiquark will most often arise from the antiproton valence distributions, and so an antisymmetric distribution persists, though the sea quark contribution to the (anti)proton washes out the effect somewhat.

Anomalous couplings spoil the radiation zero cancellations. For most choices of the anomalous TGC parameters, this results in a 'filling in' of the radiation zero dip, as shown in Figure 3.7.

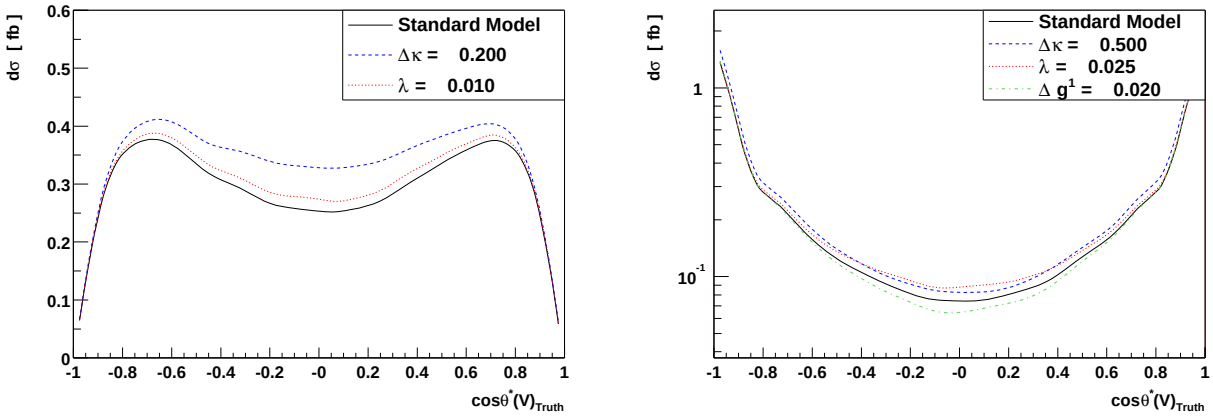

Figure 3.7: The center-of-mass frame production angle $\cos\theta_{V^\star}$ of the photon in $pp \to W^\pm\gamma$ production (left) and the Z^0 in $pp \to W^\pm Z^0$ production (right) with respect to the forward beam is shown for the LHC. The distributions are generated at NLO using the parton level generator of Ref. [Bau95] and [Bau93c] (hadronization and detector effects are not included). The kinematic cuts have been chosen to coincide with the present analysis, in particular a $P_\gamma^T > 100$ GeV cut is imposed on the photon, which is responsible for cutting off the photon distribution near $\cos\theta^\star = \pm 1$ (the other cuts are unimportant, the interested reader may refer to Chapter 4).

There are complications with reconstructing the center-of-mass frame for processes with a neutrino in the final state, as is the case for the leptonic decays in WZ and $W\gamma$ production, because the longitudinal momentum of the neutrino is not measured experimentally (this will be discussed in more detail in Section 5.1). The rapidity separation of the photon or Z^0 from the charged lepton arising in the $W^\pm$ decay $\left(Y(V) - Y(l_W^\pm)\right)$ is a distribution which can be reconstructed without assumptions, and is sensitive to the radiation zero. Like the $\cos\theta_{V^\star}$ distribution, the $Y(V) - Y(l_W^\pm)$ distribution is symmetric for pp collisions with a dip at $Y(V) - Y(l_W^\pm) = 0$. For $p\bar{p}$ collisions the dip is slightly off-center, providing the characteristic signature of the radiation zero.

In terms of the radiation zero asymmetry being masked by symmetric beams, a similar situation exists for measurements of the forward-backward asymmetry in $pp \to Z^0/\gamma^\star + X \to l^+l^- + X$ production. The asymmetry exists in the production angle of the $Z^0/\gamma^\star$ with respect to the incoming quark direction, but the two beams are symmetric and so no asymmetry exists with respect to the beams. However,

in Refs. [Fis94, Bau98a], the idea of 'signing' the forward direction according to the direction (or boost) of the $Z^0/\gamma^\star$ in the laboratory frame is presented. Valence quarks inside the proton normally have a larger momentum fraction than sea quarks. Because the quark which participates in the reaction will predominantly come from the valence distribution in the proton, whereas the antiquark will always come from the sea distribution, the Z^0 will usually be boosted in the quark direction of travel. This provides a statistical means of 'signing' the forward direction for this process.

This idea is applied to diboson production for the first time here. The longitudinal momentum of the V, $l^\pm_W$ system $P^z_{\mathrm{V,l^\pm_W}}$ is evaluated. If the longitudinal momentum is in the forward direction ($P^z_{\mathrm{V,l^\pm_W}} > 0$), the rapidity separation is not altered. If it is in the backwards direction ($P^z_{\mathrm{V,l^\pm_W}} < 0$), the sign of the rapidity separation is reversed $\Big(Y(V) - Y(l^\pm_W) \rightarrow -Y(V) + Y(l^\pm_W)\Big)$. To account for the difference in the location of the radiation zero for W^+V vs. W^-V production, the sign of the rapidity separation is also reversed when the charged lepton from the $W^\pm$ decay has a negative charge. The signed rapidity separation variable is thus

$$\text{Signed Rapidity Separation} \;=\; \mathrm{sign}(Q_{l^\pm_W}, 1) \times \mathrm{sign}(P^z_{\mathrm{V,l^\pm_W}}, 1) \times \Big(Y(V) - Y(l^\pm_W)\Big)\,, \tag{3.13}$$

where the $\mathrm{sign}(a, b)$ operator transfers the sign of a on to b. The signed rapidity separation distributions for $W^\pm\gamma$ and WZ production are compared to the unsigned distributions in Figure 3.8 for 14 TeV pp collisions at the LHC, and allow for the observation of the characteristic asymmetric rapidity separation at a pp collider.

3.4 Unitarity Limits and Form Factors

As mentioned earlier, electroweak theory is built on the $\mathrm{SU}(2)_L \times \mathrm{U}(1)_Y$ gauge group. Unitarity, which simply stated is the conservation of probability, depends directly on the model's gauge structure. Anomalous TGC's spoil the gauge structure of the model. Departure from this structure can violate unitarity at relatively low energies and so it has become standard to introduce protection in the effective Lagrangian for triple gauge-boson vertices by expressing the anomalous couplings as scale dependent

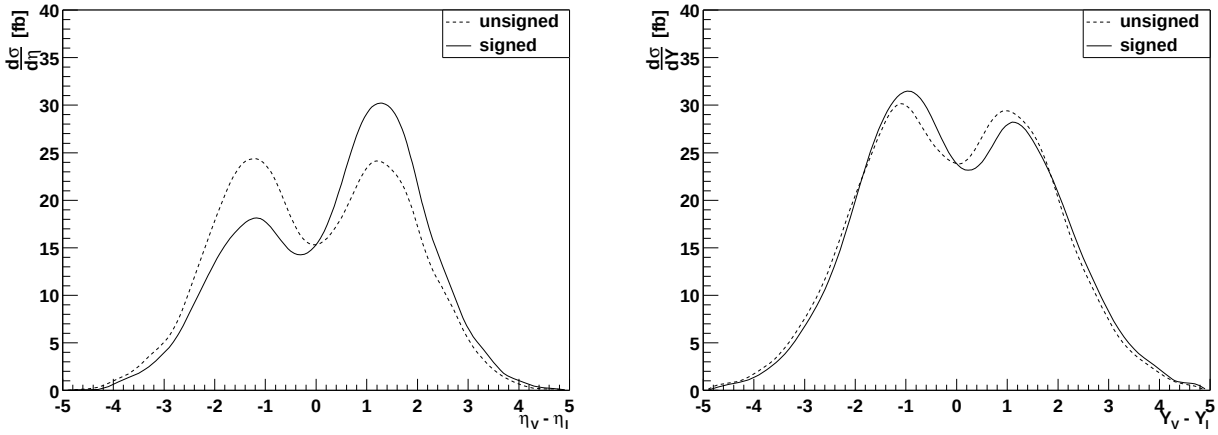

Figure 3.8: The rapidity separation of the γ or Z^0 from the $l^{\pm}_W$ is shown for $W\gamma$ production (left) and WZ production (right) at the LHC. For the solid lines, the rapidity separation has been 'signed' according to Eq. 3.13. The distributions are generated at NLO using the parton level generator of Ref. [Bau95] and [Bau93c] (hadronization and detector effects are not included). The kinematic cuts are chosen to coincide with the present analysis, with the exception of the cut on the jet transverse momentum, which is set to 30 GeV for this figure.

form factors, which are suppressed at high energy.

For experimental results at a given parton center of mass energy $\sqrt{\hat{s}}$ (i.e. e^+e^- colliders), the choice of form factor parametrization is not important because one can unambiguously translate between parameterizations. However, when results are integrated over a range of $\sqrt{\hat{s}}$ as they are at hadron colliders, no simple translation is possible and results depend crucially on the (arbitrary) choice of the form factors. Any measurement of anomalous couplings over integrated energies carries with it assumptions on the parametrization of the form factor.

This section outlines the considerations which influence the choice of form factor.

Form factor parametrization

At leading order, triple gauge-boson vertices in diboson production arise in the s-channel diagram only ($J = 1$ partial wave amplitude), see Fig. 3.1. S-matrix unitarity implies a constant bound to any partial wave amplitude. At asymptotically high energy scales partial wave unitarity is violated if constant anomalous TGC's are introduced. In other words, the SM Lagrangian is the only description of the three

gauge-boson vertex which is valid up to arbitrary energy scales.

Unambiguous and model-independent constant unitarity constraints for WV production have been derived[4] in Ref. [Bau88a],

$$\begin{array}{lll} \Lambda^2 = 0.99\ \mathrm{TeV}^2 \,/\, |\lambda_\gamma| & & \Lambda^2 = 0.54\ \mathrm{TeV}^2 \,/\, |\lambda_Z| \\ \Lambda^2 = 1.86\ \mathrm{TeV}^2 \,/\, |\Delta\kappa_\gamma| & & \Lambda^2 = 0.85\ \mathrm{TeV}^2 \,/\, |\Delta\kappa_Z| \\ & & \Lambda^2 = 0.87\ \mathrm{TeV}^2 \,/\, |\Delta g_Z^1| \end{array} \tag{3.14}$$

where Λ is the scale at which unitarity is violated if constant anomalous TGC's are introduced in the Lagrangian.

To conserve unitarity at arbitrary energies anomalous TGC's can be introduced as form factors. Thus an arbitrary anomalous coupling $\tilde{A} = \tilde{A}_0 \times\ \mathcal{F}(q_1^2, q_2^2, P^2)$ vanishes when $q_1^2,\ q_2^2$, or P^2 becomes large, where q_1^2 and q_2^2 are the invariant masses squared of the final state bosons and $P^2 = M_{\mathrm{WV}}^2$ is the virtual exchange boson invariant mass squared. $\tilde{A}_0$ is referred to as the "bare coupling" and $\tilde{A}$ is the anomalous TGC form factor which appears in the Eq. 3.1 Lagrangian, i.e.

$$\tilde{A}\ \epsilon\ \ \left\{\Delta g_V^1,\ \Delta\kappa_V,\ \lambda_V,\ g_V^4,\ g_V^5,\ \tilde{\kappa}_V,\ \tilde{\lambda}_V\right\}. \tag{3.15}$$

For diboson production the final state bosons are nearly on-shell $q_1^2, q_2^2 \simeq M_V^2$ even when finite width effects are taken into account. However, large (potentially unitarity violating) virtual exchange boson masses M_{WV} will be probed at the LHC.

The choice of parametrization for the form factors is arbitrary provided unitarity is conserved at all energies for a sufficiently small value of anomalous coupling. A step function operating at a cutoff scale Λ_{FF} is sufficient though discontinuous and thus unphysical. More common in the literature is a generalized dipole form factor which is motivated by the nucleon form factors and has further appeal because it enters the Lagrangian in a form similar to that of a propagator with mass Λ_{FF}. The parametrization[5] is

$$\tilde{A} = \frac{\tilde{A}_0}{(1 + \frac{M_{\mathrm{WV}}^2}{\Lambda_{\mathrm{FF}}^2})^n}, \tag{3.16}$$

[4]Cancellations may occur if more than one anomalous coupling is allowed non-zero at a time, which weakens the unitarity limits somewhat.

[5]At leading order $M_{\mathrm{WV}}^2 = \hat{s}$, which is the notation commonly used in the literature.

where $n > 1/2$ is sufficient for the $\Delta\kappa_V$ couplings and $n > 1$ is sufficient for the λ_V and Δg_V^1 couplings. It is conventional [Bau93c, Bau95, Bau96] to use $n = 2$ for all of the WWV vertex anomalous TGC's. Unitarity limits for generalized dipole form factors are [Sno95]

$$\begin{array}{ll} |\lambda_\gamma| \leq \frac{n^n}{(n-1)^{n-1}} \frac{0.96 \text{ TeV}^2}{\Lambda_{\text{FF}}^2} & |\lambda_Z| \leq \frac{n^n}{(n-1)^{n-1}} \frac{0.52 \text{ TeV}^2}{\Lambda_{\text{FF}}^2} \\ |\Delta\kappa_\gamma| \leq \frac{n^n}{(n-1)^{n-1}} \frac{1.81 \text{ TeV}^2}{\Lambda_{\text{FF}}^2} & |\Delta\kappa_Z| \leq \frac{n^n}{(n-1)^{n-1}} \frac{0.83 \text{ TeV}^2}{\Lambda_{\text{FF}}^2} \\ & |\Delta g_Z^1| \leq \frac{n^n}{(n-1)^{n-1}} \frac{0.84 \text{ TeV}^2}{\Lambda_{\text{FF}}^2}. \end{array} \tag{3.17}$$

For an $n = 2$ dipole form factor with scale $\Lambda_{\text{FF}} = 10$ TeV, this translates to unitarity limits of

$$\begin{array}{ll} |\lambda_\gamma| \leq 0.038 & |\lambda_Z| \leq 0.021 \\ |\Delta\kappa_\gamma| \leq 0.072 & |\Delta\kappa_Z| \leq 0.033 \\ & |\Delta g_Z^1| \leq 0.034. \end{array} \tag{3.18}$$

The form factor scale Λ_{FF} can be regarded as a regularization scale. It is related to (but not necessarily identical to) the energy scale at which new physics becomes important in the weak boson sector.

Impact of form factor on kinematic distributions

The impact of the form factor parametrization on energy dependent distributions is illustrated in Figure 3.9 where the reconstructed[6] M_{WZ} and P_{Z}^T spectra predictions are plotted for LHC W^+Z production with leptonic decays. The Standard Model expectation is compared to scenarios with a modest $\lambda_0^Z = 0.05$ bare coupling for various generalized dipole form factor parameterizations.

For the region of low invariant mass where $M_{\text{WZ}} \ll \Lambda_{\text{FF}}$ the form factors remain essentially constant and distributions with the same bare coupling agree well. As the form factor scale Λ_{FF} is approached, the distributions begin to be pushed back towards the SM expectation (visible at about $M_{\text{WZ}} = 500$ GeV for the Λ_{FF}=2 TeV case). For $M_{\text{WZ}} \gg \Lambda_{\text{FF}}$ the distribution returns to the SM expectation.

The scale Λ_{FF} determines the scale at which the anomalous coupling is pushed back to the SM expectation, while the exponent of the form factor n dictates how

[6]Reconstructing M_{WZ} requires knowledge of the neutrino longitudinal momentum which is obtained up to a two-fold ambiguity using the W-mass constraint. Each solution is given half weight in the M_{WZ} spectrum shown in Fig. 3.9.

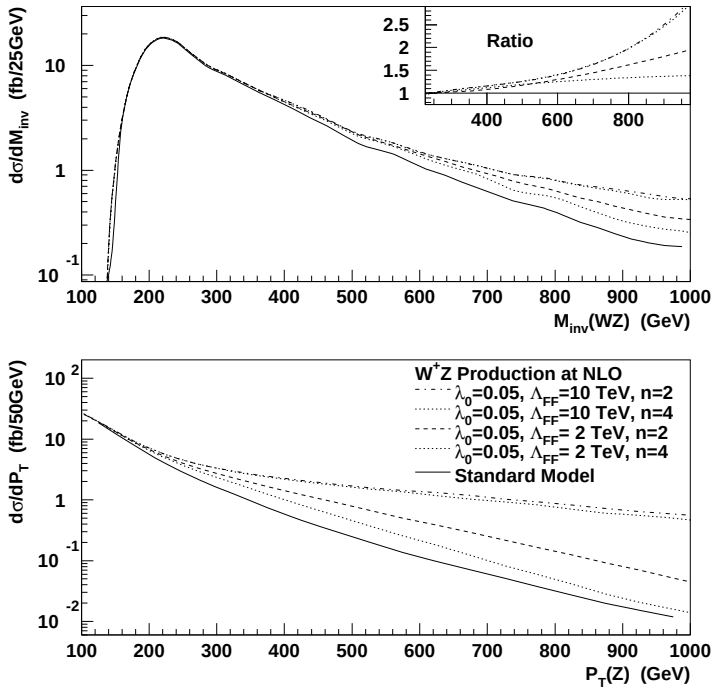

Figure 3.9: The reconstructed $M_{\rm WZ}$ and $P_{\rm Z}^T$ spectra are plotted for LHC W^+Z production with leptonic decays at $O(\alpha_s)$ for the Standard Model and various choices of the generalized dipole form factor parametrization with bare coupling $\lambda_0 = 0.05$.

fast the "pushing" occurs as $\Lambda_{\rm FF}$ is approached. A larger choice for n increases the impact of the form factor on energy dependent distributions and also increases the dependence of experimental limits on the form factor parametrization.

Since distributions are constrained to the SM expectation at invariant masses above the form factor scale, great care must be taken when fitting experimental data to a form factor parametrized model in a region with data where $M_{\rm WZ} \geq \Lambda_{\rm FF}$. Effectively, since the anomalous couplings are constrained near zero above $\Lambda_{\rm FF}$ by the parametrization model, there are no free parameters for the fit in this regime. For the case where nature provides non-zero anomalous couplings, an analysis assuming a parametrization of the form factor with fixed $\Lambda_{\rm FF}$ smaller than that provided by nature but within the energy range accessible by the machine would overestimate the anomalous coupling. This is because large bare coupling fit values are necessary in the $M_{\rm WZ} \geq \Lambda_{\rm FF}$ region to counter the (artificially imposed) form factor behavior.

Form factor assumptions for this analysis

A constant form factor has been used for this analysis. This is equivalent to $\Lambda_{\rm FF} = \infty$, and is unitarity violating at high energy. By using constant form factors, the analysis is free of arbitrary form factor assumptions, and thus can provide the most robust, informative limits. However, the limits will be better than would be obtained with a form factor, so limits as a function of the dipole form factor scale $\Lambda_{\rm FF}$ will also be presented, such that the limits without an energy dependent form factor can be translated to expectations for other form factor assumptions.

Since the parametrization of energy dependent form factors is arbitrary and introduces unnecessary dependence on the parametrization choice into the experimental results, a different strategy is advocated here. Rather than introduce protection against unitarity violating couplings into the Lagrangian, the results will be presented as a function of a diboson invariant mass cutoff which is applied to the data. This makes the behavior of the limits as a function of invariant mass apparent, provides generic information about the scale to which the experiment is sensitive, and allows for interpretations of the results at different mass scales. If the limits fall outside of the unitarity bounds, then the scale at which this occurs will be clear, and the limits can be evolved back to any mass scale. Limits of this form will be demonstrated in Sec. 5.8.

ATLAS is sensitive to diboson mass scales up to about 3 TeV, which translates to dipole form factor scales of about 5-10 TeV. It will be shown that the limits for the WWV TGC parameters attainable at ATLAS will be at a level that are below the unitarity constraints at the scales to which the data is sensitive.

3.5 Current Limits on Anomalous WWV Couplings

The WWV triple gauge-boson couplings have been probed at several experiments. In this section, the current experimental limits for the anomalous couplings are reviewed.

3.5.1 Indirect Limits

Indirect model-dependent tests of the anomalous couplings are possible at low energy experiments, which are sensitive to the TGC's through virtual corrections involving gauge-bosons.

The measurement of upper and lower limits on the $b \to s\gamma$ branching ratio by the CLEO experiment [CLEO95] provides the most stringent indirect limits on the $\Delta\kappa_\gamma$ parameter,

$$-2.6 < \Delta\kappa_\gamma < -1.2, \text{ or } -0.6 < \Delta\kappa_\gamma < 0.4 \quad (\lambda_\gamma = 0) \tag{3.19}$$

at the 95% confidence level. The region $-1.2 < \Delta\kappa_\gamma < -0.6$ is excluded by the branching ratio lower limit, while the regions $\Delta\kappa_\gamma < -2.6$ and $\Delta\kappa_\gamma > 0.4$ are excluded by the branching ratio upper limit. The $b \to s\gamma$ branching ratio measurement gives very little information about the λ_γ parameter.

Indirect limits on the λ_γ parameter can be derived from measurements of the magnetic moment of the muon $(g-2)_\mu$ (e.g. see Ref. [Mer90]). Recent measurements from the Muon $(g-2)$ Collaboration [Mg2 01] at Brookhaven National Laboratory indicate a 2.6 standard deviation difference[7] from the Standard Model expectation for the muon magnetic moment. In order to explain this result by invoking an anomalous λ_γ TGC coupling, $\lambda_\gamma \simeq -0.6$ would be necessary (see, for example, Ref. [Cza01]), which has already been ruled out from direct measurements (described below). The implications of the $(g-2)$ measurements for anomalous TGC parameters highlights the need to probe the TGC's by direct means.

3.5.2 Pre-LEP experiments

The first direct limits on anomalous TGC's were derived [Gro87] from data collected at the SLAC and DESY e^+e^- storage rings PEP and PETRA, using the process $e^+e^- \to \nu\bar{\nu}\gamma$ to probe the $WW\gamma$ vertex. Very weak limits on the $\Delta\kappa_\gamma$ were established,

$$-73.5 < \Delta\kappa_\gamma < 37 \tag{3.20}$$

[7]Since the publication of the results in Ref. [Mg2 01], the effects of light by light hadronic corrections have been re-evaluated (see Ref. [Cha02] for a review). With the inclusion of the new calculations, the significance of the $(g-2)$ Collaboration result decreases to 1.6 standard deviations.

at the 90% confidence level.

The UA2 collaboration improved the limit on $\Delta\kappa_\gamma$ by almost an order of magnitude and set the first direct limits on λ_γ [UA2 92]. The experiment probed the $WW\gamma$ vertex with proton anti-proton collisions at a center-of-mass energy of 630 GeV during a series of runs at the CERN Sp$\bar{\text{p}}$S collider from 1988-1990. Sixteen $p\bar{p} \to e\nu\gamma + X$ events were observed, with an expected background of 6.8±1. Using a binned maximum likelihood fit to the transverse momentum of the photon distribution, the 95% confidence intervals are

$$-3.6 < \lambda_\gamma < 3.5, \qquad -4.5 < \Delta\kappa_\gamma < 4.9. \tag{3.21}$$

No form factor was assumed for these measurements (i.e. $\Lambda_{\text{FF}} = \infty$).

The UA1 collaboration, which was also collecting data at the CERN Sp$\bar{\text{p}}$S, has not published TGC studies.

3.5.3 LEP experiments

The four LEP experiments ALEPH, DELPHI, L3, and OPAL have searched for anomalous TGC's. The most recent combination of the results from the four experiments is presented in Ref. [LEP01a], but includes only the data up to the end of 1999 at a centre-of-mass energy up to 202 GeV (i.e. does not yet include all of the data from LEP 2). The limits are derived from W-pair production ($e^+e^- \to W^+W^-$), single W-production ($We\nu$), and single photon production ($\gamma\nu\bar{\nu}$). The 95% confidence intervals are

$$\begin{array}{c} -0.089 < \lambda_\gamma < 0.20, \\ -0.13 < \Delta\kappa_\gamma < 0.13, \\ -0.074 < \Delta g_Z^1 < 0.028 \end{array} \tag{3.22}$$

assuming $\lambda_\gamma = \lambda_Z$ and $\Delta\kappa_Z = \Delta g_Z^1 - \Delta\kappa_\gamma \tan^2\theta_W$. No form factor has been applied. At LEP energy, imposing a $n = 2$ dipole form factor with scale Λ_{FF} =2 TeV degrades the limits by only about 2%.

3.5.4 Tevatron experiments

The D0 collaboration has published the most stringent limits from the 1.8 TeV $p\bar{p}$ Tevatron collider at Fermilab. The limits which compare best with those derived in

this thesis are from $W\gamma \to l^{\pm}\nu\gamma$ [D0 97] and $WZ \to ee\mu\nu/eee\nu$ [D0 99] which use $n = 2$ dipole form factor scales of $\Lambda_{\rm FF}$ =1.5 TeV and 2.0 TeV respectively, and result in 95% confidence intervals

$$-0.31 < \lambda_\gamma < 0.29, \qquad -0.93 < \Delta\kappa_\gamma < 0.94 \tag{3.23}$$

$$-1.42 < \lambda_Z < 1.42, \qquad -1.63 < \Delta\kappa_Z < 1.63 \tag{3.24}$$

using approximately 92 pb^{-1} of data from Run Ia and Ib.

D0 has combined the results from all WZ, $W\gamma$, and WW channels (including hadronic final states) and imposed arbitrarily $\lambda_\gamma = \lambda_Z$ and $\Delta\kappa_\gamma = \Delta\kappa_Z$ to obtain the 95% confidence intervals

$$-0.18 < \lambda_V < 0.19, \qquad -0.25 < \Delta\kappa_V < 0.39 \tag{3.25}$$

assuming $\Lambda_{\rm FF} = 2$ TeV. The most important contribution to the λ_V limit comes from $W\gamma \to l^{\pm}\nu\gamma$, whereas the WW and $WZ \to e\nu jj$ channel is most important for the $\Delta\kappa_V$ limit.

Commissioning of an upgraded 2 TeV $p\bar{p}$ Tevatron collider began in 2001. The prospects for TGC analyses assuming 2 fb^{-1} integrated luminosity (Run II) and $\Lambda_{\rm FF} = 2$ TeV have been studied in Ref. [Tev00] by simply scaling the Run I results by an integrated luminosity factor. The expectation for the $W\gamma \to l^{\pm}\nu\gamma$ and $WZ \to l^{\pm}\nu l^{+}l^{-}$ channels are

$$-0.12 < \lambda_\gamma < 0.12, \qquad -0.40 < \Delta\kappa_\gamma < 0.40 \tag{3.26}$$

$$-0.2 < \lambda_Z < 0.2, \qquad -0.3 < \Delta\kappa_Z < 0.3. \tag{3.27}$$

The expectation for a combination of all WZ, $W\gamma$, and WW channels, assuming $\lambda_\gamma = \lambda_Z$ and $\Delta\kappa_\gamma = \Delta\kappa_Z$, is

$$-0.086 < \lambda_V < 0.090, \qquad -0.12 < \Delta\kappa_V < 0.19 \tag{3.28}$$

at 95% C.L. with $\Lambda_{\rm FF} = 2$ TeV.

Chapter 4

Simulation, Backgrounds, and Event Selection

The TGC vertex will be probed at ATLAS using the muon and electron decay channels of diboson production. Hadronic decay channels are difficult to separate from QCD backgrounds, and the addition of these channels will not improve the precision of the measurements.

The processes of interest for this study are $pp \rightarrow W^{\pm}\gamma \rightarrow l^{\pm}\nu\gamma$ and $pp \rightarrow W^{\pm}Z^0 \rightarrow l^{\pm}\nu l^{+}l^{-}$, where $l^{\pm}$ denotes an electron or muon type lepton and ν is a neutrino or antineutrino. The signature of the former in the detector is a high transverse momentum (P^T) charged lepton, high P^T photon, and large missing transverse momentum P^T_{miss} arising from the neutrino, which is invisible to the detector. The signature of the later is large P^T_{miss} with three high P^T charged leptons, two of which are like-flavor opposite sign and reconstruct to the Z^0 mass. There are several other processes which look similar in the detector (irreducible backgrounds), and others which look similar because some part of the event has been reconstructed incorrectly.

This chapter focuses on the simulation and event selection for the TGC analysis. The chain of Monte Carlo programs which has been used to simulate the signal and backgrounds is described first. A section is dedicated to reviewing the particle identification capabilities of the ATLAS detector, which is particularly important for TGC studies. In the last sections, the various contributions to the backgrounds are investigated, and the kinematic cuts which optimize the selection of event candidates are described.

4.1 Simulation of Signals and Backgrounds

Several Monte Carlo programs for hadronic diboson event simulation are in common use. General purpose showering and hadronization event generators (SHG's) such as PYTHIA [Sjö01b] evaluate the matrix element at leading order (LO) and use the parton shower approach to include higher order corrections—but limited or no anomalous couplings are included.

In the past decade or so, programs have been implemented to calculate diboson production with leptonic decays to next-to-leading order (NLO) in QCD. The importance of including the NLO matrix elements in TGC studies has already been discussed in Sec. 3.2, where it was shown that NLO corrections have the largest effect in the region of high transverse momentum gauge-bosons—the same region which provides maximal sensitivity to anomalous TGC's. This is also the region where the parton shower approach does a poor job of approximating higher order corrections, and so the use of NLO programs is mandatory for an accurate description of the physics. Before discussing the specific simulation which has been used for the present study, the various NLO programs for hadronic diboson production are briefly reviewed in the following section.

4.1.1 Diboson NLO programs

The NLO diboson generators by Baur, Han, and Ohnemus [Bau93c, Bau95, Bau96, Bau98b] (BHO) handle the diboson processes $W\gamma, WZ, WW, Z\gamma$ and have been available for several years. They are based on the programs of Ref. [Ohn90] and employ the 2 parameter phase space slicing method [Ber89, Bae89] in the narrow width approximation.[1] Anomalous TGC's are included. Spin correlations in the leptonic decays are accounted for everywhere except in the virtual contribution. The authors expect a negligible overall effect from neglecting the spin correlations in the virtual corrections

[1] For the narrow width approximation, the gauge-boson resonances are always taken to be on-shell. The Breit-Wigner distribution which represents their width is replaced by a delta function $\frac{1}{(\hat{s}-M^2)^2+M^2\Gamma^2} \rightarrow \frac{\pi}{M\Gamma}\,\delta(\hat{s}-M^2)$, where $\hat{s}$ is the center-of-mass energy squared and M, Γ are the resonance mass and width. The normalization is chosen such that the integrals of the two distributions are equal, $\int_{-\infty}^{\infty} d\hat{s} \frac{1}{(\hat{s}-M^2)^2+M^2\Gamma^2} = \frac{\pi}{M\Gamma}$.

	[Mel90, Fri92]	[Bau93c, Bau95] [Bau96, Bau98b]	[Dix99, DeF00]	[Cam99]
		BHO	DKS	MCFM
Lepton Corr.	no	almost	yes	yes
Finite Width	no	no	no	'beyond'
Regularization	subtraction	phase space slicing	subtraction	subtraction
Anomalous TGC's	no	yes	yes	no
Processes	ZZ, WZ	$W\gamma, WZ, WW, Z\gamma$	$ZZ, WZ, WW,$ $W\gamma, Z\gamma$	ZZ, WZ, WW
Language	F77	F77	F77, F90	F77

Table 4.1: A comparison of the basic features of the NLO hadronic diboson production generators existing to date. F77 and F90 are the Fortran 77 and Fortran 90 programming languages. The processes for each generator are ordered to correspond to the references. The MCFM program generates several final states besides the diboson ones listed in this table.

as compared to the uncertainty from parton distribution functions and the choice of factorization scale.[2]

Frixione, Mele, Nason, and Ridolfi accomplished numerical calculations for ZZ [Mel90] and WZ [Fri92] production at about the same time as Ref. [Ohn90]. Their programs employ the subtraction method [Ell81] in the narrow width approximation. Lepton correlations and anomalous couplings are not included, and so these programs are not well suited to TGC studies.

More recently Dixon, Kunszt, and Signer (DKS) calculated the helicity amplitudes for diboson production with full lepton decay spin correlations at NLO [Dix98] and implemented Monte Carlo programs for WW, WZ, and ZZ production [Dix99]. The subtraction method [Ell81] is employed in the narrow width approximation and anomalous TGC's are included. De Florian and Signer have used these helicity amplitudes in Ref. [DeF00] for $Z\gamma$ and $W\gamma$ programs.

Another Monte Carlo program, MCFM, by Campbell and Ellis [Cam99] generates WW, WZ, and ZZ final states. The helicity amplitudes of [Dix98] are also used, and are extended to include singly resonant diagrams so as to move beyond the narrow

[2]This has been verified in Ref. [Dob99c], wherein the predictions of the BHO WZ and WW generators are compared to those of the DKS generators, which include the full correlations. The original comparison showed an $\mathcal{O}(3\%)$ discrepancy in the WW predictions. Since then, a small error was discovered and corrected in the BHO WW program (for details see Ref. [Tev00, p.152]), and the two programs are now in good agreement.

width approximation. These improvements have the largest effect in the off-resonant regions—such as near diboson production thresholds. The regions are of importance to studies of SM backgrounds to new physics (particularly the associated production of Higgs bosons ZH and WH) but contribute negligibly to the cross section in TGC studies for typical choices of kinematic cuts [Bau96]. The program does not allow for non-standard TGC's.

The features of the NLO diboson programs are summarized in Figure 4.1.

4.1.2 Signal simulation

The NLO BHO programs for hadronic $W\gamma$ and WZ production have been used to simulate the signals in this thesis. These programs are capable of producing weighted events only.[3] As such, a large number of weighted events need to be produced in order to effect the cancellations which are inherent in the NLO programs. In order to avoid spending a large fraction of the computational time processing events which will later fail the selection criteria, a number of parton level cuts are imposed. The parton level cuts are chosen to be sufficiently far from the final selection cuts such that the detector simulation is unable to smear the events such that they pass the selection. For example, in the final event selection (to be presented in the next sections) a cut of 100 GeV will be placed on the photon transverse momentum for $W\gamma$ production, and a parton level cut of 80 GeV is imposed at the generator level. Other parton level cuts are placed on the photon rapidity and charged lepton transverse momentum and rapidity. These parton level cuts are imposed before evaluating the matrix elements, such that very little computer time is wasted generating these events.

[3] As described in Chapter 2, the author has developed new techniques for unweighting NLO events in Ref. [Dob01b] and for incorporating the parton shower in Ref. [Dob01c]. These techniques were implemented for hadronic WZ production and provide a more complete simulation than a NLO program alone. However, the techniques were still under development at the time the present TGC study was well underway. The Monte Carlo techniques were generalized into the *phase space veto method* described in Ref. [Dob01d], which competes with leading order event generators in terms of computer time and efficiency, while incorporating NLO matrix elements with the parton shower approach. An event generator using the phase space veto would provide the ideal event simulation for a TGC analysis at the LHC—however, thus far it has only been implemented for single gauge-boson production. It will be important to have such a generator ready for the start of LHC running in 2006.

Further, since the generator programs employ an adaptive integration algorithm, the programs 'learn' the cuts and adapt as the numerical integration progresses such that fewer of these events are attempted. This improves the accuracy of the predictions, since more computer time can be devoted to modeling the phase space regions of interest.

At NLO the final state consists of the gauge-bosons (or their leptonic decay products) and at most one colored parton. Before these events can be simulated in the detector environment, the final state colored partons need to be hadronized into color-singlet composite hadrons. For this simple case, since no parton showering is included in the simulation chain, there is at most one colored parton in the final state, and so the method of *independent fragmentation* is used (see section 5.6.1 of Ref. [Ell96] for a description). The `PYTHIA` 6.136 [Sjö01a] hadronization routines are used for this purpose.

The event simulation chain for the signal processes is presented in the right-hand branch of Figure 4.1. Besides the NLO signal event sample which is used for the analysis, a second sample of signal events has been generated at leading order with `PYTHIA`, according to the event simulation shown on the left-hand branch of Figure 4.1. This second sample of signal events is used to optimize the event selection, so as to ensure the selection criteria does not operate on the differences which exist in the event structure of leading order events as compared to NLO events.

The generation parameters are as follows: The CTEQ4M [CTEQ97] parton density functions and two loop expression for $\alpha_{\rm S}$ are used with $\Lambda^{4,\overline{\rm MS}} = 0.298$ GeV. The Z^0 and $W^{\pm}$ masses are $M_Z = 91.187$ GeV and $M_W = 80.396$ GeV, the electroweak mixing angle is $\sin^2\theta_W = 0.23$, and the electroweak coupling is $\alpha_{\rm QED}(M_Z) = 1/128$. The Cabbibo angle is $\cos\theta_{\rm Cabbibo} = 0.975$, with no third generation mixing. The signal, background, and detector simulations have been performed using the University of Victoria High Energy Physics Linux Beowulf [Bec95] computer, which is a cluster of 18 commodity computers operating at about 500 MHz per node.

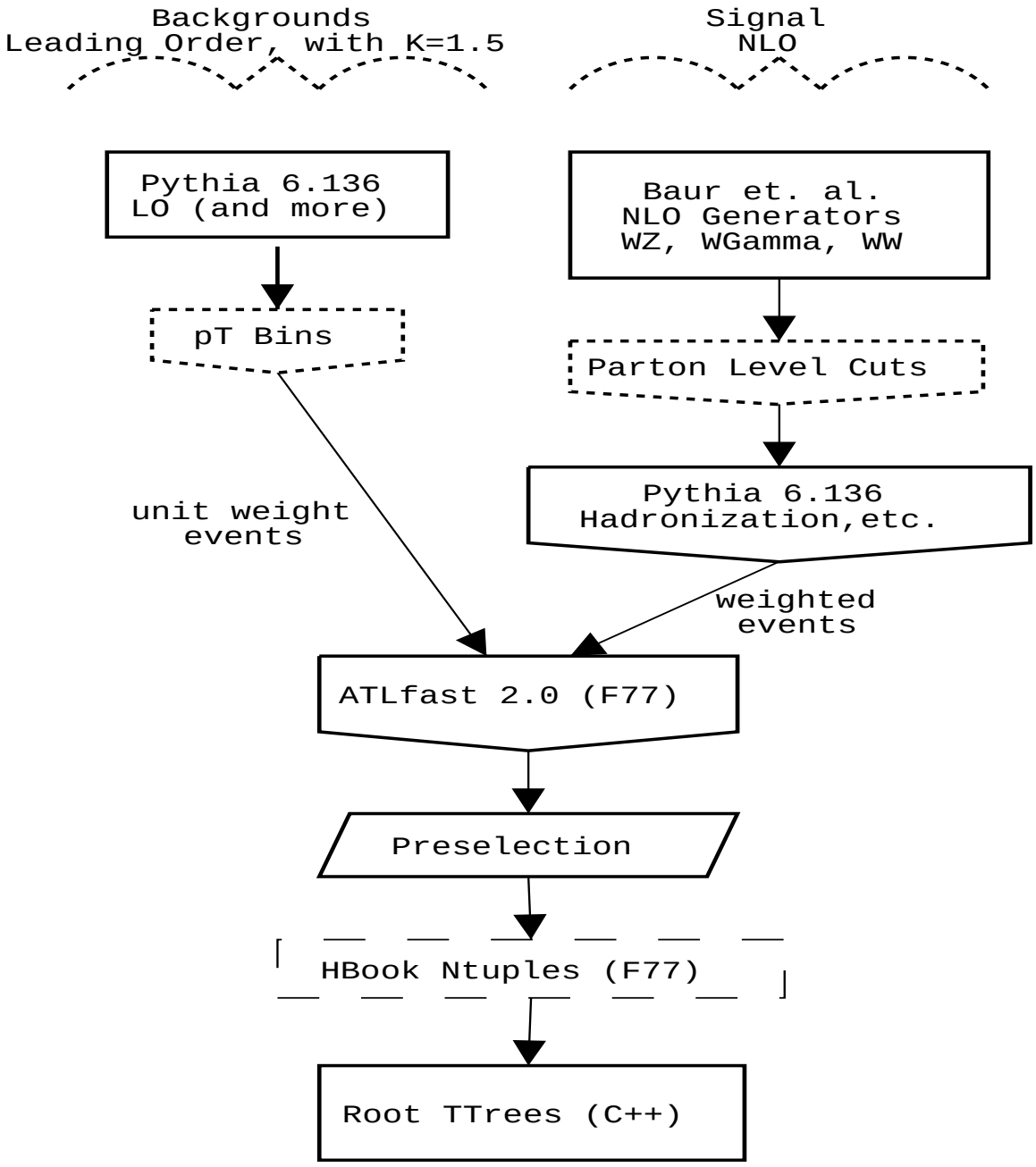

Figure 4.1: The event generation chain is shown schematically for the background processes (left branch) and the signals (right branch).

Reweighting as a function of anomalous couplings

Each event generated by the BHO programs has associated with it a weight, which is a function of the input parameters including the anomalous TGC parameters. In the analysis stage, these events will be combined into histograms. The key requirement for these histograms is that they must be known as a function of the anomalous TGC parameters. This could be accomplished by dividing the anomalous TGC parameter space into a grid of discrete points, and generating a separate event sample for each point. However, this would complicate the analysis, because differences between two points in the grid could arise not only from the different anomalous TGC parameters, but also from statistical effects owing to the finite number of events in each sample. Since there are 3 (2) anomalous TGC parameters which need to be accounted for in WZ ($W\gamma$) production, the number of event samples necessary would be 3^n (2^n), where n is the number of divisions on the grid. For an accurate description, n would have to be $\mathcal{O}(50)$. Several million events are necessary in each event sample in order to effect the cancellations inherent in the NLO simulation. With present computer technology, the simulation of a single event sample (including hadronization and fast detector simulation), is already a time consuming affair, requiring about a day on a farm of a dozen 450 MHz computers. Therefore, this sort of approach would not be feasible in terms of computer time.

A better approach is to modify the BHO programs to provide the event weights as a function of the anomalous TGC parameters. These functions can then we used to reweight the distributions, providing a prediction of the histograms for any choice of the anomalous TGC parameters.

Since the matrix elements are linear functions of the anomalous TGC parameters, the differential cross section (or event weight) is a quadratic function of the parameters. For $W\gamma$ production, there are 2 parameters, λ_γ and $\Delta\kappa_\gamma$, and so the event weight can be written

$$\text{weight}^{W\gamma}(\Delta\kappa_\gamma, \lambda_\gamma) \;=\; w_{00} + \Delta\kappa_\gamma w_{0\kappa} + \lambda_\gamma w_{0\lambda} + \lambda_\gamma \cdot \Delta\kappa_\gamma w_{\lambda\kappa} + \Delta\kappa_\gamma^2 w_{\kappa\kappa} + \lambda_\gamma^2 w_{\lambda\lambda}. \quad (4.1)$$

The SM event weight is w_{00}. For WZ production there are 3 parameters, and therefore

9 w_{ij} weights.

The six w_{ij} weights for $W\gamma$ production can be evaluated for each event by re-evaluating the event weight for the same kinematic configuration at six different linearly independent points on a grid of λ_γ, $\Delta\kappa_\gamma$ space, and inverting the resultant matrix equation to solve for the w_{ij} parameters. No form factors are applied to the anomalous TGC's for this procedure. Since interpolation is preferred over extrapolation, the λ_γ, $\Delta\kappa_\gamma$ points are chosen to be considerably larger than the sensitivity expected in the TGC analysis, and the grid is centered on the SM values.

One extra parameter besides the w_{ij}'s needs to be stored with each event in order to allow for the evaluation of the corresponding event weight for arbitrary choices of the anomalous TGC parameters. This parameter is the diboson system invariant mass, which is needed to apply form factors to the anomalous TGC parameters. Together the w_{ij}'s and the diboson invariant mass are referred to here as the *reweighting parameters*.

There is an added complication which arises because of the regularization scheme which has been used for the NLO matrix elements. The BHO programs employ the 2 parameter phase space slicing method. Each n-body event includes a numerical integration to account for the small amount of (n+1)-body phase space which has been defined as unresolvable and partitioned into the n-body event weight (see Chapter 2, Sec. 2.2.2 for details). There is also a degree of freedom which specifies the gauge-boson polarizations. Thus, two events with identical kinematics might have very different event weights (which is in no way inconsistent with the Monte Carlo method), because only a subset of the phase space degrees of freedom specify the kinematics. This means that for the calculation of the reweighting parameters, one needs to be careful to keep the phase space which specify this additional numerical integration and the gauge-boson polarizations fixed while re-evaluating the event weights at the linearly independent points on the grid.[4]

When the complete phase space (including polarizations and the additional phase

[4]This effect may be responsible for the rather large systematic error which has been associated with this type of cross section parametrization in previous studies. For example, a 2% error was specified in Ref. [CMS98].

space slicing numerical integration) is fixed for the evaluation of the reweighting parameters, the systematic bias which results for an individual event weight is only a few times larger than the machine precision. For an inclusive quantity such as a cross section, the systematic error is many orders of magnitude smaller than the statistical precision.

With the reweighting parameters known for each event, they can be used separately to construct *reweighting histograms* of any experimental observable (e.g. the transverse momentum of one vector boson). For $W\gamma$ production, six separate histograms corresponding to the six weights in Eq. 4.1 are used. Reference histograms of the experimental observable can then be obtained for any choice of the anomalous TGC parameters by adding together the reweighting histograms, with each histogram weighted by the appropriate anomalous TGC parameter(s).[5]

4.1.3 Background simulation

`PYTHIA` 6.136 has been used to simulate the background processes for this analysis. For most processes `PYTHIA` uses leading order matrix elements and higher order corrections are approximated with the parton shower. A few of the processes in `PYTHIA`, including single Z^0 and $W^{\pm}$ production, use *matrix element corrections* [Miu99], wherein the parton shower is corrected with the first order matrix element. This approach is effective in approximating NLO distribution shapes, but does not correct the normalization (cross sections). Considering the relatively small impact the backgrounds have on the analysis and the fact that the most important background—W+jet production—is modeled in `PYTHIA` at first order (tree level) in QCD, background simulations using next-to-leading order matrix elements are not expected to change the results significantly. The use of leading order background simulations has been accounted for by using rather pessimistic assumptions for assessing the systematic errors due to the background rates, which will be presented in Sec. 5.4.

To account for the effect NLO corrections will have on the total background rate,

[5] If form factors are applied, they must be included when the reweighting histograms are created, because the form factors are different for each event. This means that the reweighting histograms would have to be recreated any time the form factor parametrization is changed.

a single constant k-factor of 1.5 has been applied to all of the background process event rates.

To ensure an adequate sampling of the backgrounds, the generation of each background is divided into phase space regions based on the transverse momentum (called 'P^T bins') of the hard subprocess, and then the events from each region are combined afterwards. This ensures good statistics in the tails of the distributions. Whenever possible, a sample of events corresponding to an integrated luminosity $\mathcal{L} = 1000$ fb^{-1} has been generated (this is not possible for the low transverse momentum regions of large cross section processes like $b\bar{b}$, single-W, and single-Z—but the low transverse momentum regions are not nearly as significant as the high transverse momentum ones). The generation is performed on the University of Victoria High Energy Physics 18-node Linux Beowulf [Bec95] computer cluster. Each event is simulated with `PYTHIA`, then passed to the ATLAS fast detector simulation program `ATLfast` (discussed in the next section), before being tested against a set of preselection cuts. Each event is permuted through the various particle mis-identification possibilities (wherein jets are mis-identified as electrons or photons, which will be described in Section 4.2.4), and events which pass the preselection are written to disk. This provides a large sample of events which can be used to fine tune the final selection cuts.

Details specific to the generation of individual background processes will be discussed in Sections 4.3 and 4.4. The event simulation chain for the backgrounds is presented in the left-hand branch of Figure 4.1.

4.1.4 Detector simulation

In the final stage of the simulation chain, the response of the ATLAS detector to the final state particles is modeled. There are two versions of the ATLAS detector simulation, full simulation and fast simulation.

Full simulation takes into account the full detector geometry in as complete a manner as possible. Each element of the detector is divided into thin slices, and the passage of the particles through each of these slices is modeled. This simulation accounts for the complicated structure of the detector, including the location of

cracks, dead material, and other inhomogeneities, as well as the acceptance, resolution, and efficiency of each detector component. Full simulation is expensive in terms of computer time.

Fast simulation uses a parametrized model for the detector response and resolution. It takes into account the basic acceptance of the detector, then smears the particles according to the expected detector resolution (i.e. the performance characteristics in Table 1.3). The ATLAS fast simulation program is called `ATLfast` [Atl98c], and it is version 2.55 of this detector simulation, written in Fortran 77, which has been used for the analysis presented in this thesis.

`ATLfast` selects isolated photons and charged leptons, reconstructs jets, and estimates the missing transverse energy in the event. The detector geometry is modeled using a simple parameterization of the coverage for precision physics and calorimetry, and details about the electromagnetic calorimeter barrel/endcap transition region and the granularity of the calorimeters is included. For electrons, muons, and photons, a parametrization of the detector resolution is used, but no reconstruction efficiencies are applied. In this study, these efficiencies have been accounted for by applying the relevant factors to the cross sections—see Sec. 4.2.4. Jets are reconstructed in `ATLfast` using a cone algorithm with $\Delta R = \sqrt{\Delta\eta^2 + \Delta\phi^2} = 0.4$, where η is the pseudo-rapidity and ϕ is the azimuthal angle. The resolution parameterization includes the effect of the magnetic field on jet reconstruction and the expected jet reconstruction efficiencies, as determined from full simulation.

For processes with signatures of electrons, muons, and photons in the final state—such as the present study—fast simulation provides a very good approximation of detector response, and full simulation is generally not necessary. For the present study, several million weighted events are used to simulate the signal events, and full simulation on this scale is not feasible. One part of this analysis which would benefit from full simulation would be the mis-identification of jets as photons or electrons. For this part of the analysis, results from full simulation studies have been used to approximate the detector effects, as will be discussed in Sec. 4.2.

A complete description of the `ATLfast` detector simulation can be found in

Ref. [Atl98c], including the specific parameterizations and a detailed comparison between full and fast simulation.

`ATLfast` takes as input the event record from an event generator like `PYTHIA`. As output, it provides a binary computer file containing a listing of reconstructed isolated charged leptons, isolated photons, missing transverse momentum, and hadronic jets—as well as other event details.

Before events are written to the binary file, they are first required to pass a preselection which ensures the events have the basic properties of the signal signature. The preselection is different for the two analyses, and will be discussed in Sections 4.3.4 and 4.4.3.

The computer program for the analysis part of the present study is written in C++ within the framework of the Root [Bru96] package, and so the binary files from `ATLfast` are first converted to Root-format files before storing them on disk. These files represent the final output of the event simulation chain. Besides the reconstructed event information from `ATLfast`, two other things are incorporated into these files: the "Monte Carlo truth", which is the event record before detector simulation is applied; and the reweighting parameters for the signal events, which are used to calculate the event weights as a function of the anomalous TGC parameters.

4.2 Particle Identification in ATLAS

The contributions for many of the backgrounds depend directly on the detector's ability to distinguish one type of particle from another. Since the cross sections for processes with QCD jets in the final state are often several orders of magnitude higher than the cross section for the processes of interest, the most important contribution will be from jets mis-identified as either electrons or photons. In this section the rejection factors, efficiencies, and isolation criteria for particle identification in ATLAS are reviewed. A summary is presented in Table 4.2.

Efficiencies and Rejection Factors
$R_{\mathrm{J}-\gamma} = 3200$
$R_{\mathrm{J}-\mathrm{e}^{\pm}} = 10^5$
$\epsilon_{\gamma} = 83\%$
$\epsilon_{e^{\pm}} = 73\%$
$\epsilon_{\mu^{\pm}} = 95\%$

Table 4.2: ATLAS detector efficiencies and rejection factors which have been assumed for this study. $R_{\mathrm{J}-\gamma}$ and $R_{\mathrm{J}-\mathrm{e}^{\pm}}$ are the rejection factors for jets faking photons and electrons, and ϵ_{γ}, $\epsilon_{e^{\pm}}$, and $\epsilon_{\mu^{\pm}}$ are the efficiencies for reconstructing photons, electrons and muons.

4.2.1 Separation of jets and photons

When gluons and quarks are produced in high energy collisions, they produce collimated streams of hadrons called jets—a direct consequence of color confinement—which were first observed at the CERN Sp$\bar{\mathrm{p}}$S [UA1 83a, UA2 82]. A small fraction of the time, the jets will fragment into leading neutral mesons such as the π^0 or η^0. The π^0 decays into two photons about 98% of the time, whereas the η^0 decays 72% of the time to neutral modes such as 2γ, $3\pi^0$, or $\pi^0 2\gamma$. At high energy, the opening angle between the meson decay products will be very small, and the signature in the detector will look similar to that of a single photon, particularly for the case of very low multiplicity jets (i.e. containing only a few hadrons).

In ATLAS, photon identification will be based on the shower shape in the electromagnetic (EM) calorimeter (neutral mesons will have a wide profile), leakage into the hadron calorimeter (the hadronic component of the jets will penetrate through the EM calorimeter), and a veto on charged tracks which line up with the EM deposition (photons are neutral so they leave no trace in the tracker). Based on these criteria, the expected rejection factor for jets mis-identified as photons in the ATLAS detector has been studied in Ref. [Atl99a, Sec. 7.6] and [Atl99d]. In Figure 4.2 the jet rejection as a function of the transverse energy E^T_{jet} is shown. The rejection factors, based on an efficiency of 83.0% (83.1%) for low (high) luminosity, increase with increasing E^T up to about 50 GeV, at which point the rejection plateaus. Based on these studies, a jet rejection $R_{\mathrm{J}-\gamma} = 3200$ has been assumed for the present analysis, with a photon efficiency of $\epsilon_{\gamma} = 83\%$ (i.e. 1 out of 3200 jets will be mis-identified as a photon, and

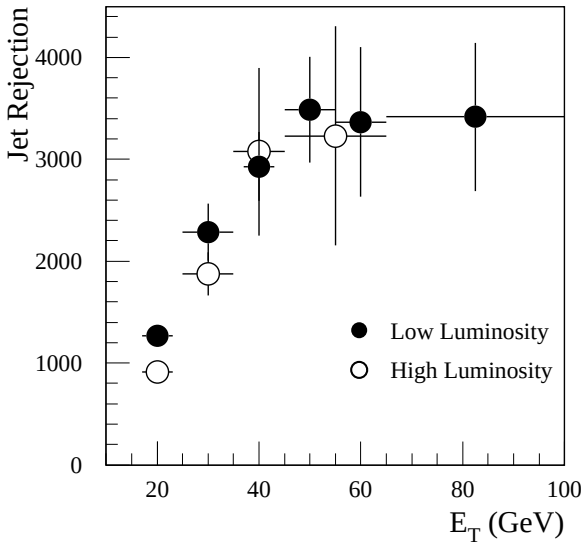

Figure 4.2: Expected ATLAS rejection factor for jets mis-identified as photons as a function of $E^T_{\rm jet}$ after photon selection cuts for low and high luminosity [Atl99a].

83% of the true photons will be correctly identified).

Since the completion of the present analysis, improvements in the jet rejection factors achievable by including isolation conditions (wherein the photon candidate is required to be isolated from other hadronic activity) have been demonstrated in Ref. [Atl01c]. The rejection factors are found to improve by about 50% to well over 4000 at high E^T without compromising the photon efficiency. As such, the rejection factor of 3200 which has been assumed here should be considered a conservative estimate.

4.2.2 Separation of jets and electrons

Jets may also be mis-identified as electrons. Electrons are considerably easier to identify than photons, because they are charged and so they can be measured in the inner detector as well as the calorimetry. Jets may look similar to electrons if, for example, a track lines up with the EM deposition from a leading neutral meson in a jet, or if a photon conversion occurs in a low multiplicity jet. These occurrences are rare.

Electron candidates will be selected in the ATLAS experiment using information from the calorimetry and inner detector. Electrons produce small pencil-sized showers in the calorimeters, whereas hadronic showers from jets are typically much larger. The expected rejection factor for jets mis-identified as electrons in the ATLAS detector has

been studied in Ref. [Atl99a, Sec. 7.4] and [Atl99c]. By cutting on the ratio of energy deposition in the first and subsequent depths of the calorimetry, rejection based on shower length can be achieved. The very fine granularity in pseudo-rapidity of the EM Accordion calorimeter can be used to identify substructures in the lateral shower profile. The EM cluster is then required to have a good inner detector track pointing to it. The energy measured by the calorimetry is required to match the momentum measured with the tracker. Cuts on the impact parameter are particularly useful for reducing contamination from photon conversions, which usually produce tracks which do not line up with the interaction point. Finally, loose transition radiation cuts are imposed. At low (high) luminosity a rejection factor of 150 000 (45 000) can be achieved for $P^T = 30$ GeV electrons with a reconstruction efficiency of 72.7% (67.5%). In the present study, a rejection factor $R_{\mathrm{J}-\mathrm{e}^{\pm}} = 10^5$ has been assumed with efficiency $\epsilon_{e^{\pm}}$ =73%. The slightly smaller $R_{\mathrm{J}-\mathrm{e}^{\pm}}$ is chosen to account for possible performance degradation which may occur at higher $P^T_{\mathrm{e}^{\pm}}$, because the inner detector momentum resolution decreases with increasing P^T.

4.2.3 Reconstruction of muons

The efficiency for reconstructing muons using information from the muon spectrometer combined with the inner detector peaks at about 97% at $P^T_{\mu^{\pm}} = 10$ GeV, and decreases slowly to about 85% at 1 TeV [Atl99a, Sec. 8.1.2.1]. This decrease in efficiency is due to the increase in probability (with increasing muon energy) for the muon to initiate electromagnetic showers. These localized showers can result in large numbers of hits in the muon system, which spoil the pattern recognition of the hit from the genuine muon. A constant muon efficiency $\epsilon_{\mu^{\pm}}$ =95% has been assumed for the present study. The rate of fake high P^T muons will be negligible in ATLAS [Atl94a].

4.2.4 Simulating particle mis-identification

The ATLAS fast simulation software `ATLfast` does not account for particle mis-identification in the reconstruction of Monte Carlo events. To simulate this effect, events are first reconstructed with the normal `ATLfast` algorithms, and then tested

against the kinematic cuts. If the event passes the cuts, it is accepted with weight one. Subsequently, a copy of the event is created with one of the reconstructed jets re-labelled as a photon, and the event-copy is tested against the kinematic cuts. If the event-copy passes the kinematic cuts, the copy is accepted with weight $1/R_{\mathrm{J}-\gamma}$. This procedure is repeated for each of the jets in the event. The same procedure is followed for the mis-identification of jets as electrons, but this time the event weight would be $1/R_{\mathrm{J}-\mathrm{e}^{\pm}}$.

4.2.5 Particle Isolation

Reconstructed electron, muon, and photon candidates are required to satisfy isolation criteria. This means that their signatures in the detector are required to be well separated from those of other particles and maximizes the probability that the energy deposition in the detector has been properly assigned to the correct particle candidate.

The isolation criteria which have been used for this study are the default criteria implemented in the `ATLfast` detector simulation. The candidate particle is required to be separated from the center of electromagnetic or hadronic calorimeter clusters[6] by a distance in the pseudo-rapidity and azimuthal plane of at least $\Delta R = \sqrt{\Delta\phi^2 + \Delta\eta^2}$=0.4. In addition, the amount of electromagnetic and hadronic calorimeter transverse energy lying within a cone of ΔR=0.2 from the particle candidate is required to be no more than 10 GeV.

These criteria are particularly relevant for the reconstruction of the Z-boson in the WZ channel. When the Z decays to e^+e^-, the reconstructed electron must be separated from the reconstructed positron by at least ΔR =0.4, whereas the muons in the $Z \rightarrow \mu^+\mu^-$ decay channel need not be separated at all (since they deposit essentially no electromagnetic or hadronic energy). For very high transverse momentum $Z \rightarrow e^+e^-$ decays, this can result in a substantial loss of efficiency, since the boost of the Z-boson can cause the decay products to be highly collimated. For a cone size ΔR =0.4, this loss in efficiency begins to occur above $P_{\mathrm{Z}}^T = 425$ GeV, and so does not affect this analysis, since fewer than a single event is expected in that

[6]Calorimeter clusters are defined using a cone algorithm with ΔR =0.4.

region for an integrated luminosity of 30 fb^{-1}. However, for high luminosity running at the LHC, this can start to be a significant effect, particularly since this is precisely the regime where the effects of anomalous TGC's are largest. TGC analyses which are applied to several years of high luminosity LHC data would have to use modified isolation criteria for electrons to account for this effect.

4.3 Backgrounds to $W\gamma$ Production

The trigger for $W\gamma$ events will be the single photon trigger, operating without prescaling at $P_\gamma^T = 40$ GeV and 60 GeV for low and high luminosity running respectively [Atl99a, Table 11-20]. This study is optimized for low luminosity. The precise setting for the trigger is not important, because the events of interest are in the kinematic region with $P_\gamma^T > 100$ GeV.

The cross section for $W\gamma$ production diverges for small values of P_γ^T, which is the result of infrared singularities arising in photon emission from the incoming massless quarks. The Feynman diagram containing the TGC vertex (Figure 3.1, right) does not involve photon radiation from fermion lines, and thus very little sensitivity to the anomalous TGC's is lost by imposing a P^T cut on the photon transverse momentum.

4.3.1 Backgrounds with a lepton and photon signature

$W(\rightarrow \tau\nu)\gamma$ with leptonic tau decays

The cross section for $W\gamma$ production with the W decaying to $\tau\nu_\tau$ is a factor two smaller than the signal. This irreducible process is essentially the same as the signal, and does contain the TGC vertex. However, since τ's are more difficult to reconstruct, it is treated as a background in this study. The $\tau^\pm \rightarrow l^\pm\nu\bar{\nu}$ decay (for $l^\pm = \mu^\pm, e^\pm$) branching ratio is about 34%. The contribution from this process will be reduced by lepton transverse momentum cuts, because the secondary charged leptons from the τ-decay will have reduced transverse momentum as compared to the direct lepton from the W-decay. At Tevatron energy, this effect renders the leptonic τ decay background negligible [D0 96]. Previous studies [CMS98] have assumed that this also holds at LHC energy, and it will be shown here that this is not the case.

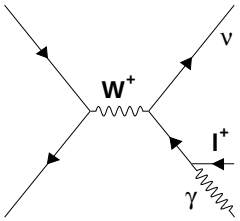

Figure 4.3: The Feynman graph for radiative W decays is shown.

The process is simulated using the PYTHIA [Sjö01a] 6.136 $W\gamma$ process (MSUB(80) switch in PYTHIA) and forcing the W decay to τ, ν. As for all of the backgrounds, the event generation uses leading order approximations for the cross sections and so a constant k-factor of 1.5 is applied to account for this.

Radiative W decays, $W^{\pm} \to l^{\pm}\nu\gamma$

This irreducible process, shown in Figure 4.3, should be included in an ideal Monte Carlo simulation of the signal. It interferes with the signal process wave functions, and is of the same order as the Born level process. However, this diagram is not included in any of the matrix elements available for $W\gamma$ production at NLO in QCD. The effect of omitting the diagram is small, so long as a kinematic cut is included which keeps the events far away from the kinematic region where this diagram becomes important. The contribution from the diagram is largest in the region where the lepton and photon are nearly collinear, and so a requirement on the separation of the lepton from the photon $\Delta R(l^{\pm}, \gamma) = \sqrt{\Delta\phi^2 + \Delta\eta^2}$ is effective for this purpose.

The process is simulated using PYTHIA 6.136 single-W production (MSUB(1) switch in PYTHIA) by forcing the W to decay to either $e\nu_e$ or $\mu\nu_\mu$ and allowing the photon to come from a final state shower of the charged lepton. There is no double counting with the $W\gamma$ process, because in that case the photon arises from the initial state quarks or from a TGC vertex. In generating this process initial state QCD radiation is turned off to avoid double counting with the W+jet process, which will be considered later. Generation of events in the kinematic region of interest has been sped up by enhancing the final state QED shower by a factor 20 (PARJ(83) parameter in PYTHIA), and ending the QED shower at a rather large invariant mass of 10 GeV (PARJ(84) parameter in PYTHIA). The event rate after kinematic cuts has been compared with

a simulation which uses PHOTOS[7] [Bar93] 2.02, and good agreement is found.

$Z^0\gamma$ production with leptonic decays

This diboson process looks similar to the signal when one of the two charged leptons escapes detection, either because it is outside of the central region of the detector, has insufficient transverse momentum, or is simply missed because of lepton reconstruction efficiencies.

The process is simulated with the PYTHIA 6.136 $Z^0\gamma$ process (MSUB(19) switch in PYTHIA) by forcing the Z^0 to decay to charged leptons.

Heavy flavors $t\bar{t}(\gamma)$ and $b\bar{b}(\gamma)$

These heavy flavor processes typically have several jets in the final state. Nevertheless, since their cross sections are so large in comparison to the signal, a small fraction of the events having signal-like signatures can result in significant backgrounds. The lepton can be produced from leptonic bottom-meson decays or from $t \to Wb$ with the W decaying leptonically. These processes also contribute to the fake-lepton and fake-photon backgrounds, in the case where a jet is mis-identified as an electron or photon. The primary means of reducing the contributions from these processes is to cut on the jet activity in the events.

The heavy flavor processes are simulated with PYTHIA 6.136 (MSEL=5,6 switches in PYTHIA). The final states with and without a photon are generated separately. The $t\bar{t}\gamma$ and $b\bar{b}\gamma$ final states are simulated with the final state radiation enhanced in the same manner that was used for radiative W decays. For this sample, no jet-photon mis-identification is applied, as the real-photon is of interest here. The number of events passing the cuts has been checked against a simulation using PHOTOS for final state bremsstrahlung. A separate sample of events is generated using the $t\bar{t}$ and $b\bar{b}$ processes with QED showering turned off (so as to avoid double counting the phase space which has already been populated with the $t\bar{t}\gamma$ and $b\bar{b}\gamma$ final states), to

[7] PHOTOS estimates the size of QED bremsstrahlung in the leading-logarithmic approximation. It can be used in conjunction with any Monte Carlo generator for any type of decay.

account for the jet-photon mis-identification scenario. The contribution arising from mis-identified jets is significantly larger than the real photon contribution.

4.3.2 Jets mis-identified as electrons

Direct photon production, γ+jet

This process mimics the signal in the case where the jet is mis-identified as an electron. Because there is no direct source of missing energy for this background, a cut on $P^T_{\rm miss}$ will be effective in reducing its contribution.

This process is simulated using the PYTHIA 6.136 processes $q\bar{q} \to \gamma g$, $g\overset{(-)}{q} \to \gamma\overset{(-)}{q}$, and $gg \to \gamma g$ (MSUB(14),MSUB(29),MSUB(115) switches in PYTHIA).

4.3.3 Jets mis-identified as photons

W+jet production

The cross section for single-W production is over 10^4 times larger than that of the signal. When the final state jet fakes a photon, the signature for this process will be identical to that of the signal. This will be the most challenging background to $W\gamma$ production.

PYTHIA 6.136 processes $q\bar{q}' \to W^{\pm}g$ and $g\overset{(-)}{q} \to W^{\pm}\overset{(-)}{q}$ (MSUB(16),MSUB(31) switches in PYTHIA) with the $W^{\pm}$ forced to decay to leptons are used to simulate this background.

Z^0+jet production

Because the cross section for this process is so large, the rare cases when the jet is mis-identified as a photon and the Z^0 decays leptonically with one charged lepton escaping detection, will be important.

PYTHIA 6.136 is used to simulate the process in the same manner as for W+jet production (MSUB(15),MSUB(30) switches in PYTHIA).

4.3.4 Event selection and efficiency

The simulation of the $W\gamma$ signal process is performed at NLO. The backgrounds are simulated at leading order, with higher order corrections entering through the parton shower. When performing the event selection, extra care must be taken to ensure none of the event selection criteria operate on the differences between the NLO and LO simulations. One example would be a cut on the number of jets reconstructed in the event. The NLO simulation does not use a parton shower (doing so would double-count regions of phase space)—and so there is at most one colored parton (coming from the order α_S emission) in the event. This parton is hadronized using `PYTHIA`, and so it may be divided further into multiple jets, but the probability of this is considerably smaller than would be the case if the parton shower were used, and multiple colored partons were present in the event before hadronization. This means that a cut on the number of jets reconstructed in the event (which would be a logical cut to use against the $t\bar{t}$ and $b\bar{b}$ backgrounds) is *not allowed*, because the signal simulation does not give a reasonable prediction of the number of jets in the event.

To ensure these differences in the simulation do not play a role in the choice of cuts, the kinematic cuts which are employed to maximize the signal purity are optimized using a leading order simulation of both the signal and backgrounds.

A preselection is applied to the events at generation time, and ensures the events have the basic properties of the signal signature. The $W\gamma$ analysis preselection requires exactly one high P^T isolated photon and exactly one high P^T isolated $e^{\pm}$ or $\mu^{\pm}$ in the region of precision physics ($|\eta| < 2.5$). It further requires that the P^T_{miss} reconstruction is consistent with the hypothesis that the missing transverse momentum arises from a neutrino, which together with the charged lepton, reconstructs to the W-mass (this will be discussed in more detail in the analysis section), i.e.

$$\begin{array}{l}\underline{W\gamma \text{ Preselection}} \\ \qquad \text{one isolated photon, } P^T_\gamma > 80 \text{ GeV}, \ |\eta_\gamma| < 2.5 \\ \qquad \text{one isolated electron or muon, } P^T_{l^\pm} > 20 \text{ GeV}, \ |\eta_{l^\pm}| < 2.5 \\ \qquad \text{solution to neutrino longitudinal momentum exists.}\end{array} \tag{4.2}$$

The number of events remaining for $\mathcal{L} = 30$ fb^{-1} after the preselection are shown

	$Z\gamma$	W+jet	Z+jet	$t\bar{t}(\gamma)$	$b\bar{b}(\gamma)$	γ+jet	$W \to l\nu\gamma$	$W\gamma \to \tau\nu\gamma$
preselection	2436	4367	7398	1561	253	956	20	710
$P_\gamma^T > 100$ GeV	1277	2097	2101	945	160	894	14	665
$P_{\mathrm{l}^\pm}^T > 25$ GeV	1196	1938	1800	837	64	664	13	586
$P_{\mathrm{miss}}^T > 25$ GeV	377	1557	215	689	43	44	12	574
$\Delta R(\gamma, \mathrm{l}^\pm) > 1$	376	1543	183	611	42	44	12	574
$\sum_{jets} \vec{P}_{\mathrm{jet}_i}^T < 100$ GeV	341	1280	133	286	26	11	12	534

	# events			Spread in Stat. 95% C.L.	
	Backgrounds	$W\gamma$ Signal	$\frac{S}{B}$	λ_γ	$\Delta\kappa_\gamma$
preselection	17701	17717	1.0	0.0076	0.18
$P_\gamma^T > 100$ GeV	8153	10638	1.30	0.0076	0.18
$P_{\mathrm{l}^\pm}^T > 25$ GeV	7098	10066	1.42	0.0075	0.18
$P_{\mathrm{miss}}^T > 25$ GeV	3511	7311	2.08	0.0074	0.18
$\Delta R(\gamma, \mathrm{l}^\pm) > 1$	3385	6791	2.01	0.0074	0.18
$\sum_{jets} \vec{P}_{\mathrm{jet}_i}^T < 100$ GeV	2623	4262	1.62	0.0066	0.15

Table 4.3: The number of events surviving after each of the kinematic cuts is applied cumulatively for the $W\gamma$ analysis. An integrated luminosity $\mathcal{L} = 30$ fb^{-1} at the LHC has been assumed, and reconstruction efficiencies have been applied. The statistical spread in the 95% confidence intervals have been derived using a binned maximum likelihood fit to the P_γ^T distribution and the results are averaged over 1000 simulated ATLAS experiments.

in the first column of Table 4.3. The signal and background rates are similar after the selection. The numbers reported in this table employ the full NLO simulation for the signal, and a k-factor of 1.5 has been applied to the backgrounds, which are generated at leading order.

The goal of the present analysis is not to observe the signal process over the backgrounds (as would be the case for a search), but rather to obtain the maximum sensitivity to non-standard TGC couplings in the signal process. As such, the purpose of the kinematic cuts is not just to optimize the signal purity, but to optimize the contribution to the signal from the regions of phase space where anomalous TGC's affect the signal most. With this in mind, the sensitivity to the anomalous TGC's is also tabulated in Table 4.3 after each subsequent cut is applied. The sensitivity reported in this table is statistical only and a lower number represents a better sensitivity. The method for evaluating this sensitivity is not important for the present

discussion, it will be presented in Sec. 5.3.

The first three kinematic cuts are imposed on the transverse momentum of the photon, lepton, and missing energy. These cuts do not improve nor degrade the sensitivity to the anomalous TGC's because they are not isolating nor removing information which is relevant for the couplings (at small transverse momentum the effects of the anomalous TGC's on the matrix elements are extremely small). These cuts are designed to improve the signal purity. The smaller the background contribution is in the final sample, the less the results will depend upon our ability to properly model these backgrounds. The transverse momentum cuts are optimized by maximizing the signal to background ratio using leading order simulations for both the signal and backgrounds, while monitoring the statistical sensitivity to the anomalous TGC's (using NLO simulations for the signal) to ensure the cut is not increased to a point where the sensitivity is degraded. As an example of when this can happen, consider the P_γ^T cut. If this cut were increased to values of the order 500 GeV, the signal to background (S/B) ratio would be very large, but information which is relevant for the anomalous TGC's (and in particular for the $\Delta\kappa_\gamma$ parameter) would be lost, and so the sensitivity would start to degrade. The transverse momentum cuts chosen for the photon, charged lepton, and missing energy are:

$$\begin{array}{l} P_\gamma^T > 100 \text{ GeV}, \ |\eta_\gamma| < 2.5 \\ P_{l^\pm}^T > 25 \text{ GeV}, \ |\eta_{l^\pm}| < 2.5 \\ P_{\text{miss}}^T > 25 \text{ GeV}. \end{array} \tag{4.3}$$

The absence of additional high-P^T photons or charged leptons has already been ensured by the preselection. The exact location of these additional photon and charged lepton cuts has very little effect on the purity. Hard photons (or hard jets misidentified as photons) are rare for the background processes, so the P_γ^T cut is effective at improving S/B by 30%. The P_{miss}^T cut greatly reduces the contributions from backgrounds (Z+jet and $Z\gamma$) which do not produce direct neutrinos.

As discussed in the previous section, the simulation of the signal has omitted the Feynman diagram arising from radiative W-decays. A cut on $\Delta R(\gamma, l^\pm)$ is included to ensure the signal events are far from the region of phase space where this diagram becomes non-negligible. Thus the motivation for this cut is purely to ensure this

approximation, which has been made in the modeling of the signal, does not affect the final results. Note that the event rate coming from the radiative W-decay background is rather small from the onset. This is because isolation criteria has been applied in the reconstruction phase, and so is already part of the preselection.

The last cut which is applied operates on the jet activity in the event and is included to optimize the sensitivity to the anomalous TGC's. NLO corrections degrade the sensitivity to the TGC couplings because a large number of extra diagrams are included in the calculation, the majority of which do not include the TGC vertex (see Figure 3.5). The NLO corrections become largest when the jet activity is large. This means that a cut on P_{jet}^T will serve to moderate the influence of these extra diagrams. When P_{jet}^T is small, the signal is Born-like. When it is large, the diboson system will be recoiling against a hard central jet, and the influence of the TGC vertex will be minimal.

Because the signal is generated at NLO and the backgrounds are generated at LO, care must be taken when applying a cut such as this. The distribution of P_{jet}^T at NLO for diboson production is most accurately interpreted as the inclusive jet transverse momentum. This means that the cut should not operate on a particular jet (e.g. the hardest or second hardest jet), but rather on the vector sum of the jet activity, $\sum_{jets} \vec{P}_{\text{jet}_i}^T$. It should be stressed that this is necessary because of the fixed order approach which has been used to model the signal, and would not be true if a calculation accurate to all orders were possible.

The $\sum_{jets} \vec{P}_{\text{jet}_i}^T$ cut is optimized strictly on the basis of the sensitivity to the anomalous TGC's. The sensitivity as a function of the cut is shown in Table 4.4. As the cut is increased, the purity goes down, but at the same time the sensitivity increases. This is because the signal itself (in kinematic regions where the anomalous TGC's have little effect) is washing out the sensitivity. At about 100 GeV, the sensitivity begins to be degraded by the cut. This is the value which is chosen.

After all kinematic cuts have been applied, the signal exceeds the backgrounds by a factor 1.6. About 6900 event candidate will be observed with an integrated luminosity of 30 fb^{-1}, 2600 of these events will be background. The dominant back-

$\sum_{jets} \vec{P}^T_{\mathrm{jet}_i}$ [GeV]	S/B	$S/\sqrt{B}$	Spread in 95% C.L. λ_γ	$\Delta\kappa_\gamma$
no cut	2.0	120	0.00738	0.179
< 400	2.0	120	0.00653	0.158
< 300	2.0	110	0.00659	0.156
< 200	1.8	100	0.00644	0.151
< 150	1.8	96	0.00652	0.150
$\underline{< 100}$	1.6	83	0.00656	0.149
< 75	1.6	77	0.00656	0.150
< 50	1.6	70	0.00670	0.150
< 40	1.6	66	0.00683	0.152
< 30	1.6	62	0.00696	0.155
< 20	1.8	57	0.00745	0.159
< 10	2.0	47	0.00773	0.168

Table 4.4: The effect of the $\sum_{jets} \vec{P}^T_{\mathrm{jet}_i}$ cut on the sensitivity to anomalous TGC's, purity, and significance is tabulated for $W\gamma$ production. An integrated luminosity of 30 fb^{-1} is assumed and efficiencies have been applied. The statistical spread in the 95% confidence intervals have been derived using a binned maximum likelihood fit to the P^T_γ distribution and the results are averaged over 1000 simulated ATLAS experiments. The numbers reported in this table employ the full NLO simulation for the signal, and a k-factor of 1.5 has been applied to the backgrounds, which are generated at leading order.

$W\gamma$ Selection
one isolated photon, $P_\gamma^T > 100$ GeV, $\lvert\eta_\gamma\rvert < 2.5$
no other photon with $P_\gamma^T > 80$ GeV, $\lvert\eta_\gamma\rvert < 2.5$
one isolated electron or muon, $P_{\mathrm{l}^\pm}^T > 25$ GeV, $\lvert\eta_{\mathrm{l}^\pm}\rvert < 2.5$
no other charged lepton with $P_{\mathrm{l}^\pm}^T > 20$ GeV, $\lvert\eta_{\mathrm{l}^\pm}\rvert < 2.5$
$P_{\mathrm{miss}}^T > 25$ GeV
$\sum_{\mathrm{jets}} \vec{P}_{\mathrm{jet}_i}^T < 100$ GeV
$\Delta R(l^\pm, \gamma) = \sqrt{\Delta\phi^2 + \Delta\eta^2} > 1$
solution to neutrino longitudinal momentum exists

Table 4.5: The kinematic cuts imposed for the $W\gamma$ analysis are presented.

ground is W+jet production, with the jet mis-identified as a photon. Further improvements in the separation of jets from photons (as have already been achieved in Ref. [Atl01c]) will help to reduce this background. The diboson processes $Z\gamma$ and $W(\tau,\nu)\gamma$ are significant backgrounds as well, with $W(\tau,\nu)\gamma$ being the second most important background. It is unlikely that its contribution can be further reduced by other cuts.

The final selection cuts for the $W\gamma$ analysis are summarized in Table 4.5.

4.4 Backgrounds to WZ Production

The trigger for WZ events will be the single muon and single electron triggers, operating at $P_\mu^T = 20$ GeV and $P_{\mathrm{e}}^T = 25$ GeV respectively for low luminosity running [Atl99a, Table 11-20].[8] At high luminosity, the electron trigger will be further increased to at least $P_{\mathrm{e}}^T = 30$ GeV, in this case the $P_{\mathrm{e}}^T = 20$ GeV two-electron trigger (which requires the presence of two electrons, each having at least $P_{\mathrm{e}}^T = 20$ GeV) can be used in conjunction with the $P_\mu^T = 20$ GeV muon trigger. If changes in the ATLAS event size necessitate further increases in these trigger thresholds, the WZ analysis will start to be affected.

[8]The `e20i` $P_{\mathrm{e}}^T = 20$ GeV single electron trigger reported in Table 11-20 of Ref. [Atl99a] has been increased to a `e25i` ($P_{\mathrm{e}}^T = 25$ GeV) trigger. This reduces the event rate enough to allow for an expected increase in the size of the data to be written to disk for each event (the limiting quantity is the event rate times the event data size). A pre-scaled `e20i` trigger will still be available.

The WZ process provides a striking signature in the detector, three high transverse momentum charged leptons and missing transverse energy. Only a few backgrounds mimic this signature.

4.4.1 Backgrounds with a tri-lepton signature

ZZ with leptonic decays

This diboson process will mimic the signature for WZ production when one of the charged leptons from the Z decays escapes detection.

The process is simulated with the `PYTHIA` 6.136 ZZ process (`MSUB(22)` switch in `PYTHIA`) by forcing the Z^0's to decay to charged leptons. The scenario where one Z^0 decays to electron or muon type leptons and the other one decays to τ's (with one $\tau^{\pm} \rightarrow l^{\pm}\nu\nu$) provides a difficult signature (three charged leptons and $P^T_{\rm miss}$). Fortunately the branching ratio BR($ZZ \rightarrow l^+l^-\tau^+\tau^- \rightarrow l^+l^-\tau^{\pm}l^{\mp}\overset{(-)}{\nu}_{\tau}\overset{(-)}{\nu}_{l}$)=0.16% is quite small.

4.4.2 Jets mis-identified as electrons

Heavy flavors $t\bar{t}$

Heavy flavors can provide significant backgrounds, particularly $t\bar{t} \rightarrow WbW\bar{b}$ with the W's decaying leptonically. The contribution from $b\bar{b}$ is negligible (and has been checked).

This process is simulated with `PYTHIA` 6.136 (`MSEL=5,6` switches in `PYTHIA`). The simulation with `PYTHIA` does not account for the $t\bar{t}Z$ final state, which is a potentially dangerous background when the Z decays to charged leptons. The cross section for $pp \rightarrow t\bar{t}Z \rightarrow 3l^{\pm} + X$ at 16 TeV has been calculated in Ref. [Mai92] to be about 18 fb (for a top quark mass of 175 GeV) requiring $P^T_{\rm l^{\pm}}$ >20 GeV and $|\eta_{\rm l^{\pm}}|$ <2.5 for all of the charged leptons. The slightly lower LHC energy (14 TeV), together with a jet veto and lepton isolation criteria should be sufficient to bring the $t\bar{t}Z$ contribution well below 1 fb, making its contribution very small. The $t\bar{t}Z$ background is neglected in this analysis.

Z^0+jet production

Though the cross section for this process is very large, the rejection factor for jets mis-identified as electrons is also large (10^5). There is no direct source of missing transverse energy for this background, so a $P^T_{\rm miss}$ cut will be effective at reducing its contribution.

PYTHIA 6.136 processes $q\bar{q} \to Z^0 g$ and $g\overset{(-)}{q} \to Z^0\overset{(-)}{q}$ (MSUB(15),MSUB(30) switches in PYTHIA) with the Z^0 forced to decay to leptons are used to simulate this background.

4.4.3 Event selection and efficiency

The preselection for WZ production requires exactly three isolated high transverse momentum electron or muon type leptons in the region of precision physics ($|\eta| < 2.5$). Two of these leptons must be like flavor and opposite sign. The $P^T_{\rm miss}$ reconstruction must be consistent with the hypothesis that the missing transverse momentum arises from a neutrino which together with one of the charged leptons reconstructs to the W-mass (this will be discussed in more detail in the analysis section), i.e.

$$\begin{array}{l}\underline{WZ \text{ Preselection}} \\ \qquad \text{three isolated electrons or muons, } P^T_{\rm l^\pm} > 20 \text{ GeV}, \ |\eta_{\rm l^\pm}| < 2.5 \\ \qquad \text{two of which are like flavor, opposite sign} \\ \qquad \text{solution to neutrino longitudinal momentum exists.}\end{array} \tag{4.4}$$

The preselection alone is enough to provide an event sample consisting of 65% signal, as shown in the first column of Table 4.6, where the event rates are enumerated for $\mathcal{L} = 30$ fb^{-1}.

Increasing the $P^T_{\rm l^\pm}$ cut to 25 GeV improves the signal to background ratio (S/B) from 1.9 to 2.4. The $P^T_{\rm miss}$ cut, set at 25 GeV, is effective at greatly reducing the backgrounds the $Z(l^+l^-)$+jet and $ZZ \to l^+l^-l^+l^-$, which do not produce direct neutrinos.

After the transverse momentum cuts, $t\bar{t}$ is the largest background. The charged leptons from this process are usually from W-boson's and not Z^0-boson's, so a cut on the mass of the like flavor opposite sign lepton pair is effective at reducing the $t\bar{t}$ background. A window of 10 GeV around the Z^0 mass is chosen. The window has been optimized by generating the signal with PYTHIA (with includes finite width effects).

	Z+jet	ZZ	$t\bar{t}$
preselection	631	576	745
3 leptons, $P^T_{\mathrm{l}^\pm} > 25$ GeV	398	500	461
$P^T_{\mathrm{miss}} > 25$ GeV	3.2	90	357
$\lvert M_{\mathrm{l}^+\mathrm{l}^-} - M_{\mathrm{Z}}\rvert < 10$ GeV	2.8	76	65
$\sum_{jets} \vec{P^T_{\mathrm{jet}_i}} < 100$ GeV	2.5	72	44

	# events			Spread in Stat. 95% C.L.		
	Backgrounds	WZ Signal	$\frac{S}{B}$	λ_Z	$\Delta\kappa_Z$	Δg^1_Z
preselection	1952	3663	1.88	0.014	0.29	0.020
3 leptons, $P^T_{\mathrm{l}^\pm} > 25$ GeV	1359	3285	2.42	0.014	0.29	0.020
$P^T_{\mathrm{miss}} > 25$ GeV	450	2453	5.44	0.014	0.28	0.019
$\lvert M_{\mathrm{l}^+\mathrm{l}^-} - M_{\mathrm{Z}}\rvert < 10$ GeV	144	2331	16.2	0.014	0.29	0.020
$\sum_{jets} \vec{P^T_{\mathrm{jet}_i}} < 100$ GeV	119	1987	16.7	0.013	0.23	0.016

Table 4.6: The number of events surviving after each of the kinematic cuts is applied for the WZ analysis. An integrated luminosity $\mathcal{L} = 30$ fb^{-1} at the LHC has been assumed, and reconstruction efficiencies have been applied. The statistical spread in the 95% confidence intervals have been derived using a binned maximum likelihood fit to the $P^T_{\mathrm{Z}^0}$ distribution and the results are averaged over 1000 simulated ATLAS experiments. The numbers reported in this table employ the full NLO simulation for the signal, and a k-factor of 1.5 has been applied to the backgrounds, which are generated at leading order.

$\sum_{jets} \vec{P}^T_{\mathrm{jet}_i}$ [GeV]	S/B	$S/\sqrt{B}$	Spread in 95% C.L. λ_Z	$\Delta\kappa_Z$	Δg_Z^1
no cut	16	200	0.0144	0.289	0.0195
< 400	16	190	0.0130	0.263	0.0176
< 300	16	190	0.0131	0.256	0.0172
< 200	16	180	0.0128	0.243	0.0165
< 150	17	190	0.0129	0.239	0.0163
< 100	17	180	0.0130	0.239	0.0161
< 75	18	180	0.0132	0.238	0.0163
< 50	24	200	0.0139	0.246	0.0168
< 40	28	210	0.0141	0.247	0.0171
< 30	30	210	0.0148	0.259	0.0182
< 20	35	210	0.0153	0.273	0.0192
< 10	48	210	0.0168	0.304	0.0218

Table 4.7: The effect of the $\sum_{jets} \vec{P}^T_{\mathrm{jet}_i}$ cut on the sensitivity to anomalous TGC's, purity, and significance is tabulated for WZ production. An integrated luminosity of 30 fb^{-1} is assumed and efficiencies have been applied. The statistical spread in the 95% confidence intervals have been derived using a binned maximum likelihood fit to the P_γ^T distribution and the results are averaged over 1000 simulated ATLAS experiments.

The NLO simulation of WZ production assumes the narrow width approximation (i.e. the gauge-bosons are always on shell), and so it cannot be used to evaluate width effects. This window, being 20 GeV wide, is sufficiently large that finite width effects are not be important to the signal simulation.[9]

The last cut operates on the jet activity in the event, and has been optimized in a manner identical to that used for $W\gamma$ production. The sensitivity to the anomalous TGC's as a function of the vector sum of the jet transverse momentum $\sum_{jets} \vec{P}^T_{\mathrm{jet}_i}$ is shown in Table 4.7. A cut at $\sum_{jets} \vec{P}^T_{\mathrm{jet}_i}$=100 GeV is effective at isolating the region of phase space which is most sensitive to the anomalous TGC's. This is the same cut which has been used for $W\gamma$ production—and like that process, this choice does not give the best signal purity, because it is the signal itself which is washing out the sensitivity to the anomalous TGC's.

Final selection cuts for WZ are shown in Table 4.8.

[9]The window which extends from -10 GeV to 10 GeV around the Z^0 mass contains 92% of the Z-width.

WZ Selection
three isolated electron or muons, $P_{\mathrm{l}^{\pm}}^{T} > 25$ GeV, $\lvert\eta_{\mathrm{l}^{\pm}}\rvert < 2.5$
two of which are like flavor, opposite sign leptons satisfying
$\lvert M(l^{+}, l^{-}) - M_{\mathrm{Z}}\rvert < 10$ GeV
no other charged lepton with $P_{\mathrm{l}^{\pm}}^{T} > 20$ GeV, $\lvert\eta_{\mathrm{l}^{\pm}}\rvert < 2.5$
$P_{\mathrm{miss}}^{T} > 25$ GeV
$\sum_{\mathrm{jets}} \vec{P}_{\mathrm{jet}_i}^{T} < 100$ GeV
solution to neutrino longitudinal momentum exists

Table 4.8: The kinematic cuts imposed for the WZ analysis are presented.

Chapter 5

Analysis Methods and Results

Having established the procedure for obtaining a sample of diboson event candidates, the goal is to establish the degree to which the data is consistent with the Standard Model prediction for the three gauge-boson couplings. This comparison of the data to theory is quantified by means of the λ, $\Delta\kappa$, and Δg^1 parameters of the most general gauge-invariant C and P conserving Lagrangian for the TGC interaction (Eq. 3.1), described in Sec. 3.1.

In anticipation of the ATLAS experiment data, there are two scenarios to prepare for: the anomalous TGC parameters could be in agreement with the Standard Model values within experimental errors, or non-standard couplings might be observed. In the former scenario, limits may be placed on the anomalous TGC parameters. In the latter, the collaboration will be in a position to measure the characteristics of the couplings, i.e. disentangle the contributions from the different anomalous TGC parameters and study their energy dependence.

This chapter focuses on how to perform measurements of the three gauge-boson couplings and the radiation zero with ATLAS experiment data. After discussing the reconstruction of the event kinematics in the first section, the prospects for observing the radiation zero are evaluated in Section 5.2. Different techniques for performing the anomalous TGC measurements are evaluated and compared in Section 5.3. A discussion of the systematic errors is presented next, and focuses primarily on the dominant contribution, which is the theoretical uncertainty arising in the modeling of higher order QCD effects. In the following section the expected ATLAS experiment limits

are derived and enumerated, which will be relevant for the case when the measurements are consistent with the Standard Model. In the last section of the chapter, the second scenario—the measurement of non-standard anomalous TGC's—is addressed by studying the feasibility for measuring the energy dependence of anomalous TGC's at ATLAS.

5.1 Reconstructing the Center-of-Mass System

Many of the methods for measuring anomalous TGC parameters which will be discussed in the latter sections of this chapter will require the reconstruction of event kinematics. This section describes the considerations which are important for this reconstruction.

For processes such as $pp \to Z(\to l^+l^-)\gamma$ which produce final state particles with directly observable momenta, the center-of-mass system energy and momentum can be directly inferred from the measured four-vectors. For the leptonic decay channels of hadronic $W^\pm V$ production, a complete reconstruction of the center-of-mass system is made difficult by the presence of an invisible neutrino from the W-decay. Unlike the lepton-collider case, the energy and longitudinal boost of the partons inside the colliding (anti-)protons participating in the hard interaction are unknown, and so their momentum fractions x_a, x_b can only be inferred from the final state particles.

5.1.1 Reconstructing the neutrino from the $W^\pm$ decay

When the final state contains a single invisible neutrino coming from a $W^\pm$, such as for $p\overset{(-)}{p} \to W^\pm(\to l^\pm\nu)\gamma$ or $p\overset{(-)}{p} \to W^\pm(\to l^\pm\nu)Z(\to l^+l^-)$, then the final state four-vectors and center-of-mass can be reconstructed up to a two-fold ambiguity by making some simple assumptions:

1. assume the missing transverse momentum arises exclusively from the invisible neutrino

$$\vec{P}_\nu^T \equiv \vec{P}_{\text{miss}}^T \tag{5.1}$$

2. assume the $W^{\pm}$ is on-shell ("on-shell W-mass constraint")

$$(P_{\nu} + P_{l^{\pm}_{\rm W}})^2 \equiv M^2_{\rm W}. \tag{5.2}$$

The first constraint removes the degrees of freedom associated with the neutrino transverse directions, while the second constraint maps the neutrino longitudinal momentum degree of freedom onto the W-mass degree of freedom. With these assumptions, there are two neutrino momentum solutions. They can be calculated by enforcing mass/momentum conservation, and are given by

$$\begin{aligned} P^x_{\nu} &= P^x_{\rm miss} \\ P^y_{\nu} &= P^y_{\rm miss} \\ P^z_{\nu} &= \frac{1}{2P^{T\ 2}_{l^{\pm}_{\rm W}}} \left[P^z_{l^{\pm}_{\rm W}} \left(M^2_W + 2\vec{P}^T_{l^{\pm}_{\rm W}} \cdot \vec{P}^T_{\nu} \right) \pm |\vec{P}_{l^{\pm}_{\rm W}}| \sqrt{\left(M^2_W + 2\vec{P}^T_{l^{\pm}_{\rm W}} \cdot \vec{P}^T_{\nu} \right)^2 - 4P^{T\ 2}_{l^{\pm}_{\rm W}} P^{T\ 2}_{\rm miss}} \right] \end{aligned} \tag{5.3}$$

where $l^{\pm}_W$ is the charged lepton from the W-decay.

5.1.2 Reconstructing the WV system mass

The two-fold ambiguity arising in the reconstruction of the neutrino longitudinal momentum results in two solutions for the WV system mass,[1] $M_{\rm WV}$. When extracting anomalous coupling limits, this has no profound consequence aside from a reduction in sensitivity since the effect of the ambiguity is easily accounted for by also including the wrong-solutions in the reference Monte Carlo distributions to which the experimental data is compared.

The situation is different when attempting to measure the energy dependence of anomalous couplings. For on-shell diboson production, the relevant scale for the TGC vertex is the WV system invariant mass, and so the measurement of anomalous couplings as a function of $M_{\rm WV}$ will be the goal. This is made difficult by the existence of two mass solutions ($M_{\rm Sol1}, M_{\rm Sol2}$) for each event. Of the two solutions, one may be considered the truth solution, $M_{\rm Truth}$ and the other the incorrect solution $M_{\rm WrongSolution}$. Experimentally there is no way to ascertain which solution is the

[1] The $l^{\pm}, P^T_{\rm miss}$ signature arising from a W-decay always has one or two solutions if the momenta are perfectly reconstructed. However, detector resolution effects and the contributions from backgrounds means that in practice there will be many cases in which a $l^{\pm}, P^T_{\rm miss}$ signature does not have any solution (i.e. the discriminant of Eq. 5.3 is negative).

truth, and so $M_{\rm Truth}$ and $M_{\rm WrongSolution}$ are not observable quantities. However, with a Monte Carlo simulation, the correct solution is known, and so the simulation may be used to evaluate an effective estimator for $M_{\rm Truth}$.

For proton-antiproton collisions (such as at the Tevatron), the valence quarks dominate the interaction and the radiation zero conspires with the structure functions to give a preferred direction for P_ν^z. The correct solution may be obtained 73% of the time by simply choosing the forward (i.e. $\max(P^z_{\nu\,\rm Sol1}, P^z_{\nu\,\rm Sol2})$) neutrino solution for $W^+\gamma$ production, and the backward ($\min(P^z_{\nu\,\rm Sol1}, P^z_{\nu\,\rm Sol2})$) neutrino solution for $W^-\gamma$ production [Tev95]. The situation is different for symmetric pp beam colliders such as the LHC.

The diboson production differential cross section falls exponentially with increasing $M_{\rm WV}$, and so the smaller of the two solutions

$$M_{\rm Min} \;=\; \min(M_{\rm Sol1}, M_{\rm Sol2}) \tag{5.4}$$

is more probable. The correlations between $M_{\rm Min}$ and $M_{\rm Truth}$ have been studied in Ref. [DeF00]. The quantities are found to be highly correlated under LHC conditions, but there has been no evaluation of the effect on the confidence limits of using an estimator like $M_{\rm Min}$. One might expect the differences to be more pronounced for the confidence limits than in the distributions, since the limits derive a large portion of their sensitivity from the high mass region, and an estimator like $M_{\rm Min}$ is biased towards low masses. It will be shown in this section that this is not the case.

The average of the two solutions is another estimator. Two definitions may be used for the distribution arising from this estimator, which has caused some confusion in the literature. The average value

$$M_{\rm Ave} = \frac{M_{\rm Sol1} + M_{\rm Sol2}}{2} \tag{5.5}$$

may be histogrammed or each solution may be included in the histogram with half weight

$$M_{\rm BothSolutions}: \text{ histogram } M_{\rm Sol1},\ M_{\rm Sol2} \text{ each with weight } \frac{1}{2}. \tag{5.6}$$

The cluster transverse mass is a directly observable estimator which does not rely

	Unobservable	
	M_{Truth}	the 'true' solution
	$M_{\text{WrongSolution}}$	the 'incorrect' solution
	Reconstructible without assumptions	
(Eq. 5.7)	M_{Tran}	$(l_W V; P^T_{\text{miss}})$ cluster transverse (or minimum) mass
	Reconstructible with assumptions of Eqs. 5.1 and 5.2	
	$M_{\text{Sol1}}, M_{\text{Sol2}}$	two solutions from the two-fold ambiguity in neutrino longitudinal momentum, Eq. 5.3
(Eq. 5.4)	M_{Min}	smaller of the two solutions above
(Eq. 5.5)	M_{Ave}	average of the two solutions above
(Eq. 5.6)	$M_{\text{BothSolutions}}$	each of two solutions above is given weight $\frac{1}{2}$

Table 5.1: The WV system mass estimators are tabulated.

on the assumptions of Eqs. 5.1 and 5.2,

$$M_{\text{Tran}}(l^{\pm}_W V; P^T_{\text{miss}}) \;=\; \sqrt{\left(\sqrt{M^{\text{inv}}(l^{\pm}_{\text{W}}\text{V})^2 + |\vec{P}^T_{\text{V}} + \vec{P}^T_{l^{\pm}_{\text{W}}}|^2} + P^T_{\text{miss}}\right)^2 - \left|\vec{P}^T_{\text{V}} + \vec{P}^T_{l^{\pm}_{\text{W}}} + \vec{P}^T_{\text{miss}}\right|^2} \tag{5.7}$$

where $M^{\text{inv}}(l^{\pm}_{\text{W}}\text{V})$ is the invariant mass of the $l^{\pm}_W$, V system. The M_{Tran} estimator represents the minimum invariant mass of the $V, l^{\pm}_W, \vec{P}^T_{\text{miss}}$ cluster, and so it is always smaller than M_{Truth}.

For the convenience of the reader, the various definitions of the WV system mass estimators are enumerated in Table 5.1.

In order to evaluate the effectiveness of the estimators, the mass resolution is defined $M_{\text{Truth}} - M_{\text{Reconstructed}}$, where $M_{\text{Reconstructed}}$ is any of the estimators of Table 5.1. These distributions are shown in Figure 5.1. A non-zero mean indicates a bias, whereas the root-mean-square is an indicator of the estimator resolution. The distributions for high P^T_γ events have been checked and are similar to what is presented in Figure 5.1.

The $M_{\text{WrongSolution}}$ resolution represents the case where the incorrect mass is chosen

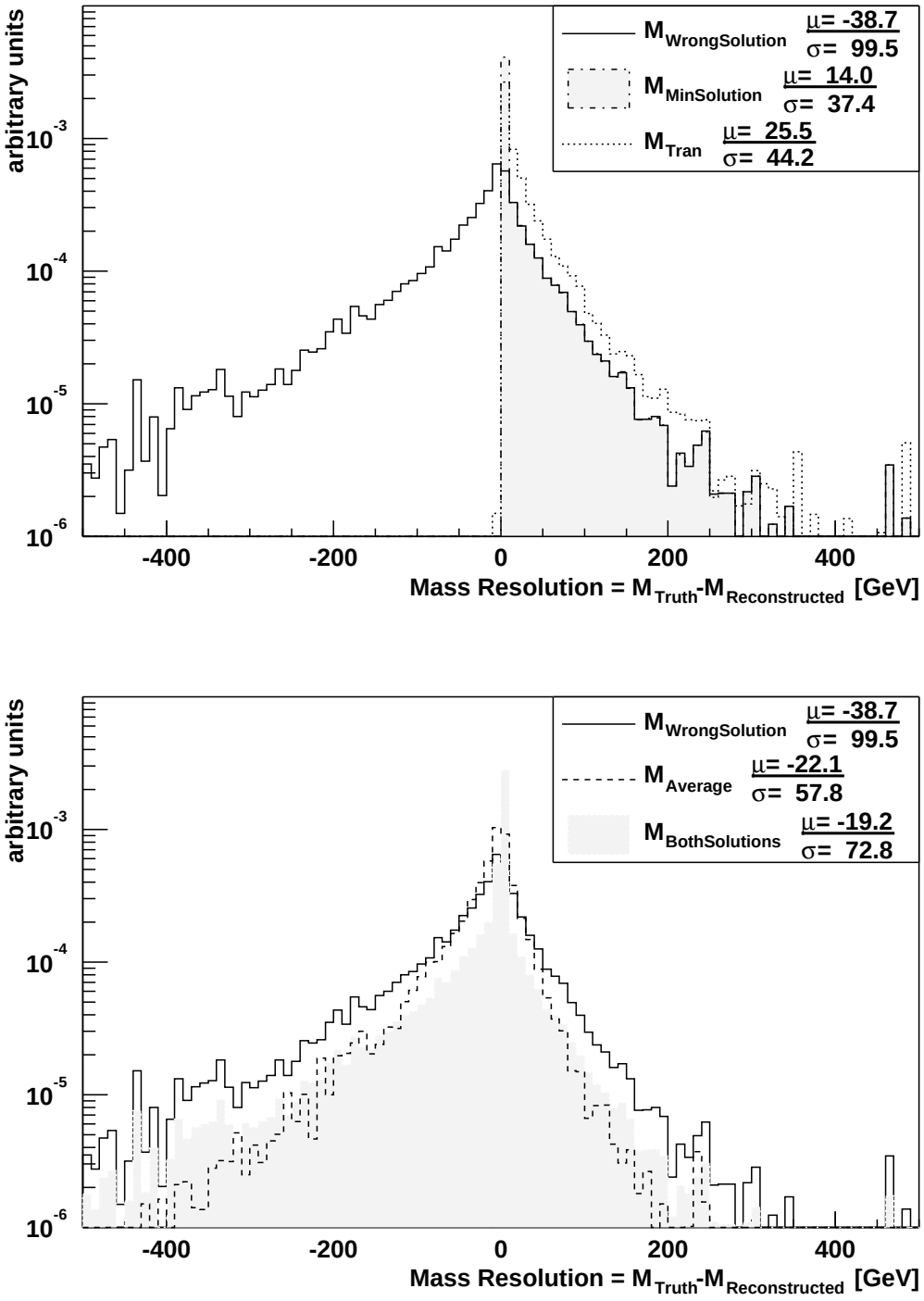

Figure 5.1: The mass resolution for the WV system invariant mass estimators of Table 5.1 are shown. The mean and root-mean-square (μ and σ, in GeV) of each distribution are printed in the legend. The event sample is $pp \rightarrow W^{+}(\rightarrow l^{\pm}\nu)\ \gamma$ generated using the BHO NLO generator at the parton level with no detector smearing or backgrounds.

every time, and so reflects the worse case situation when the mass is reconstructed using the assumptions of Eqs. 5.1 and 5.2. Whenever the true mass is the larger of the two solutions, $M_{\rm Min}$ corresponds precisely to $M_{\rm WrongSolution}$, and so the two distributions coincide in the positive resolution region. Being the minimum solution, $M_{\rm Min}$ is biased towards small mass values. The average mass $M_{\rm Ave}$ is biased towards large reconstructed mass values because the relative probability of the larger mass solution is usually considerably smaller than for the small mass solution. In the positive mass resolution region of Figure 5.1, the transverse mass $M_{\rm Tran}$ resolution is considerably worse than the $M_{\rm WrongSolution}$ or $M_{\rm Min}$ resolutions. The $M_{\rm BothSolutions}$ distribution appears narrower than any other in the central region of Figure 5.1, but suffers from long tails, resulting in a large root-mean-square.

The best resolution is obtained from the $M_{\rm Min}$ estimator, which has a root-mean-square of about 35 GeV. This estimator is biased, but the bias is similar or smaller than the biases from other estimators. As such, $M_{\rm Min}$ is a good choice for evaluating the WV system mass. It is also necessary to evaluate the effect the use of an estimator such as this has on the confidence limits, which is the subject of the next section.

5.1.3 WV system mass estimator sensitivity to anomalous couplings

The relative sensitivity of the various estimators to anomalous couplings are presented in Table 5.2 for the specific case of LHC $W^+\gamma$ production. The relative sensitivity is quantified using the anomalous TGC statistical 95% confidence intervals for the different mass estimators normalized to the anomalous TGC 95% confidence intervals derived from the $P_{\rm V}^T$ distribution, which is the observable normally used to extract anomalous coupling limits at hadron colliders. Methods for extracting the confidence intervals will be described in the sections which follow, for the present discussion it is enough to know that a larger value indicates the distribution of the estimator is less sensitive to the anomalous TGC. A value of one indicates the estimator has the same sensitivity to the anomalous TGC as does the $P_{\rm V}^T$ distribution. These sensitivities are derived at the parton level without detector smearing or backgrounds, and thus

should be regarded as indicators of the distribution sensitivities only.

	Relative Sensitivity	
Distribution	λ_γ	$\Delta\kappa_\gamma$
M_{Truth}	1.53	1.11
$M_{\text{WrongSolution}}$	1.58	1.07
M_{Tran}	1.39	1.02
M_{Min}	1.45	1.05
M_{Ave}	1.53	1.03
$M_{\text{BothSolutions}}$	1.63	1.14

Table 5.2: The relative sensitivity to anomalous TGC's of the WV system mass estimators enumerated in Table 5.1 are shown for LHC $W\gamma$ production.

The sensitivity does not depend strongly on the choice of estimator for the WV system mass. Indeed, the limits on anomalous couplings derived from $M_{\text{WrongSolution}}$ differ by only 4% from the M_{Truth} distribution. The M_{Tran} and M_{Min} estimators provide similar sensitivity, while limits derived using distributions obtained from averages (M_{Ave} and $M_{\text{BothSolutions}}$) are slightly worse.

This implies that a distribution such as M_{Tran} which is reconstructible event by event without assumptions, is a good choice for extracting limits on anomalous couplings. For measuring the energy dependence of the couplings, the resolution and bias are important considerations since the M_{WV} is used primarily as a kinematic cut and the confidence limits on anomalous couplings are extracted using other distributions. Thus an estimator with good resolution such as M_{Min} is preferred, and will be used in this study for such purposes.

5.2 Observing the Radiation Zero at LHC

The radiation zero has been discussed in Section 3.3, where it was suggested that the 'signed' rapidity separation (see Eq. 3.13) of the photon from the charged lepton arising in the $W^\pm$ decay would be the best distribution for observing this electroweak effect at the LHC. In this section the relevant distributions are presented for 30 fb^{-1} of LHC data, so as to evaluate the prospects for observing this Standard Model signature at ATLAS.

The kinematic cuts for this part of the analysis are identical to those of the TGC analysis, with one exception. The transverse momentum for the jet veto is made more stringent, $P_{\text{jet}}^T < 30$ GeV, as compared to the $P_{\text{jet}}^T < 100$ GeV veto which is used for the TGC analysis. This change is imposed because the radiation zero is a leading order effect, and so hard central jets tend to 'fill in' the radiation zero, masking its signature. The stringent jet veto effectively recovers the leading order behavior.

In Figure 5.2 the signed and unsigned $W\gamma$ production rapidity separation distributions are shown for an integrated luminosity of 30 fb^{-1} from one simulated ATLAS experiment. This data has been simulated using SM TGC parameters, and includes the background contributions. The radiation zero is already evident in the unsigned distribution. In addition, for the signed distribution, the characteristic radiation zero asymmetry is also visible. Using 30 fb^{-1} of integrated luminosity, the radiation zero will be observable at LHC.

5.3 Methods for Extracting Anomalous Couplings

The conventional method for measuring TGC's at hadron colliders has been a maximum likelihood fit to the transverse momentum distribution of one of the gauge-bosons P_{V}^T. The reason for this is twofold: (1) the P_{V}^T distribution is sensitive to both angular and energy information, and so is very sensitive to anomalous TGC's (2) the P_{V}^T distribution is reconstructible without any assumptions or ambiguities.

In this section several different methods for deriving anomalous TGC measurements and confidence intervals are described, and their statistical sensitivity to the anomalous TGC parameters is studied. A discussion of the results and a comparison of the methods will be presented after the systematic uncertainties are addressed in the following section.

5.3.1 Inclusive event rate

The diboson production matrix elements depend linearly on the anomalous TGC parameters, which results in a quadratic dependence for the event rate. For example,

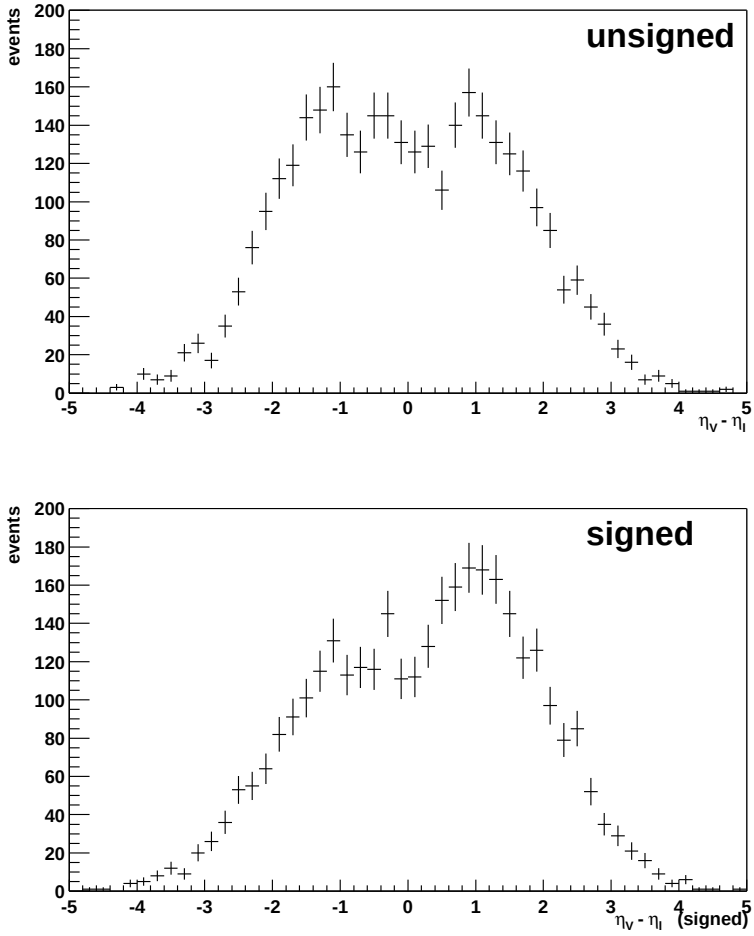

Figure 5.2: The rapidity separation (top) of the photon from the charged lepton is shown for $W\gamma$ production at the LHC. For the bottom distribution the rapidity separation has been 'signed' according to Eq. 3.13. The kinematic cuts of Chapter 4 have been applied, with the exception of the jet veto, for which the transverse momentum is changed to $P_{\text{jet}}^T < 30$ GeV. The points with error bars represent "mock" data for one ATLAS experiment with integrated luminosity of 30 fb^{-1}. This data has been simulated using the SM TGC parameters, and includes the background contributions.

the $W\gamma$ cross section can be written

$$\sigma^{p\overset{(-)}{p}\to W\gamma}(\Delta\kappa_\gamma, \lambda_\gamma) \;=\; \sigma_{00} + \Delta\kappa_\gamma\sigma_{0\kappa} + \lambda_\gamma\sigma_{0\lambda} + \lambda_\gamma \cdot \Delta\kappa_\gamma\sigma_{\lambda\kappa} + \Delta\kappa_\gamma^2\sigma_{\kappa\kappa} + \lambda_\gamma^2\sigma_{\lambda\lambda}. \quad (5.8)$$

In this notation, the Standard Model cross section is σ_{00}. By comparing the observed number of events to the expected event rate, the degree of compatibility with the Standard Model can be ascertained and limits can be set on the anomalous TGC parameters. This is one of the methods which has been used by the UA2 collaboration in Ref. [UA2 92].

While the fully inclusive cross section is sensitive to the anomalous TGC's, the sensitivity at hadron colliders is washed out by the low $P_{\rm V}^T$ region, where the cross section is large, and the effects of anomalous TGC's are small. For this reason, a considerable advantage can be obtained by introducing kinematic cuts restricting the measurement to the high $P_{\rm V}^T$ region. This has been studied for $W\gamma$ and WZ production at ATLAS in Ref. [Atl94b], where it has been shown that statistical limits comparable (within about a factor 1.5) to what will be presented in this thesis can be obtained. The primary disadvantage of the event rate measurement technique is that the results depend directly on the overall normalization, and thus are very sensitive to systematic uncertainties such as the luminosity measurement, the theoretical knowledge of higher order QCD corrections, and the internal proton structure. The uncertainty in the luminosity may be as high as 10% at LHC, NNLO corrections have yet to be calculated and are expected to be large at high transverse momentum due to the opening of the gg channel, and our knowledge of the structure functions is at about the 2-5% level. For these reasons, competitive limits on the anomalous TGC's using this technique would be very difficult, and would certainly require a significant improvement in theoretical modeling of the diboson processes. Systematic effects such as these were not taken into account for the limits reported in Ref. [Atl94b]. A further disadvantage of the technique is that if non-standard results are observed, it gives very little information as to where the source of the deviation comes from, and thus would make disentangling the contributions from the various anomalous TGC's difficult. This method is not a promising avenue for establishing confidence limits on

the anomalous TGC's, and is not explored further here.

5.3.2 Parameter estimation with binned maximum likelihood

Measurements of the anomalous couplings can be made by comparing the experimentally observed spectrum of a kinematic observable (such as the transverse momentum of one of the gauge-bosons, $P_{\rm V}^T$) to Monte Carlo reference distributions which are known as a function of the anomalous TGC parameters.

The maximum likelihood method provides a measure for parameter estimation.[2] In our study, the parameters of interest are the anomalous TGC's: $\Delta g_V^1,\ \Delta\kappa_V,\ \lambda_V$. Taking the $P_{\rm V}^T$ distribution as an example, the joint probability density for the data is

$$Ł(\Delta g_V^1, \Delta\kappa_V, \lambda_V) \ = \ \prod_{i=1}^{N} \mathcal{P}(P_{{\rm V}\,i}^T; \Delta g_V^1, \Delta\kappa_V, \lambda_V) \tag{5.9}$$

where the product runs over all events, $\mathcal{P}(P_{{\rm V}\,i}^T; \Delta g_V^1, \Delta\kappa_V, \lambda_V)$ is the probability of an event with $P_{\rm V}^T = P_{{\rm V}\,i}^T$ occurring given the parameters $\Delta g_V^1,\ \Delta\kappa_V,\ \lambda_V$ (i.e. "the probability of $P_{{\rm V}\,i}^T$ given $\Delta g_V^1,\ \Delta\kappa_V,\ \lambda_V$"), and $Ł(\Delta g_V^1, \Delta\kappa_V, \lambda_V)$ is the likelihood.

The maximum likelihood estimate for the parameters $\Delta g_V^1,\ \Delta\kappa_V,\ \lambda_V$ is defined by

$$\frac{\partial^3 \ln Ł(\Delta g_V^1, \Delta\kappa_V, \lambda_V)}{\partial g_V^1\ \partial\kappa_V\ \partial\lambda_V} \ = \ 0. \tag{5.10}$$

Eq. 5.10 will have a unique solution if an efficient estimator for the parameters exists (see Ref. [Ead71] for a proof).

In the case where the data is binned in a histogram (as for this study), Eq. 5.9 is modified

$$Ł(\Delta g_V^1, \Delta\kappa_V, \lambda_V) \ = \ \prod_{i=1}^{\#\ \text{bins}} \Big[\mathcal{P}(P_{{\rm V}\,i}^T; \Delta g_V^1, \Delta\kappa_V, \lambda_V)\Big]^{N_i} \tag{5.11}$$

where the sum runs over all bins in the histogram, N_i is the number of entries in bin number i, and $P_{{\rm V}\,i}^T$ is the $P_{\rm V}^T$ for bin number i. Parameter estimation from binned

[2]The maximum likelihood method is an excellent means of parameter estimation, but is not a sensible test for goodness-of-fit. This is because of the underlying assumption that the independently measured quantities x_i (the data) arose from the probability distribution function $f(x, \alpha)$, where α are the parameters to be estimated. This means an accurate modeling of $f(x, \alpha)$ is assumed, and the maximum likelihood method does not provide any information as to whether or not this is true.

Confidence Limit	1 parameter	2 parameter
68.27%	1 σ	1.52 σ
90. %	1.64 σ	2.15 σ
95. %	1.96 σ	2.49 σ
99. %	2.58 σ	3.03 σ

Table 5.3: The relationship between the percent confidence intervals and the number of standard deviations σ for one and two parameter maximum likelihood estimates is tabulated. Refer to Ref. [PDG00a] for more detailed tables.

distributions using this likelihood is referred to as the binned maximum likelihood method.

For TGC studies, the number of parameters may be reduced by arbitrarily setting some of the parameters to their Standard Model values. When only one anomalous TGC parameter is left free in the estimation, this is referred to as a one-parameter estimate.

The maximum likelihood method can be used to derive confidence intervals. In the limit of large statistics, the likelihood Ł is Gaussian and the s standard deviation forms a contour in the parameter space such that

$$-\ln Ł_{s \text{ std. dev.}} = -\ln Ł_{\text{MAX}} + \frac{s^2}{2} \tag{5.12}$$

where $-\ln Ł_{\text{MAX}}$ is the solution to Eq. 5.10. Refer to Table 5.3 for the relationship between standard deviation and the percentage confidence limits.

In Figure 5.3 the transverse momentum distribution of the photon in $W\gamma$ production is shown, after applying the kinematic cuts described in Chapter 4. The points with error bars represent "mock" data for one ATLAS experiment with integrated luminosity of 30 fb^{-1}. This data has been simulated using the SM TGC parameters, and includes the background contributions. The "mock" data histogram is constructed by sampling each bin according to a Poisson distribution with the mean given by the relevant bin content of the SM reference histogram. The lines in Figure 5.3 (bottom) are the reference distributions (i.e. theoretical expectation) for several choices of the anomalous TGC parameters. The contribution of backgrounds to the reference distributions is shown as a shaded histogram, and does not depend

on the anomalous TGC parameters. The one and two parameter negative log likelihood curves are shown as a function of the λ_γ and $\Delta\kappa_\gamma$ parameters with the 68, 90, and 95% confidence limits indicated. These confidence limits correspond to the single experiment which has been simulated for this figure. When another ATLAS experiment is simulated, the confidence limits will be different, on account of statistical fluctuations (indeed it is the sensitivity of the distribution to these fluctuations which the likelihood method measures). If many such experiments are simulated, only 68% of the simulated experiments will yield results which are consistent with the input parameters (SM couplings in this case) to within one standard deviation. In order to obtain the best estimate of the limits that will be achieved at ATLAS, it is necessary to average the confidence limits over many simulated ATLAS experiments (the limits tabulated here are averaged over 5000 simulated experiments). The fluctuation in these confidence limits represents the confidence with which the confidence limits are known (or the *error on the error*), and is not studied here.

The P_{V}^T distribution is very sensitive to the anomalous TGC's because it projects out central production angles and large diboson invariant masses. In Figure 5.4 the transverse mass distribution for WZ production is shown (refer to Table 5.1 for the definition), which is a directly observable quantity that is sensitive mostly to the energy dependence of the anomalous couplings. A distribution which is sensitive to the gauge-boson helicity states is the transverse momentum of the lepton in $W\gamma$ production, which is shown in Figure 5.5.

The spread in the statistical 95% confidence limits for several distributions are compared in Table 5.4. Not all of the distributions which have been studied in Table 5.4 are shown in the figures of this chapter. Those which have not been shown have been included in the appendix. For the λ_V and g_V^1 couplings, the P_{V}^T distribution always provides the best statistical limits. For $\Delta\kappa_V$, competitive confidence limits can be derived with any of the diboson mass or transverse momentum distributions. The confidence limits including systematic effects for each of these distributions will be compared in Section 5.6.

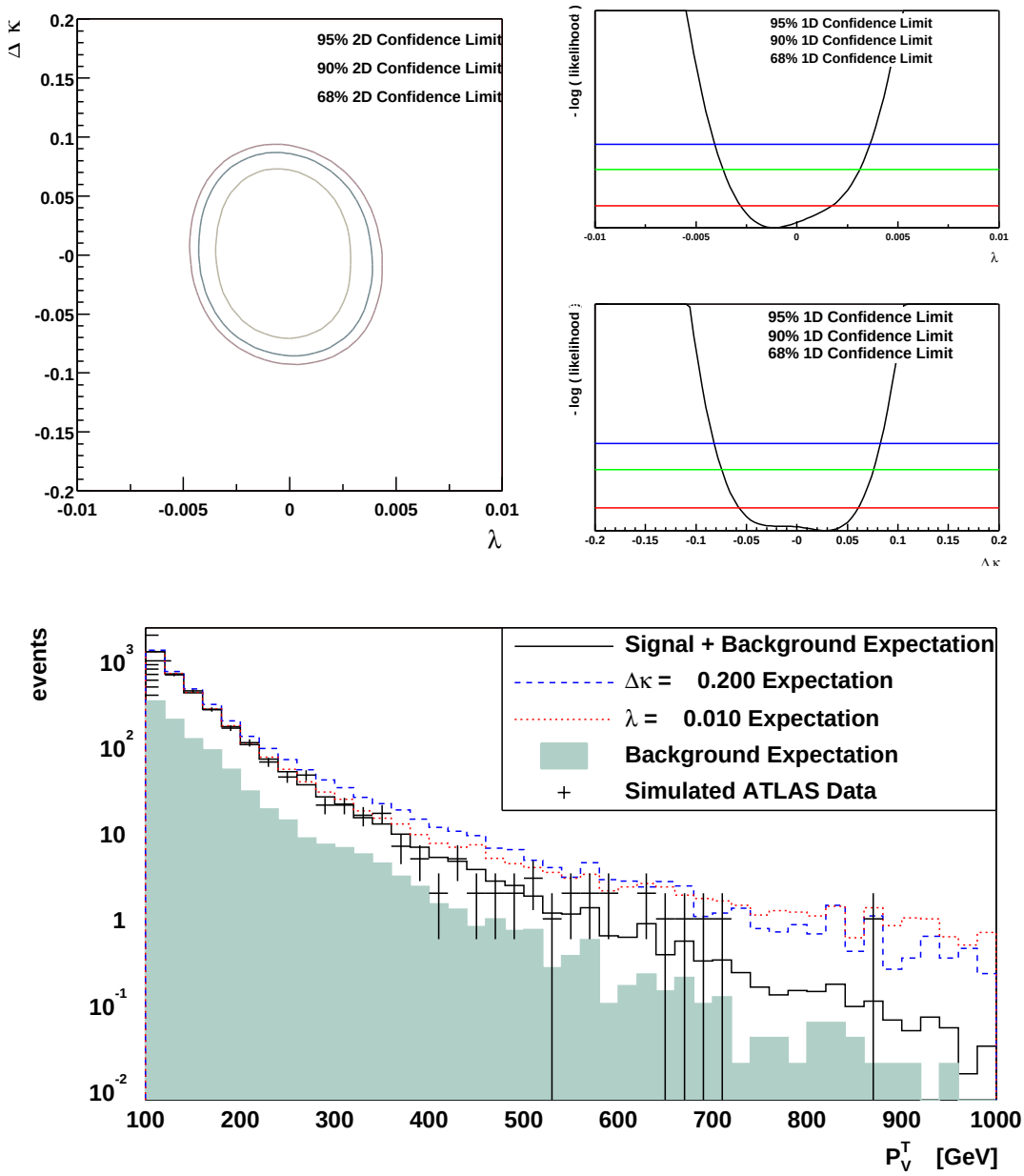

Figure 5.3: The transverse momentum distribution of the photon in $W\gamma$ production is shown (bottom), after applying the kinematic cuts described in Chapter 4. The points with error bars represent "mock" data for one ATLAS experiment with integrated luminosity of 30 fb^{-1}. This data has been simulated using the SM TGC parameters, and includes the background contributions. The lines are the reference distributions for several choices of the anomalous TGC parameters. The contribution of backgrounds to the reference distributions is shown as a shaded histogram, and does not depend on the anomalous TGC parameters. The one (top right) and two (top left) parameter negative log likelihood curves are shown as a function of the λ_γ and $\Delta\kappa_\gamma$ parameters with the 68, 90, and 95% confidence limits indicated. These confidence limits correspond to the single experiment which has been simulated for this figure.

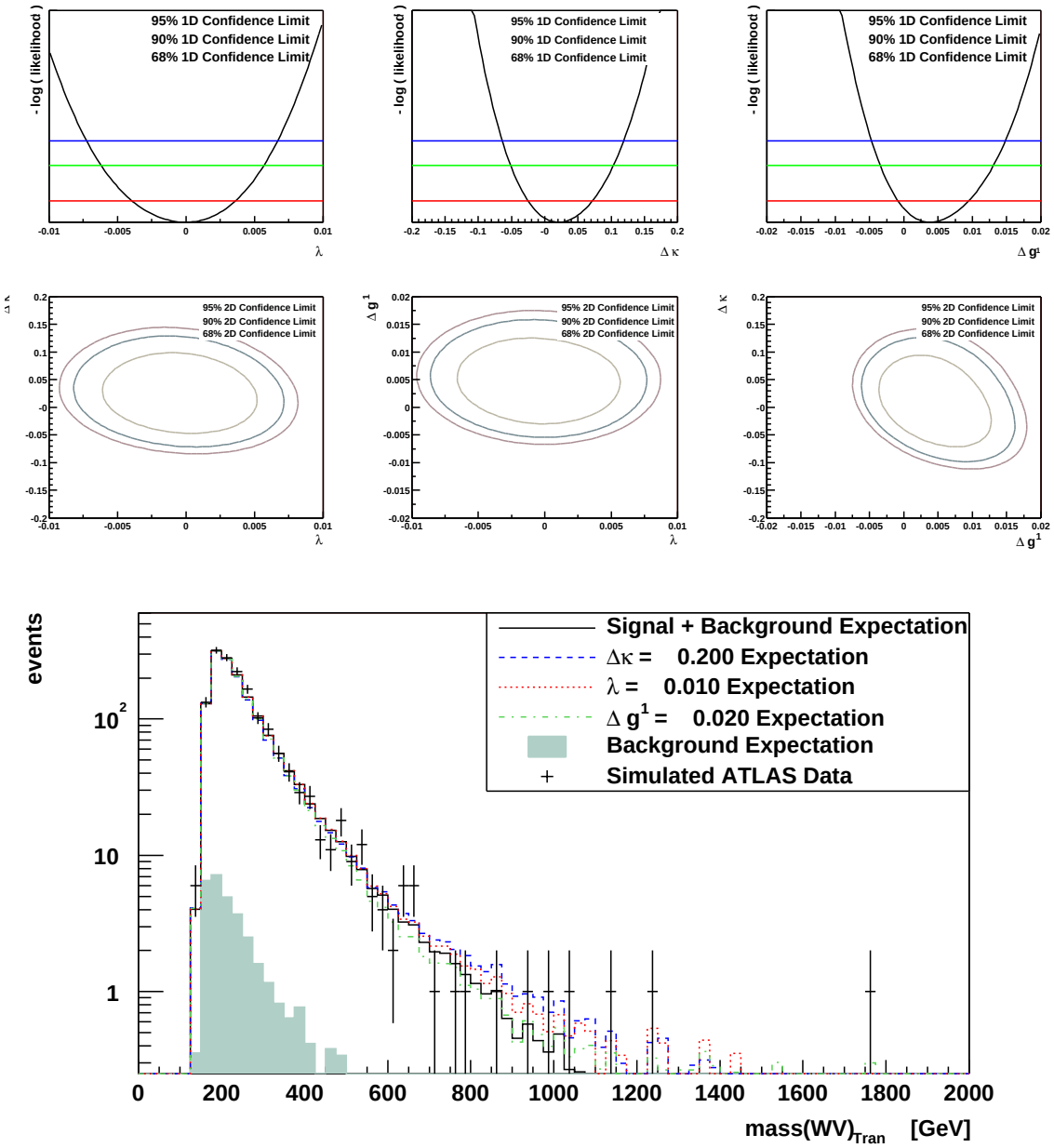

Figure 5.4: The transverse mass distribution in WZ production is shown (bottom), after applying the kinematic cuts described in Chapter 4. The points with error bars represent "mock" data for one ATLAS experiment with integrated luminosity of 30 fb^{-1}. This data has been simulated using the SM TGC parameters, and includes the background contributions. The lines are the reference distributions for several choices of the anomalous TGC parameters. The contribution of backgrounds to the reference distributions is shown as a shaded histogram, and does not depend on the anomalous TGC parameters. The one (top three plots) and two (middle three plots) parameter negative log likelihood curves are shown as a function of the λ_Z, $\Delta\kappa_Z$, and Δg_Z^1 parameters with the 68, 90, and 95% confidence limits indicated. These confidence limits correspond to the single experiment which has been simulated for this figure.

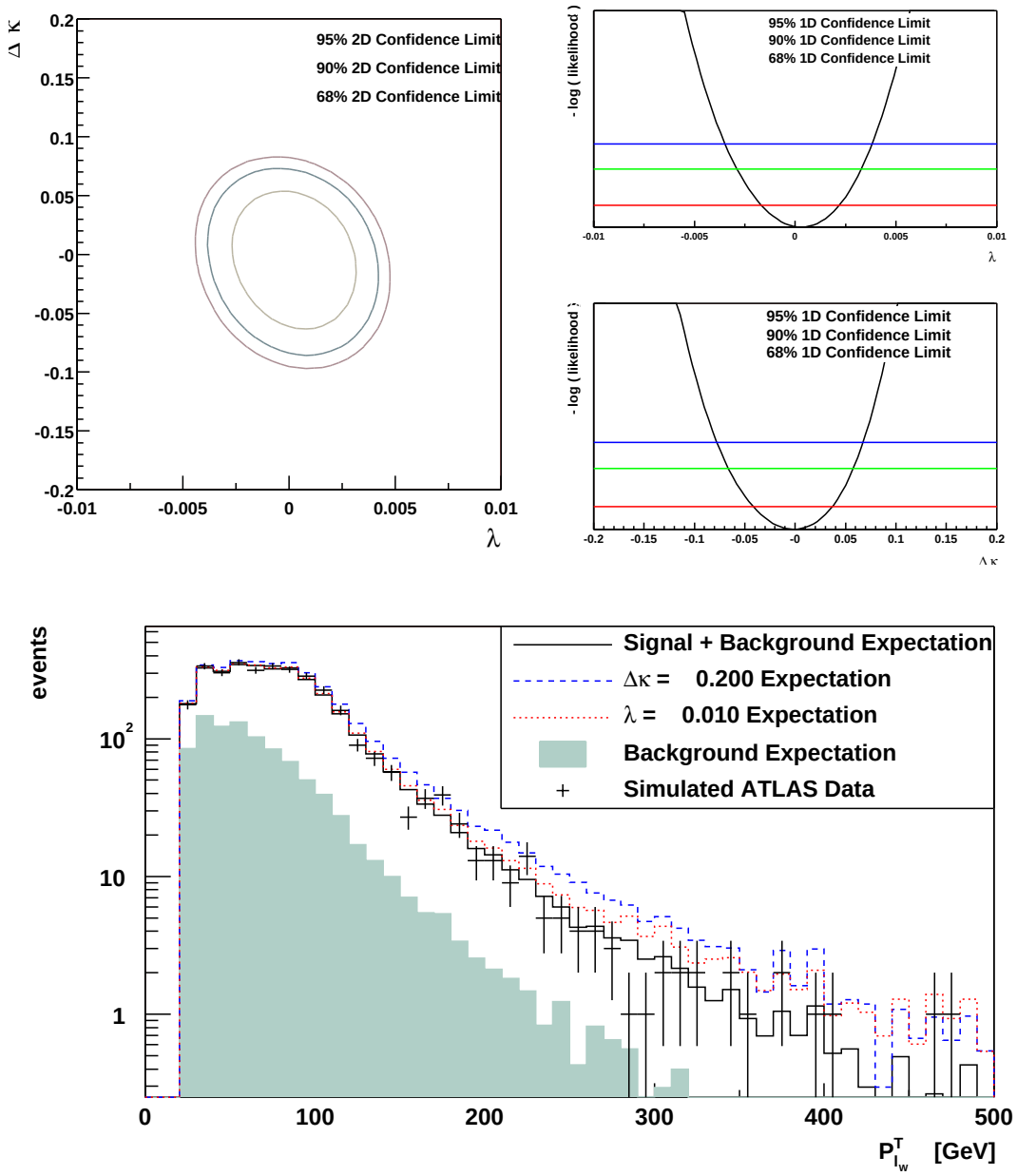

Figure 5.5: The transverse momentum distribution of the charged lepton in $W\gamma$ production is shown (bottom), after applying the kinematic cuts described in Chapter 4. The points with error bars represent "mock" data for one ATLAS experiment with integrated luminosity of 30 fb^{-1}. This data has been simulated using the SM TGC parameters, and includes the background contributions. The lines are the reference distributions for several choices of the anomalous TGC parameters. The contribution of backgrounds to the reference distributions is shown as a shaded histogram, and does not depend on the anomalous TGC parameters. The one (top right) and two (top left) parameter negative log likelihood curves are shown as a function of the λ_γ and $\Delta\kappa_\gamma$ parameters with the 68, 90, and 95% confidence limits indicated. These confidence limits correspond to the single experiment which has been simulated for this figure.

	Spread in Statistical 95% Confidence Interval				
Distribution	λ_γ	$\Delta\kappa_\gamma$	λ_Z	$\Delta\kappa_Z$	Δg_Z^1
P_V^T	0.0066	0.15	0.013	0.24	0.016
$P_{\mathrm{l}_W}^T$	0.0094	0.19	0.017	0.21	0.018
P_{miss}^T	0.0099	0.17	0.017	0.23	0.019
$\mathrm{mass(WV)}_{Both\ Sol.}$	0.011	0.20	0.019	0.26	0.023
$\mathrm{mass(WV)}_{Min}$	0.0094	0.17	0.017	0.22	0.020
$\mathrm{mass(WV)}_{Tran}$	0.0086	0.16	0.016	0.22	0.018
$\eta_{\mathrm{V}} - \eta_{\mathrm{l}}$	0.032	0.17	0.056	0.34	0.075
$\cos\theta^*(V)_{Ave}$	0.029	0.36	0.043	0.24	0.055

Table 5.4: Spread in the 95% statistical confidence intervals for various one dimensional distributions derived with the binned maximum likelihood method. An integrated luminosity of 30 fb^{-1} at the LHC has been assumed. The definition of the various distributions are summarized in Table 5.17.

5.3.3 Parameter estimation with multi-dimension maximum likelihood

In the previous section, the anomalous TGC's were estimated using a projection of the event kinematic configurations onto a single distribution. Instead, one can extract more information about the data by using the maximum likelihood method with multi-dimensional histograms.

The limiting factor in extrapolating to higher dimensional fits is the computer time required to generate the reference distributions. If each histogram dimension has N bins, and there are d dimensions, then the computational time scales as N^d. The computer time[3] necessary to generate adequate statistics for one dimensional histograms is the order of a day (this includes generating millions of events using the NLO matrix elements, hadronizing the events—which consumes most of the computer time, and fast simulation in the detector). Since each histogram dimension might typically be divided into 50 bins, the amount of computer time necessary in moving from 1 to 2 dimensional histograms becomes cumbersome, and the computer time for 3 dimensions is unreasonable ($\geq$ 1 year).

In order to produce reference histograms for two dimensional distributions in a reasonable amount of time, the number of bins in each dimension is reduced. Thus

[3]The computer times quoted here are for a 650 MHz Pentium III processor.

	Spread in Statistical 95% Confidence Interval				
Distribution	λ_γ	$\Delta\kappa_\gamma$	λ_Z	$\Delta\kappa_Z$	Δg_Z^1
P_V^T vs. $P_{\mathrm{l}_W}^T$	0.0068	0.14	0.013	0.23	0.016
$\mathrm{mass(WV)}_{Tran}$ vs. $\lvert\eta_\mathrm{V} - \eta_\mathrm{l}\rvert$	0.0069	0.13	0.014	0.18	0.014
$\mathrm{mass(WV)}_{Both\ Sol.}$ vs. $\cos\theta^*(V)_{Ave}$	0.0070	0.13	0.014	0.16	0.014

Table 5.5: The spread in the 95% statistical confidence intervals for various two dimensional distributions are derived with the binned maximum likelihood method. An integrated luminosity of 30 fb^{-1} at the LHC has been assumed. The definition of the various distributions are summarized in Table 5.17.

increasing the number of dimensions in the fit is a tradeoff: sensitivity is gained because of the information contained in the extra dimension, and sensitivity is lost because of the reduced granularity in the binning of each dimension.

An example of parameter estimation using a two-dimensional maximum likelihood is shown in Figure 5.6, where the angular and energy degrees of freedom are projected out separately in a 2 dimensional histogram of the diboson invariant mass (reconstructed using both solutions, as in Eq. 5.6) versus the reconstructed center-of-mass frame photon production angle (as for the invariant mass, the center-of-mass reconstruction has two solutions, and both solutions are included in the histogram).

The spread in the statistical 95% confidence limits for several two dimensional distributions are compared in Table 5.5. Those distributions which are included in Table 5.5 but have not been shown in the figures of this chapter have been included in the appendix.

5.3.4 Optimal Observables

Certain kinematic observables are more sensitive to anomalous TGC's than others, because these distributions are able to project out more information which is relevant for the couplings. The method of Optimal Observables (OO) [Die94] attempts to project onto a single variable the kinematic information which is most sensitive to a particular anomalous TGC parameter. This method has been used extensively by the LEP collaborations for TGC measurements [Ale01, Opa01, L3 99, Del99b].

Optimal Observables have not previously been applied to TGC studies in hadronic

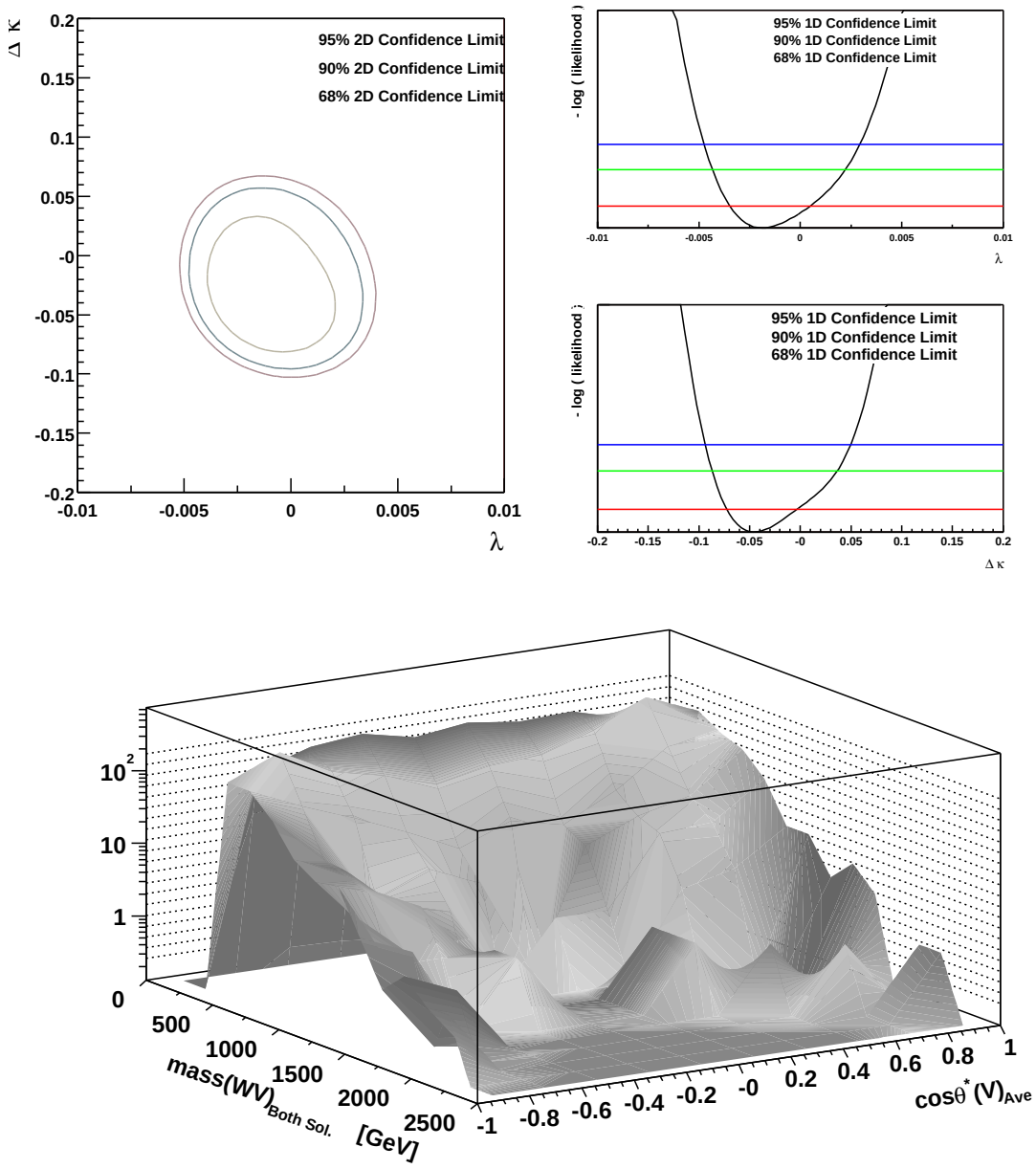

Figure 5.6: The reconstructed diboson invariant mass (both solutions, Eq. 5.6) versus the reconstructed center-of-mass frame photon production angle (both solutions are included in the histogram) for $W\gamma$ production is shown (bottom), after applying the kinematic cuts described in Chapter 4 for the Standard Model reference histogram (including contributions from backgrounds). The one (top right) and two (top left) parameter negative log likelihood curves are shown as a function of the λ_γ and $\Delta\kappa_\gamma$ parameters with the 68, 90, and 95% confidence limits indicated. These confidence limits correspond to the single experiment which has been simulated for this figure.

collisions. In this section, the OO equations for e^+e^- collisions are generalized to hadron collisions in the simplest possible way, and the sensitivity of the OO method to the anomalous TGC parameters is investigated.

Each anomalous TGC has its own OO. The OO for the λ_V parameter of a given event is

$$\mathrm{OO}(\lambda_V) \;=\; \lim_{\epsilon_{\lambda_V}\to 0} \frac{d\sigma(\mathrm{SM}+\epsilon_{\lambda_V}) - d\sigma(\mathrm{SM})}{\epsilon_{\lambda_V}\; d\sigma(\mathrm{SM})} \tag{5.13}$$

where $d\sigma$ is the differential cross section (i.e. probability) for the event to have occurred. The OO for λ_V is the relative change in the event probability when the λ_V parameter is moved from its SM value by some small amount ϵ_{λ_V}.

The differential cross section depends on the identity and kinematic configuration of all the particles involved in the reaction. For a process like $e^+e^- \to W^+W^- \to q\bar{q}'l^-\bar{\nu}$, $d\sigma$ can be directly evaluated by restricting the calculation to the leading order, and using the Born level matrix elements ($d\sigma$ appears as a ratio, so overall factors can be neglected).

For the case of hadronic $W^\pm\gamma$ production, $d\sigma$ depends on the kinematic configuration and flavor of the $q, \bar{q}', l^\pm, \nu, \gamma$ particles. This complicates the application of Optimal Observables, because there are two solutions for the neutrino momentum, the flavor of the quarks which participate in the hard subprocess is unknown, and there is a further twofold ambiguity as to whether the q ($\bar{q}'$) has origin in the forward or backward proton beam.

Yet another complication is that QCD corrections are large at hadron colliders, and the OO method derived here makes use of leading order matrix elements only.[4]

These complications will wash out the sensitivity of the Optimal Observables

[4]It is not known how to calculate a differential cross section at higher orders for a specific kinematic configuration (NLO calculations always integrate—either analytically or numerically—over a region of kinematic configurations). This means that it *is not* possible to calculate the OO using NLO matrix elements for a particular event (i.e. a particular kinematic configuration) which has been observed in a detector. However, it *is* possible to apply the OO technique using NLO matrix elements for a distribution of phase space points generated in a computer simulation (indeed OO distributions using NLO matrix elements will be shown in this section). This apparent contradiction arises because the events observed in the detector have been sampled by nature according to the "true distribution", which (at least thus far) physicists are unable to calculate, even if it is assumed they know the equations (i.e. the Standard Model) which govern this behavior. Instead an approximation is used—fixed order perturbation theory—which has the unfortunate side effect that the matrix elements may have positive (physical) and negative (unphysical) probability.

method for hadronic collisions. The goal of this study is to investigate the feasibility of the OO method in the face of these challenges.

To evaluate the OO of Eq. 5.13, the neutrino solution which gives the minimum diboson invariant mass (motivated by the study of Sec. 5.1.2) has been used, and all other ambiguities have been summed over, exactly as is normal for the calculation of event weights in a Monte Carlo event generator. The differential cross section for each $W^{\pm}\gamma$ event is

$$d\sigma \propto \sum^{\text{quark flavors}} \Big[f_{\mathrm{p}_1\to\mathrm{q}}(x,Q^2) f_{\mathrm{p}_2\to\bar{\mathrm{q}}}(x,Q^2) |\mathcal{M}^2_{\mathrm{q}\bar{\mathrm{q}}'\to\mathrm{l}^{\pm}\nu\gamma}| + f_{\mathrm{p}_1\to\bar{\mathrm{q}}}(x,Q^2) f_{\mathrm{p}_2\to\mathrm{q}}(x,Q^2) |\mathcal{M}^2_{\bar{\mathrm{q}}'\mathrm{q}\to\mathrm{l}^{\pm}\nu\gamma}| \Big] \tag{5.14}$$

where $f_{\mathrm{p_i}\to\overset{(-)}{\mathrm{q}}}(x,Q^2)$ is the structure function of the p_i beam, and reflects the probability of resolving parton $\overset{(-)}{q}$ in the beam at Bjorken momentum fraction x and scale Q. The Born level matrix element ($\mathcal{M}$) expressions of Ref. [Dix99] have been used for the evaluation of $d\sigma$.

Distributions of Optimal Observables

Since this study represents the first application of the OO technique to hadronic collisions, the theoretical OO distributions are first examined without background contributions. In Figure 5.7 the OO distributions for $W\gamma$ and WZ production at LHC are shown (using the usual kinematic cuts outlined in Chapter 4). The simulated events from which these figures are constructed were generated at NLO. The solid lines are the OO's calculated according to Eq. 5.14 which uses leading order matrix elements and the neutrino solution which gives the smallest diboson system invariant mass. These solid lines are the theoretical expectation for the OO's as defined in this thesis.

To gain an understanding of how the approximation of the event probabilities with leading order matrix elements affects the distributions, OO's derived using re-weighted NLO event weights are shown as dotted lines. Recall from Sec. 4.1.2 that the event weights from the NLO Monte Carlo simulation are tabulated as a function of the anomalous couplings for each individual event. This information is used directly

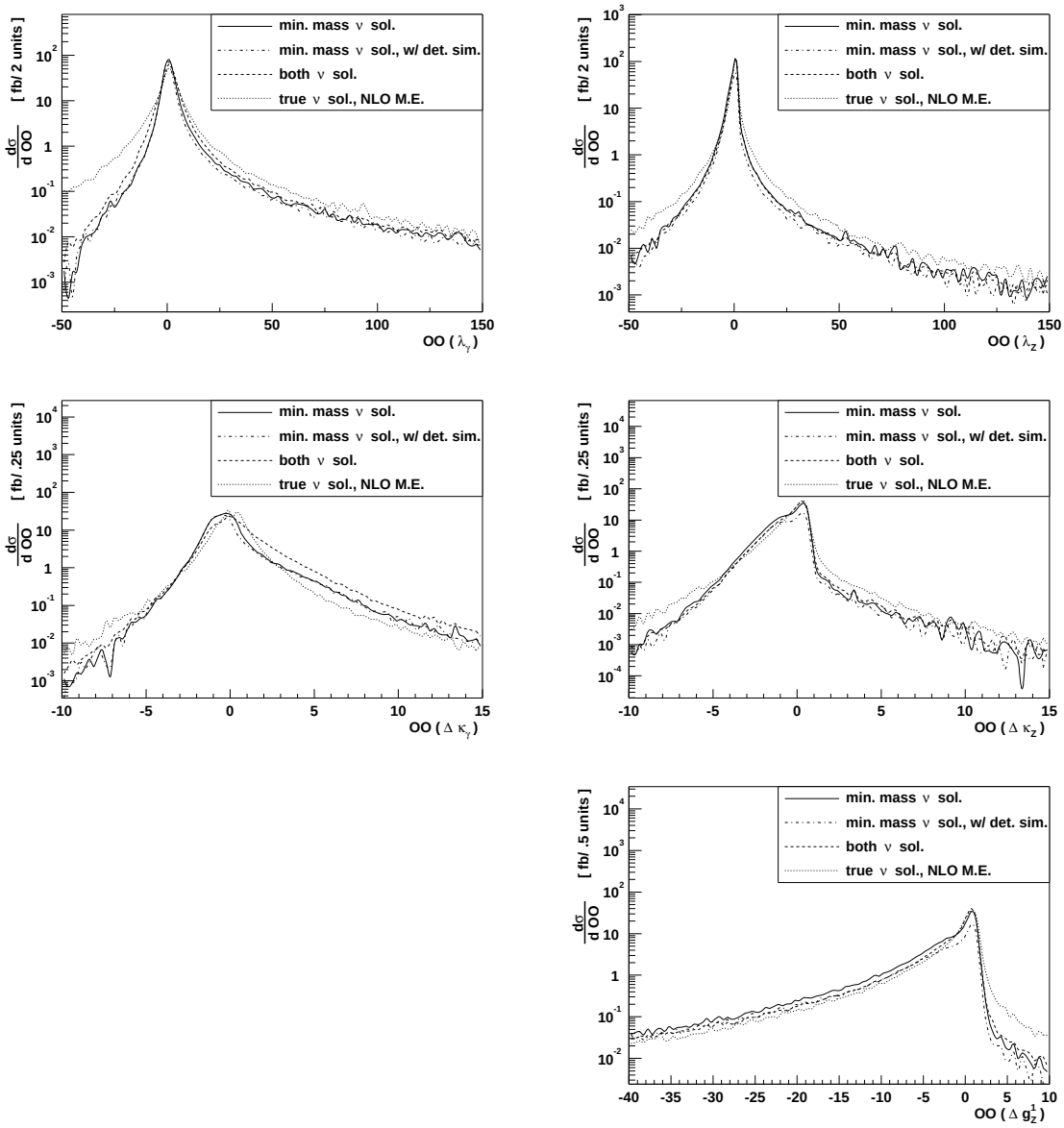

Figure 5.7: The dependence of the λ_V optimal observable (top), $\Delta\kappa_V$ optimal observable (middle), and g_V^1 optimal observable (bottom) on the assumptions used to construct the optimal observables are shown for $W\gamma$ production (left) and WZ production (right) at the LHC. The plots are described in more detail in the text. The irregularities in the tails of the distributions are caused by low Monte Carlo simulation statistics in this region, and are not physical in nature.

in Eq. 5.13 to construct the dotted lines. Note that this approach can *only be used for distributions of phase space points*, and is not applicable to individual events collected by an experiment. The general shape of the two distributions is similar, which serves as a cross-check that the equations for the OO have been properly implemented in the analysis. The quantitative difference between the two distributions is large in all cases, indicating the effect of QCD corrections on these distributions is significant.

The dashed lines in Figure 5.7 are derived using the leading order matrix elements, but both neutrino solutions are included in the histograms, each with half weight. The difference between the solid lines and the dashed lines gives an indication of the effect the two-fold ambiguity in the neutrino solution has on the distributions. The effect is most significant for the κ-type couplings in the region away from $\mathrm{OO}(\Delta\kappa_V) = 0$. This will diminish the sensitivity of these distributions to anomalous TGC's.

The sensitivity of the distributions to detector effects is small, as indicated by the dot-dashed lines in the figures, for which detector effects have been included using fast Monte Carlo detector simulation.

The effect non-standard couplings have on the OO distributions is shown in Figure 5.8. In this figure the leading order matrix elements and the neutrino solution which gives the smaller diboson mass are used (corresponds to the solid line in Figure 5.7). The anomalous TGC parameters employed for these plots have been chosen such that the effects of the non-standard couplings are clearly visible, and the effect of the individual parameters on the OO distributions should not be compared directly since different values of the parameters have been used in each case. In general, non-standard couplings affect the OO distributions most in the region far from zero, as is expected. The $\mathrm{OO}(\Delta g_Z^1)$ distribution appears least sensitive to anomalous TGC's of any type. An important difference between these OO distributions and the OO distributions obtained at e^+e^- experiments (e.g. LEP) is that the mean of the distributions shown in Figure 5.8 is not very sensitive to anomalous TGC's (the distributions are plotted on a logarithmic scale). This implies that the technique used at LEP, wherein the mean values of the distributions are tabulated as a function of the anomalous TGC's, will not be feasible at hadron colliders.

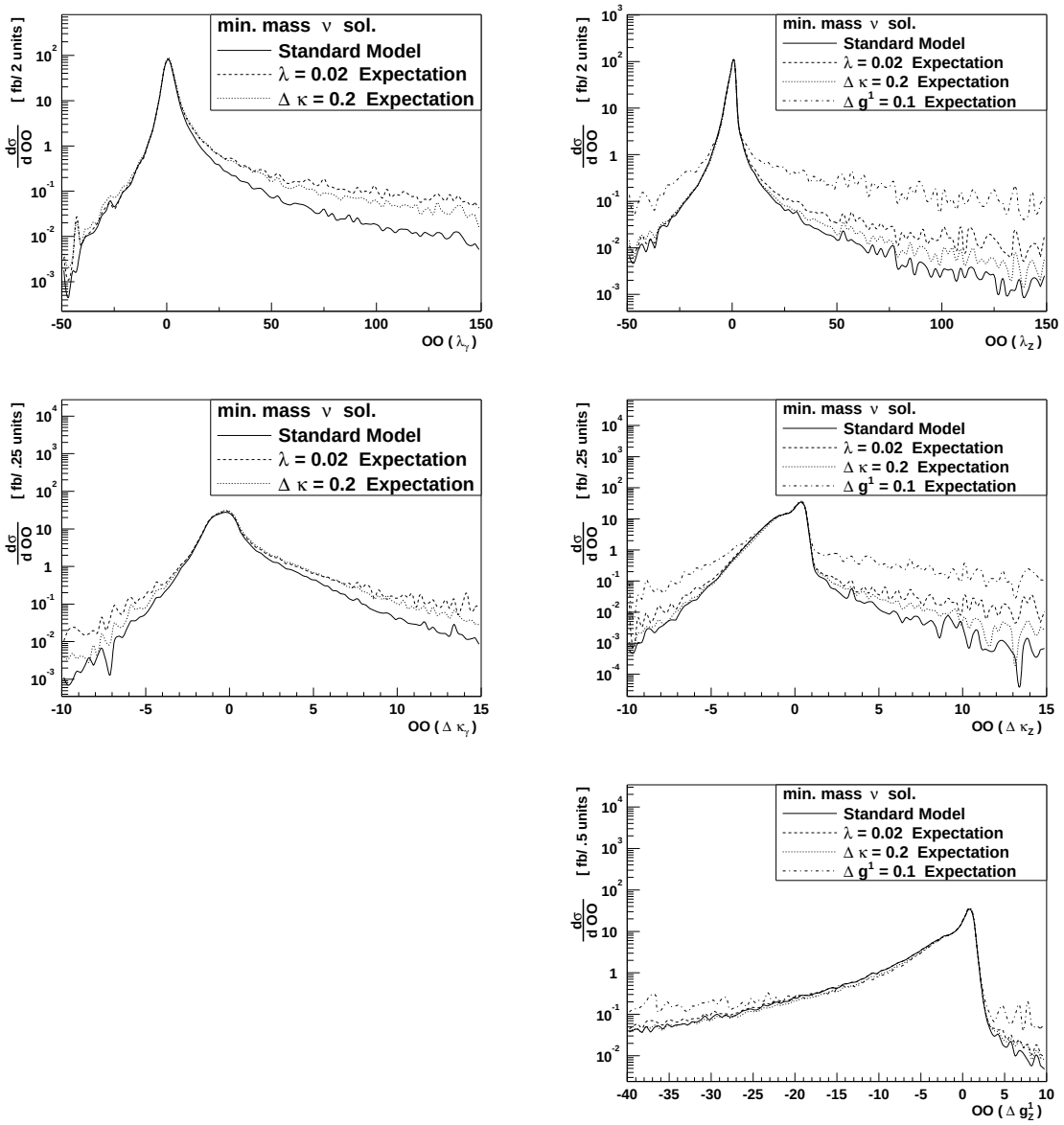

Figure 5.8: The dependence of the λ_V optimal observable (top), $\Delta\kappa_V$ optimal observable (middle), and g_V^1 optimal observable (bottom) on the anomalous TGC parameters are shown for $W\gamma$ production (left) and WZ production (right) at the LHC. The irregularities in the tails of the distributions are caused by low Monte Carlo simulation statistics in this region, and are not physical in nature.

The OO(λ_γ) distribution for $W\gamma$ production at the LHC is shown in Figure 5.9, including detector effects and the contribution from backgrounds. The expectation for SM couplings and two choices of anomalous TGC's are indicated. 'Mock' data from one simulated ATLAS experiment is superimposed and the corresponding likelihood curves are shown. The events which populate the regions of OO(λ_γ) far from zero are most sensitive to changes in the λ_γ parameter. Note also that the backgrounds populate the distribution more evenly than for the P_γ^T distribution, meaning the effect of the backgrounds on the sensitivity from this distribution will be more pronounced.

Deriving confidence limits from the Optimal Observables

Measurements and confidence limits can be calculated for the anomalous TGC parameters from a collection of experimental events using a binned maximum likelihood fit to the OO distributions in the same manner presented in Sec. 5.3.2 for other distributions. The location of the distribution mean is commonly used by LEP collaborations for measurements of the anomalous TGC's. As discussed above, this is not a very sensitive way to extract the couplings at hadron colliders, where the center-of-mass energy varies event by event.

The spread in the 95% statistical limits derived using a binned maximum likelihood fit to the OO distributions are shown in Table 5.6 for an integrated luminosity of 30 fb^{-1} at the LHC. Background contamination and detector effects have been taken into account. In order to evaluate the sensitivity of the OO distributions to anomalous TGC's, the spread in the statistical 95% confidence limits for the $P_{\rm V}^T$ distribution are also shown. The limits are statistical only.

The limits derived from the OO(λ_V) and OO(Δg_V^1) distributions are not competitive with the limits derived from the $P_{\rm V}^T$ distribution. The OO distributions require significant reconstruction and theoretical input: to calculate the OO for a particular event, the center-of-mass system needs to be fully reconstructed such that all particle momenta are known, and phenomenological parton density functions are included in the calculation. The measurement of $P_{\rm V}^T$ is robust and simple, requiring only the reconstruction of the photon P^T for the $W\gamma$ case, and the $P_{l^+l^-}^T$ for the WZ

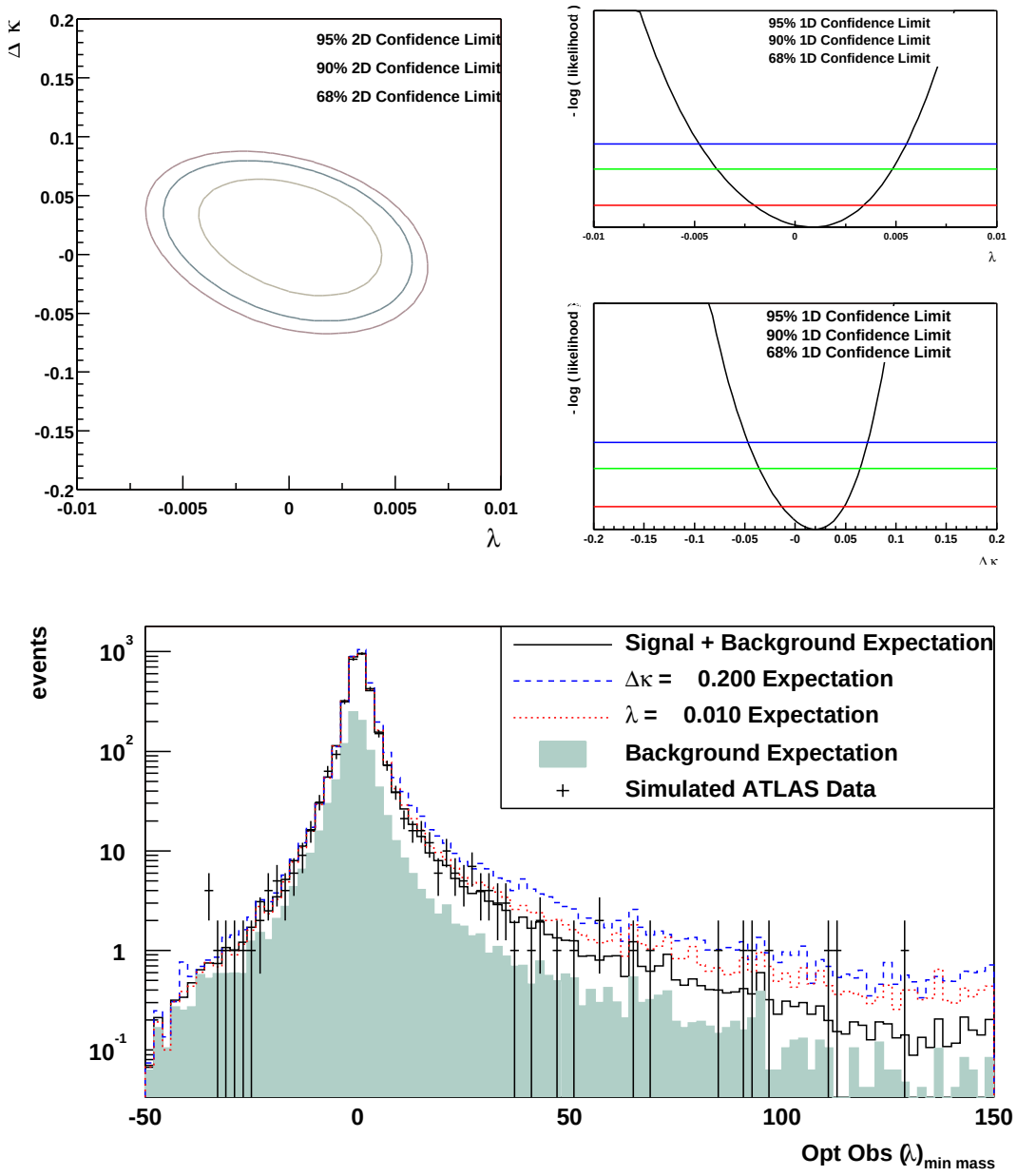

Figure 5.9: The distribution of the λ_γ optimal observable in $W\gamma$ production is shown (bottom), after applying the kinematic cuts described in Chapter 4. The points with error bars represent "mock" data for one ATLAS experiment with integrated luminosity of 30 fb^{-1}. This data has been simulated using the SM TGC parameters, and includes the background contributions. The lines are the reference distributions for several choices of the anomalous TGC parameters. The contribution of backgrounds to the reference distributions is shown as a shaded histogram, and does not depend on the anomalous TGC parameters. The one (top right) and two (top left) parameter negative log likelihood curves are shown as a function of the λ_γ and $\Delta\kappa_\gamma$ parameters with the 68, 90, and 95% confidence limits indicated. These confidence limits correspond to the single experiment which has been simulated for this figure.

	Spread in Statistical 95% Confidence Interval	
anomalous TGC parameter	P_{V}^{T} distribution	OO distribution
λ_γ	.0066	.014
$\Delta\kappa_\gamma$	.15	.17
λ_Z	.013	.023
$\Delta\kappa_Z$	.24	.16
Δg_Z^1	.016	.025

Table 5.6: The spread in the statistical 95% confidence intervals are compared for the P_{V}^{T} distribution and the OO distributions. An integrated luminosity of 30 fb^{-1} at the LHC in assumed and the limits are derived using the binned maximum likelihood method.

case. Another important attribute of the P_{V}^{T} observable is that its functional form ($P_{\mathrm{V}}^{T} = |p_V| \sin\theta_V$) is very similar to the functional form which would be expected for OO(λ_V) and OO(Δg_V^1). This is apparent from the approximate equations for $\Delta\mathcal{M}$ presented in Equations. 3.6-3.11, where the dominant change in the Born level matrix element at high energy arising from the λ_V and Δg_V^1 parameters is seen to be proportional to $\hat{s}\sin\theta_V$. This is the reason the P_{V}^{T} is so sensitive to the λ_V and Δg_V^1 parameters—it is an easily reconstructed observable which is functionally similar to our expectation for an λ_V and Δg_V^1 optimal observable.

The case is different for the OO($\Delta\kappa_Z$) distribution, which is more sensitive to the $\Delta\kappa_Z$ coupling than the P_{Z}^{T} distribution is. Again, this result is to be expected from an examination of Equations 3.6-3.11. An improvement in the statistical confidence limits is not enough to justify using an alternative method for extracting the confidence limits—systematic effects also need to be taken into account. Since the calculation of the OO's requires more in the way of reconstruction and phenomenological input, it is expected that these distributions will be more sensitive to systematic effects. A detailed comparison including these systematic effects will be explored in Sec. 5.6.

5.4 Systematic Uncertainties

The LHC will provide an unprecedented event rate for diboson production. It is important to understand to what extent a measurement of anomalous TGC parameters

is limited by statistics (i.e. limited by the size of the data sample) and to what extent it is limited by systematics, such as our understanding of the detector, or our ability to model the theory which is being tested. In this section, the contributions of the various systematic effects to the confidence limits are evaluated.

As described in Sec. 5.3, the expected statistical confidence limits are extracted by comparing histograms which represent 'mock' ATLAS data (sampled from the SM reference histogram with Poisson statistics) to reference histograms (constructed from large samples of simulated Monte Carlo events) which are evaluated as a function of the anomalous TGC parameters.

For the evaluation of each systematic contribution, the histograms which represent the 'mock' ATLAS data have been replaced with histograms which use a different model assumption. The reference histogram assumptions *are not changed*. Thus, for example, to evaluate the systematic effect a change in the background rate has on the confidence limits, the background process cross sections are increased (or decreased) in the data histograms, but are left unchanged in the reference histograms. The change in the model assumptions causes a shift in the preferred value for each anomalous TGC parameter. This shift is independent of luminosity and is taken as an estimate of the systematic error.

This is a worst case scenario strategy for evaluating the systematic effects because it assumes that a mis-modeling of some effect (the background rate in this example) has occurred, and that it has not been possible to correct for this mis-modeling. A more likely scenario for the ATLAS measurement of the TGC couplings is that significant mis-modeling does exist (for example in the cross-section for the W+jet background process), but these model-assumptions will be independently extracted from the data, such that the modeling can be corrected.

Before describing the various contributions to the systematic errors, a few comments are in order concerning the manner in which the model assumptions are changed. Several of the systematics can be evaluated in the manner described above without re-generating the reference histograms from which the "mock" data is sampled with Poisson statistics. An example is the systematic arising from the modeling

of the backgrounds, which is evaluated by simply changing the normalization of the background contributions in the reference histograms. Other systematics are evaluated by re-generating the reference histograms, and so the systematic shift in the preferred anomalous TGC parameters receives contributions from the systematic effect being studied, but also from statistical fluctuations in the reference histograms. This second contribution results in an uncertainty on the knowledge of the systematic effect $\Delta\sigma_{\text{syst}}$ (an "error on the error"). For each anomalous TGC, $\Delta\sigma_{\text{syst}}$ is evaluated by replacing the 'mock' ATLAS data histograms with histograms which use a *the same* model assumption, but are derived from a different sample of Monte Carlo events. In cases where the systematic effects are a significant fraction of the total confidence interval, the $\Delta\sigma_{\text{syst}}$'s are small.

In the following sections, the systematics will be evaluated for the specific case of the λ_γ TGC parameter in LHC $W\gamma$ production extracted using a binned maximum likelihood fit to the P_γ^T distribution. Tables enumerating the systematic effects for the other anomalous TGC parameters and other measurement methods will be presented afterward.

5.4.1 Background rate systematics

NLO calculations have been used for the computer modeling of the signal process to account for the significant modifications higher order corrections have on the distributions in the physical region of interest for TGC studies. However, only leading order event generators have been used for the backgrounds (new Monte Carlo tools are now becoming available which will make NLO simulations more accessible for studies like this one, such as the new generator for $p\overset{(-)}{p} \to Z + X \to l^+l^- + X$ which has been developed by the author in Ref. [Dob01d]).

To partially account for this discrepancy, a single constant k-factor of 1.5 has been applied to all backgrounds. This is slightly larger than the k-factor expected for hadronic single gauge-boson production (1.4), and is probably a reasonable 'average' guess for the k-factors of the background processes which are significant for diboson production.

The systematic effect of the background rate has been evaluated by varying this background process k-factor in the 'mock' data histograms from 1.5 up to 2 and down to 1. The statistical 95% confidence interval for the λ_γ parameter in $W\gamma$ production is $-0.0033 < \lambda_\gamma < 0.0033$, and a change of the background k-factor in the 'mock' data histograms to 1 (2) produces a -0.00025 (0.00011) shift on the mean value of λ_γ preferred by the 'mock' data. This shift is the same order of magnitude as $\Delta\sigma_{\rm syst} = \pm 0.00025$, and provides a negligible contribution to the total confidence interval.

5.4.2 Parton density function systematics

The CTEQ4 [CTEQ97] parton density functions[5] (p.d.f.'s) have been used for the reference and 'mock' data histograms in this study. To evaluate the systematic effects associated with the mis-modeling of p.d.f.'s, the CTEQ4 p.d.f.'s have been replaced with the CTEQ3 [CTEQ94] series p.d.f.'s in the 'mock' data histograms.

The phenomenological p.d.f.'s are estimated from experimental data, by fitting the p.d.f.'s to the data constrained by the theoretical expectation for the Bjorken momentum fraction x and scale Q evolution. The change in the phenomenological structure functions from one series to the next for a specific p.d.f. author group (e.g. the difference between CTEQ3 and CTEQ4) reflects the change that an increase in the available experimental data has on the p.d.f.'s. This change is an indication of the mis-modeling which existed in the older p.d.f. set which was of importance to the newly collected data. As such, this difference is taken as a reasonable estimate for how the p.d.f.'s might evolve over the course of LHC running.[6]

The systematic shift on the mean value of the λ_γ parameter preferred by the 'mock' data due to changing the p.d.f. from CTEQ4 to CTEQ3 is 0.00042 which is about 13% as large as the 95% statistical confidence limit of $-0.0033 < \lambda_\gamma < 0.0033$.

[5]Newer versions of the p.d.f.'s, including CTEQ5 and CTEQ6 are now available.

[6]The LHC machine will explore regions of Bjorken x and scale q which have never before been probed experimentally. This means a considerable change in the p.d.f.'s is likely to occur in these newly explored regions when the LHC data becomes available. This large change in the p.d.f.'s will be of little concern for a study such as this one, because the change will be corrected for in the reference histograms. For the present study, the concern is with mis-modeling of the p.d.f.'s after this initial change has occurred.

The p.d.f.'s provide a small contribution to the total confidence interval for the λ_γ parameter.

5.4.3 Systematics arising from neglected higher orders

The effect of neglecting higher order diagrams (for our signal this would be order ${\alpha_S}^{\geq 2}$ diagrams) is traditionally evaluated by varying the (somewhat arbitrarily chosen) renormalization and factorization scales up and down by a factor 2. This is also the strategy which has been adopted here.

The systematic shift on the mean value of the λ_γ parameter preferred by the 'mock' data due to multiplying the factorization and renormalization scales by a factor $\frac{1}{2}$ (2) is 0.00107 (0.00093). This provides the dominant systematic effect for the λ_γ parameter measurement.

5.4.4 Detector effects

The modeling of the ATLAS detector will affect the measurements and confidence intervals for anomalous couplings. For example, if the reconstructed transverse momentum of photons was systematically shifted upward, then it would appear as if an excess of events was observed at high P_γ^T, which is the characteristic signature of anomalous TGC's.

The systematic effects associated with detector modeling are evaluated for this study in a very simple manner. The analysis has been repeated assuming a fictional 'perfect' detector. A fictional detector such as this is easily simulated by simply turning off the detector smearing in the event generation software chain. The mean shift of the TGC parameters preferred by the 'mock' data (simulated with the fictional 'perfect' detector) is then evaluated by comparing them to reference histograms which use the standard ATLAS fast detector simulation.

The effect is largest for the $\Delta\kappa_V$ TGC parameters. These parameters are enhanced by an amount proportional only to the diboson mass (c.f. Eqs. 3.6-3.11), and so receive a more even contribution from the full spectrum of events, as compared to the other anomalous TGC's, which derive their sensitivity primarily from just the highest P^T

events.

For the case of the λ_γ and $\Delta\kappa_\gamma$ parameters the shift is -0.00018 and 0.0055 respectively. This shift is small compared to the statistical 95% confidence limits of $-0.0033 < \lambda_\gamma < 0.0033$ and $-0.073 < \Delta\kappa_\gamma < 0.076$.

Note that this evaluation of the detector systematics takes into account the reconstruction of the events, but not detector effects which would affect the event rates. Since the analysis does not use information from the overall normalization, a change in the total event rate will not affect the measurements (hence the luminosity need not be considered). However, a change which effects the background rates differently from the signal rates would produce an effect on the measurements. One example of a detector effect like this would be the rejection rate of jets faking photons or electrons in the detector. This, however, has already been taken into account with the systematic effects in the background rate, discussed in Sec. 5.4.1.

5.5 Controlling Systematics

The evaluation of systematic errors for this study has been performed using "worst case scenarios" in most instances. In this section a method for controlling the systematic effects which contribute to the confidence levels is explored.

By neglecting the normalization when extracting the anomalous couplings, uncertainties due to luminosity are removed. An important systematic effect comes from our limited knowledge of QCD corrections—the QCD theoretical error dominates the systematics.

The issue is, if data is observed which differs from our reference histogram expectation, is it possible to determine whether the difference arises from anomalous couplings, or from something else such as mis-modeled QCD effects?

The calculation employed for the signal Monte Carlo is exact up to next-to-leading order QCD. In addition, the leading logarithms have been re-summed to all orders in the parton density functions.

It is expected that as a calculation is performed at successively higher orders, the calculation will become more precise (i.e. we assume the series converges). Further,

it is expected that the effect of adding each new order is usually smaller than the effect of adding the previous order (e.g. the difference in going from NLO to NNLO will be smaller than the difference in going from LO to NLO. One conservative way[7] to estimate the error associated with neglected higher orders is to find the change in the result when going from the second-highest to the highest calculated order. In the present study, only two orders of QCD calculations exist: LO and NLO, so the differences between LO and NLO represent the uncertainty due to neglected orders.

To illustrate this scenario, a set of reference histograms have been generated according to our usual model parameters using the BHO NLO generator. These histograms encompass our knowledge of the Standard Model, and the effects anomalous couplings have on that model. Rather than comparing this model to data generated using the same model, it is compared to data generated at LO (with Parton Shower) using the Pythia 6.136 Monte Carlo.[8] The LO data has been normalized to the NLO expectation, such that only changes in distribution shapes are relevant. The usual kinematic cuts have been imposed, with the exception of the jet veto (removed so as to emphasize the difference in the simulations). The P_γ^T distribution and resulting confidence limits are shown in Figure 5.10, for an integrated luminosity of 100 fb^{-1}.

The 1-dimensional likelihood functions suggest that anomalous couplings have been observed at about the 90% confidence level, with a values of $\lambda_\gamma = -0.001$ and $\Delta\kappa_\gamma = -0.02$ preferred by the 'mock' data. The P_γ^T distribution is suspicious, however, because a deficit of 'data' seems to be observed at mid to high P^T. A cross check sensitive to QCD corrections, but insensitive to anomalous couplings is required. The recoil of the gauge-boson pair $P_{\mathrm{W}\gamma}^T$ is very sensitive to (indeed almost equivalent to) the inclusive jet structure in the event, and so is a natural choice. This distribution is shown in Figure 5.11, wherein the LO 'mock' data has been normalized to the NLO expectation using a constant k-factor. In order to obtain this distribution,

[7]It is more common—and considered more appropriate—to vary the factorization scale up and down by a factor of two (the factor 2 being convention only), which is the method that has been used to assign a quantitative number to systematic error associated with neglected higher orders in this study, see Sec. 5.4.3.

[8]The NLO generation uses the CTEQ4M NLO structure function, while the LO generation uses CTEQ4L, a leading order structure function. This is consistent with our labelling of the two processes as NLO and LO.

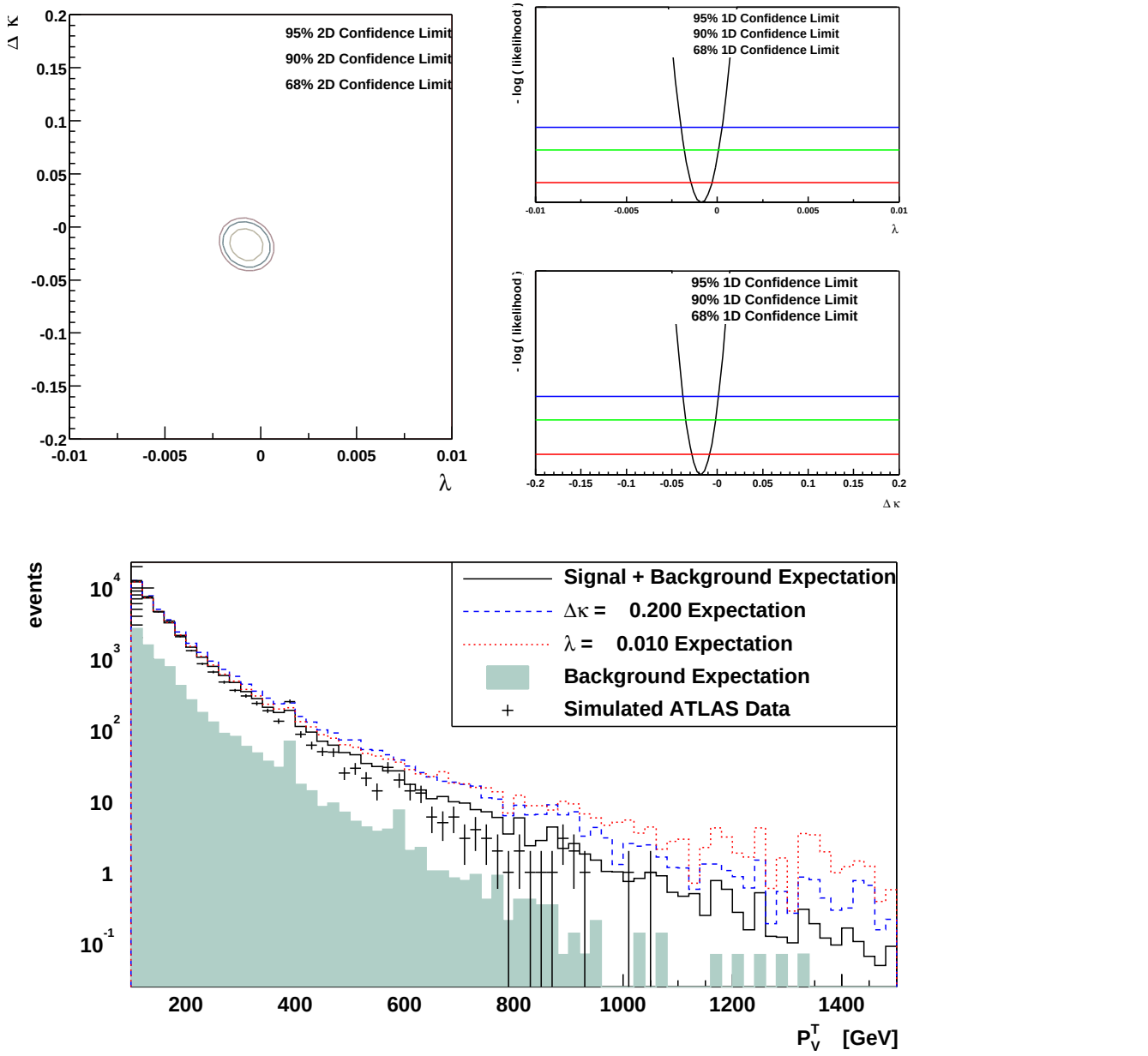

Figure 5.10: Differences arising from a mis-modeling of QCD effects are presented. The reference histograms are generated using the BHO NLO generator, while the data is generated using the Pythia LO Monte Carlo. The 2-dimension (top left) and 1-dimension (top right) confidence intervals for λ_γ and $\Delta\kappa_\gamma$ are extracted from the P_γ^T distribution (bottom) using an integrated luminosity of 100 fb^{-1}.

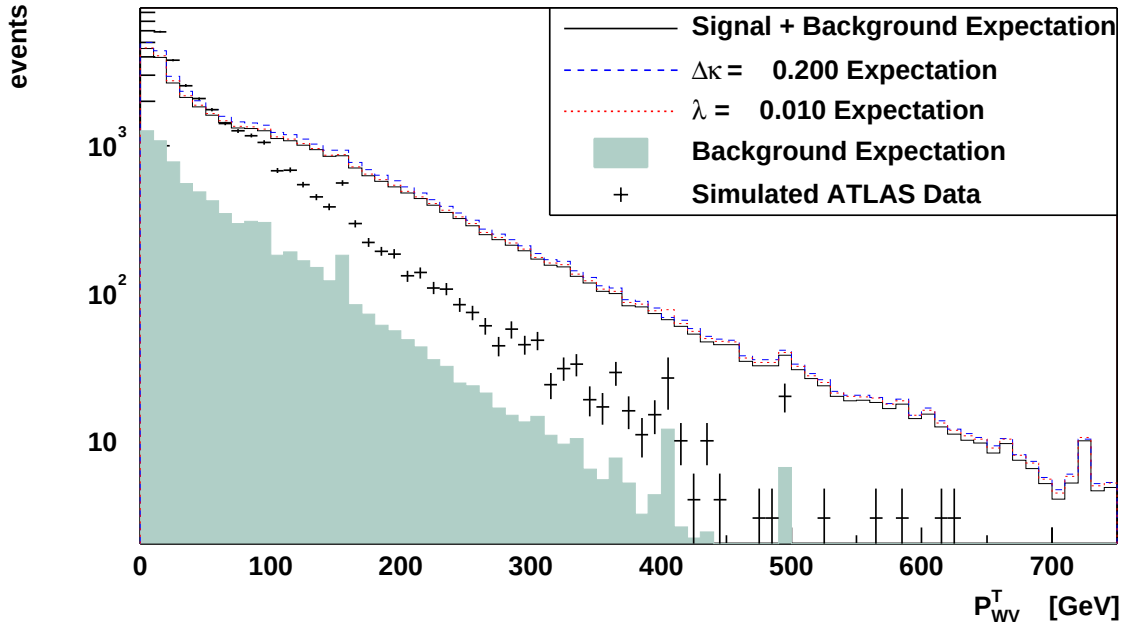

Figure 5.11: The distribution of gauge-boson-pair transverse momentum is shown for reference histograms generated using the BHO NLO generator, and the 'mock' data generated using the Pythia LO Monte Carlo for an integrated luminosity of 100 fb^{-1}. The LO 'mock' data has been normalized to the NLO expectation.

the jet veto cut has been removed for the event selection.

This $P^T_{\mathrm{W}\gamma}$ distribution has very little sensitivity to anomalous couplings. The change in the expectation from an anomalous $\Delta\kappa_\gamma = 0.2$ (already excluded by LEP) and $\lambda_\gamma = 0.01$ (large by LHC standards) are superimposed,[9] and are nearly indistinguishable from the Standard Model expectation.

The 'mock' data differs significantly from the model expectation. Since the distribution has essentially no sensitivity to anomalous couplings, the difference arises elsewhere.

As a second example illustrating how the P^T_{WV} distribution can be used to validate the QCD parameters chosen for the reference histograms, a change in the factorization and renormalization scales by a factor 2 is considered. In this example both reference and 'mock' data histograms are generated at NLO, but the data employs a fixed

[9]The confidence limits obtainable at LHC from the $P^T_{\mathrm{W}\gamma}$ distribution have already been excluded by LEP.

factorization scale equal to the W-mass for all events. The reference uses a fixed factorization scale of two times the W-mass. The effect of such a scale variation on the P_γ^T distribution is shown in Figure 5.12 (top), where it is seen that the change in scale resembles an anomalous coupling. The $P_{\mathrm{W}\gamma}^T$ distribution is shown at the bottom of the figure. Here the data is seen to differ from the reference by an amount that cannot be accounted for by the anomalous couplings alone.

In this manner the P_{WV}^T distribution (with jet veto cuts relaxed) may be used in hadron collider experiments to evaluate the ability of the theory to model the data. A good fit between the Monte Carlo and the data for this distribution should first be achieved before attempting to extract anomalous couplings. Since this distribution is primarily sensitive to QCD effects, improvements in the fit may be achieved by tuning the parton density functions, varying the factorization scale, and adjusting the QCD coupling.

There are other regions of phase space which also exhibit a reduced sensitivity to anomalous couplings, and so could be used to validate Monte Carlo modeling independently of the anomalous couplings. The regions include rapidities far from the radiation zero $|\eta_\gamma - \eta_{\mathrm{l_W}}| > 1.5$, and the low gauge-boson transverse momentum region, where the gauge-boson transverse momentum can be dis-entangled from the inclusive subprocess transverse momentum by requiring that $P_{\mathrm{V}}^T < 200$ GeV in the frame where the WV system has been boosted in the transverse direction such that $P_{\mathrm{WV}}^T = 0$.

5.6 Comparison of Methods

Having derived the statistical confidence limits and enumerated the systematic effects, it is now possible to assess the various methods for extracting measurements of the anomalous TGC parameters.

The systematic effects described in the previous sections are uncorrelated, and so the individual shifts[10] are added together in quadrature to obtain the total system-

[10]Some of the systematic effects (such as the change in the renormalization and factorization scale for λ_γ) produce a shift which goes only in one direction (i.e. a variation of the scale up or down

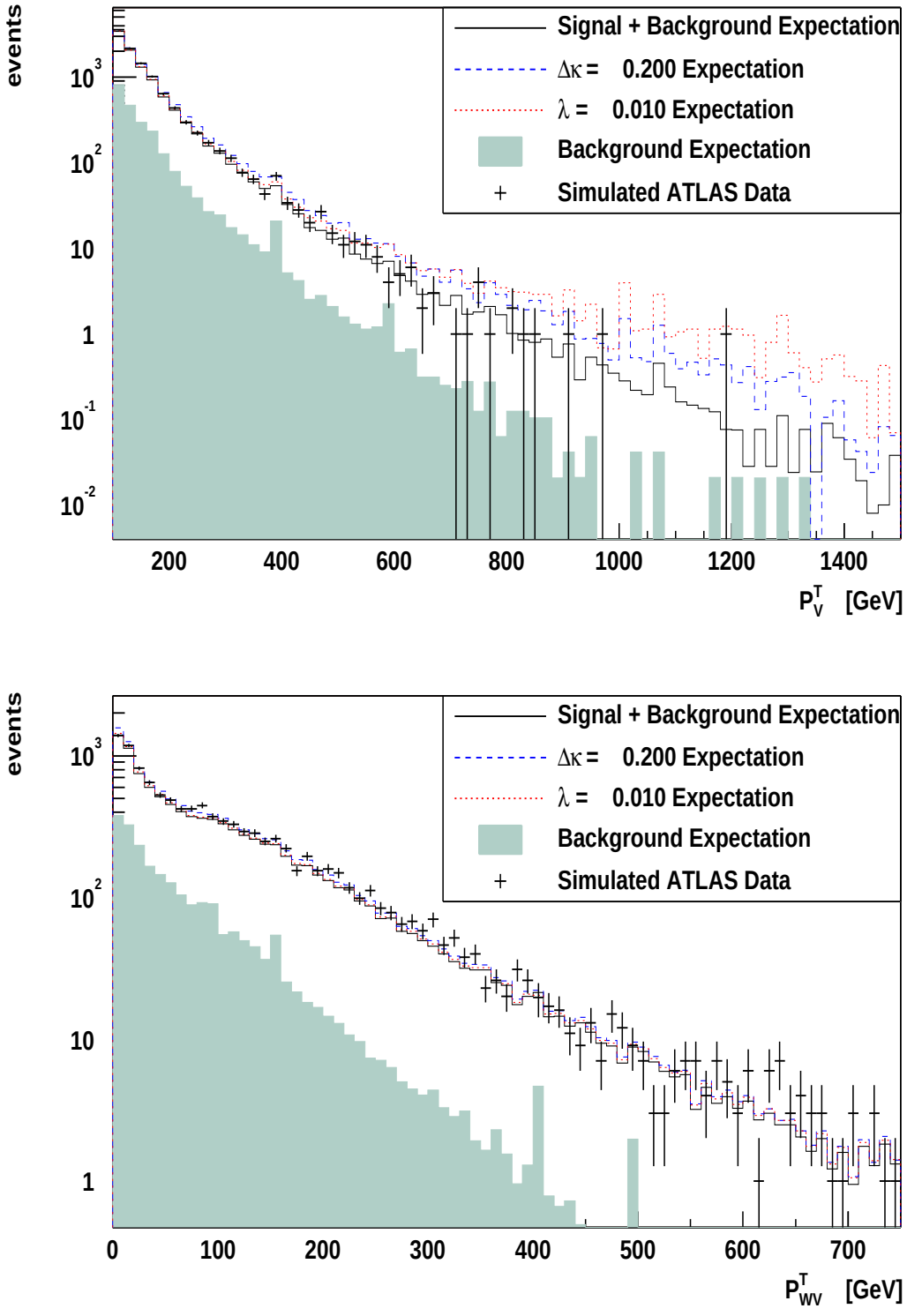

Figure 5.12: Differences arrising from a factor two change in the QCD factorization scale are presented. Both data and reference histograms are generated at NLO, but the data uses a fixed scale M_{W}, while the reference uses 2 M_{W}. The P_{γ}^{T} distribution is shown at top, and the $P_{\mathrm{W}\gamma}^{T}$ distribution is shown bottom for an integrated luminosity of 30 fb^{-1}.

atic error for the measurements. Enumerations of the systematic effects is presented in Table 5.7 and Table 5.11 for $W\gamma$ and WZ production at the LHC. This total systematic error is then added in quadrature to the statistical 95% confidence intervals (derived by averaging over 5000 simulated ATLAS experiments) to obtain the confidence intervals which define the ATLAS experiment sensitivity to the anomalous TGC parameters. These intervals are presented in Table 5.9 and Table 5.14 for $W\gamma$ and WZ production at the LHC, assuming an integrated luminosity of 30 fb^{-1}. The definition of the various distributions are summarized in Table 5.17.

5.6.1 The λ_V parameters

A binned maximum likelihood fit to the transverse momentum of the Z^0 or γ distribution P_{V}^T has been the conventional means of extracting limits on the anomalous coupling parameters at hadron colliders (e.g. Sp$\bar{\mathrm{p}}$S, Tevatron).

For the λ_γ and λ_Z parameters, the P_{V}^T distribution provides the best limits, both with and without accounting for systematic effects. This is because the P_{V}^T observable mimics the behavior which the λ_V parameter affects on the matrix elements (Eq. 3.7 and 3.9). The P_{V}^T observable has the further advantage of being reconstructible without the assumptions which would otherwise be necessary to determine the center-of-mass system. This observable encodes angular and energy information. Information about the helicity states of the gauge-bosons is missing, which motivates the use of a 2-dimensional distribution of P_{V}^T vs. P_{lW}^T. This 2-dimension distribution uses a coarse binning granularity such that the bins are a factor 5 wider. It is this coarse granularity which keeps the 2-dimensional P_{V}^T vs. P_{lW}^T distribution from showing an improvement over the single dimension P_{V}^T distribution. Systematic effects are also small for P_{V}^T vs. P_{lW}^T, indicating that slight improvements in the confidence limits

by a factor 2, shifts the λ_γ parameter in the positive direction for both cases). This is because the likelihood function is often-times nearly symmetric about λ_γ=0. In cases such as these (or when only a single shift is reported such as for the p.d.f. systematic), the systematic effect is assumed to go in both directions (the systematic errors which have been used in the combination with statistical limits are reported in parentheses in the tables which follow). For example, the systematic shift produced by varying the scale by a factor $\frac{1}{2}$ and 2 for the λ_γ parameter extracted from the P_γ^T distribution is 0.00107 and 0.00093. The systematic error which has been assumed in this case is ($\pm\max(|0.00107|, |0.00093|)$= (-0.00107,0.00107).

		Background $k=2,\ k=1$	PDF	Scale $\times 2,\ \times \frac{1}{2}$	Detector	$\oplus$All Systematics
P_V^T	λ	0.00011,-0.00025	0.00042	0.00093,0.00107	-0.00018	(-0.00119,0.00117)
		(-0.00025,0.00011)	(-0.00042,0.00042)	(-0.00107,0.00107)	(-0.00018,0.00018)	$\Delta\sigma_{\rm syst} = \pm 0.00025$
P_V^T	$\Delta\kappa$	-0.0136,0.00425	0.00288	0.00063,0.00022	0.00552	(-0.015,0.00756)
		(-0.0136,0.00425)	(-0.00288,0.00288)	(-0.00063,0.00063)	(-0.00552,0.00552)	$\Delta\sigma_{\rm syst} = \pm 0.00509$
$P_{\rm lw}^T$	λ	-0.00042,0.00252	0.002	0.00133,0.00092	0.00279	(-0.00371,0.00446)
		(-0.00042,0.00252)	(-0.002,0.002)	(-0.00133,0.00133)	(-0.00279,0.00279)	$\Delta\sigma_{\rm syst} = \pm 0.000941$
$P_{\rm lW}^T$	$\Delta\kappa$	0.00089,-0.1	0.0704	0.0275,0.0463	0.115	(-0.174,0.142)
		(-0.1,0.00089)	(-0.0704,0.0704)	(-0.0463,0.0463)	(-0.115,0.115)	$\Delta\sigma_{\rm syst} = \pm 0.0196$
$P_{\rm miss}^T$	λ	0.00232,-0.00026	-0.00121	0.00052,0.00121	0.00016	(-0.00174,0.00289)
		(-0.00026,0.00232)	(-0.00121,0.00121)	(-0.00121,0.00121)	(-0.00016,0.00016)	$\Delta\sigma_{\rm syst} = \pm 0.000307$
$P_{\rm miss}^T$	$\Delta\kappa$	-0.0708,0.0267	0.0234	-0.00031,-0.0129	0.0332	(-0.0826,0.0503)
		(-0.0708,0.0267)	(-0.0234,0.0234)	(-0.0129,0.0129)	(-0.0332,0.0332)	$\Delta\sigma_{\rm syst} = \pm 0.00743$
mass$(\mathrm{WV})_{\mathrm{Both\ Sol.}}$	λ	-0.00058,0.00015	0.00382	0.00319,-0.00214	0.00091	(-0.00451,0.00506)
		(-0.00058,0.00015)	(-0.00382,0.00382)	(-0.00214,0.00319)	(-0.00091,0.00091)	$\Delta\sigma_{\rm syst} = \pm 0.00201$
mass$(\mathrm{WV})_{\mathrm{Both\ Sol.}}$	$\Delta\kappa$	0.00925,-0.00853	-0.0202	-0.0427,0.0656	0.0431	(-0.0644,0.0816)
		(-0.00853,0.00925)	(-0.0202,0.0202)	(-0.0427,0.0656)	(-0.0431,0.0431)	$\Delta\sigma_{\rm syst} = \pm 0.044$
mass$(\mathrm{WV})_{Min}$	λ	-9e-05,0.00144	0.00397	0.0035,0.00419	0.00211	(-0.00615,0.00631)
		(-9e-05,0.00144)	(-0.00397,0.00397)	(-0.00419,0.00419)	(-0.00211,0.00211)	$\Delta\sigma_{\rm syst} = \pm 0.00221$
mass$(\mathrm{WV})_{Min}$	$\Delta\kappa$	0.0161,-0.0321	-0.0485	0.0897,0.0869	-0.0192	(-0.109,0.105)
		(-0.0321,0.0161)	(-0.0485,0.0485)	(-0.0897,0.0897)	(-0.0192,0.0192)	$\Delta\sigma_{\rm syst} = \pm 0.0137$
mass$(\mathrm{WV})_{Tran}$	λ	-7e-05,0.00111	0.00386	0.00062,0.00484	0.0013	(-0.00633,0.00642)
		(-7e-05,0.00111)	(-0.00386,0.00386)	(-0.00484,0.00484)	(-0.0013,0.0013)	$\Delta\sigma_{\rm syst} = \pm 0.000728$
mass$(\mathrm{WV})_{Tran}$	$\Delta\kappa$	0.0261,-0.044	-0.0607	-0.0298,-0.0498	-0.0235	(-0.0931,0.0861)
		(-0.044,0.0261)	(-0.0607,0.0607)	(-0.0498,0.0498)	(-0.0235,0.0235)	$\Delta\sigma_{\rm syst} = \pm 0.0114$
$\eta_{\rm W} - \eta_{\rm l}$	λ	0.00946,-0.00241	0.00305	-0.00071,0.0159	0.0108	(-0.0115,0.0216)
		(-0.00241,0.00946)	(-0.00305,0.00305)	(-0.00071,0.0159)	(-0.0108,0.0108)	$\Delta\sigma_{\rm syst} = \pm 0.00528$
$\eta_{\rm W} - \eta_{\rm l}$	$\Delta\kappa$	0.0532,-0.178	-0.0338	-0.0176,0.095	0.0655	(-0.193,0.132)
		(-0.178,0.0532)	(-0.0338,0.0338)	(-0.0176,0.095)	(-0.0655,0.0655)	$\Delta\sigma_{\rm syst} = \pm 0.0244$
$\cos\theta^*(V)_{Ave}$	λ	0.00765,-0.0017	-0.0045	-0.00189,0.0138	0.0103	(-0.0115,0.0194)
		(-0.0017,0.00765)	(-0.0045,0.0045)	(-0.00189,0.0138)	(-0.0103,0.0103)	$\Delta\sigma_{\rm syst} = \pm 0.00291$
$\cos\theta^*(V)_{Ave}$	$\Delta\kappa$	0.0483,-0.131	-0.209	-0.0273,0.0978	0.0725	(-0.258,0.246)
		(-0.131,0.0483)	(-0.209,0.209)	(-0.0273,0.0978)	(-0.0725,0.0725)	$\Delta\sigma_{\rm syst} = \pm 0.0193$

Table 5.7: The systematic errors for the $W\gamma$ production anomalous TGC parameters at the LHC are enumerated (continued in Table 5.8). The precision to which the systematic errors are known is denoted by $\Delta\sigma_{\rm syst}$ in the last column.

		Background $k=2,\ k=1$	PDF	Scale $\times 2,\ \times \frac{1}{2}$	Detector	$\oplus$All Systematics
Opt Obs$(\lambda)_{\mathrm{min}\ mass}$	λ	-0.00536,0.0028	0.00416	0.00039,0.00313	0.00637	(-0.00982,0.00869)
		(-0.00536,0.0028)	(-0.00416,0.00416)	(-0.00313,0.00313)	(-0.00637,0.00637)	$\Delta\sigma_{\mathrm{syst}} = \pm 0.00139$
Opt Obs$(\kappa)_{\mathrm{min}\ mass}$	$\Delta\kappa$	-0.0385,0.00173	0.0596	-0.0133,0.0469	0.091	(-0.116,0.118)
		(-0.0385,0.00173)	(-0.0596,0.0596)	(-0.0133,0.0469)	(-0.091,0.091)	$\Delta\sigma_{\mathrm{syst}} = \pm 0.019$
P_V^T vs. $P_{1_W}^T$	λ	-0.00022,0.00032	0.00098	-0.00099,0.00062	0.00018	(-0.00142,0.00122)
		(-0.00022,0.00032)	(-0.00098,0.00098)	(-0.00099,0.00062)	(-0.00018,0.00018)	$\Delta\sigma_{\mathrm{syst}} = \pm 0.000392$
P_V^T vs. $P_{1_W}^T$	$\Delta\kappa$	-0.0107,0.0299	0.0319	0.0133,0.0078	0.0223	(-0.0425,0.0508)
		(-0.0107,0.0299)	(-0.0319,0.0319)	(-0.0133,0.0133)	(-0.0223,0.0223)	$\Delta\sigma_{\mathrm{syst}} = \pm 0.00744$
mass$(\mathrm{WV})_{Tran}$ vs. $\lvert\eta_V - \eta_l\rvert$	λ	0.00049,-0.00075	0.00077	0.00155,8e-05	0.0007	(-0.00201,0.00193)
		(-0.00075,0.00049)	(-0.00077,0.00077)	(-0.00155,0.00155)	(-0.0007,0.0007)	$\Delta\sigma_{\mathrm{syst}} = \pm 0.000301$
mass$(\mathrm{WV})_{Tran}$ vs. $\lvert\eta_V - \eta_l\rvert$	$\Delta\kappa$	0.0328,-0.0372	0.00116	0.0177,0.0548	0.032	(-0.0736,0.0715)
		(-0.0372,0.0328)	(-0.00116,0.00116)	(-0.0548,0.0548)	(-0.032,0.032)	$\Delta\sigma_{\mathrm{syst}} = \pm 0.0176$
mass$(\mathrm{WV})_{Min}$ vs. $\lvert\eta_V - \eta_l\rvert$	λ	0.00052,-0.00073	0.0007	0.00128,0.00299	0.00066	(-0.00322,0.00318)
		(-0.00073,0.00052)	(-0.0007,0.0007)	(-0.00299,0.00299)	(-0.00066,0.00066)	$\Delta\sigma_{\mathrm{syst}} = \pm 0.000433$
mass$(\mathrm{WV})_{\mathrm{Min}}$ vs. $\lvert\eta_V - \eta_l\rvert$	$\Delta\kappa$	0.0335,-0.0364	0.00874	0.00746,0.0543	0.0324	(-0.0735,0.0721)
		(-0.0364,0.0335)	(-0.00874,0.00874)	(-0.0543,0.0543)	(-0.0324,0.0324)	$\Delta\sigma_{\mathrm{syst}} = \pm 0.014$
mass$(\mathrm{WV})_{Both\ Sol.}$ vs. $\cos\theta^*(V)_{Ave}$	λ	0.00031,-0.00037	0.00079	0.00128,0.00128	0.00047	(-0.00162,0.00161)
		(-0.00037,0.00031)	(-0.00079,0.00079)	(-0.00128,0.00128)	(-0.00047,0.00047)	$\Delta\sigma_{\mathrm{syst}} = \pm 0.000354$
mass$(\mathrm{WV})_{Both\ Sol.}$ vs. $\cos\theta^*(V)_{Ave}$	$\Delta\kappa$	0.0279,-0.0204	0.00696	-0.0082,0.0586	0.0327	(-0.04,0.073)
		(-0.0204,0.0279)	(-0.00696,0.00696)	(-0.0082,0.0586)	(-0.0327,0.0327)	$\Delta\sigma_{\mathrm{syst}} = \pm 0.0133$

Table 5.8: Continuation of Table 5.7.

	95% Statistical Limit	⊕All Systematics	95% Confidence Limit (stat⊕syst)
P_V^T	-0.00328< λ <0.0033	(-0.00119,0.00117)	-0.00349< λ <0.0035
	λ spread= 0.00657		λ spread= 0.00698
P_V^T	-0.0732< $\Delta\kappa$ <0.0761	(-0.015,0.00756)	-0.0747< $\Delta\kappa$ <0.0764
	$\Delta\kappa$ spread= 0.149		$\Delta\kappa$ spread= 0.151
$P_{\mathrm{l}_W}^T$	-0.00461< λ <0.00479	(-0.00371,0.00446)	-0.00591< λ <0.00655
	λ spread= 0.0094		λ spread= 0.0125
$P_{\mathrm{l}_W}^T$	-0.0969< $\Delta\kappa$ <0.0926	(-0.174,0.142)	-0.199< $\Delta\kappa$ <0.17
	$\Delta\kappa$ spread= 0.189		$\Delta\kappa$ spread= 0.369
P_{miss}^T	-0.00486< λ <0.00506	(-0.00174,0.00289)	-0.00516< λ <0.00583
	λ spread= 0.00992		λ spread= 0.011
P_{miss}^T	-0.0786< $\Delta\kappa$ <0.0955	(-0.0826,0.0503)	-0.114< $\Delta\kappa$ <0.108
	$\Delta\kappa$ spread= 0.174		$\Delta\kappa$ spread= 0.222
$\mathrm{mass(WV)}_{\mathit{Both\ Sol.}}$	-0.00531< λ <0.00582	(-0.00451,0.00506)	-0.00696< λ <0.00771
	λ spread= 0.0111		λ spread= 0.0147
$\mathrm{mass(WV)}_{\mathit{Both\ Sol.}}$	-0.0744< $\Delta\kappa$ <0.123	(-0.0644,0.0816)	-0.0984< $\Delta\kappa$ <0.148
	$\Delta\kappa$ spread= 0.197		$\Delta\kappa$ spread= 0.246
$\mathrm{mass(WV)}_{\mathrm{Min}}$	-0.00456< λ <0.00487	(-0.00615,0.00631)	-0.00765< λ <0.00797
	λ spread= 0.00943		λ spread= 0.0156
$\mathrm{mass(WV)}_{\mathrm{Min}}$	-0.0712< $\Delta\kappa$ <0.0972	(-0.109,0.105)	-0.13< $\Delta\kappa$ <0.143
	$\Delta\kappa$ spread= 0.168		$\Delta\kappa$ spread= 0.273
$\mathrm{mass(WV)}_{\mathrm{T}ran}$	-0.00425< λ <0.00435	(-0.00633,0.00642)	-0.00762< λ <0.00776
	λ spread= 0.0086		λ spread= 0.0154
$\mathrm{mass(WV)}_{\mathrm{T}ran}$	-0.0698< $\Delta\kappa$ <0.0914	(-0.0931,0.0861)	-0.116< $\Delta\kappa$ <0.126
	$\Delta\kappa$ spread= 0.161		$\Delta\kappa$ spread= 0.242
$\eta_{\mathrm{V}} - \eta_{\mathrm{l}}$	-0.0179< λ <0.0137	(-0.0115,0.0216)	-0.0212< λ <0.0256
	λ spread= 0.0316		λ spread= 0.0468
$\eta_{\mathrm{V}} - \eta_{\mathrm{l}}$	-0.085< $\Delta\kappa$ <0.0829	(-0.193,0.132)	-0.211< $\Delta\kappa$ <0.155
	$\Delta\kappa$ spread= 0.168		$\Delta\kappa$ spread= 0.366
$\cos\theta^*(V)_{\mathrm{Ave}}$	-0.016< λ <0.0131	(-0.0115,0.0194)	-0.0198< λ <0.0234
	λ spread= 0.0292		λ spread= 0.0432
$\cos\theta^*(V)_{\mathrm{Ave}}$	-0.266< $\Delta\kappa$ <0.0941	(-0.258,0.246)	-0.371< $\Delta\kappa$ <0.264
	$\Delta\kappa$ spread= 0.36		$\Delta\kappa$ spread= 0.635

Table 5.9: The 95% confidence intervals for $W\gamma$ production anomalous TGC parameters at the LHC assuming an integrated luminosity of 30 fb^{-1} (continued in Table 5.10).

	95% Statistical Limit	⊕All Systematics	95% Confidence Limit (stat⊕syst)
Opt Obs(λ)$_{min\ mass}$	-0.00754< λ <0.00649	(-0.00982,0.00869)	-0.0124< λ <0.0108
	λ spread= 0.014		λ spread= 0.0232
Opt Obs(κ)$_{min\ mass}$	-0.0876< $\Delta\kappa$ <0.0783	(-0.116,0.118)	-0.145< $\Delta\kappa$ <0.142
	$\Delta\kappa$ spread= 0.166		$\Delta\kappa$ spread= 0.287
P_V^T vs. $P_{l_W}^T$	-0.00337< λ <0.00344	(-0.00142,0.00122)	-0.00366< λ <0.00365
	λ spread= 0.00682		λ spread= 0.00731
P_V^T vs. $P_{l_W}^T$	-0.0685< $\Delta\kappa$ <0.0722	(-0.0425,0.0508)	-0.0806< $\Delta\kappa$ <0.0883
	$\Delta\kappa$ spread= 0.141		$\Delta\kappa$ spread= 0.169
mass(WV)$_{Tran}$	-0.00346< λ <0.00346	(-0.00201,0.00193)	-0.004< λ <0.00396
vs. $\lvert\eta_V - \eta_l\rvert$	λ spread= 0.00692		λ spread= 0.00796
mass(WV)$_{Tran}$	-0.0638< $\Delta\kappa$ <0.0611	(-0.0736,0.0715)	-0.0974< $\Delta\kappa$ <0.094
vs. $\lvert\eta_V - \eta_l\rvert$	$\Delta\kappa$ spread= 0.125		$\Delta\kappa$ spread= 0.191
mass(WV)$_{Min}$	-0.00348< λ <0.00352	(-0.00322,0.00318)	-0.00474< λ <0.00475
vs. $\lvert\eta_V - \eta_l\rvert$	λ spread= 0.007		λ spread= 0.00949
mass(WV)$_{Min}$	-0.0635< $\Delta\kappa$ <0.0613	(-0.0735,0.0721)	-0.0971< $\Delta\kappa$ <0.0946
vs. $\lvert\eta_V - \eta_l\rvert$	$\Delta\kappa$ spread= 0.125		$\Delta\kappa$ spread= 0.192
mass(WV)$_{Both\ Sol.}$	-0.00349< λ <0.00356	(-0.00162,0.00161)	-0.00385< λ <0.0039
vs. $\cos\theta^*(V)_{Ave}$	λ spread= 0.00704		λ spread= 0.00775
mass(WV)$_{Both\ Sol.}$	-0.065< $\Delta\kappa$ <0.0627	(-0.04,0.073)	-0.0763< $\Delta\kappa$ <0.0962
vs. $\cos\theta^*(V)_{Ave}$	$\Delta\kappa$ spread= 0.128		$\Delta\kappa$ spread= 0.173

Table 5.10: Continuation of Table 5.9.

		Background $k=2,\ k=1$	PDF	Scale $\times 2,\ \times \frac{1}{2}$	Detector	$\oplus$All Systematics
P_V^T	λ	2e-05,-4e-05	0.00259	0.00156,-0.00175	0.00052	(-0.00317,0.00307)
		(-4e-05,2e-05)	(-0.00259,0.00259)	(-0.00175,0.00156)	(-0.00052,0.00052)	$\Delta\sigma_{\rm syst} = \pm 0.000612$
P_V^T	$\Delta\kappa$	0.00706,-0.00749	-0.0778	-0.009,-0.009	0.0357	(-0.0864,0.0864)
		(-0.00749,0.00706)	(-0.0778,0.0778)	(-0.009,0.009)	(-0.0357,0.0357)	$\Delta\sigma_{\rm syst} = \pm 0.0215$
P_V^T	Δg^1	0.00019,-0.00019	-0.00332	-0.0014,-0.00071	0.00594	(-0.00695,0.00695)
		(-0.00019,0.00019)	(-0.00332,0.00332)	(-0.0014,0.0014)	(-0.00594,0.00594)	$\Delta\sigma_{\rm syst} = \pm 0.000734$
$P_{\rm lW}^T$	λ	0.00032,-0.00042	0.00634	-0.00083,-0.00052	0.00038	(-0.00642,0.00641)
		(-0.00042,0.00032)	(-0.00634,0.00634)	(-0.00083,0.00083)	(-0.00038,0.00038)	$\Delta\sigma_{\rm syst} = \pm 0.000849$
$P_{\rm lW}^T$	$\Delta\kappa$	0.012,-0.0103	-0.0732	0.00763,-0.0225	0.0459	(-0.0898,0.0875)
		(-0.0103,0.012)	(-0.0732,0.0732)	(-0.0225,0.00763)	(-0.0459,0.0459)	$\Delta\sigma_{\rm syst} = \pm 0.00508$
$P_{\rm lW}^T$	Δg^1	0.00044,-0.00041	-0.00552	0.00104,-0.00095	0.00764	(-0.00948,0.00949)
		(-0.00041,0.00044)	(-0.00552,0.00552)	(-0.00095,0.00104)	(-0.00764,0.00764)	$\Delta\sigma_{\rm syst} = \pm 0.000283$
$P_{\rm miss}^T$	λ	-0.00037,0.00066	0.00427	0.00087,0.00127	0.00031	(-0.00448,0.00451)
		(-0.00037,0.00066)	(-0.00427,0.00427)	(-0.00127,0.00127)	(-0.00031,0.00031)	$\Delta\sigma_{\rm syst} = \pm 0.00111$
$P_{\rm miss}^T$	$\Delta\kappa$	-0.00499,0.00645	-0.0869	-0.00758,-0.00758	0.0514	(-0.101,0.101)
		(-0.00499,0.00645)	(-0.0869,0.0869)	(-0.00758,0.00758)	(-0.0514,0.0514)	$\Delta\sigma_{\rm syst} = \pm 0.0279$
$P_{\rm miss}^T$	Δg^1	3e-05,-3e-05	-0.00582	-0.00055,0.001	0.0082	(-0.0101,0.0101)
		(-3e-05,3e-05)	(-0.00582,0.00582)	(-0.00055,0.001)	(-0.0082,0.0082)	$\Delta\sigma_{\rm syst} = \pm 0.00068$
mass$(\mathrm{WV})_{Both\ Sol.}$	λ	2e-05,-0.00069	0.00832	-0.00208,-0.00146	0.00552	(-0.0102,0.0102)
		(-0.00069,2e-05)	(-0.00832,0.00832)	(-0.00208,0.00208)	(-0.00552,0.00552)	$\Delta\sigma_{\rm syst} = \pm 0.000423$
mass$(\mathrm{WV})_{Both\ Sol.}$	$\Delta\kappa$	0.00548,-0.00591	-0.129	-0.0258,-0.0191	0.129	(-0.185,0.185)
		(-0.00591,0.00548)	(-0.129,0.129)	(-0.0258,0.0258)	(-0.129,0.129)	$\Delta\sigma_{\rm syst} = \pm 0.0316$
mass$(\mathrm{WV})_{Both\ Sol.}$	Δg^1	0.00056,-0.00052	-0.0102	-0.00431,-0.00228	0.0122	(-0.0165,0.0165)
		(-0.00052,0.00056)	(-0.0102,0.0102)	(-0.00431,0.00431)	(-0.0122,0.0122)	$\Delta\sigma_{\rm syst} = \pm 0.00293$
mass$(\mathrm{WV})_{Min}$	λ	6e-05,-0.00056	0.00768	-0.00108,0.00083	0.00318	(-0.0084,0.00835)
		(-0.00056,6e-05)	(-0.00768,0.00768)	(-0.00108,0.00083)	(-0.00318,0.00318)	$\Delta\sigma_{\rm syst} = \pm 0.000428$
mass$(\mathrm{WV})_{Min}$	$\Delta\kappa$	0.00772,-0.00801	-0.109	0.00303,-0.0081	-0.0504	(-0.12,0.12)
		(-0.00801,0.00772)	(-0.109,0.109)	(-0.0081,0.00303)	(-0.0504,0.0504)	$\Delta\sigma_{\rm syst} = \pm 0.0304$
mass$(\mathrm{WV})_{Min}$	Δg^1	0.00061,-0.00055	-0.00868	-0.00173,-0.0011	-0.00388	(-0.00968,0.00968)
		(-0.00055,0.00061)	(-0.00868,0.00868)	(-0.00173,0.00173)	(-0.00388,0.00388)	$\Delta\sigma_{\rm syst} = \pm 0.00103$

Table 5.11: The systematic errors for the WZ production anomalous TGC parameters at the LHC are enumerated (continued in Table 5.12). The precision to which the systematic errors are known is denoted by $\Delta\sigma_{\rm syst}$ in the last column.

		Background $k=2,\ k=1$	PDF	Scale $\times 2,\ \times \frac{1}{2}$	Detector	$\oplus$All Systematics
mass$(WV)_{Tran}$	λ	0.00026,-0.00066	0.00757	0.00236,0.00229	-0.00161	(-0.00812,0.0081)
		(-0.00066,0.00026)	(-0.00757,0.00757)	(-0.00236,0.00236)	(-0.00161,0.00161)	$\Delta\sigma_{\rm syst} = \pm 0.00105$
mass$(WV)_{Tran}$	$\Delta\kappa$	0.015,-0.0128	-0.11	0.00884,0.0147	-0.00878	(-0.112,0.112)
		(-0.0128,0.015)	(-0.11,0.11)	(-0.0147,0.0147)	(-0.00878,0.00878)	$\Delta\sigma_{\rm syst} = \pm 0.0294$
mass$(WV)_{Tran}$	Δg^1	0.00064,-0.00056	-0.00865	0.00105,0.0011	-0.00036	(-0.00875,0.00875)
		(-0.00056,0.00064)	(-0.00865,0.00865)	(-0.0011,0.0011)	(-0.00036,0.00036)	$\Delta\sigma_{\rm syst} = \pm 0.000461$
$\eta_V - \eta_l$	λ	-0.00723,0.00332	-0.0194	0.00561,0.00756	0.00302	(-0.0222,0.0213)
		(-0.00723,0.00332)	(-0.0194,0.0194)	(-0.00756,0.00756)	(-0.00302,0.00302)	$\Delta\sigma_{\rm syst} = \pm 0.00776$
$\eta_V - \eta_l$	$\Delta\kappa$	-0.0197,0.0222	-0.0935	0.0502,0.00819	0.262	(-0.283,0.283)
		(-0.0197,0.0222)	(-0.0935,0.0935)	(-0.0502,0.0502)	(-0.262,0.262)	$\Delta\sigma_{\rm syst} = \pm 0.011$
$\eta_V - \eta_l$	Δg^1	-0.00292,0.00328	-0.0136	0.00567,0.0017	0.0296	(-0.0332,0.0333)
		(-0.00292,0.00328)	(-0.0136,0.0136)	(-0.00567,0.00567)	(-0.0296,0.0296)	$\Delta\sigma_{\rm syst} = \pm 0.0019$
$\cos\theta^*(V)_{Ave}$	λ	-0.00408,0.00295	-0.0103	0.00284,-0.00294	0.00248	(-0.0117,0.0114)
		(-0.00408,0.00295)	(-0.0103,0.0103)	(-0.00294,0.00284)	(-0.00248,0.00248)	$\Delta\sigma_{\rm syst} = \pm 0.0052$
$\cos\theta^*(V)_{Ave}$	$\Delta\kappa$	-0.0106,0.0114	-0.0402	0.00521,-0.0122	0.232	(-0.236,0.235)
		(-0.0106,0.0114)	(-0.0402,0.0402)	(-0.0122,0.00521)	(-0.232,0.232)	$\Delta\sigma_{\rm syst} = \pm 0.00614$
$\cos\theta^*(V)_{Ave}$	Δg^1	-0.0014,0.00154	-0.0054	0.00108,-0.00135	0.0269	(-0.0275,0.0275)
		(-0.0014,0.00154)	(-0.0054,0.0054)	(-0.00135,0.00108)	(-0.0269,0.0269)	$\Delta\sigma_{\rm syst} = \pm 0.0008$
Opt Obs$(\lambda)_{\rm min\ mass}$	λ	-0.00151,0.00117	-0.0119	0.00128,2e-05	0.00364	(-0.0126,0.0126)
		(-0.00151,0.00117)	(-0.0119,0.0119)	(-0.00128,0.00128)	(-0.00364,0.00364)	$\Delta\sigma_{\rm syst} = \pm 0.00167$
Opt Obs$(\kappa)_{\rm min\ mass}$	$\Delta\kappa$	-0.0102,0.0116	-0.0829	0.00523,0.00153	0.19	(-0.208,0.208)
		(-0.0102,0.0116)	(-0.0829,0.0829)	(-0.00523,0.00523)	(-0.19,0.19)	$\Delta\sigma_{\rm syst} = \pm 0.00884$
Opt Obs$(g^1)_{\rm min.\ mass}$	Δg^1	-0.0005,0.00053	-0.00844	0.0009,-0.00164	0.0473	(-0.0481,0.048)
		(-0.0005,0.00053)	(-0.00844,0.00844)	(-0.00164,0.0009)	(-0.0473,0.0473)	$\Delta\sigma_{\rm syst} = \pm 0.00141$

Table 5.12: Continuation of Table 5.11 (continued in Table 5.13).

		Background $k=2,\ k=1$	PDF	Scale $\times 2,\ \times \frac{1}{2}$	Detector	$\oplus$All Systematics
P_V^T vs. $P_{\mathrm{l}\nu}^T$	λ	-6e-05,-6e-05	0.00284	8e-05,-0.00187	-6e-05	(-0.0034,0.00284)
		(-6e-05,6e-05)	(-0.00284,0.00284)	(-0.00187,8e-05)	(-6e-05,6e-05)	$\Delta\sigma_{\mathrm{syst}} = \pm 0.000721$
P_V^T vs. $P_{\mathrm{l}\nu}^T$	$\Delta\kappa$	0.0102,-0.00998	-0.00189	0.00358,-0.00075	0.0215	(-0.0238,0.0241)
		(-0.00998,0.0102)	(-0.00189,0.00189)	(-0.00075,0.00358)	(-0.0215,0.0215)	$\Delta\sigma_{\mathrm{syst}} = \pm 0.0149$
P_V^T vs. $P_{\mathrm{l}\nu}^T$	Δg^1	0.00024,-0.00025	-0.00197	0.00087,0.00183	0.00508	(-0.00575,0.00575)
		(-0.00025,0.00024)	(-0.00197,0.00197)	(-0.00183,0.00183)	(-0.00508,0.00508)	$\Delta\sigma_{\mathrm{syst}} = \pm 0.000971$
mass(WV)$_{Tran}$	λ	-0.00021,0.00026	0.00313	-0.00096,0.00191	0.00123	(-0.0035,0.00388)
vs. $\lvert\eta_V - \eta_{\mathrm{l}}\rvert$		(-0.00021,0.00026)	(-0.00313,0.00313)	(-0.00096,0.00191)	(-0.00123,0.00123)	$\Delta\sigma_{\mathrm{syst}} = \pm 0.000738$
mass(WV)$_{Tran}$	$\Delta\kappa$	-0.00199,0.00233	-0.0658	0.0138,0.0281	0.101	(-0.124,0.124)
vs. $\lvert\eta_V - \eta_{\mathrm{l}}\rvert$		(-0.00199,0.00233)	(-0.0658,0.0658)	(-0.0281,0.0281)	(-0.101,0.101)	$\Delta\sigma_{\mathrm{syst}} = \pm 0.00503$
mass(WV)$_{Tran}$	Δg^1	4e-05,-5e-05	-0.00249	0.00028,-0.00017	0.0106	(-0.0109,0.0109)
vs. $\lvert\eta_V - \eta_{\mathrm{l}}\rvert$		(-5e-05,4e-05)	(-0.00249,0.00249)	(-0.00017,0.00028)	(-0.0106,0.0106)	$\Delta\sigma_{\mathrm{syst}} = \pm 0.000344$
mass(WV)$_{Min}$	λ	-0.00024,0.0003	0.00328	0.00042,0.00042	0.00134	(-0.00358,0.00358)
vs. $\lvert\eta_V - \eta_{\mathrm{l}}\rvert$		(-0.00024,0.0003)	(-0.00328,0.00328)	(-0.00042,0.00042)	(-0.00134,0.00134)	$\Delta\sigma_{\mathrm{syst}} = \pm 0.000895$
mass(WV)$_{Min}$	$\Delta\kappa$	-0.00274,0.00326	-0.0621	0.00722,0.00626	0.102	(-0.12,0.12)
vs. $\lvert\eta_V - \eta_{\mathrm{l}}\rvert$		(-0.00274,0.00326)	(-0.0621,0.0621)	(-0.00722,0.00722)	(-0.102,0.102)	$\Delta\sigma_{\mathrm{syst}} = \pm 0.0117$
mass(WV)$_{Min}$	Δg^1	2e-05,-2e-05	-0.00263	0.00033,0.00092	0.0108	(-0.0112,0.0112)
vs. $\lvert\eta_V - \eta_{\mathrm{l}}\rvert$		(-2e-05,2e-05)	(-0.00263,0.00263)	(-0.00092,0.00092)	(-0.0108,0.0108)	$\Delta\sigma_{\mathrm{syst}} = \pm 0.000374$
mass(WV)$_{Both\ Sol.}$	λ	-0.00027,0.00032	-0.00349	0.00125,0.00129	0.00125	(-0.00393,0.00394)
vs. $\cos\theta^*(V)_{\mathrm{Ave}}$		(-0.00027,0.00032)	(-0.00349,0.00349)	(-0.00129,0.00129)	(-0.00125,0.00125)	$\Delta\sigma_{\mathrm{syst}} = \pm 0.00082$
mass(WV)$_{Both\ Sol.}$	$\Delta\kappa$	-0.00347,0.00397	-0.0584	-0.00305,-0.00946	0.105	(-0.12,0.12)
vs. $\cos\theta^*(V)_{\mathrm{Ave}}$		(-0.00347,0.00397)	(-0.0584,0.0584)	(-0.00946,0.00946)	(-0.105,0.105)	$\Delta\sigma_{\mathrm{syst}} = \pm 0.00535$
mass(WV)$_{Both\ Sol.}$	Δg^1	-4e-05,4e-05	-0.0032	9e-05,9e-05	0.0118	(-0.0122,0.0122)
vs. $\cos\theta^*(V)_{\mathrm{Ave}}$		(-4e-05,4e-05)	(-0.0032,0.0032)	(-9e-05,9e-05)	(-0.0118,0.0118)	$\Delta\sigma_{\mathrm{syst}} = \pm 0.000319$

Table 5.13: Continuation of Table 5.12.

	95% Statistical Limit	⊕All Systematics	95% Confidence Limit (stat⊕syst)
P_V^T	-0.00652< λ <0.0066	(-0.00317,0.00307)	-0.00725< λ <0.00727
	λ spread= 0.0131		λ spread= 0.0145
P_V^T	-0.113< $\Delta\kappa$ <0.126	(-0.0864,0.0864)	-0.143< $\Delta\kappa$ <0.153
	$\Delta\kappa$ spread= 0.239		$\Delta\kappa$ spread= 0.295
P_V^T	-0.00641< Δg^1 <0.00972	(-0.00695,0.00695)	-0.00945< Δg^1 <0.012
	Δg^1 spread= 0.0161		Δg^1 spread= 0.0214
$P_{\mathrm{l}_W}^T$	-0.00823< λ <0.00844	(-0.00642,0.00641)	-0.0104< λ <0.0106
	λ spread= 0.0167		λ spread= 0.021
$P_{\mathrm{l}_W}^T$	-0.0757< $\Delta\kappa$ <0.129	(-0.0898,0.0875)	-0.117< $\Delta\kappa$ <0.156
	$\Delta\kappa$ spread= 0.205		$\Delta\kappa$ spread= 0.273
$P_{\mathrm{l}_W}^T$	-0.00666< Δg^1 <0.0111	(-0.00948,0.00949)	-0.0116< Δg^1 <0.0146
	Δg^1 spread= 0.0178		Δg^1 spread= 0.0262
$P_{\mathrm{m}iss}^T$	-0.0083< λ <0.00836	(-0.00448,0.00451)	-0.00944< λ <0.0095
	λ spread= 0.0167		λ spread= 0.0189
$P_{\mathrm{m}iss}^T$	-0.0857< $\Delta\kappa$ <0.139	(-0.101,0.101)	-0.133< $\Delta\kappa$ <0.172
	$\Delta\kappa$ spread= 0.225		$\Delta\kappa$ spread= 0.305
$P_{\mathrm{m}iss}^T$	-0.00699< Δg^1 <0.0119	(-0.0101,0.0101)	-0.0123< Δg^1 <0.0156
	Δg^1 spread= 0.0189		Δg^1 spread= 0.0279
mass(WV)$_{\mathrm{B}oth\ Sol.}$	-0.00912< λ <0.00947	(-0.0102,0.0102)	-0.0137< λ <0.0139
	λ spread= 0.0186		λ spread= 0.0276
mass(WV)$_{\mathrm{B}oth\ Sol.}$	-0.105< $\Delta\kappa$ <0.15	(-0.185,0.185)	-0.213< $\Delta\kappa$ <0.238
	$\Delta\kappa$ spread= 0.255		$\Delta\kappa$ spread= 0.45
mass(WV)$_{\mathrm{B}oth\ Sol.}$	-0.00914< Δg^1 <0.0142	(-0.0165,0.0165)	-0.0189< Δg^1 <0.0218
	Δg^1 spread= 0.0234		Δg^1 spread= 0.0407
mass(WV)$_{\mathrm{M}in}$	-0.00826< λ <0.00829	(-0.0084,0.00835)	-0.0118< λ <0.0118
	λ spread= 0.0166		λ spread= 0.0236
mass(WV)$_{\mathrm{M}in}$	-0.089< $\Delta\kappa$ <0.129	(-0.12,0.12)	-0.15< $\Delta\kappa$ <0.176
	$\Delta\kappa$ spread= 0.218		$\Delta\kappa$ spread= 0.326
mass(WV)$_{\mathrm{M}in}$	-0.00753< Δg^1 <0.012	(-0.00968,0.00968)	-0.0123< Δg^1 <0.0154
	Δg^1 spread= 0.0195		Δg^1 spread= 0.0277
mass(WV)$_{\mathrm{T}ran}$	-0.00775< λ <0.00787	(-0.00812,0.0081)	-0.0112< λ <0.0113
	λ spread= 0.0156		λ spread= 0.0225
mass(WV)$_{\mathrm{T}ran}$	-0.0859< $\Delta\kappa$ <0.129	(-0.112,0.112)	-0.141< $\Delta\kappa$ <0.171
	$\Delta\kappa$ spread= 0.215		$\Delta\kappa$ spread= 0.312
mass(WV)$_{\mathrm{T}ran}$	-0.00703< Δg^1 <0.0114	(-0.00875,0.00875)	-0.0112< Δg^1 <0.0144
	Δg^1 spread= 0.0184		Δg^1 spread= 0.0256

Table 5.14: The 95% confidence intervals for WZ production anomalous TGC parameters at the LHC assuming an integrated luminosity of 30 fb^{-1} (continued in Table 5.15).

	95% Statistical Limit	⊕All Systematics	95% Confidence Limit (stat⊕syst)
$\eta_{\rm V} - \eta_{\rm l}$	-0.0256< λ <0.0305 λ spread= 0.0562	(-0.0222,0.0213)	-0.0339< λ <0.0372 λ spread= 0.0712
$\eta_{\rm V} - \eta_{\rm l}$	-0.134< $\Delta\kappa$ <0.201 $\Delta\kappa$ spread= 0.335	(-0.283,0.283)	-0.313< $\Delta\kappa$ <0.347 $\Delta\kappa$ spread= 0.660
$\eta_{\rm V} - \eta_{\rm l}$	-0.0184< Δg^1 <0.0561 Δg^1 spread= 0.0745	(-0.0332,0.0333)	-0.038< Δg^1 <0.0652 Δg^1 spread= 0.103
$\cos\theta^*(V)_{Ave}$	-0.0198< λ <0.0237 λ spread= 0.0434	(-0.0117,0.0114)	-0.023< λ <0.0262 λ spread= 0.0492
$\cos\theta^*(V)_{Ave}$	-0.0942< $\Delta\kappa$ <0.142 $\Delta\kappa$ spread= 0.236	(-0.236,0.235)	-0.254< $\Delta\kappa$ <0.275 $\Delta\kappa$ spread= 0.529
$\cos\theta^*(V)_{Ave}$	-0.0131< Δg^1 <0.0416 Δg^1 spread= 0.0548	(-0.0275,0.0275)	-0.0304< Δg^1 <0.0499 Δg^1 spread= 0.0803
Opt Obs$(\lambda)_{min\ mass}$	-0.0123< λ <0.0108 λ spread= 0.0231	(-0.0126,0.0126)	-0.0176< λ <0.0166 λ spread= 0.0342
Opt Obs$(\kappa)_{min\ mass}$	-0.0662< $\Delta\kappa$ <0.0893 $\Delta\kappa$ spread= 0.156	(-0.208,0.208)	-0.218< $\Delta\kappa$ <0.226 $\Delta\kappa$ spread= 0.445
Opt Obs$(g^1)_{min.\ mass}$	-0.0106< Δg^1 <0.0139 Δg^1 spread= 0.0245	(-0.0481,0.048)	-0.0492< Δg^1 <0.05 Δg^1 spread= 0.0992

Table 5.15: Continuation of Table 5.14 (continued in Table 5.16).

may be possible using this distribution by focusing computer resources on improving the granularity of the 2 dimensional $P_{\rm V}^T$ vs. $P_{\rm lW}^T$ reference histograms.

Detector related systematics for the λ_V parameter are negligible, being a factor 5 or more smaller than the theoretical systematics. For an integrated luminosity of 30 fb^{-1}, the systematics are smaller than the statistical error by a factor 3.

The expected 95% confidence intervals for the λ_γ and λ_Z parameters using the $P_{\rm V}^T$ distribution are

$$-0.0033_{\rm stat.},\quad -0.0012_{\rm syst.} < \lambda_\gamma < +0.0033_{\rm stat.},\quad +0.0012_{\rm syst.} \tag{5.15}$$

$$-0.0065_{\rm stat.},\quad -0.0032_{\rm syst.} < \lambda_Z < +0.0066_{\rm stat.},\quad +0.0031_{\rm syst.} \tag{5.16}$$

which gives

$$-0.0035 < \lambda_\gamma < 0.0035 \tag{5.17}$$

$$-0.0073 < \lambda_Z < 0.0073 \tag{5.18}$$

when the statistical and systematic contributions are added in quadrature.

	95% Statistical Limit	⊕All Systematics	95% Confidence Limit (stat⊕syst)
P_V^T vs. $P_{l_W}^T$	-0.00666< λ <0.00667	(-0.0034,0.00284)	-0.00748< λ <0.00725
	λ spread= 0.0133		λ spread= 0.0147
P_V^T vs. $P_{l_W}^T$	-0.104< $\Delta\kappa$ <0.122	(-0.0238,0.0241)	-0.106< $\Delta\kappa$ <0.124
	$\Delta\kappa$ spread= 0.225		$\Delta\kappa$ spread= 0.231
P_V^T vs. $P_{l_W}^T$	-0.00641< Δg^1 <0.00999	(-0.00575,0.00575)	-0.00861< Δg^1 <0.0115
	Δg^1 spread= 0.0164		Δg^1 spread= 0.0201
mass(WV)$_{Tran}$	-0.00678< λ <0.00682	(-0.0035,0.00388)	-0.00763< λ <0.00784
vs. $\lvert\eta_V - \eta_l\rvert$	λ spread= 0.0136		λ spread= 0.0155
mass(WV)$_{Tran}$	-0.0702< $\Delta\kappa$ <0.109	(-0.124,0.124)	-0.142< $\Delta\kappa$ <0.165
vs. $\lvert\eta_V - \eta_l\rvert$	$\Delta\kappa$ spread= 0.18		$\Delta\kappa$ spread= 0.307
mass(WV)$_{Tran}$	-0.00535< Δg^1 <0.00819	(-0.0109,0.0109)	-0.0121< Δg^1 <0.0136
vs. $\lvert\eta_V - \eta_l\rvert$	Δg^1 spread= 0.0135		Δg^1 spread= 0.0257
mass(WV)$_{Min}$	-0.00679< λ <0.00681	(-0.00358,0.00358)	-0.00767< λ <0.0077
vs. $\lvert\eta_V - \eta_l\rvert$	λ spread= 0.0136		λ spread= 0.0154
mass(WV)$_{Min}$	-0.0708< $\Delta\kappa$ <0.108	(-0.12,0.12)	-0.139< $\Delta\kappa$ <0.161
vs. $\lvert\eta_V - \eta_l\rvert$	$\Delta\kappa$ spread= 0.178		$\Delta\kappa$ spread= 0.3
mass(WV)$_{Min}$	-0.00538< Δg^1 <0.00813	(-0.0112,0.0112)	-0.0124< Δg^1 <0.0138
vs. $\lvert\eta_V - \eta_l\rvert$	Δg^1 spread= 0.0135		Δg^1 spread= 0.0263
mass(WV)$_{Both\ Sol.}$	-0.00687< λ <0.00695	(-0.00393,0.00394)	-0.00792< λ <0.00798
vs. $\cos\theta^*(V)_{Ave}$	λ spread= 0.0138		λ spread= 0.0159
mass(WV)$_{Both\ Sol.}$	-0.0645< $\Delta\kappa$ <0.0991	(-0.12,0.12)	-0.137< $\Delta\kappa$ <0.156
vs. $\cos\theta^*(V)_{Ave}$	$\Delta\kappa$ spread= 0.164		$\Delta\kappa$ spread= 0.293
mass(WV)$_{Both\ Sol.}$	-0.00536< Δg^1 <0.00809	(-0.0122,0.0122)	-0.0134< Δg^1 <0.0147
vs. $\cos\theta^*(V)_{Ave}$	Δg^1 spread= 0.0135		Δg^1 spread= 0.028

Table 5.16: Continuation of Table 5.15.

	1 dimension distributions	# Bins
P_V^T	transverse momentum of the γ / Z^0	70
$P_{l_W}^T$	transverse momentum of the charged lepton from the $W^{\pm}$ decay	50
P_{miss}^T	missing transverse momentum	50
mass(WV)$_{Both\ Sol.}$	diboson invariant mass, each solution is histogrammed with weight $\frac{1}{2}$, (Eq. 5.6)	100
mass(WV)$_{Min}$	smaller of the two solutions for the diboson invariant mass (Eq. 5.4)	100
mass(WV)$_{Tran}$	$(l_W V; P_{\rm miss}^T)$ cluster transverse mass (Eq. 5.7)	100
$\eta_{\rm V} - \eta_{\rm l}$	pseudorapidity separation of the γ / Z^0 and the lepton from the $W^{\pm}$ decay	50
$\cos\theta^*(V)_{Ave}$	cosine of the production angle for the γ / Z^0 with respect to the beam-line in the reconstructed diboson center-of-mass frame, each of the two solutions are included with weight $\frac{1}{2}$	40
	Optimal Observables	
Opt Obs$(\kappa)_{min\ mass}$	the OO from Eq. 5.13 using the $\Delta\kappa_V$ parameter and the ν solution which gives the smaller diboson mass	100
Opt Obs$(\lambda)_{min\ mass}$	the OO from Eq. 5.13 using the λ_V parameter and the ν solution which gives the smaller diboson mass	100
Opt Obs$(g^1)_{min\ mass}$	the OO from Eq. 5.13 using the Δg_V^1 parameter and the ν solution which gives the smaller diboson mass	100
	2 dimension distributions	
P_V^T vs. $P_{l_W}^T$	transverse momentum of the γ / Z^0 vs. transverse momentum of the l_W	14×10
mass(WV)$_{Tran}$ vs. $\lvert\eta_{\rm V} - \eta_{\rm l}\rvert$	diboson transverse mass vs. the pseudorapidity separation of the γ / Z^0 and l_W	15×10
mass(WV)$_{Both\ Sol.}$ vs. $\cos\theta^*(V)_{Ave}$	the diboson invariant mass vs. the production angle of the γ / Z^0 in the center-or-mass frame, each of the two solutions are included with weight $\frac{1}{2}$	15×10

Table 5.17: Definition of the distributions which are used to extract the confidence intervals for anomalous TGC's in Tables 5.7 and 5.11. The number of bins used for the histograms of each distribution are shown on the right side of the table.

Maximum likelihood fits to the Optimal Observable distribution are not competitive for the λ_γ and λ_Z parameters. The Optimal Observable requires reconstruction of the full event, which significantly increases the effects of detector related systematics.

5.6.2 The $\Delta\kappa_V$ parameters

The $\Delta\kappa_V$ parameter enters the matrix elements proportional to $\sqrt{\hat{s}}(1\mp\cos\theta^\star_V)$, and so it does not exhibit the same enhancements in the central region that the λ_V parameter does. It is, however, very sensitive to the helicity of the W-boson, because it appears only in the $H_W = 0$ helicity states. This is evident in the confidence limits (especially for WZ production) where the P^T_{lW} distribution (which acts as a helicity projector) is seen to have similar or greater sensitivity than the P^T_{V} distribution.

Substantial gains in sensitivity can be achieved for the $\Delta\kappa_V$ parameter by using analysis techniques which encode more information than simple one dimensional distributions do. For the $\Delta\kappa_Z$ parameter, Optimal Observables provide the best limits when statistics are considered alone. Systematics (and in particular detector related effects) have a substantial effect on the Optimal Observables distributions and dominate the confidence intervals, making the limits not competitive with other methods. If the systematics can be controlled to a degree beyond what has been assumed in this work, Optimal Observables may provide a viable means of measuring the $\Delta\kappa_V$ parameters at the LHC.

Two dimensional distributions are an excellent means of extracting confidence intervals for the $\Delta\kappa_V$ parameters. The P^T_{V} vs. P^T_{lW} distribution is directly reconstructible, and provides the best overall confidence intervals for the $\Delta\kappa_Z$ parameter. Systematic effects are easily controlled, as they are a factor 2 smaller than the statistical contribution. Another distribution which is promising, but has not been studied here, is the mass$(WV)_{\mathrm{Tran}}$ vs. P^T_{lW} distribution, which would project out the energy and helicity information.

The expected 95% confidence intervals for the $\Delta\kappa_\gamma$ and $\Delta\kappa_Z$ parameters using the one dimensional P^T_{V} distribution and two dimensional P^T_{V} vs. P^T_{lW} distribution

respectively are

$$-0.073_{\text{stat.}}, \quad -0.015_{\text{syst.}} < \Delta\kappa_\gamma < +0.076_{\text{stat.}}, \quad +0.0076_{\text{syst.}} \tag{5.19}$$

$$-0.10_{\text{stat.}}, \quad -0.024_{\text{syst.}} < \Delta\kappa_Z < +0.12_{\text{stat.}}, \quad +0.024_{\text{syst.}} \tag{5.20}$$

which gives

$$-0.075 < \Delta\kappa_\gamma < 0.076 \tag{5.21}$$

$$-0.11 < \Delta\kappa_Z < 0.12 \tag{5.22}$$

when the statistical and systematic contributions are added in quadrature.

5.6.3 The Δg_Z^1 parameter

The Δg_Z^1 sensitivity behaves very differently from the other parameters, since this anomalous coupling parameter is very sensitive to systematic effects.

Because of the energy squared enhancement the Δg_Z^1 coupling receives in the $(H_Z, H_W) = (0, 0)$ helicity state, the statistical confidence limits for Δg_Z^1 are comparable to the λ_Z statistical limits. The best distribution for measuring the Δg_Z^1 parameter is the P_{V}^T vs. P_{lW}^T distribution, which gives the most stringent statistical and total confidence intervals. Comparable sensitivity is obtained with the one dimension P_{V}^T distribution.

In all cases the systematic contribution is comparable with the statistical contribution, and so a careful understanding and evaluation of the systematic uncertainties will be particularly important for measurements of this parameter at the LHC.

The expected 95% confidence intervals for the Δg_Z^1 parameter using the P_{V}^T distribution is

$$-0.0064_{\text{stat.}}, \quad -0.0058_{\text{syst.}} < \Delta g_Z^1 < +0.010_{\text{stat.}}, \quad +0.0058_{\text{syst.}} \tag{5.23}$$

which gives

$$-0.0086 < \Delta g_Z^1 < 0.011 \tag{5.24}$$

when the statistical and systematic contributions are added in quadrature.

5.7 Limits as a Function of Integrated Luminosity

The confidence intervals for the anomalous TGC parameters are limited primarily by statistics. With an increase in the size of the data sample, the limits will improve. In this section the confidence intervals are studied as a function of integrated luminosity.

Tables 5.18 and 5.19 show confidence intervals for the anomalous TGC parameters for data samples of $\mathcal{L}$ = 10, 30, 100, 300, 1000, and 10^6 fb^{-1} at the LHC. The spread in the confidence intervals are shown graphically in Figure 5.13. These results should be interpreted with caution, because they have been derived by simply scaling the histograms which were constructed to study the sensitivity of the ATLAS experiment for low luminosity LHC running and changes in effects like pile-up have not been accounted for. Nevertheless, the results provide a valuable indication of how an increase in luminosity will improve the sensitivity to anomalous TGC's. The ATLAS experiment is expected to collect 30 fb^{-1} at low luminosity and 300 fb^{-1} at high luminosity. The confidence intervals for 1000 and 10^6 fb^{-1} are included for interest only, and do not represent expectations for ATLAS.

Confidence intervals for the λ_γ and λ_Z parameters are dominated by statistics for integrated luminosities up to about 300 fb^{-1}, meaning the confidence limits for λ_V will always be statistically limited at the LHC experiments. This is because the sensitivity to the λ_V parameters is derived from those events at the highest transverse momentum, such that the measurement relies on just a few of these high P_{V}^T events, regardless of the total diboson event rate.

Statistics dominate the $\Delta\kappa_\gamma$ confidence intervals for integrated luminosities well above the LHC expectation—systematics will not be a concern for the measurement of this parameter. For the $\Delta\kappa_Z$ parameter, statistics dominate the confidence intervals up to about $\mathcal{L}$ = 100 fb^{-1}. These parameters are particularly sensitive to the modeling of the proton structure with the p.d.f.'s. A careful understanding and evaluation of these effects will be necessary for measurements of the $\Delta\kappa_Z$ parameter at the LHC using data samples in excess of 100 fb^{-1}.

The systematics and statistics provide contributions of similar size to the con-

	95% Statistical Limit	⊕All Systematics	95% Confidence Limit (stat⊕syst)
Integrated Luminosity = 10 fb^{-1}			
P_V^T	-0.00476< λ <0.00486	(-0.00119,0.00117)	-0.00491< λ <0.00499
	λ spread= 0.00962		λ spread= 0.00991
P_V^T	-0.101< $\Delta\kappa$ <0.104	(-0.015,0.00756)	-0.103< $\Delta\kappa$ <0.105
	$\Delta\kappa$ spread= 0.206		$\Delta\kappa$ spread= 0.207
Integrated Luminosity = 30 fb^{-1}			
P_V^T	-0.00328< λ <0.0033	(-0.00119,0.00117)	-0.00349< λ <0.0035
	λ spread= 0.00657		λ spread= 0.00698
P_V^T	-0.0732< $\Delta\kappa$ <0.0761	(-0.015,0.00756)	-0.0747< $\Delta\kappa$ <0.0764
	$\Delta\kappa$ spread= 0.149		$\Delta\kappa$ spread= 0.151
Integrated Luminosity = 100 fb^{-1}			
P_V^T	-0.00218< λ <0.00218	(-0.00119,0.00117)	-0.00248< λ <0.00247
	λ spread= 0.00436		λ spread= 0.00496
P_V^T	-0.052< $\Delta\kappa$ <0.0545	(-0.015,0.00756)	-0.0541< $\Delta\kappa$ <0.055
	$\Delta\kappa$ spread= 0.106		$\Delta\kappa$ spread= 0.109
Integrated Luminosity = 300 fb^{-1}			
P_V^T	-0.00154< λ <0.00149	(-0.00119,0.00117)	-0.00195< λ <0.00189
	λ spread= 0.00303		λ spread= 0.00384
P_V^T	-0.0379< $\Delta\kappa$ <0.0403	(-0.015,0.00756)	-0.0407< $\Delta\kappa$ <0.041
	$\Delta\kappa$ spread= 0.0782		$\Delta\kappa$ spread= 0.0817
Integrated Luminosity = 1000 fb^{-1}			
P_V^T	-0.00106< λ <0.000973	(-0.00119,0.00117)	-0.0016< λ <0.00152
	λ spread= 0.00204		λ spread= 0.00312
P_V^T	-0.0266< $\Delta\kappa$ <0.0286	(-0.015,0.00756)	-0.0305< $\Delta\kappa$ <0.0296
	$\Delta\kappa$ spread= 0.0552		$\Delta\kappa$ spread= 0.0601
Integrated Luminosity = 10^6 fb^{-1}			
P_V^T	-0.000101< λ <9.93e-05	(-0.00119,0.00117)	-0.00119< λ <0.00117
	λ spread= 0.0002		λ spread= 0.00237
P_V^T	-0.00235< $\Delta\kappa$ <0.00255	(-0.015,0.00756)	-0.0152< $\Delta\kappa$ <0.00798
	$\Delta\kappa$ spread= 0.00491		$\Delta\kappa$ spread= 0.0232

Table 5.18: The 95% confidence intervals for anomalous TGC parameters as a function of integrated luminosity for $W\gamma$ production at the LHC.

	95% Statistical Limit	⊕All Systematics	95% Confidence Limit (stat⊕syst)
Integrated Luminosity = 10 fb^{-1}			
P_V^T	-0.00999< λ <0.00998	(-0.00317,0.00307)	-0.0105< λ <0.0104
	λ spread= 0.02		λ spread= 0.0209
P_V^T	-0.176< $\Delta\kappa$ <0.177	(-0.0864,0.0864)	-0.196< $\Delta\kappa$ <0.197
	$\Delta\kappa$ spread= 0.353		$\Delta\kappa$ spread= 0.393
P_V^T	-0.011< Δg^1 <0.0152	(-0.00695,0.00695)	-0.013< Δg^1 <0.0167
	Δg^1 spread= 0.0262		Δg^1 spread= 0.0297
Integrated Luminosity = 30 fb^{-1}			
P_V^T	-0.00652< λ <0.0066	(-0.00317,0.00307)	-0.00725< λ <0.00727
	λ spread= 0.0131		λ spread= 0.0145
P_V^T	-0.113< $\Delta\kappa$ <0.126	(-0.0864,0.0864)	-0.143< $\Delta\kappa$ <0.153
	$\Delta\kappa$ spread= 0.239		$\Delta\kappa$ spread= 0.295
P_V^T	-0.00641< Δg^1 <0.00972	(-0.00695,0.00695)	-0.00945< Δg^1 <0.012
	Δg^1 spread= 0.0161		Δg^1 spread= 0.0214
Integrated Luminosity = 100 fb^{-1}			
P_V^T	-0.00415< λ <0.00429	(-0.00317,0.00307)	-0.00522< λ <0.00527
	λ spread= 0.00843		λ spread= 0.0105
P_V^T	-0.0707< $\Delta\kappa$ <0.0881	(-0.0864,0.0864)	-0.112< $\Delta\kappa$ <0.123
	$\Delta\kappa$ spread= 0.159		$\Delta\kappa$ spread= 0.235
P_V^T	-0.00359< Δg^1 <0.00581	(-0.00695,0.00695)	-0.00782< Δg^1 <0.00906
	Δg^1 spread= 0.0094		Δg^1 spread= 0.0169
Integrated Luminosity = 300 fb^{-1}			
P_V^T	-0.00283< λ <0.00293	(-0.00317,0.00307)	-0.00425< λ <0.00424
	λ spread= 0.00576		λ spread= 0.00849
P_V^T	-0.0474< $\Delta\kappa$ <0.0633	(-0.0864,0.0864)	-0.0985< $\Delta\kappa$ <0.107
	$\Delta\kappa$ spread= 0.111		$\Delta\kappa$ spread= 0.206
P_V^T	-0.00216< Δg^1 <0.00336	(-0.00695,0.00695)	-0.00728< Δg^1 <0.00772
	Δg^1 spread= 0.00552		Δg^1 spread= 0.015
Integrated Luminosity = 1000 fb^{-1}			
P_V^T	-0.00187< λ <0.00195	(-0.00317,0.00307)	-0.00368< λ <0.00363
	λ spread= 0.00382		λ spread= 0.00732
P_V^T	-0.0295< $\Delta\kappa$ <0.0429	(-0.0864,0.0864)	-0.0913< $\Delta\kappa$ <0.0964
	$\Delta\kappa$ spread= 0.0724		$\Delta\kappa$ spread= 0.188
P_V^T	-0.00124< Δg^1 <0.00175	(-0.00695,0.00695)	-0.00706< Δg^1 <0.00717
	Δg^1 spread= 0.00299		Δg^1 spread= 0.0142
Integrated Luminosity = 10^6 fb^{-1}			
P_V^T	-0.000196< λ <0.000201	(-0.00317,0.00307)	-0.00318< λ <0.00307
	λ spread= 0.000397		λ spread= 0.00625
P_V^T	-0.00149< $\Delta\kappa$ <0.00151	(-0.0864,0.0864)	-0.0864< $\Delta\kappa$ <0.0864
	$\Delta\kappa$ spread= 0.003		$\Delta\kappa$ spread= 0.173
P_V^T	-9.95e-05< Δg^1 <0.000101	(-0.00695,0.00695)	-0.00695< Δg^1 <0.00695
	Δg^1 spread= 0.0002		Δg^1 spread= 0.0139

Table 5.19: The 95% confidence intervals for anomalous TGC parameters as a function of integrated luminosity for WZ production at the LHC.

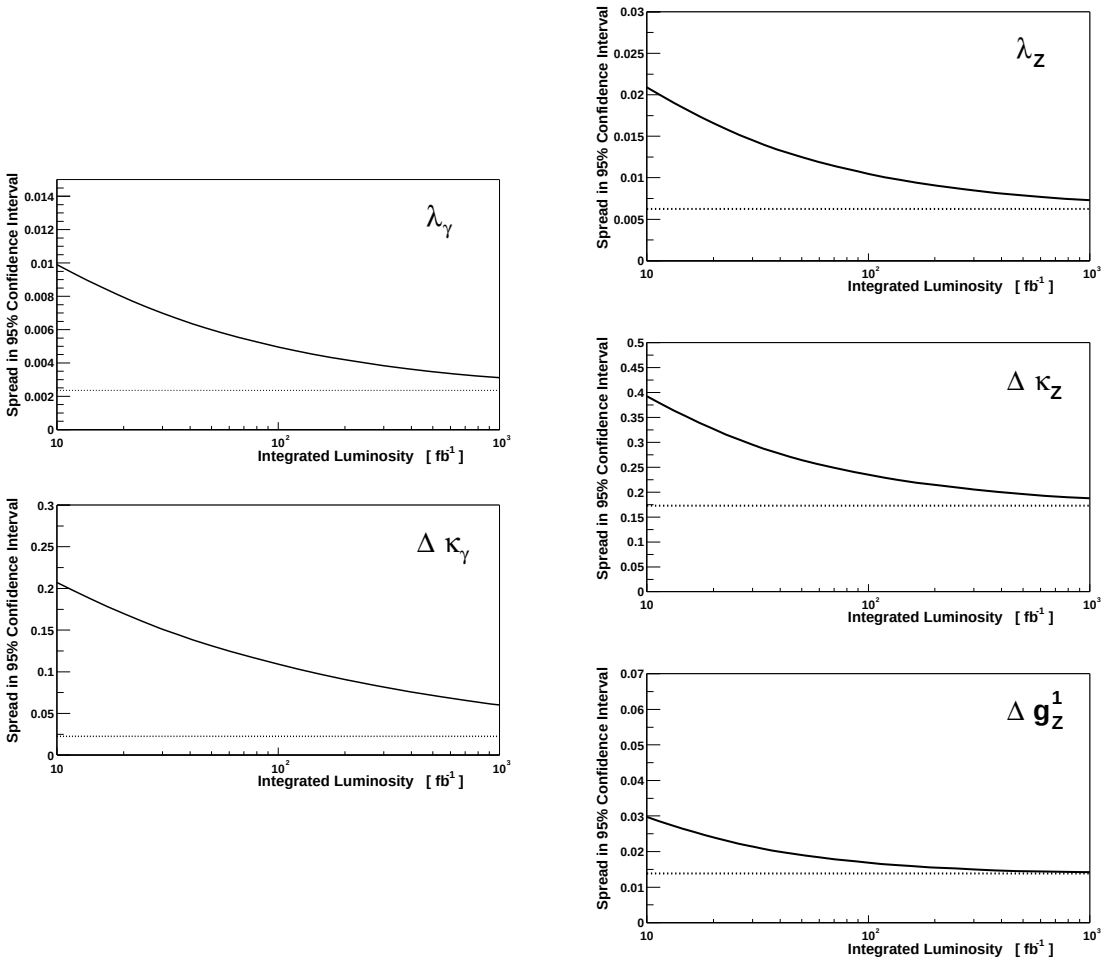

Figure 5.13: The 95% confidence intervals (solid lines) are shown as a function of integrated luminosity for $W\gamma$ production (left) and WZ production (right) at the LHC. The dotted lines indicate the magnitude of the systematic contributions, which are added in quadrature to the 95% statistical confidence limits to obtain the total confidence intervals (shown as solid lines).

fidence intervals for the Δg_Z^1 parameter at 30 fb^{-1}. Very little can be gained for this parameter by increasing the integrated luminosity, unless the systematics can be controlled at a level beyond what has been assumed for this study (recall that the systematics considered here are pessimistic).

5.8 Limits as a Function of Form Factor Scale and Mass Scale

Any measurement of anomalous TGC's integrated over a range of diboson invariant mass (which is equivalent to parton center-of-mass at leading order) depends on the form factor assumptions, as described in Sec. 3.4. For the results presented thus far, the anomalous TGC's are assumed constant (i.e. $\Lambda_{\rm FF} = \infty$). In this section, the effect of introducing a dipole form factor (which is the conventional form factor assumption) is studied, and the impact on the confidence intervals is evaluated. After showing that the constant form factor limits at LHC are consistent with the limits that would be obtained with a unitarity-safe dipole form factor, a new strategy of presenting the limits as a function of a diboson mass cutoff is presented.

The form factor scale $\Lambda_{\rm FF}$ acts as a cutoff on the effects of the anomalous TGC parameters. As such, a smaller $\Lambda_{\rm FF}$ will result in a reduced impact of the anomalous TGC parameters, making their effect more difficult to observe. As the $\Lambda_{\rm FF}$ scale assumed in an analysis is increased from a small scale to a larger scale, the confidence intervals will decrease, until eventually an asymptotic limit is reached. This asymptotic limit occurs when the $\Lambda_{\rm FF}$ is so large that the form factor is operating at a scale at which the experimental data has no sensitivity. In this way, the point at which the limits turn asymptotic reflects the maximum scale at which the experiment is able to probe new physics which has been integrated out using the parametrized TGC Lagrangian. In a previous study of form factors [Dob99b], the $\Lambda_{\rm FF}$ scale at which the limits turn asymptotic was labelled $\Lambda_{\rm machine}$, and it was argued that $\Lambda_{\rm machine}$ is a property of the collider machine, and the most natural choice for a dipole form factor scale in the case where confidence limits are being derived. This strategy was adopted

in Refs. [Atl02a] and [CMS00], and is the natural strategy for dipole form factors.

The spread in the statistical 95% confidence limits are presented in Figure 5.14 as a function of form factor scale $\Lambda_{\rm FF}$, assuming the dipole (n=2) form factor expression of Eq. 3.16. The limits turn asymptotic at about $\Lambda_{\rm machine}$ = 5 to 10 TeV. Increasing $\Lambda_{\rm FF}$ beyond this value will not improve the anomalous TGC limits. This implies TGC measurements at the LHC are able to probe new physics operating at a scale up to about 5 or 10 TeV. The unitarity limits (as presented in Eq. 3.17) are superimposed on the plots as dotted lines.

For the limits presented in this thesis, constant anomalous TGC's have been used, which is equivalent to $\Lambda_{\rm FF} = \infty$, and violates unitarity at high energy scales. Figure 5.14 can be used to evolve these limits back to any dipole form factor scale choice. From the figure, one may see that the $\Lambda_{\rm FF} = \infty$ form factor scale provides equivalent results down to scales of about 5 to 10 TeV. This is $\Lambda_{\rm machine}$ for WWV couplings at the LHC. For the λ_V and Δg_Z^1 parameters, the limits which will be obtained at the LHC are well below the unitarity limit.

Unitarity provides stricter bounds on the $\Delta\kappa_Z$ parameter for $\Lambda_{\rm FF}$ >5 TeV than will be obtained with 30 fb^{-1} at the LHC. This means that if one wishes to have limits which are strictly within the unitarity allowed region, a form factor scale smaller than 5 TeV would need to be employed.

Before introducing a new approach for presenting the limits as a function of mass scale, a few comments are in order about the choice of scale for a dipole form factor. The author advocates against an approach which uses a form factor scale which is significantly smaller than $\Lambda_{\rm machine}$ (5 to 10 TeV at the LHC, and about 2 TeV at the Tevatron) and prefers to present limits using $\Lambda_{\rm machine}$ even if those limits would be in violation of unitarity. The primary argument in support of this philosophy is that the $\Lambda_{\rm FF}$ defines the scale at which the effective Lagrangian description (wherein the new physics has been integrated out and described in terms of a small number of low-dimensional operators) breaks down. Effectively, a scale has been reached at which the effects of the new physics are directly visible. There is no reason to expect the effects of this new physics to turn off at that scale—rather it will appear

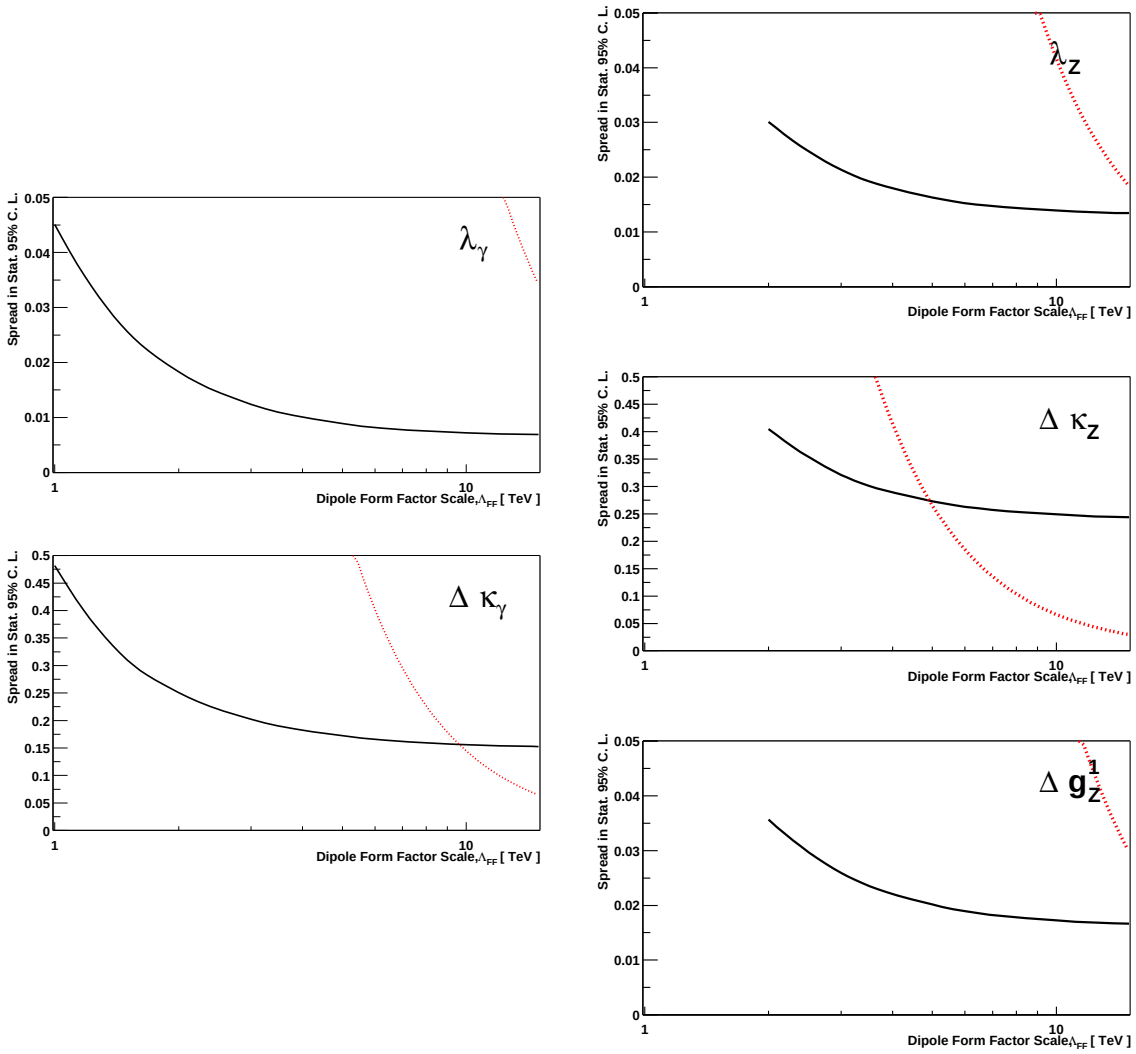

Figure 5.14: The spread in statistical 95% confidence intervals (solid lines) are shown as a function of the dipole form factor scale assumption $\Lambda_{\rm FF}$ for $W\gamma$ production (left) and WZ production (right) at the LHC (assuming an integrated luminosity of 30 fb^{-1}). The dotted lines indicate the approximate Born level unitarity limits from Eq. 3.17. The region above the solid line is excluded by the experiment, while the region to the right of the dotted line is excluded by unitarity.

directly, but will not be parameterizable in terms of the effective TGC Lagrangian. If a form factor scale smaller than Λ_{machine} is used, then it will be absolutely essential to *neglect data* collected at the scales where the assumed form factor operates. This is because in that energy regime, the effective model Lagrangian is fully constrained to the Standard Model (since the anomalous TGC's $\rightarrow 0$ at Λ_{FF}), and it makes no sense to include such data in a fit to extract the anomalous TGC's.[11] However, the data which is collected at the largest scales is potentially the most interesting, and one does not wish to be in a position where it needs to be discarded.

In Figure 5.15 a new method for reporting the limits is presented. Here the limits are presented as a function of a diboson mass cutoff (the minimum mass solution of Eq. 5.4 is used). For example, the limits at $\text{Mass}(WV)_{\text{min}} = 2$ TeV use only the data for which the reconstructed minimum mass solution is less than 2 TeV. As for the dipole form factor scale, an asymptotic limit is reached. This time the limit is at about 3 TeV. The unitarity limit is superimposed on the plots as a dotted line (here the limits of Eq. 3.14 are the relevant ones). The region above the solid line is excluded by the experiment, while the region to the right of the dotted line is excluded by unitarity.

This strategy allows for the presentation of limits without introducing arbitrary choices for the energy dependent form factor parametrization. It shows the ultimate reach of the experiment, while allowing the interpretation of the results at any mass scale. Further, if an anomalous coupling 'turns on' or 'turns off' at some mass scale, that would be reflected in the limits.

In summary, the use of a specific energy dependent form factor parametrization in the effective TGC Lagrangian is arbitrary, and contrary to the underlying assumption of being able to integrate out the physics which is producing the anomaly. Rather than safeguarding unitarity by invoking these form factors, the author advocates presenting the confidence intervals as a function of a diboson mass cutoff which is applied to the

[11] The danger of performing such a fit is demonstrated by an example in Ref. [Dob99b], wherein it was shown that a measurement of a small anomalous TGC parameter which is constant at scales $\leq \Lambda_{\text{machine}}$ will be vastly over-estimated if a form factor scale smaller than Λ_{machine} is artificially imposed.

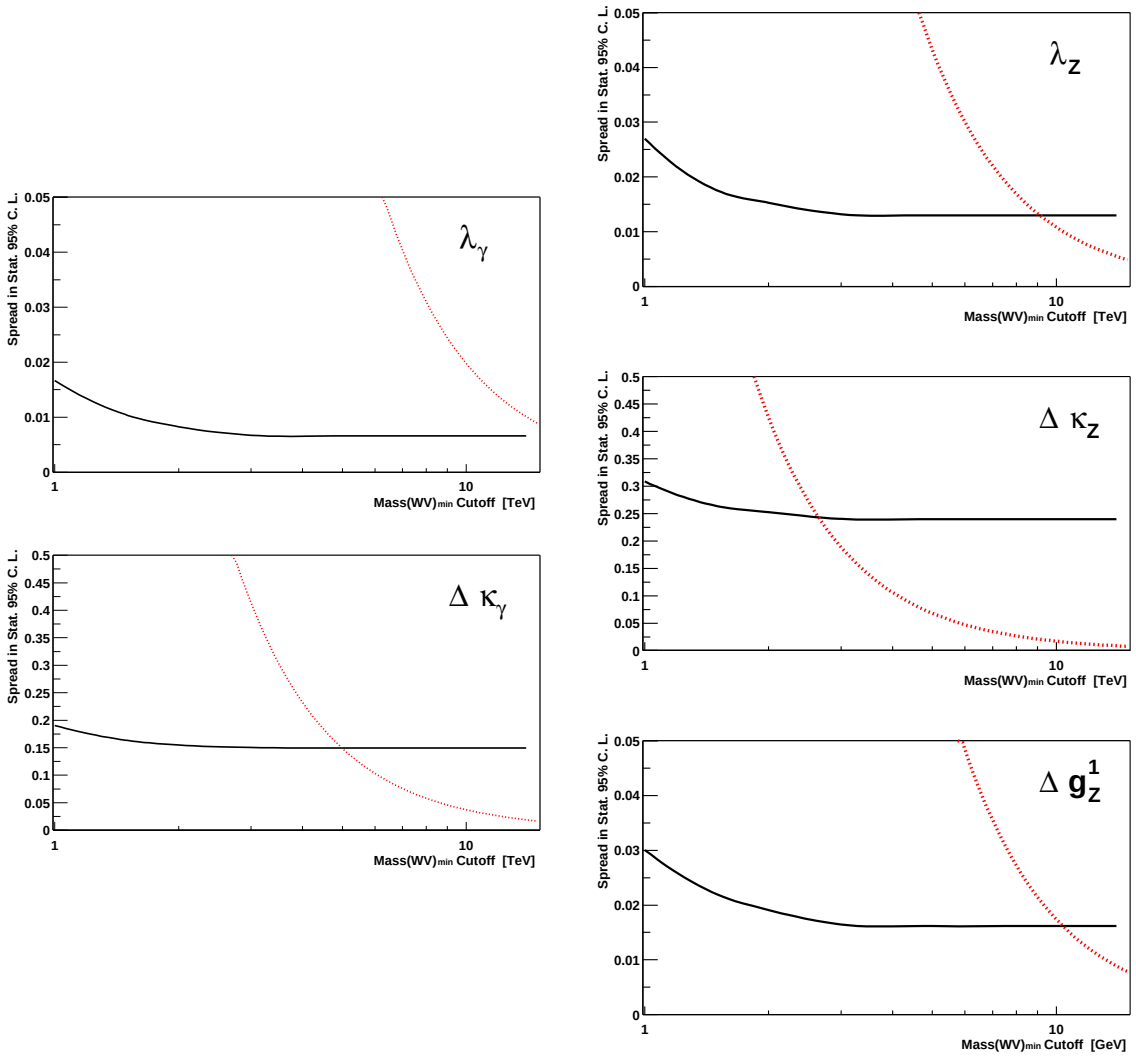

Figure 5.15: The spread in statistical 95% confidence intervals (solid lines) are shown as a function the diboson mass cutoff, which is used as a selection criteria for events included in the analysis. Limits for the $W\gamma$ production parameters are shown at left and the WZ production parameters at right, assuming an integrated luminosity of 30 fb^{-1} at the LHC. The dotted lines indicate the approximate Born level unitarity limits from Eq. 3.14. The region above the solid line is excluded by the experiment, while the region to the right of the dotted line is excluded by unitarity.

data. The point where these limits turn asymptotic is a measure of the ultimate reach of the experiment. These limits provide information about the anomalous TGC's in a manner which is as free as possible from arbitrary assumptions.

5.9 Measuring the Energy Dependence of Anomalous TGC's

The form factor discussion of the previous section raises the question which has been posed in Ref. [Gou99]: if anomalous TGC measurements at LHC are inconsistent with the Standard Model, is it possible to measure the energy dependence (i.e. form factor behavior) of the anomalous TGC parameters? The feasibility of such a measurement at hadron colliders has been demonstrated in Ref. [Dob99b]. In this section, energy dependent measurements of anomalous TGC's are explored.

A large data sample of diboson events will be necessary to perform such a measurement, because the data needs to be separated out into bins of diboson mass. For $W\gamma$ and WZ production, this is complicated by the two-fold ambiguity in reconstructing the diboson invariant mass. In Sec. 5.1.2 the $M_{\rm Min}$ solution (c.f. Eq. 5.4) is shown to be a good estimator of the true diboson mass. This is the solution which is used here to divide the events into bins of diboson mass. For each diboson mass bin, the anomalous TGC parameters can be estimated using any of the techniques of Sec. 5.3. In this case, no form factor should be imposed on the reference distributions, since it is this form factor which is being measured. For this study the anomalous TGC's have been estimated in each bin using a maximum likelihood fit to the $P_{\rm V}^T$ distribution.

To demonstrate the method, 'mock' ATLAS data has been generated with bare coupling $\lambda_{V0} = 0.04$ and a dipole (n=2) form factor[12] with $\Lambda_{\rm FF} = 1500$ GeV. This 'mock data' is then compared to reference histograms of the bare coupling λ_{V0} (i.e. the reference histograms do not use a form factor) for each of the diboson mass bins. The results are presented in Figure 5.16 for $W\gamma$ and WZ production. The events have been separated out into diboson mass bins ranging from 250 GeV to 3000 GeV

[12] i.e. the coupling is $\lambda_V = \lambda_{V0}/(1 + \frac{M^2_{WV}}{\Lambda^2_{\rm FF}})^2$.

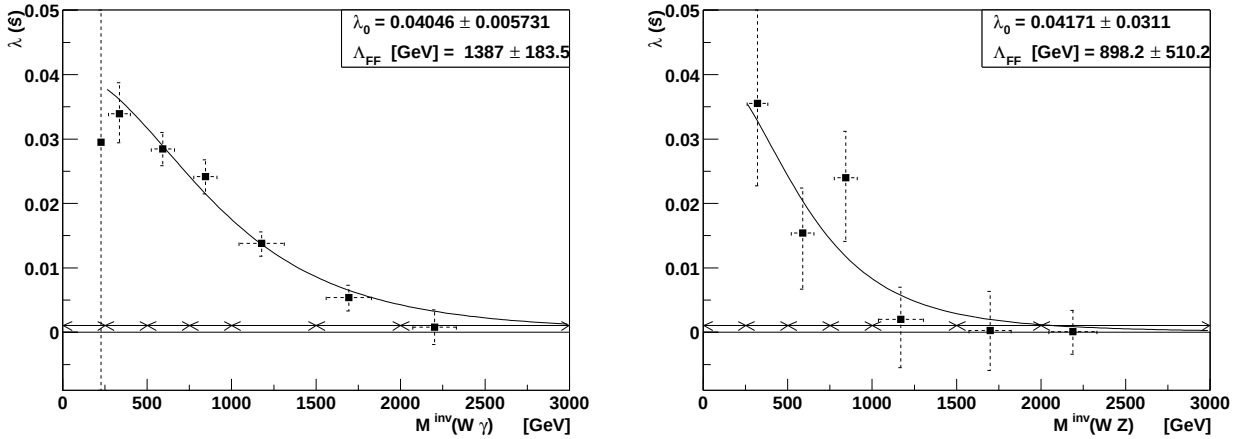

Figure 5.16: Measurements of the λ_V parameter as a function of energy are demonstrated using 30 fb^{-1} integrated luminosity for LHC $W\gamma$ production (left) and WZ production (right). The 'mock' ATLAS data has been generated with λ_{V0}=0.04 using a dipole form factor of scale $\Lambda_{\rm FF}$ = 1500 GeV. The solid line is a fit to $\Lambda_{\rm FF}$ and the bare coupling λ_{V0} assuming the dipole form factor. The arrows along the x-axis indicate the diboson mass bin widths.

with variable width, to ensure adequate statistics in each bin. Since the distribution of events within each bin is not uniform, the measured value for λ_{V0} inside each bin is indicated at the location of the mean diboson mass for the events inside the bin. The behavior of the couplings as a function of energy is clearly visible. A fit to the dipole form factor function is also indicated with a solid line. The parameters which were used to generate the 'mock' data are reproduced within the precision of the fit.

The increased event rate and sensitivity to the anomalous TGC couplings for $W\gamma$ production makes measurements of the λ_γ parameter feasible with as little as 10 fb^{-1} of data, whereas the λ_Z parameter measurement becomes feasible with about 30 fb^{-1} of data. Measurements of the $\Delta\kappa_V$ parameters require more data, and will likely not be feasible at the LHC with precisions that have not already been excluded by LEP and Tevatron data.

Chapter 6

Summary and Conclusions

This work focuses on the physics of gauge-boson production at multi-TeV hadron colliders. Experimental and phenomenological aspects have been addressed.

New techniques for incorporating next-to-leading order quantum chromodynamics matrix elements into showering and hadronization event generators have been presented. The method employs a veto which enforces the cancellations between next-to-leading order virtual and real emission contributions. The resultant calculation maintains the next-to-leading normalization and reduced scale dependence, while allowing for a consistent interface to the parton shower and probabilistic (i.e. unweighted) event generation. The method is referred to as the *phase space veto*, and has been implemented as an event generator for $p\overset{(-)}{p} \rightarrow Z^0/\gamma^\star + X \rightarrow l^+l^- + X$. It competes with leading order generators in terms of computer time and efficiency. The method is also well suited to diboson production, for which no implementation exists at this time. In order to take full advantage of the LHC physics, the construction of event generators for diboson production using the phase space veto will be a priority.

The ATLAS experiment and Large Hadron Collider (LHC) are currently under construction at CERN, with the first data expected in 2006. The LHC provides an ideal environment for testing the Standard Model through the self interactions of gauge-bosons by measuring the triple gauge-boson couplings (TGC's) which parametrize in a generic way the interactions between three gauge-bosons. This research focuses on the measurement of $WW\gamma$ and WWZ vertices through the $W\gamma$ and WZ production mechanisms, with the massive gauge-bosons decaying to electron and

muon type leptons.

The analysis is optimized for proton-proton collisions at 14 TeV and a luminosity of $10^{33}\text{cm}^{-2}\text{s}^{-1}$, which corresponds to the low luminosity running period at the LHC. An integrated luminosity of 30 fb^{-1} has been assumed for all of the results. For the $W\gamma$ analysis, W+jet production with the jet misidentified as a photon is the most important background. The $W(\rightarrow \tau\nu), \gamma$ channel is an important irreducible background. WZ production provides a very clean signal, with the backgrounds being about a factor 20 smaller than the signal.

The radiation zero refers to a particular emission angle of the photon in $W\gamma$ production which is forbidden by subtle gauge cancellations. An approximate radiation zero exists for WZ production. The radiation zero has yet to be observed experimentally. The effect will be clearly observable with 30 fb^{-1} of data from the LHC, and the characteristic asymmetric shape can be observed with symmetric proton-proton collisions by 'signing' the rapidity separation distribution according to the boost of the $\gamma, l_W^{\pm}$ system—which is suggested for the first time here.

In the scenario where the anomalous TGC parameters are consistent with the Standard Model, the LHC experiments will be in a position to set confidence limits on the anomalous parameters. A log likelihood fit to the transverse momentum of the photon or Z^0-boson (P_{V}^T) has been the conventional method for extracting the confidence intervals. It has been compared to several other methods, including a number of other one and two dimension distributions, and the method of optimal observables. The P_{V}^T distribution remains the best means of extracting the couplings for most of the TGC parameters. The two dimensional distribution of P_{V}^T versus the transverse momentum of the charged lepton from the W-decay is also very effective, and provides the best limits for the κ_V parameters. The optimal observables, which are derived and applied for the first time to hadronic collisions in this thesis, are not competitive—primarily because they require a full reconstruction of the event kinematics and a knowledge of the parton density distributions, which drastically increases the contributions from systematic effects. The expected 95% confidence

intervals for anomalous couplings are

$$\begin{array}{cccccc}
-0.0033_{\text{stat.}}, & -0.0012_{\text{syst.}} & < \lambda_\gamma < & +0.0033_{\text{stat.}}, & +0.0012_{\text{syst.}} \\
-0.0065_{\text{stat.}}, & -0.0032_{\text{syst.}} & < \lambda_Z < & +0.0066_{\text{stat.}}, & +0.0031_{\text{syst.}} \\
-0.073_{\text{stat.}}, & -0.015_{\text{syst.}} & < \Delta\kappa_\gamma < & +0.076_{\text{stat.}}, & +0.0076_{\text{syst.}} \\
-0.10_{\text{stat.}}, & -0.024_{\text{syst.}} & < \Delta\kappa_Z < & +0.12_{\text{stat.}}, & +0.024_{\text{syst.}} \\
-0.0064_{\text{stat.}}, & -0.0058_{\text{syst.}} & < \Delta g_Z^1 < & +0.010_{\text{stat.}}, & +0.0058_{\text{syst.}}
\end{array}$$

using 30 fb^{-1} (about 3 years) of low luminosity LHC data.

For all of the anomalous TGC parameters except Δg_Z^1, the confidence intervals are dominated by statistics for integrated luminosities up to 300 fb^{-1}, which is the total expected LHC luminosity. For Δg_Z^1, systematics and statistics provide equal contributions to the confidence intervals for 30 fb^{-1}, and so a detailed understanding of the systematics is necessary for measurements of this parameter at LHC.

The theoretical modeling of higher order QCD effects is the dominant systematic. The distribution of the recoil of the gauge-bosons P_{WV}^T, is a useful tool for understanding and correcting these effects because the distribution is highly sensitive to QCD corrections, but is not sensitive to anomalous TGC's at a level which has not already been excluded by previous experiments (LEP and Tevatron). A comparison of data to simulation using this distribution will provide an important cross-check that higher order corrections have been properly modeled when measuring TGC's at the LHC.

Dipole form factors have been the conventional means of guaranteeing unitarity in the TGC Lagrangian. The parametrization of the form factors is arbitrary, and introduces unnecessary dependence on the parametrization choice into the experimental results. Though the confidence intervals as a function of a dipole form factor parametrization have been included in this study, it has been argued here that it is preferable to report the limits as a function of a diboson invariant mass cutoff which is applied to the data. The LHC data will directly probe diboson invariant mass scales up to about 3 TeV, which is the scale at which the limits as a function of the mass cutoff turn asymptotic. Since unitarity is violated only for diboson mass cutoffs above 3 TeV (or in the $\Delta\kappa_Z$ case, at about 3 TeV), the limits reported here are unitarity safe, and are presented without any cutoff or form factor.

In the scenario where non-standard anomalous TGC parameters are observed, the LHC event rate will be sufficiently large to bin the data according to the diboson invariant mass. The couplings can then be measured separately in each of these bins so as to observe the energy dependent (i.e. form factor) behavior of the couplings, without assuming a particular form factor parametrization.

In addition to Monte Carlo techniques and TGC studies, the author's substantial contributions to the ATLAS hadronic calorimeter test beams, ATLAS software, and generic tools for Monte Carlo generator event records have been briefly described.

Bibliography

[†] *The references in this thesis are ordered according to collaboration or first author, and then publication date. When the title of a publication is not sufficient to communicate the relation of the publication to the thesis subject, or when historical information is pertinent, extra information is provided as comments enclosed in square brackets.*

[Acc01] E. Accomando, A. Denner and S. Pozzorini, "Electroweak-correction effects in gauge-boson pair production at the LHC," Phys. Rev. D **65**, 073003 (2002) [hep-ph/0110114].

[Ale99] R. Barate *et al.* [ALEPH Collaboration], "Measurement of W pair production in e^+e^- collisions at 183 GeV," Physics Letters B **453**, 107 (1999) [hep-ex/9903053].

[Ale01] A. Heister *et al.* [ALEPH Collaboration], "Measurement of triple gauge boson couplings at LEP energies up to 189 GeV," European Physical Journal C **21**, 423 (2001) [hep-ex/0104034].

[Ali95] The ALICE Collaboration, *ALICE - Technical Proposal for a Large Ion Collider Experiment at the CERN LHC*, CERN/LHCC/95-71, 1995.

[Alt79] G. Altarelli, R. K. Ellis and G. Martinelli, "Large Perturbative Corrections to the Drell-Yan Process in QCD," Nuclear Physics B **157**, 461 (1979);
J. Kubar-Andre and F. E. Paige, "Gluon Corrections to the Drell-Yan Model," Physical Review D **19**, 221 (1979);
K. Harada, T. Kaneko and N. Sakai, "Hadronic Lepton Pair Production Beyond the Leading Order in Perturbative QCD," Nuclear Physics B **155**, 169 (1979) [Erratum-ibid. B **165**, 545 (1979)];
J. Abad and B. Humpert, "Perturbative QCD Corrections in Drell-Yan Processes," Physics Letters B **80**, 286 (1979);
J. Abad, B. Humpert and W. L. van Neerven, "Perturbative Versus Asymptotic Freedom Corrections in Drell-Yan Processes," Physics Letters B **83**, 371 (1979);
B. Humpert and W. L. Van Neerven, "Ambiguities in the Infrared Regularization of QCD," Physics Letters B **84**, 327 (1979) [Erratum-ibid. B **85**, 471 (1979)];
B. Humpert and W. L. Van Neerven, "On the Nonleading $q\bar{q}$ and qg

Contributions in Drell-Yan Processes," Physics Letters B **85**, 293 (1979). [QCD corrections to Drell-Yan processes]

[Atl94a] The ATLAS Collaboration, *ATLAS Technical Proposal*, CERN/LHCC/94-43, 15 December 1994.

[Atl94b] D. Fouchez, "Gauge boson pairs production study with Atlas", ATLAS Internal Note PHYS-NO-060, 24 November, 1994. [first study of anomalous TGC's at ATLAS]

[Atl97a] The ATLAS Inner Detector Collaboration, *Inner Detector Technical Design Report*, CERN/LHCC/97-16 and CERN/LHCC/97-17, 30 April 1997.

[Atl97b] The ATLAS Muon Collaboration, *ATLAS Muon Spectrometer Technical Design Report*, CERN/LHCC/97-22, 5 June 1997.

[Atl98a] J.B. Hansen, "Triple Gauge-boson Couplings in Boson Pair Production", presented at the Atlas Physics Week in Grenoble April 1998. [leading order study, included in Ref. [Atl99a]]

[Atl98b] The ATLAS Collaboration, *ATLAS DAQ, EF, LVL2 and DCS Technical Progress Report*, CERN/LHCC/98-16, 30 June 1998.

[Atl98c] E. Richter-Was, D. Froidevaux, and L. Poggioli, "ATLFAST 2.0 a fast simulation package for ATLAS", ATLAS Internal Communication ATL-PHYS-98-131, 1998.

[Atl99a] The ATLAS Collaboration, *ATLAS Detector and Physics Performance Technical Design Report*, CERN/LHCC/99-14 and CERN/LHCC/99-15, 25 May 1999.

[Atl99b] M. Dobbs, M Lefebvre, and D. O'Neil, "Hadronic Endcap Modules Zero Pion and Electron Energy Scan Analysis from April 1998 Testbeam Data," ATLAS Internal Note ATL-LARG-99-001, 1999.

[Atl99c] P. Pralavorio, "Electron/Jet Separation with the ATLAS Detector", ATLAS Internal Communication ATL-COM-PHYS-99-045, 1999.

[Atl99d] M. Wielers, "Photon Identification with the ATLAS Detector", ATLAS Internal Note ATL-PHYS-99-016, 1999.

[Atl01a] F. Gianotti and P. Jenni, "Physics Impact of Staging ATLAS Detector Components", ATLAS Internal Note ATL-GEN-2001-002, September 28, 2001.

[Atl01b] S. George (on behalf of the ATLAS Collaboration), "ATLAS Trigger and Event Selection", ATLAS Internal Communication ATL-COM-CONF-2001-008, submitted to EPJdirect, 2001.

[Atl01c] M. Wielers, "Isolation of Photons", ATLAS Internal Communication ATL-COM-PHYS-2001-024, 2001.

[Atl01d] ATLAS Hadronic Endcap Collaboration, "The ATLAS Hadronic Endcap Calorimeter Beam Calibration", Nuclear Instruments and Methods **A482**, (2002) 94-124 [ATL-LARG-2001-019].

[Atl02a] S. Hassani, "Prospects for Measuring Neutral Gauge Boson Couplings in ZZ Production with the ATLAS Detector", ATLAS Internal Communication ATL-COM-PHYS-2002-012, 2002;
S. Hassani, "Prospects for Measuring Neutral Gauge Boson Couplings in $Z\gamma$ Production with the ATLAS Detector", ATLAS Internal Communication ATL-COM-PHYS-2002-013, 2002.

[Aur81] P. Aurenche and J. Lindfors, "QCD Corrections to Direct Lepton Production in Hadronic Collisions," Nuclear Physics B **185**, 274 (1981). [A factor $1/k^2$ is missing from the second term of Eq. 8 in this reference.]

[Bae89] H. Baer, J. Ohnemus and J. F. Owens, "A Next-to-Leading Logarithm Calculation of Jet Photoproduction," Physical Review D **40**, 2844 (1989).

[Bae91] H. Baer and M. H. Reno, "A Complete O(α_S) event generator for $p\bar{p} \to W + X \to e + \nu + X$ with parton showering," Physical Review D **44**, 3375 (1991);
H. Baer and M. H. Reno, "W and Z production at $p\bar{p}$ colliders: Parton showers merged with O(α_S) Monte Carlo approach," Physical Review D **45**, 1503 (1992).

[Bae99] H. Baer, F. E. Paige, S. D. Protopopescu and X. Tata, "ISAJET 7.48: A Monte Carlo event generator for pp, $\bar{p}p$, and e^+e^- reactions," hep-ph/0001086, 2000.

[Bar93] E. Barberio and Z. Was, "PHOTOS: A Universal Monte Carlo for QED radiative corrections. Version 2.0," Computer Physics Communications **79**, 291 (1994).

[Bau88a] U. Baur, D. Zeppenfeld, "Unitarity Constraints on the Electroweak Three Vector Boson Vertices," Physics Letters B **201**, 383 (1988).

[Bau88b] U. Baur and D. Zeppenfeld, "Probing the $WW\gamma$ Vertex At Future Hadron Colliders," Nuclear Physics B **308**, 127 (1988).

[Bau93a] U. Baur and E.L. Berger, "Probing the weak boson sector in $Z\gamma$ production at hadron colliders," Physical Review D **47**, 4889 (1993).

[Bau93b] Baur U., Errede S., and Ohnemus J., "Ratios of $W^{\pm}\gamma$ and $Z\gamma$ cross-sections: New tools in probing the weak boson sector at the tevatron", Physical Review D **48**, 4103-4120 (1993) [hep-ph/9304239].

[Bau93c] U. Baur, T. Han and J. Ohnemus, "QCD corrections to hadronic $W\gamma$ production with nonstandard $WW\gamma$ couplings," Physical Review D **48**, 5140 (1993).

[Bau94a] U. Baur, S. Errede and G. Landsberg, "Rapidity correlations in $W\gamma$ production at hadron colliders," Physical Review D **50**, 1917 (1994) [hep-ph/9402282].

[Bau94b] U. Baur, T. Han and J. Ohnemus, "Amplitude zeros in $W^{\pm}Z$ production," Physical Review Letters **72**, 3941 (1994) [hep-ph/9403248].

[Bau95] U. Baur, T. Han and J. Ohnemus, "WZ production at hadron colliders: Effects of nonstandard WWZ couplings and QCD corrections," Physical Review D **51**, 3381 (1995) [hep-ph/9410266].

[Bau96] U. Baur, T. Han and J. Ohnemus, "QCD corrections and nonstandard three vector boson couplings in W^+W^- production at hadron colliders," Physical Review D **53**, 1098 (1996) [hep-ph/9507336].

[Bau97] U. Baur, T. Han, N. Kauer, R. Sobey and D. Zeppenfeld, "$W\gamma\gamma$ production at the Fermilab Tevatron collider: Gauge invariance and radiation amplitude zero," Phys. Rev. **D56**, 140 (1997) [hep-ph/9702364].

[Bau98a] U. Baur, S. Keller and W. K. Sakumoto, "QED radiative corrections to Z boson production and the forward backward asymmetry at hadron colliders," Physical Review D **57**, 199 (1998) [hep-ph/9707301].

[Bau98b] U. Baur, T. Han and J. Ohnemus, "QCD corrections and anomalous couplings in $Z\gamma$ production at hadron colliders," Physical Review D **57**, 2823 (1998) [hep-ph/9710416].

[Bau01] U. Baur, O. Brein, W. Hollik, C. Schappacher and D. Wackeroth, "Electroweak radiative corrections to neutral-current Drell-Yan processes at hadron colliders," Phys. Rev. D **65**, 033007 (2002) [hep-ph/0108274].

[Bec95] D.J. Becker, T. Sterling, D. Savarese, J.E. Dorband, U.A. Ranawak, C.V. Packer, "BEOWULF: A Parallel Workstation for Scientific Computation" Proceedings, International Conference on Parallel Processing, 1995.

[Bel98] A.S. Belyaev, O.J. Eboli, M.C. Gonzalez-Garcia, J.K. Mizukoshi, S.F. Novaes and I. Zacharov, "Strongly interacting vector bosons at the LHC: Quartic anomalous couplings," Physical Review D **59**, 015022 (1999) [hep-ph/9805229].

[Ber89] L. J. Bergmann, *Next-to-leading-log QCD calculation of symmetric di-hadron production*, Ph.D. thesis, Florida State University, 1989;
H. Baer, J. Ohnemus and J. F. Owens, "A Next-to-Leading Logarithm Calculation of Jet Photoproduction," Physical Review D **40**, 2844 (1989).

[Formulation of the 2 parameter phase space slicing method for NLO QCD calculations.]

[Boo01] E. Boos, M. Dobbs, W. Giele, I. Hinchliffe, J. Huston, V. Ilyin, J. Kanzaki, K. Kato, Y. Kurihara, L. Lönnblad, M. Mangano, S. Mrenna, F. Paige, E. Richter-Was, M. Seymour, T. Sjöstrand, B. Webber, D. Zeppenfeld, "Generic User Process Interface for Event Generators", hep-ph/0109068, to be published in the *Proceedings of the Physics at TeV Colliders Workshop* held in Les Houches, France 2001.

[Bru96] R. Brun and F. Rademakers, "Root: An Object Oriented Data Analysis Framework," Proceedings AIHENP'96 Workshop, Lausanne, September 1996, Nuclear Instruments and Methods A **389**, 81 (1997), see also http://root.cern.ch/.

[Cam99] J. M. Campbell and R. K. Ellis, "An update on vector boson pair production at hadron colliders," Physical Review D **60**, 113006 (1999) [hep-ph/9905386]. [Describes the `MCFM` Monte Carlo generator.]

[Cat97] S. Catani and M. H. Seymour, "A general algorithm for calculating jet cross sections in NLO QCD," Nuclear Physics B **485**, 291 (1997) [Erratum-ibid. B **510**, 503 (1997)] [hep-ph/9605323]. [Formulation of the dipole method for NLO QCD calculations.]

[CDF95] F. Abe *et al.* [CDF Collaboration], "Observation of top quark production in $\bar{p}p$ collisions," Physical Review Letters **74**, 2626 (1995) [hep-ex/9503002].

[Cha02] U. Chattopadhyay, A. Corsetti and P. Nath, "Theoretical status of muon (g-2)," hep-ph/0202275, 2002.

[Che88] H. Y. Cheng, "The Strong CP Problem Revisited," Physics Reports **158**, 1 (1988).

[CLEO95] M. S. Alam *et al.* [CLEO Collaboration], "First measurement of the rate for the inclusive radiative penguin decay $b \to s\gamma$," Phys. Rev. Lett. **74**, 2885 (1995). [Indirect limits on the $\Delta\kappa_\gamma$ anomalous TGC.]

[CMS94] The CMS Collaboration, *CMS: The Compact Muon Solenoid Technical Proposal*, CERN/LHCC/94-38, 1994.

[CMS98] Catherine K. Mackay, *The Electromagnetic Calorimeter for CMS and a Study of the $WW\gamma$ Vertex*, Ph.D. Thesis, Brunel University, September 1998 [CMS 1999/012 THESIS];
C. K. Mackay, "Observing Anomalous Di-Boson Couplings in the $WW\gamma$ Vertex at CMS", CMS NOTE-2001/052;
C. K. Mackay, "Sensitivity of CMS to CP Conserving Anomalous Di-Boson Couplings in $W\gamma$ Events", CMS NOTE-2001/056.

[CMS00] T. Müller, D. Neuberger, W.H. Thuemmel, "Sensitivities for anomalous $WW\gamma$ and $ZZ\gamma$ couplings at CMS", CMS Internal Note CMS NOTE-2000/017, 2000.

[Col87] J. C. Collins and D. E. Soper, "The Theorems of Perturbative QCD," Annual Review of Nuclear and Particle Science **37**, 383 (1987), and references therein.

[Col01] J. Collins, "Monte-Carlo event generators at NLO," hep-ph/0110113, 2001;
Y. Chen, J. C. Collins and N. Tkachuk, "Subtraction method for NLO corrections in Monte-Carlo event generators for Z boson production," Journal of High Energy Physics **0106**, 015 (2001) [hep-ph/0105291];
J. C. Collins, "Subtraction method for NLO corrections in Monte Carlo event generators for leptoproduction," Journal of High Energy Physics **0005**, 004 (2000) [hep-ph/0001040].

[Cor01] G. Corcella *et al.*, "HERWIG 6: An event generator for hadron emission reactions with interfering gluons (including supersymmetric processes)," Journal of High Energy Physics **0101**, 010 (2001) [hep-ph/0011363].

[CTEQ94] H. L. Lai *et al.*, "Global QCD analysis and the CTEQ parton distributions," Physical Review D **51**, 4763 (1995) [hep-ph/9410404].

[CTEQ97] H. L. Lai *et al.*, "Improved parton distributions from global analysis of recent deep inelastic scattering and inclusive jet data," Physical Review D **55**, 1280 (1997) [hep-ph/9606399].

[Cza01] A. Czarnecki and W. J. Marciano, "The muon anomalous magnetic moment: A harbinger for 'new physics'," Phys. Rev. D **64**, 013014 (2001) [hep-ph/0102122].

[D0 95] S. Abachi *et al.* [D0 Collaboration], "Observation of the top quark," Physical Review Letters **74**, 2632 (1995) [hep-ex/9503003].

[D0 96] M. Kelly [D0 Experiment], "Test of the standard model of electroweak interactions by measuring the anomalous $WW\gamma$ coupling at $\sqrt{s}$ = 1.8 TeV", Notre Dame Ph.D. Thesis, South Bend Indiana, 1996. [Shows $W(\tau\nu)\gamma$ is a negligible background to $W\gamma$ production at Tevatron energy.]

[D0 97] S. Abachi *et al.* [D0 Collaboration], "Limits on anomalous $WW\gamma$ couplings from $p\bar{p} \to W\gamma + X$ events at $\sqrt{s} = 1.8$ GeV," Physical Review Letters **78**, 3634 (1997) [hep-ex/9612002].

[D0 99] B. Abbott *et al.* [D0 Collaboration], "Studies of WW and WZ production and limits on anomalous $WW\gamma$ and WWZ couplings," Physical Review D **60**, 072002 (1999) [hep-ex/9905005].

[Dav85] C. T. Davies, B. R. Webber and W. J. Stirling, "Drell-Yan Cross-Sections at Small Transverse Momentum," Nuclear Physics B **256**, 413 (1985). [Sudakov suppression]

[DeF00] D. De Florian and A. Signer, "$W\gamma$ and $Z\gamma$ production at hadron colliders," European Physical Journal C **16**, 105 (2000) [hep-ph/0002138]. [Implementation of [Dix98] for $p\overset{(-)}{p} \to W\gamma, Z\gamma$ as a NLO Monte Carlo Program, extends [Dix98] to include anomalous couplings, uses narrow width.]

[Del99a] P. Abreu *et al.* [DELPHI Collaboration], "W pair production cross-section and W branching fractions in e^+e^- interactions at 183 GeV," Physics Letters B **456**, 310 (1999).

[Del99b] P. Abreu *et al.* [DELPHI Collaboration], "Measurements of the trilinear gauge boson couplings WWV ($V = \gamma, Z$) in e^+e^- collisions at 183 GeV," Physics Letters B **459**, 382 (1999).

[Die94] M. Diehl and O. Nachtmann, "Optimal observables for the measurement of three gauge boson couplings in $e^+e^- \to W^+W^-$," Zeitschrift für Physik C **62**, 397 (1994).

[Dix98] L. Dixon, Z. Kunszt and A. Signer, "Helicity amplitudes for O(α_S) production of $W^+W^-, W^\pm Z, ZZ, W^\pm\gamma$, or $Z\gamma$ pairs at hadron colliders," Nuclear Physics B **531**, 3 (1998). [First derivation of the NLO diboson matrix elements including full spin correlations (previous calculations did not include the lepton decay angle correlations for the one-loop diagrams).]

[Dix99] L. Dixon, Z. Kunszt and A. Signer, "Vector boson pair production in hadronic collisions at O(α_S): Lepton correlations and anomalous couplings," Physical Review D **60**, 114037 (1999) [hep-ph/9907305]. [Implementation of [Dix98] for $p\overset{(-)}{p} \to WW, ZZ, WZ$ as a NLO Monte Carlo Program, extends [Dix98] to include anomalous couplings, uses narrow width.]

[Dob99a] M. Dobbs, "Performance of the ATLAS Hadronic Endcap Calorimeter in Particle Beams", Ph.D. Candidacy Paper, University of Victoria, April 28, 1999.

[Dob99b] M. Dobbs, "Unitarity Limits and Form Factors", contribution to the *Proceedings of the Standard model physics (and more) at the LHC workshop*, see [LHC99].

[Dob99c] M. Dobbs, "Partonic Simulation Tools for Diboson Production", contribution to the *Proceedings of the Standard model physics (and more) at the LHC workshop*, see [LHC99].

[Dob01a] M. Dobbs and J. B. Hansen, "The HepMC C++ Monte Carlo event record for High Energy Physics," Computer Physics Communications **134**, 41 (2001).

[Dob01b] M. Dobbs and M. Lefebvre, "Unweighted event generation in hadronic WZ production at order α_S," Physical Review D **63**, 053011 (2001) [hep-ph/0011206].

[Dob01c] M. Dobbs, "Incorporating next-to-leading order matrix elements for hadronic diboson production in showering event generators," Physical Review D **64**, 034016 (2001) [hep-ph/0103174].

[Dob01d] M. Dobbs, "Phase space veto method for next-to-leading order event generators in hadronic collisions", to appear in Physical Review D, May 2002 [hep-ph/0111234].

[Dok80] Y. L. Dokshitzer, D. Diakonov and S. I. Troian, "Hard Processes in Quantum Chromodynamics," Physics Reports **58**, 269 (1980).

[Dre70] S. D. Drell and T. M. Yan, "Massive Lepton Pair Production in Hadron - Hadron Collisions at High-Energies," Physical Review Letters **25**, 316 (1970) [Erratum-ibid. **25**, 902 (1970)].

[Ead71] W.T. Eadie, D. Drijard, F.E. James, M. Roos, and B. Sadoulet, *Statistical Methods in Experimental Physics*, North Holland, Amsterdam, and London, 1971.

[Ell81] R. K. Ellis, D. A. Ross and A. E. Terrano, "The Perturbative Calculation of Jet Structure in e^+e^- Annihilation," Nuclear Physics B **178**, 421 (1981). [Formulation of the subtraction method for NLO calculations.]

[Ell96] R. K. Ellis, W. J. Stirling and B. R. Webber, "QCD and Collider Physics," Cambridge Monographs in Particle Physics, Nuclear Physics and Cosmology **8**, 1 (1996).

[Fab81] K. Fabricius, I. Schmitt, G. Kramer and G. Schierholz, "Higher Order Perturbative QCD Calculation of Jet Cross-Sections in e^+e^- Annihilation," Zeitschrift für Physik C **11**, 315 (1981);
G. Kramer and B. Lampe, "Jet Cross-Sections in e^+e^- Annihilation," Fortschritte der Physik **37**, 161 (1989). [Formulation of the 1 parameter phase space slicing method for NLO QCD calculations.]

[Fis94] P. Fisher, U. Becker and J. Kirkby, "Very high precision tests of the electroweak theory," Physics Letters B **356**, 404 (1995).

[Fri92] S. Frixione, P. Nason and G. Ridolfi, "Strong corrections to WZ production at hadron colliders," Nuclear Physics B **383**, 3 (1992).

[Fri93] S. Frixione, "A Next-to-leading order calculation of the cross-section for the production of W^+W^- pairs in hadronic collisions," Nuclear Physics B **410**, 280 (1993).

[Gie92] W. T. Giele and E. W. Glover, "Higher order corrections to jet cross-sections in e^+e^- annihilation," Physical Review D **46**, 1980 (1992). [Formulation of the '$S_{\min}$ slicing' method for NLO QCD calculations.]

[Gie93] W. T. Giele, E. W. Glover and D. A. Kosower, "Higher order corrections to jet cross-sections in hadron colliders," Nuclear Physics B **403**, 633 (1993) [hep-ph/9302225].

[Gla61] S. L. Glashow, "Partial Symmetries of Weak Interactions," Nuclear Physics **22**, 579 (1961).

[GLAP72] L. N. Lipatov, "The Parton Model and Perturbation Theory," Yadernaya Fizika **20**, 181 (1975) [Soviet Journal of Nuclear Physics **20**, 94 (1975)];
V. N. Gribov and L. N. Lipatov, "e^+e^- Pair Annihilation and Deep Inelastic E P Scattering in Perturbation Theory," Yadernaya Fizika **15**, 1218 (1972) [Soviet Journal of Nuclear Physics **15**, 675 (1972)];
G. Altarelli and G. Parisi, "Asymptotic Freedom in Parton Language," Nuclear Physics B **126**, 298 (1977);
Y. L. Dokshitzer, "Calculation of the Structure Functions for Deep Inelastic Scattering and e^+e^- Annihilation by Perturbation Theory in Quantum Chromodynamics," Zhurnal Eksperimental'noi i Teoreticheskoi Fiziki **73**, 1216 (1977) [Soviet Physics JETP **46**, 641 (1977)]. [GLAP evolution equations]

[Gou99] G. J. Gounaris, J. Layssac and F. M. Renard, "Signatures of the anomalous $Z\gamma$ and ZZ production at the lepton and hadron colliders," Physical Review D **61**, 073013 (2000) [hep-ph/9910395]. [Proposes measuring TGC's in invariant mass bins.]

[Gro87] H. Grotch and R. W. Robinett, "New Limits From Single Photon Searches at e^+e^- Colliders," Physical Review D **36**, 2153 (1987). [First direct limits on anomalous TGC's are derived from PEP and PETRA e^+e^- storage ring data.]

[Hag87] K. Hagiwara, R. D. Peccei, D. Zeppenfeld and K. Hikasa, "Probing the Weak Boson Sector in $e^+e^- \to W^+W^-$," Nuclear Physics B **282**, 253 (1987). [Original derivation of the effective Lagrangian describing the triple gauge-boson vertex.]

[Hag93] K. Hagiwara, S. Ishihara, R. Szalapski and D. Zeppenfeld, "Low-energy effects of new interactions in the electroweak boson sector," Physical Review D **48**, 2182 (1993). [Introduces the HISZ scenario for parametrizing the effective TGC Lagrangian.]

[Har01] B. W. Harris and J. F. Owens, "The two cutoff phase space slicing method," hep-ph/0102128, 2001. [review paper]

[Hig64] P. W. Higgs, "Broken Symmetries and the Masses of Gauge Bosons," Physical Review Letters **13**, 508 (1964).

[Kaw95] S. Kawabata, "A New version of the multidimensional integration and event generation package BASES/SPRING," Computer Physics Communications **88**, 309 (1995). [The C++ version is provided by private communication from the author.]

[L3 98] M. Acciarri *et al.* [L3 Collaboration], "Measurement of W pair cross sections in e^+e^- interactions at $\sqrt{s} = 183$ GeV and W decay branching fractions," Physics Letters B **436**, 437 (1998).

[L3 99] M. Acciarri *et al.* [L3 Collaboration], "Measurement of triple-gauge-boson couplings of the W boson at LEP," Physics Letters B **467**, 171 (1999) [hep-ex/9910008].

[LEP95] G. Gounaris, J.L. Kneur, D. Zeppenfeld, Z. Ajaltouni, A. Arhrib, G. Bella, F. Berends, M. Bilenkii, A. Blondel, J. Busenitz, D. Charlton, D. Choudhury, P. Clarke, J.E. Conboy, M. Diehl, D. Fassouliotis, J.M. Frere, C. Georgiopoulos, M. Gibbs, M. Grunewald, J.B. Hansen, C. Hartmann, B.N. Jin, J. Jousset, J. Kalinowski, M. Kocian, A. Lahanas, J. Layssac, E. Lieb, C. Markou, C. Matteuzzi, P. Mattig, J.M. Moreno, G. Moultaka, A. Nippe, J. Orloff, C.G. Papadopoulos, J. Paschalis, C. Petridou, H. Phillips, F. Podlyski, M. Pohl, F.M. Renard, J.M. Rossignol, R. Rylko, R.L. Sekulin, A. van Sighem, E. Simopoulou, A. Skillman, V. Spanos, A. tonazzo, M. Tytgat, S. Tzamarias, C. Verzegnassi, N.D. Vlachos, E. Zevgolatakos, "Triple Gauge Boson Couplings", in **Physics at LEP2**, vol. 1 525-576 [hep-ph/9601233], 1996.

[LEP01a] The LEP Collaborations Aleph, Delphi, L3, OPAL and the Electroweak Working Group, "A combination of preliminary electroweak measurements and constraints on the standard model," hep-ex/0103048, February 2001.

[LEP01b] The LEP Collaborations Aleph, Delphi, L3, OPAL and the Electroweak Working Group, "A combination of preliminary electroweak measurements and constraints on the standard model," hep-ex/0103048, March 2001.

[LEP01c] The LEP Collaborations Aleph, Delphi, L3, OPAL and the Higgs Working Group, "Search for the standard model Higgs boson at LEP," hep-ex/0107029, July 2001.

[Lep78] G. P. Lepage, "A New Algorithm for Adaptive Multidimensional Integration," Journal of Computer Physics **27**, 192 (1978);
G. P. Lepage, "Vegas: An Adaptive Multidimensional Integration Program," CLNS-80/447, 1980.

[LHC95] The LHC Study Group, *The Large Hadron Collider Conceptual Design*, CERN/AC/95-05, 1995.

[LHC99] S. Haywood, P.R. Hobson, W. Hollik, Z. Kunszt, G. Azuelos, U. Baur, J. van der Bij, D. Bourilkov, O. Brein, R. Casalbuoni, A. Deandrea, S. De Curtis, D. De Florian, A. Denner, S. Dittmaier, M. Dittmar, A. Dobado, M. Dobbs, D. Dominici, R. Gatto, A. Ghinculov, F. Gianotti, M. Grazzini, J.B. Hansen, R. Harper, S. Heinemeyer, M.J. Herrero, W. Hollik, M. Lefebvre, M. Kramer, C.K. Mackay, R. Mazini, A. Miagkov, T. Muller, D. Neuberger, R. Orr, B. Osculati, J.R. Pelaez, A. Pich, D. Rainwater, M. Redi, S. Riley, E. Ruiz Morales, C. Schappacher, A. Signer, K. Sliwa, H. Spiesberger, W.H. Thummel, D. Wackeroth, G. Weiglein, D. Zeppenfeld, D. Zurcher, "Electroweak Physics", *Proceedings of the Standard model physics (and more) at the LHC workshop*, Geneva, 1999, CERN-TH-2000-102 [hep-ph/0003275].

[LHCb95] The LHCb Collaboration, *LHC-B: A Dedicated LHC Collider Beauty Experiment for Precision Measurements of CP-Violation*, CERN/LHCC/95-5, 1995.

[M-T93] T. Ishikawa, T. Kaneko, K. Kato, S. Kawabata, Y. Shimizu and H. Tanaka [MINAMI-TATEYA group Collaboration], "GRACE manual: Automatic generation of tree amplitudes in Standard Models: Version 1.0," KEK-92-19, 1992.

[Mai92] E. Maina and S. Moretti, "Z^0, γ production in association with top quark pairs," Phys. Lett. B **286**, 370 (1992).

[Mar88] G. Marchesini and B. R. Webber, "Monte Carlo Simulation of General Hard Processes with Coherent QCD Radiation," Nuclear Physics B **310**, 461 (1988).

[Mel90] B. Mele, P. Nason and G. Ridolfi, "QCD Radiative Corrections to Z Boson Pair Production in Hadronic Collisions," Nuclear Physics B **357**, 409 (1991).

[Mer90] P. Mery, S. E. Moubarik, M. Perrottet and F. M. Renard, "Constraints On Nonstandard Effects From Present And Future Muon G-2 Measurements," Z. Phys. C **46**, 229 (1990).

[Mg2 01] H. N. Brown *et al.* [Muon g-2 Collaboration], "Precise measurement of the positive muon anomalous magnetic moment," Phys. Rev. Lett. **86**, 2227 (2001) [hep-ex/0102017].

[Mik78] K. O. Mikaelian, "Photoproduction of Charged Intermediate Vector Bosons," Physical Review **D 17**, 750 (1978);
R. W. Brown, D. Sahdev and K. O. Mikaelian, "$W^{\pm}Z^0$ and $W^{\pm}\gamma$ Pair Production in νe, pp, $\bar{p}p$ Collisions," Physical Review D **20**, 1164 (1979);

K. O. Mikaelian, M. A. Samuel and D. Sahdev, "The Magnetic Moment of Weak Bosons Produced in pp and $\bar{p}p$ Collisions," Physical Review Letters **43**, 746 (1979).

[Miu99] G. Miu and T. Sjöstrand, "W production in an improved parton shower approach," Physics Letters B **449**, 313 (1999) [hep-ph/9812455];
T. Sjöstrand, "Recent progress in PYTHIA," hep-ph/0001032, 2000. [In this reference the `PYTHIA` prediction is compared to experimental data. The authors realized after publication that the experimental data had not been unfolded from detector effects, and so any interpretations of the comparison should be made with this in mind.]

[MRST98] J. S. Chen and J. R. Li, "The nonlinear spatial damping rate in QGP," Physics Letters B **430**, 209 (1998) [hep-ph/9803455].

[Ohn90] J. Ohnemus and J. F. Owens, "An Order α_S Calculation of Hadronic ZZ Production," Physical Review D **43**, 3626 (1991);
J. Ohnemus, "An Order α_S calculation of hadronic W^-W^+ production," Physical Review D **44**, 1403 (1991);
J. Ohnemus, "An Order α_S calculation of hadronic $W^\pm Z$ production," Physical Review D **44**, 3477 (1991);
J. Ohnemus, "Order α_S calculations of hadronic $W^\pm\gamma$ and $Z\gamma$ production," Physical Review D **47**, 940 (1993).

[Opa97] G. Bella, D. Charlton, P. Clarke, "Triple Gauge Boson Parameters", OPAL Technical Note TN-492, July 1, 1997. [Clarifies the relationship between various parametrizations of the anomalous TGC parameters.]

[Opa98] G. Abbiendi *et al.* [OPAL Collaboration], "W^+W^- production and triple gauge boson couplings at LEP energies up to 183 GeV," European Physical Journal C **8**, 191 (1999) [hep-ex/9811028].

[Opa99] G. Abbiendi *et al.* [OPAL Collaboration], "Measurement of the $W^+W^-\gamma$ cross-section and first direct limits on anomalous electroweak quartic gauge couplings," Phys. Lett. B **471**, 293 (1999) [hep-ex/9910069].

[Opa01] G. Abbiendi *et al.* [OPAL Collaboration], "Measurement of triple gauge boson couplings from W^+W^- production at LEP energies up to 189 GeV," European Physical Journal C **19**, 1 (2001) [hep-ex/0009022].

[Pap99] J. Papavassiliou and K. Philippides, "Probing the $WW\gamma$ vertex at hadron colliders," Physical Review D **60**, 113007 (1999) [hep-ph/9907376]. [Suggests a model-independent method for extracting anomalous coupling bounds which allows for the extraction of $\Delta\kappa_\gamma$ without having to assume the absence of other anomalous parameters.]

[PDG00a] F. James and R. Cousins, "Statistics: in Review of Particle Physics (RPP 2000)," European Physical Journal C **15**, 195 (2000).

[PDG00b] P. Igo-Kemenes, "Searches for Higgs Bosons: in Review of Particle Physics (RPP 2000)," European Physical Journal C **15**, 274 (2000).

[PDG00c] R.J. Donahue and A. Fasso, "Radioactivity and Radiation Protection: in Review of Particle Physics (RPP 2000)," European Physical Journal C **15**, 186 (2000).

[Pöt01a] B. Pötter, "Combining QCD matrix elements at next-to-leading order with parton showers," Physical Review D **63**, 114017 (2001) [hep-ph/0007172].

[Pöt01b] B. Pötter and T. Schorner, "Combining parton showers with next-to-leading order QCD matrix elements in deep-inelastic *ep* scattering," Physics Letters B **517**, 86 (2001) [hep-ph/0104261].

[Puk99] A. Pukhov *et al.*, "CompHEP: A package for evaluation of Feynman diagrams and integration over multi-particle phase space. User's manual for version 33," hep-ph/9908288, 1999.

[Sal69] A. Salam, in *Elementary Particle Theory*, edited by N. Svartholm (Almquist and Wiksells, Stockholm), p. 467.

[Sjö85] T. Sjöstrand, "A Model for Initial State Parton Showers," Physics Letters B **157**, 321 (1985).

[Sjö89] T. Sjöstrand et al., in "Z physics at LEP 1", eds. G. Altarelli, R. Kleiss and C. Verzegnassi, CERN 89-08 (Geneva, 1989), Vol. 3, p. 327.

[Sjö01a] T. Sjöstrand, P. Eden, C. Friberg, L. Lönnblad, G. Miu, S. Mrenna and E. Norrbin, "High-energy-physics event generation with PYTHIA 6.1," Computer Physics Communications **135**, 238 (2001) [hep-ph/0010017].

[Sjö01b] T. Sjöstrand, L. Lönnblad and S. Mrenna, "Pythia 6.2 User Manual" LU TP 01-21, [hep-ph/0108264], 2001. [Despite being a user manual, this reference provides an excellent and pedagogical review of Monte Carlo event generators.]

[Sno95] H. Aihara, T. Barklow, U. Baur, J. Busenitz, S. Errede, T.A. Fuess, T. Han, D. London, J. Ohnemus, R. Szalapski, C. Wendt, D. Zeppenfeld, "Anomalous gauge boson interactions", Summary of the Working Subgroup on Anomalous Gauge Boson Interactions of the DPF Long-Range Planning Study, published in *Electroweak Symmetry Breaking and Beyond the Standard Model*, eds. T. Barklow, S. Dawson, H. Haber and J. Seigrist, LBL-37155, March 1995, 53 pages [hep-ph/9503425].

[Sno96] T. Barklow, U. Baur, F. Cuypers, S. Dawson, D. Errede, S. Errede, S. Godfrey, T. Han, P. Kalyniak, K. Riles, T. Rizzo, R. Sobey, D. Strom, R. Szalapski, B.F.L. Ward, J. Womersley, J. Wudka, D. Zeppenfeld,

"Anomalous Gauge Boson Couplings", Talk given at 1996 DPF / DPB Summer Study on New Directions for High-Energy Physics (Snowmass 1996), SLAC-PUB-7366 (1996) [hep-ph/9611454].

[Ste94] T. Stelzer and W. F. Long, "Automatic generation of tree level helicity amplitudes," Computer Physics Communications **81**, 357 (1994) [hep-ph/9401258].

[Tev95] D. Benjamin, "$W\gamma$ and $Z\gamma$ production at the Tevatron," FERMILAB-CONF-95-241-E *Presented at 10th Topical Workshop on Proton-Antiproton Collider Physics, Batavia, IL, 9-13 May 1995.* [Results from Tevatron experiments D0 and CDF.]

[Tev00] U. Baur, R.K. Ellis, and D. Zeppenfeld (Editors), "QCD and Weak Boson Physics in Run II" Workshop Proceedings, March-November 1999, FERMILAB-PUB-00-297 (November 2000). [Expectation for physics potential of Tevatron experiments D0 and CDF at Run II.]

[UA1 83a] G. Arnison *et al.* [UA1 Collaboration], "Observation of Jets in High Transverse Energy Events at the Cern Proton - Anti-Proton Collider," Physics Letters B **123**, 115 (1983). [Experimental verification of jets at the Sp$\bar{\text{p}}$S.]

[UA1 83b] G. Arnison *et al.* [UA1 Collaboration], "Experimental Observation of Isolated Large Transverse Energy Electrons with Associated Missing Energy at $\sqrt{s} = 540$ Gev," Physics Letters B **122**, 103 (1983). [Experimental discovery of the W-boson at the Sp$\bar{\text{p}}$S.]

[UA1 83c] G. Arnison *et al.* [UA1 Collaboration], "Experimental Observation of Lepton Pairs of Invariant Mass Around 95 GeV/C^2 at the Cern SpS Collider," Physics Letters B **126**, 398 (1983). [Experimental discovery of the Z^0-boson at the Sp$\bar{\text{p}}$S.]

[UA2 82] M. Banner *et al.* [UA2 Collaboration], "Observation of Very Large Transverse Momentum Jets at the Cern $\bar{p}p$ Collider," Physics Letters B **118**, 203 (1982). [Experimental verification of jets at the Sp$\bar{\text{p}}$S.]

[UA2 83a] M. Banner *et al.* [UA2 Collaboration], "Observation of Single Isolated Electrons of High Transverse Momentum in Events with Missing Transverse Energy at the Cern $\bar{p}p$ Collider," Physics Letters B **122**, 476 (1983). [Experimental discovery of the W-boson at the Sp$\bar{\text{p}}$S.]

[UA2 83b] P. Bagnaia *et al.* [UA2 Collaboration], "Evidence for $Z^0 \to e^+e^-$ at the Cern $\bar{p}p$ Collider," Physics Letters B **129**, 130 (1983). [Experimental discovery of the Z^0-boson at the Sp$\bar{\text{p}}$S.]

[UA2 92] J. Alitti *et al.* [UA2 Collaboration], "Direct measurement of the $W\gamma$ coupling at the CERN $\bar{p}p$ collider," Physics Letters B **277**, 194 (1992).

[Wei67] S. Weinberg, "A Model of Leptons," Physical Review Letters **19**, 1264 (1967).

[Zep88] D. Zeppenfeld and S. Willenbrock, "Probing the Three Vector-Boson Vertex at Hadron Colliders," Physical Review D **37**, 1775 (1988). [Hadronic WZ production only, includes unitarity limits on the anomalous couplings.]

Appendix A

Staged Detector Installation

The current plan [Atl01a] for the ATLAS detector installation foresees a staging of some of the detector components. The installation of the staged components will be deferred by 1-2 years during the initial low luminosity running of the LHC. It should be emphasized that the extent of the staging cannot be finalized until much closer to the time when the LHC ring is closed.

Several considerations necessitate the need for detector staging: (1) a nine month delay is foreseen in the civil engineering of the ATLAS cavern, which significantly reduces the installation time available before the LHC ring is closed at the end of 2005, (2) several of the ATLAS detector components are on extremely tight construction schedules, (3) cost over-runs may not be recoverable in a timely manner, especially in light of the current (November 2001) LHC funding difficulties.

The staged detector concept has been optimized to maintain the discovery potential for:

- the SM Higgs boson, particularly in the low mass ($M_{\text{Higgs}} < 130$ GeV) region favored by the LEP electroweak fit [LEP01b] where the $H \to \gamma\gamma$ and $t\bar{t}H \to t\bar{t}b\bar{b}$ channels are most important.
- supersymmetry, which should mainly manifest itself as events with hard jets and missing transverse energy, necessitating hermetic calorimetry (meaning the staging of one end-cap is not feasible).
- the minimal supersymmetric Standard Model (MSSM) Higgs, wherein the $H \to \tau\bar{\tau}$ channel is also important.

The staged detector components are described in the sections which follow. The effect of the staging has been studied mainly in the context of the Standard Model Higgs discovery potential. The main conclusion from these studies [Atl01a] is a loss of significance of about 10% in several channels. This loss is expected to be recoverable by a 20% increase in integrated luminosity.

Inner Detector: one pixel layer and outermost TRT end-cap wheels

One of the two outer-most pixel layers will be staged (the inner-most layer is essential for good B-tagging performance). The staged layer will result in a 20% deterioration in the B-tagging rejection against light quarks.

In addition to the pixel layer, the outer-most wheels of the TRT will be staged. This layer provides coverage in the range $1.7< |\eta| <2.4$ and will result in a degradation of the track momentum resolution by 50% in this region (which accounts for about 20% of the inner detector acceptance).

Cryostat-Gap Scintillator

This detector sits in the gap between the electromagnetic barrel and end-cap at $1.0< |\eta| <1.6$ and helps to recover the energy resolution which is lost to the additional material (e.g. cryostat walls) in this region. The absence of this detector element would most likely result in discarding electrons and photons which fall in the crack between the EMC barrel and endcaps at $1.4< |\eta| <1.6$, reducing the detector acceptance.

Calorimetry: reduction in the readout drivers

A reduction in the number of calorimeter readout drivers will impact the maximum trigger rate, limiting it to 50 events per second, rather than the design 100 Hz.

Muon System

The muon spectrometer, positioned as it is on the outside of the detector, is a natural candidate for staging, since its components can be added most easily at a later date. MDT chambers will be staged in the transition region between barrel and end-caps, and part of the end-cap end-wall. This affects the stand-alone muon system momentum resolution by up to a factor four in the relevant regions. Half of the CSC layers including the electronics and mechanics will be staged. This will have a negligible effect on the physics performance for low luminosity running.

High Level Trigger and Data Acquisition

A scaled down and easily upgradeable version of these systems is foreseen. This should not affect the physics for low luminosity running. The computer processor farm will also be implemented in a reduced and expandable manner.

The study presented in this thesis assumes a complete ATLAS detector—the staging of the various detector components have not been included in the detector simulation.

Appendix B

Distributions for $W\gamma$ Production

The $W\gamma$ production distributions which have been used to extract the confidence intervals in Table 5.7, and have not already been presented in the text, are shown in this appendix. The P_γ^T, P_{lw}^T, mass($W\gamma$) vs. $\cos\theta_\gamma^\star$, and OO(λ_γ) distributions have already been shown in Figures 5.3, 5.5, 5.6, and 5.9 respectively.

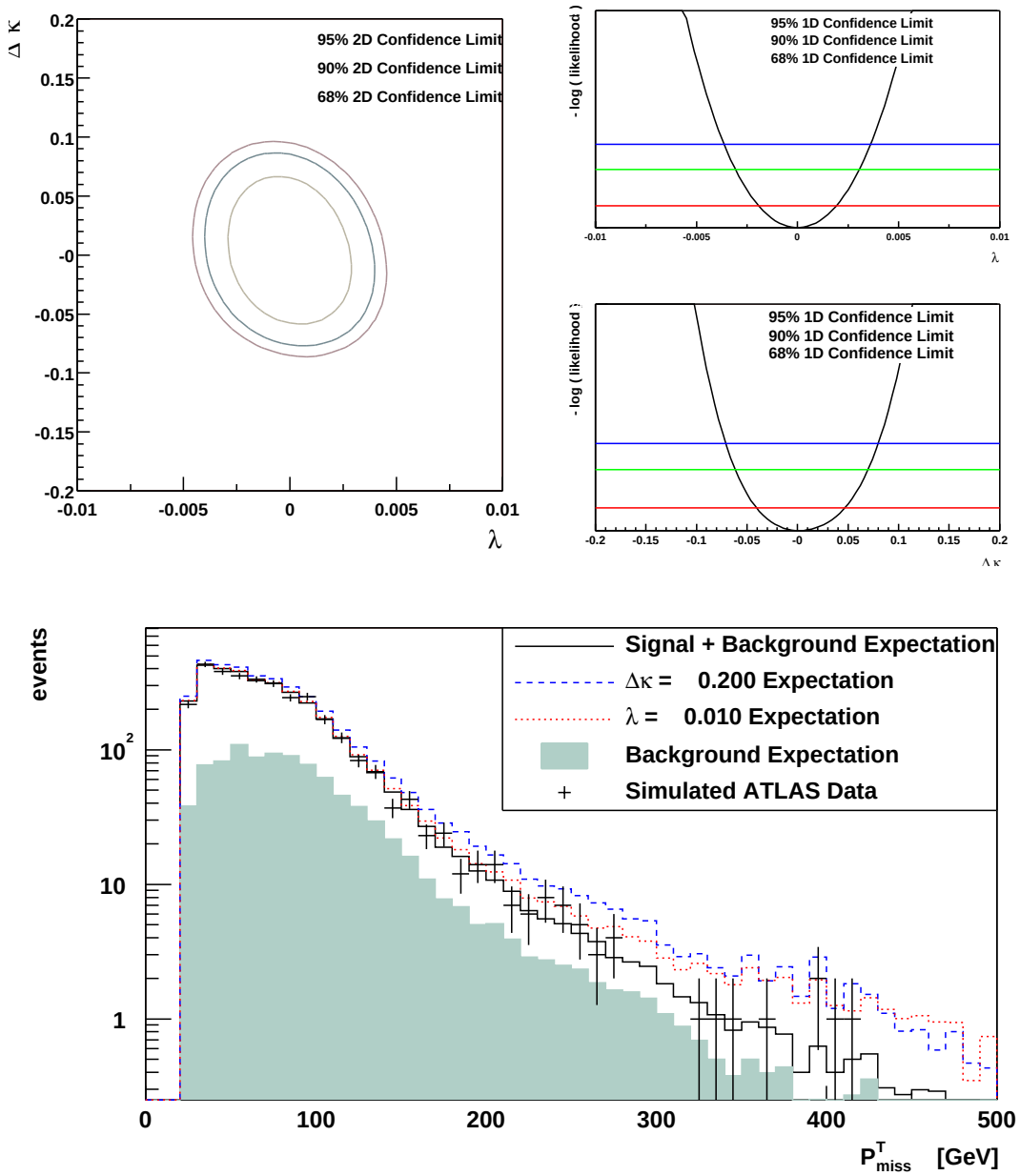

Figure B.1: The missing transverse momentum distribution in $W\gamma$ production is shown (bottom), after applying the kinematic cuts described in Chapter 4. The points with error bars represent "mock" data for one ATLAS experiment with integrated luminosity of 30 fb^{-1}. This data has been simulated using the SM TGC parameters, and includes the background contributions. The lines are the reference distributions for several choices of the anomalous TGC parameters. The contribution of backgrounds to the reference distributions is shown as a shaded histogram, and does not depend on the anomalous TGC parameters. The one (top right) and two (top left) parameter negative log likelihood curves are shown as a function of the λ_γ and $\Delta\kappa_\gamma$ parameters with the 68, 90, and 95% confidence limits indicated. These confidence limits correspond to the single experiment which has been simulated for this figure.

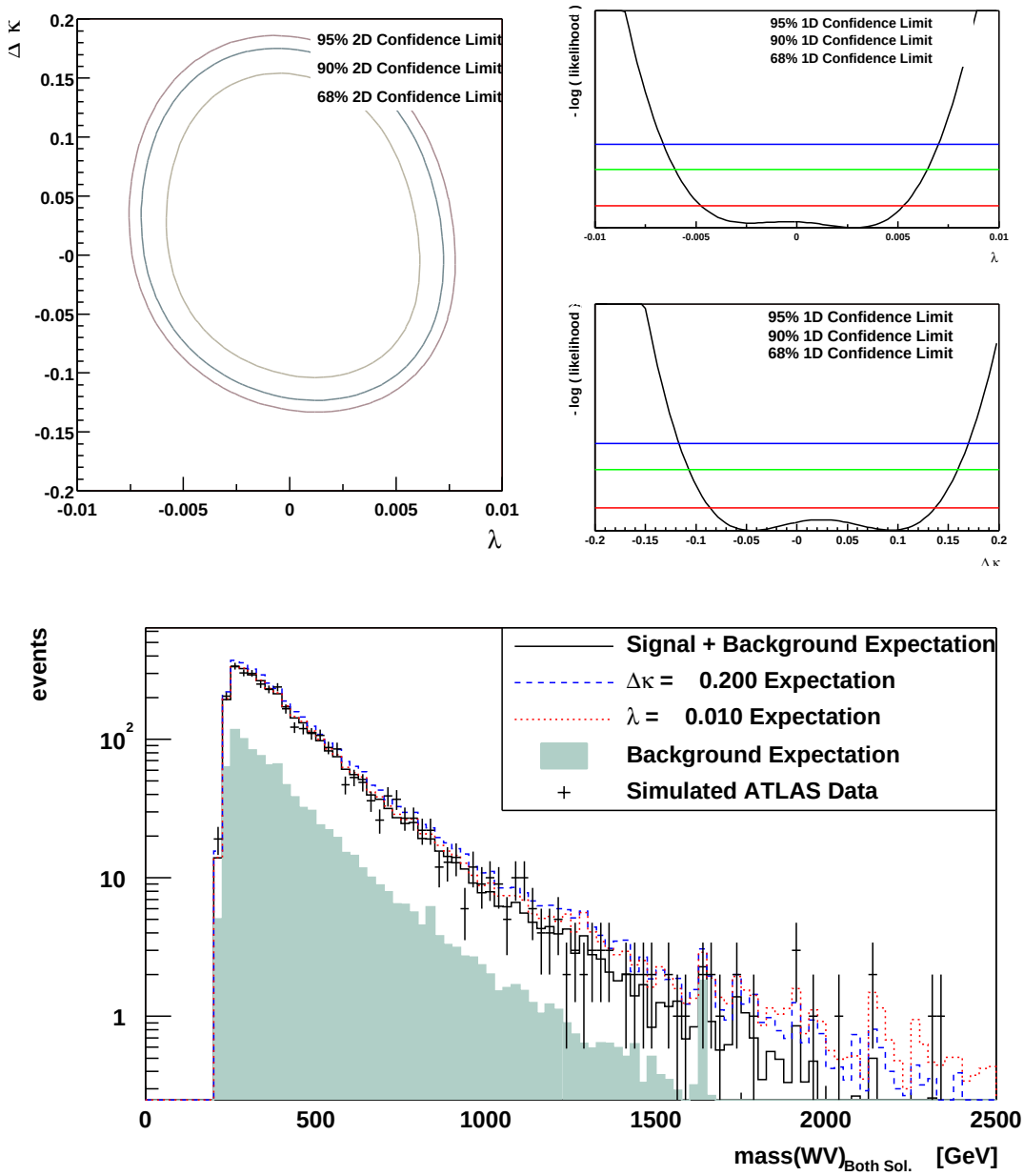

Figure B.2: The reconstructed diboson invariant mass (both solutions, Eq. 5.6) distribution in $W\gamma$ production is shown (bottom), after applying the kinematic cuts described in Chapter 4. The points with error bars represent "mock" data for one ATLAS experiment with integrated luminosity of 30 fb^{-1}. This data has been simulated using the SM TGC parameters, and includes the background contributions. The lines are the reference distributions for several choices of the anomalous TGC parameters. The contribution of backgrounds to the reference distributions is shown as a shaded histogram, and does not depend on the anomalous TGC parameters. The one (top right) and two (top left) parameter negative log likelihood curves are shown as a function of the λ_γ and $\Delta\kappa_\gamma$ parameters with the 68, 90, and 95% confidence limits indicated. These confidence limits correspond to the single experiment which has been simulated for this figure.

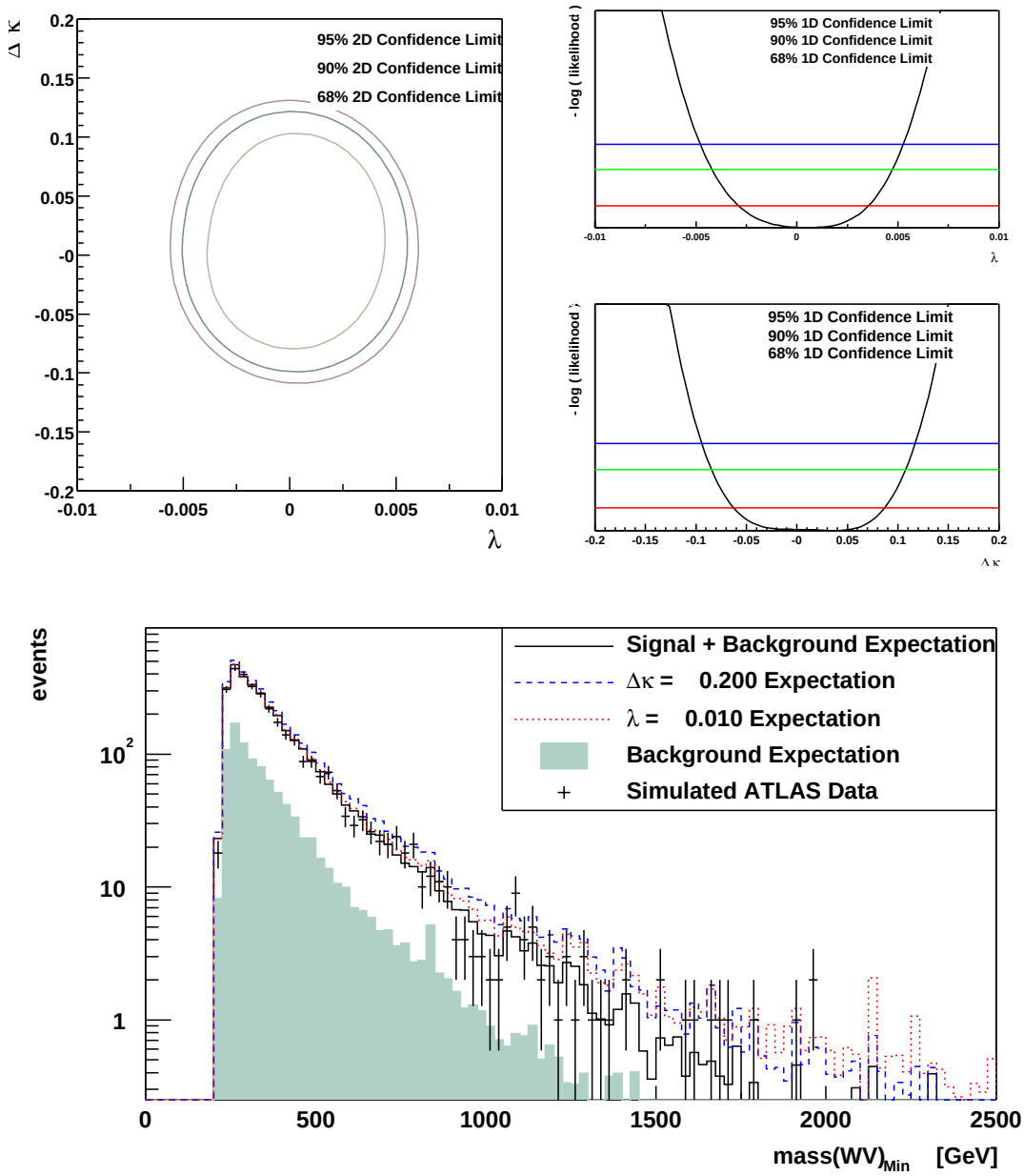

Figure B.3: The diboson invariant mass (minimum solution) distribution in $W\gamma$ production is shown (bottom), after applying the kinematic cuts described in Chapter 4. The points with error bars represent "mock" data for one ATLAS experiment with integrated luminosity of 30 fb^{-1}. This data has been simulated using the SM TGC parameters, and includes the background contributions. The lines are the reference distributions for several choices of the anomalous TGC parameters. The contribution of backgrounds to the reference distributions is shown as a shaded histogram, and does not depend on the anomalous TGC parameters. The one (top right) and two (top left) parameter negative log likelihood curves are shown as a function of the λ_γ and $\Delta\kappa_\gamma$ parameters with the 68, 90, and 95% confidence limits indicated. These confidence limits correspond to the single experiment which has been simulated for this figure.

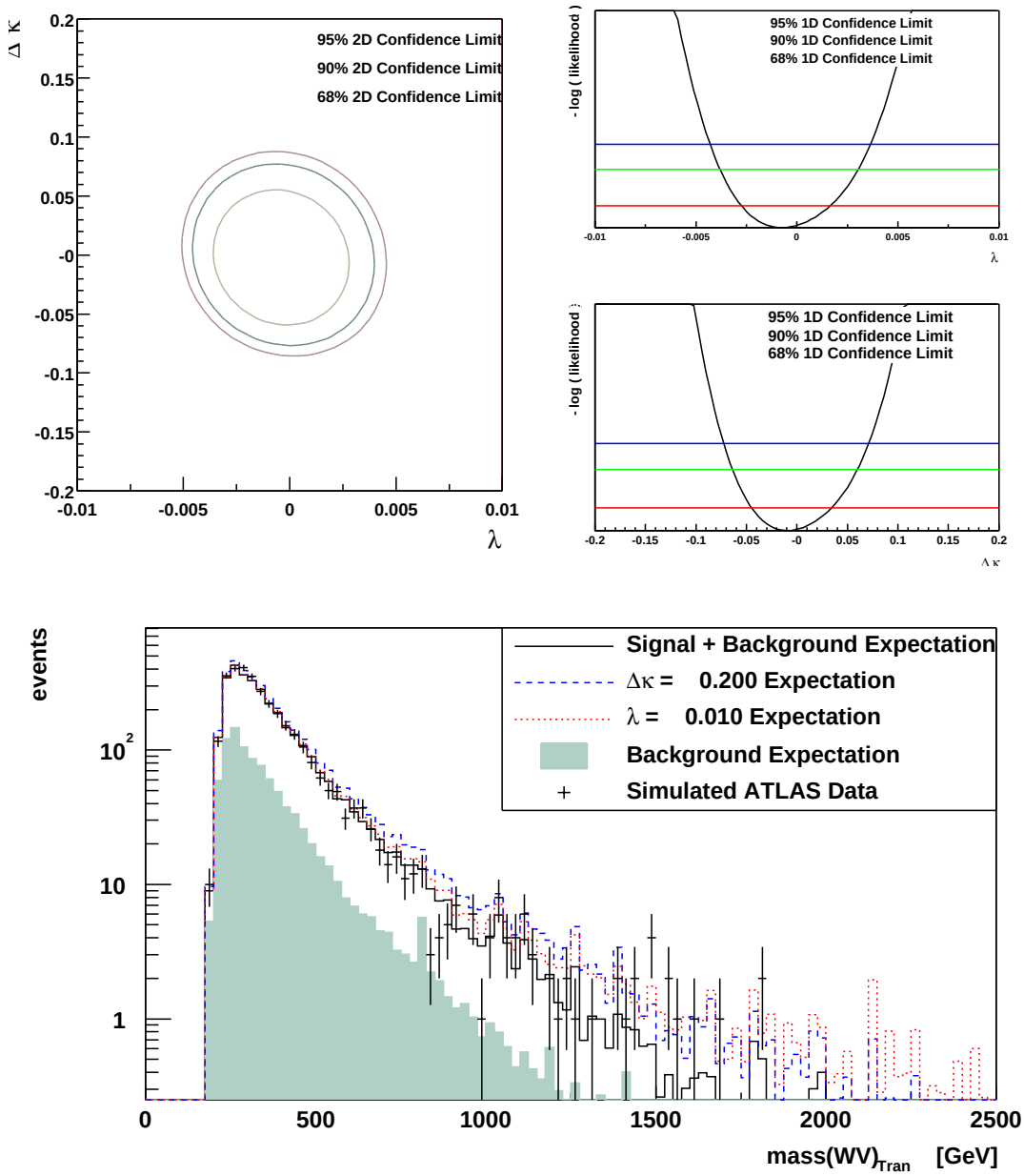

Figure B.4: The diboson transverse mass distribution in $W\gamma$ production is shown (bottom), after applying the kinematic cuts described in Chapter 4. The points with error bars represent "mock" data for one ATLAS experiment with integrated luminosity of 30 fb^{-1}. This data has been simulated using the SM TGC parameters, and includes the background contributions. The lines are the reference distributions for several choices of the anomalous TGC parameters. The contribution of backgrounds to the reference distributions is shown as a shaded histogram, and does not depend on the anomalous TGC parameters. The one (top right) and two (top left) parameter negative log likelihood curves are shown as a function of the λ_γ and $\Delta\kappa_\gamma$ parameters with the 68, 90, and 95% confidence limits indicated. These confidence limits correspond to the single experiment which has been simulated for this figure.

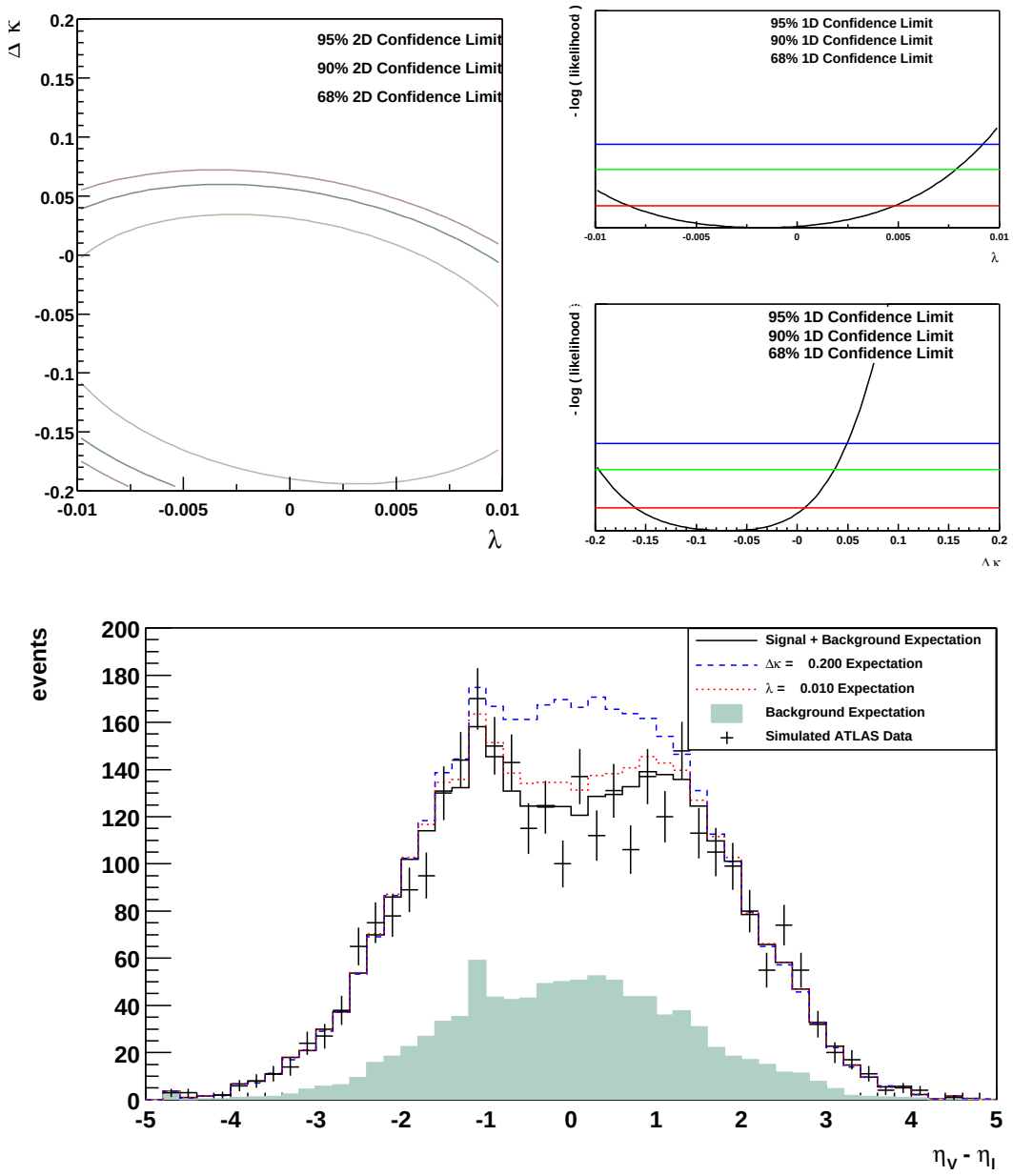

Figure B.5: The rapidity separation distribution of the photon from the charged lepton arising in the $W^{\pm}$ decay in $W\gamma$ production is shown (bottom), after applying the kinematic cuts described in Chapter 4. The points with error bars represent "mock" data for one ATLAS experiment with integrated luminosity of 30 fb^{-1}. This data has been simulated using the SM TGC parameters, and includes the background contributions. The lines are the reference distributions for several choices of the anomalous TGC parameters. The contribution of backgrounds to the reference distributions is shown as a shaded histogram, and does not depend on the anomalous TGC parameters. The one (top right) and two (top left) parameter negative log likelihood curves are shown as a function of the λ_γ and $\Delta\kappa_\gamma$ parameters with the 68, 90, and 95% confidence limits indicated. These confidence limits correspond to the single experiment which has been simulated for this figure. Note Fig. 5.2 uses a different jet veto cut as compared to here.

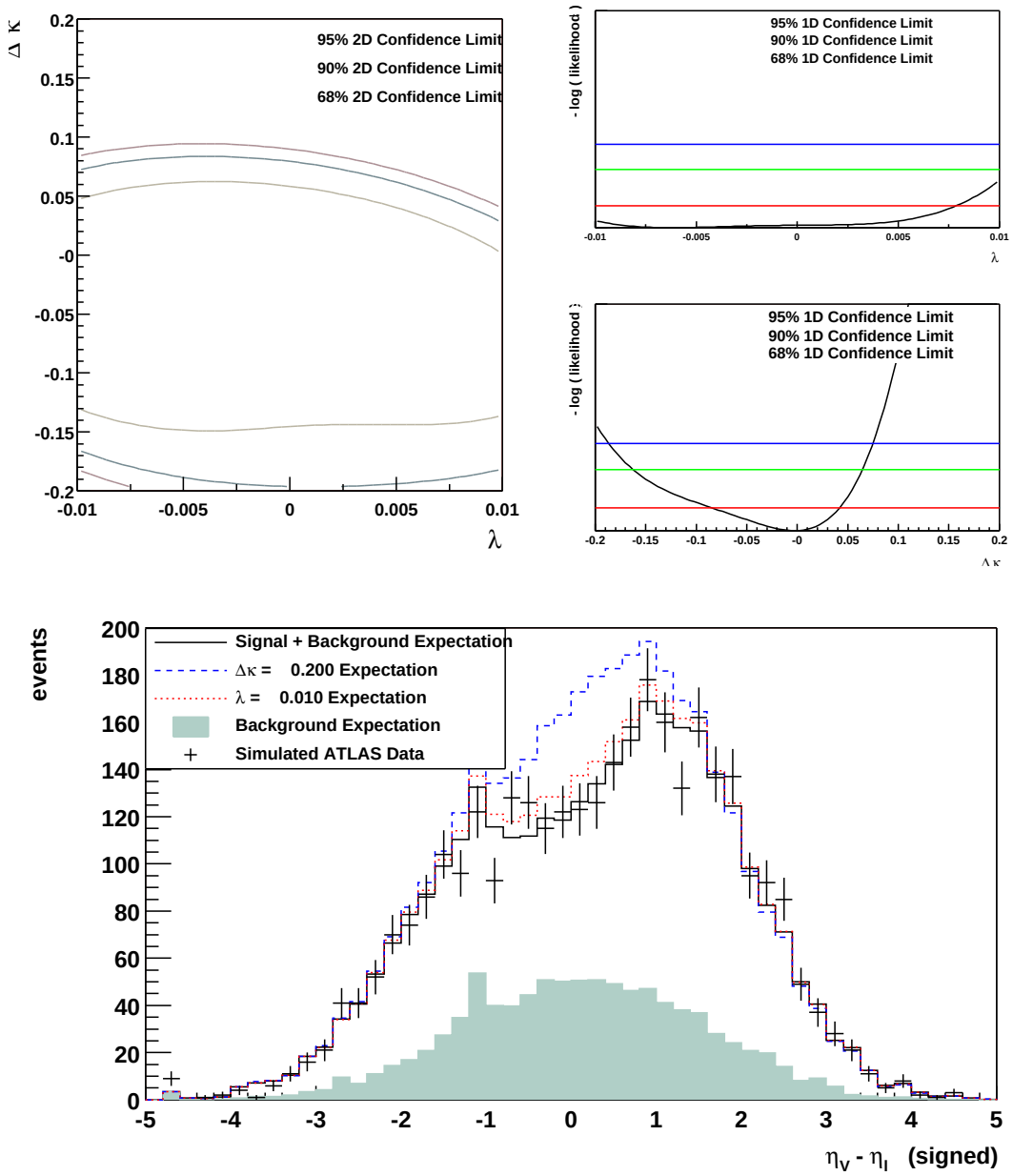

Figure B.6: The signed rapidity separation (Eq. 3.13) distribution of the photon from the charged lepton arising in the $W^{\pm}$ decay in $W\gamma$ production is shown (bottom), after applying the kinematic cuts described in Chapter 4. The points with error bars represent "mock" data for one ATLAS experiment with integrated luminosity of 30 fb^{-1}. This data has been simulated using the SM TGC parameters, and includes the background contributions. The lines are the reference distributions for several choices of the anomalous TGC parameters. The contribution of backgrounds to the reference distributions is shown as a shaded histogram, and does not depend on the anomalous TGC parameters. The one (top right) and two (top left) parameter negative log likelihood curves are shown as a function of the λ_γ and $\Delta\kappa_\gamma$ parameters with the 68, 90, and 95% confidence limits indicated. These confidence limits correspond to the single experiment which has been simulated for this figure. Note Fig. 5.2 uses a different jet veto cut as compared to here.

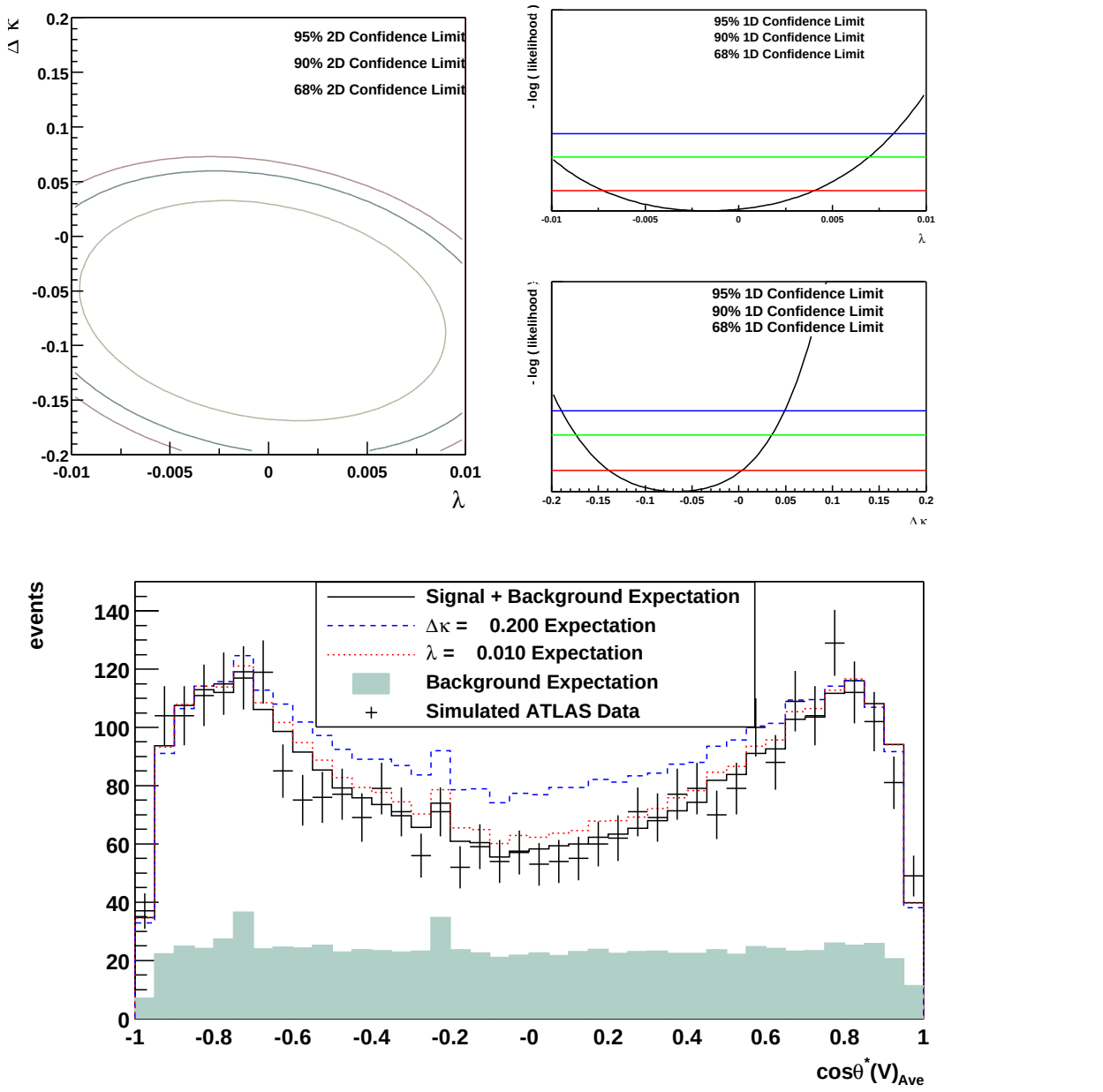

Figure B.7: The reconstructed center-of-mass frame photon production angle (both solutions are included in the histogram) distribution in $W\gamma$ production is shown (bottom), after applying the kinematic cuts described in Chapter 4. The points with error bars represent "mock" data for one ATLAS experiment with integrated luminosity of 30 fb^{-1}. This data has been simulated using the SM TGC parameters, and includes the background contributions. The lines are the reference distributions for several choices of the anomalous TGC parameters. The contribution of backgrounds to the reference distributions is shown as a shaded histogram, and does not depend on the anomalous TGC parameters. The one (top right) and two (top left) parameter negative log likelihood curves are shown as a function of the λ_γ and $\Delta\kappa_\gamma$ parameters with the 68, 90, and 95% confidence limits indicated. These confidence limits correspond to the single experiment which has been simulated for this figure.

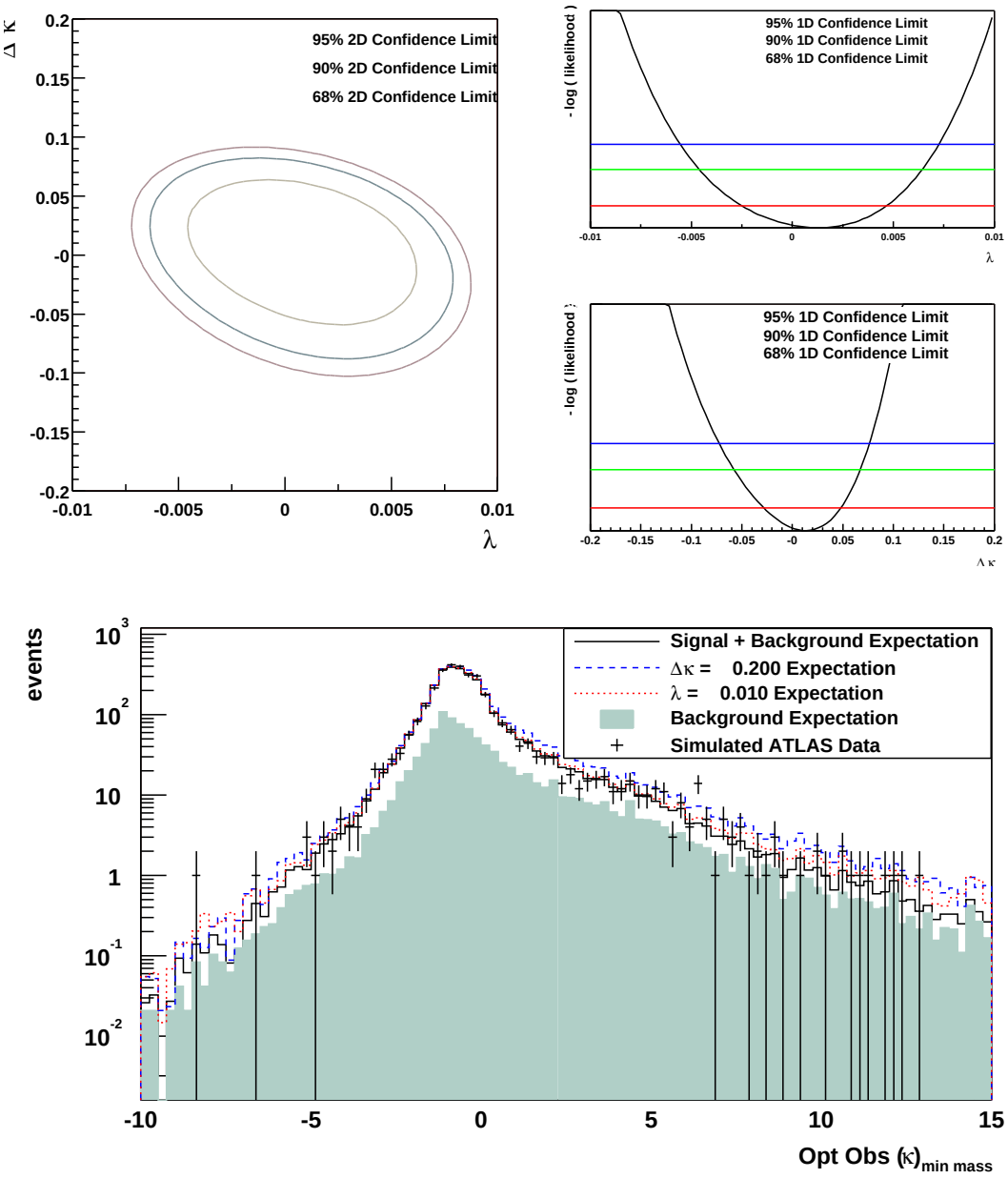

Figure B.8: The distribution of the $\Delta\kappa_\gamma$ optimal observable in $W\gamma$ production is shown (bottom), after applying the kinematic cuts described in Chapter 4. The points with error bars represent "mock" data for one ATLAS experiment with integrated luminosity of 30 fb^{-1}. This data has been simulated using the SM TGC parameters, and includes the background contributions. The lines are the reference distributions for several choices of the anomalous TGC parameters. The contribution of backgrounds to the reference distributions is shown as a shaded histogram, and does not depend on the anomalous TGC parameters. The one (top right) and two (top left) parameter negative log likelihood curves are shown as a function of the λ_γ and $\Delta\kappa_\gamma$ parameters with the 68, 90, and 95% confidence limits indicated. These confidence limits correspond to the single experiment which has been simulated for this figure.

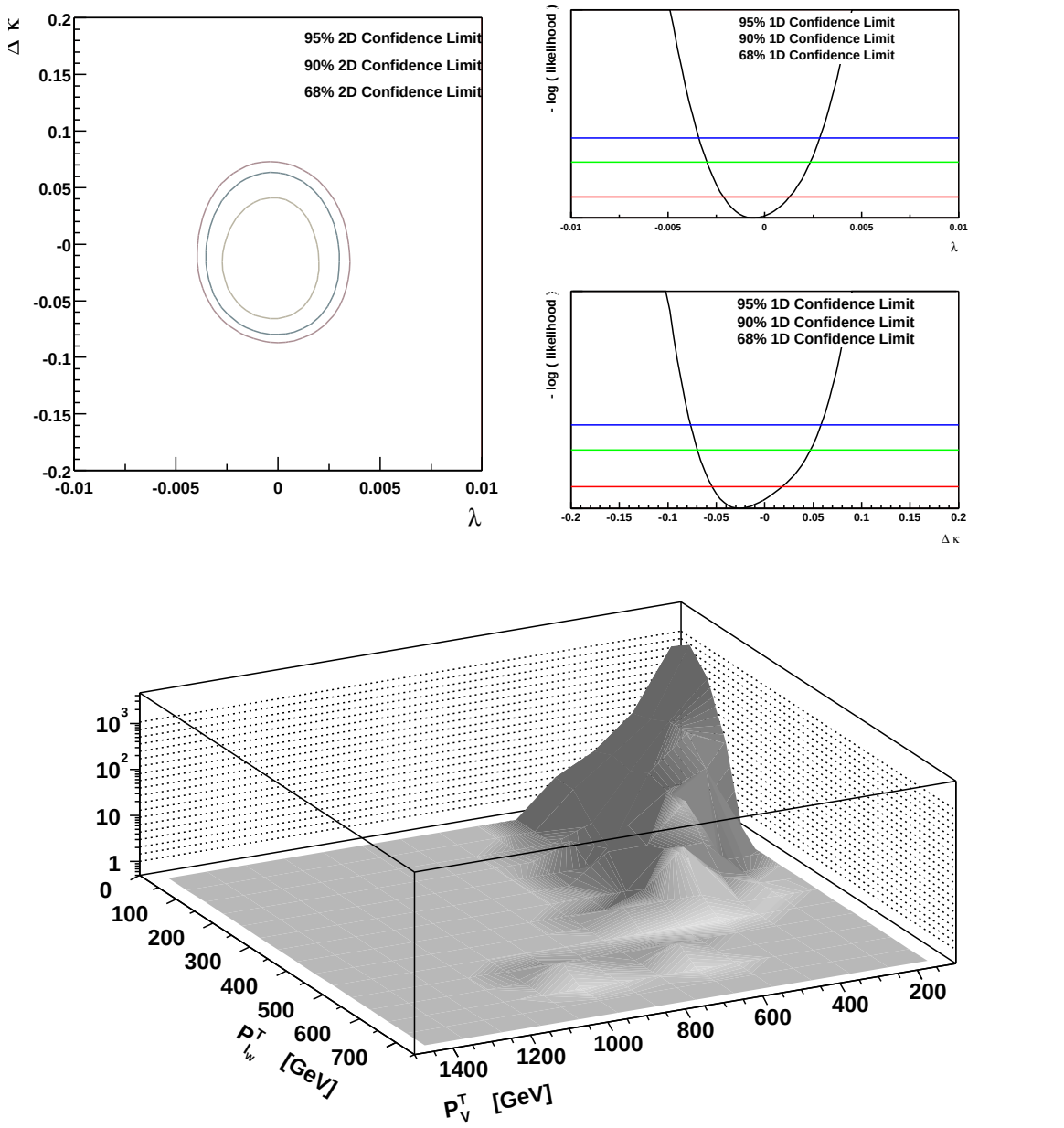

Figure B.9: The transverse momentum of the photon versus the transverse momentum of the charged lepton arising in the $W^{\pm}$ decay distribution for $W\gamma$ production is shown (bottom), after applying the kinematic cuts described in Chapter 4 for the Standard Model reference histogram (including contributions from backgrounds). The one (top right) and two (top left) parameter negative log likelihood curves are shown as a function of the λ_γ and $\Delta\kappa_\gamma$ parameters with the 68, 90, and 95% confidence limits indicated. These confidence limits correspond to the single experiment which has been simulated for this figure.

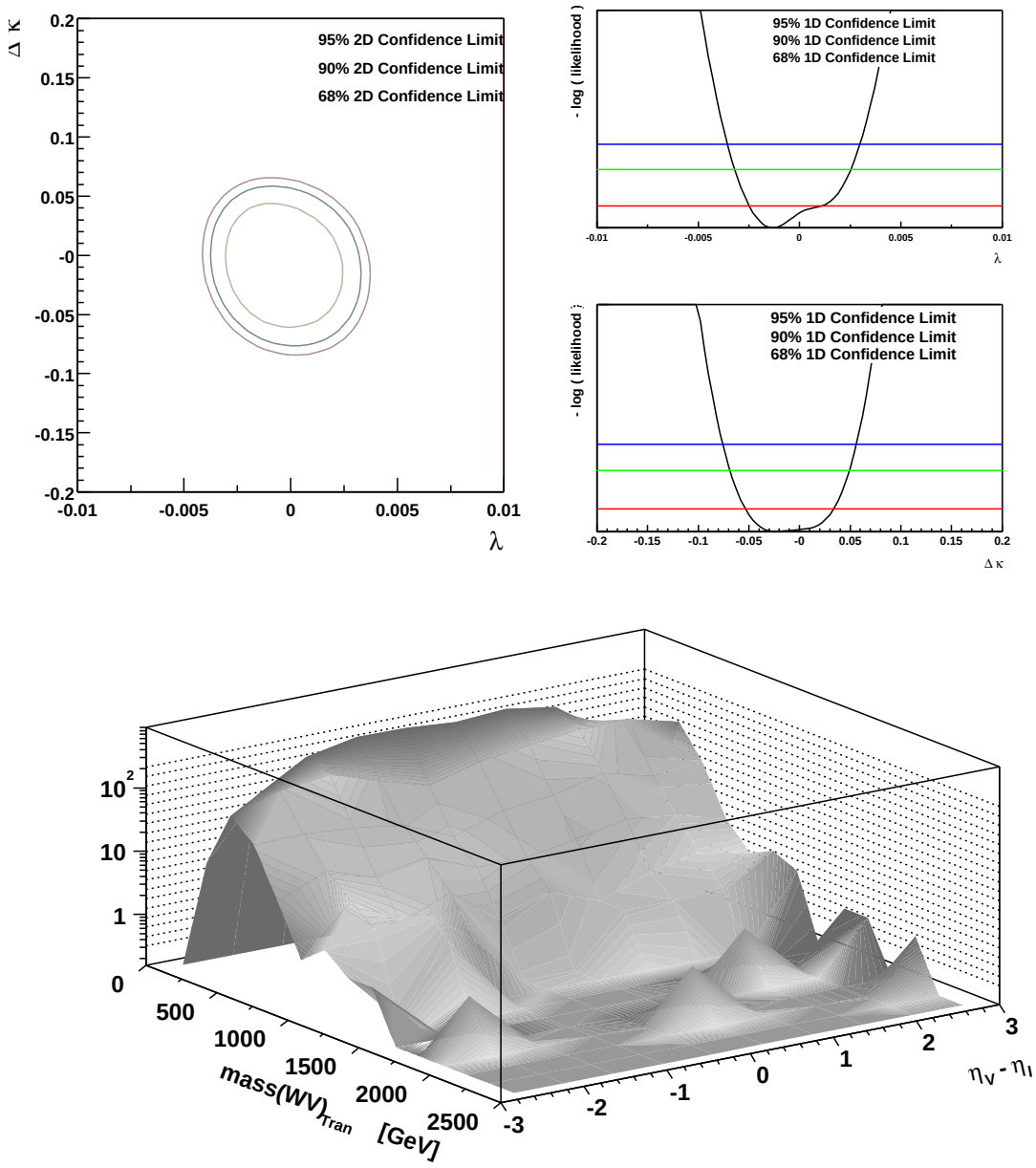

Figure B.10: The diboson transverse mass versus the rapidity separation of the photon from the charged lepton distribution for $W\gamma$ production is shown (bottom), after applying the kinematic cuts described in Chapter 4 for the Standard Model reference histogram (including contributions from backgrounds). The one (top right) and two (top left) parameter negative log likelihood curves are shown as a function of the λ_γ and $\Delta\kappa_\gamma$ parameters with the 68, 90, and 95% confidence limits indicated. These confidence limits correspond to the single experiment which has been simulated for this figure.

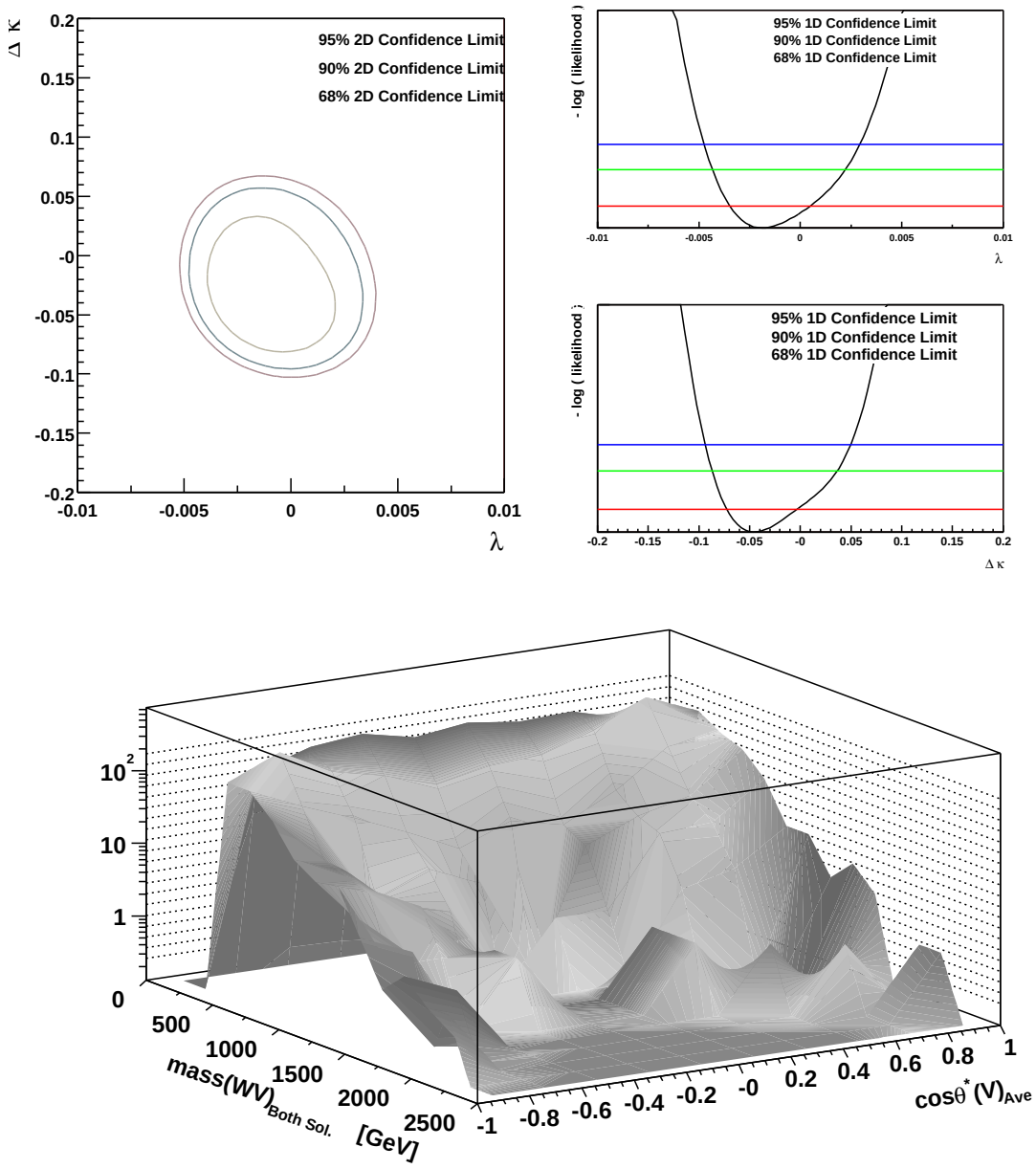

Figure B.11: The reconstructed diboson invariant mass (Eq. 5.6) versus the reconstructed center-of-mass frame photon production angle (both solutions are included in the histogram) for $W\gamma$ production is shown (bottom), after applying the kinematic cuts described in Chapter 4 for the Standard Model reference histogram (including contributions from backgrounds). The one (top right) and two (top left) parameter negative log likelihood curves are shown as a function of the λ_γ and $\Delta\kappa_\gamma$ parameters with the 68, 90, and 95% confidence limits indicated. These confidence limits correspond to the single experiment which has been simulated for this figure.

Appendix C

Distributions for WZ Production

The WZ production distributions which have been used to extract the confidence intervals in Table 5.11, and have not already been presented in the text, are shown in this appendix. The transverse mass distribution has already been shown in Figure 5.4.

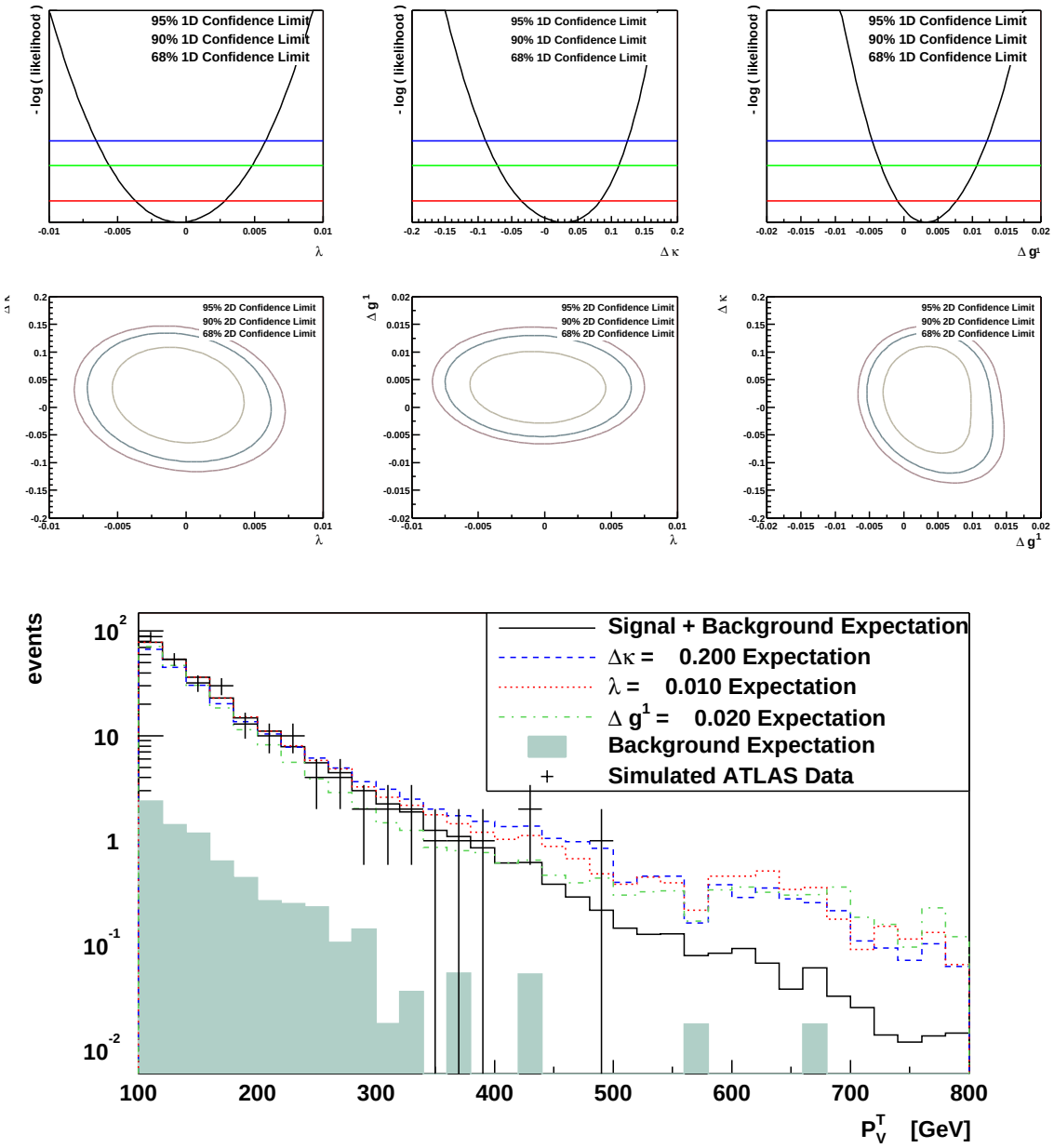

Figure C.1: The transverse momentum distribution of the Z in WZ production is shown (bottom), after applying the kinematic cuts described in Chapter 4. The points with error bars represent "mock" data for one ATLAS experiment with integrated luminosity of 30 fb^{-1}. This data has been simulated using the SM TGC parameters, and includes the background contributions. The lines are the reference distributions for several choices of the anomalous TGC parameters. The contribution of backgrounds to the reference distributions is shown as a shaded histogram, and does not depend on the anomalous TGC parameters. The one (top three plots) and two (middle three plots) parameter negative log likelihood curves are shown as a function of the λ_Z, $\Delta\kappa_Z$, and Δg_Z^1 parameters with the 68, 90, and 95% confidence limits indicated. These confidence limits correspond to the single experiment which has been simulated for this figure.

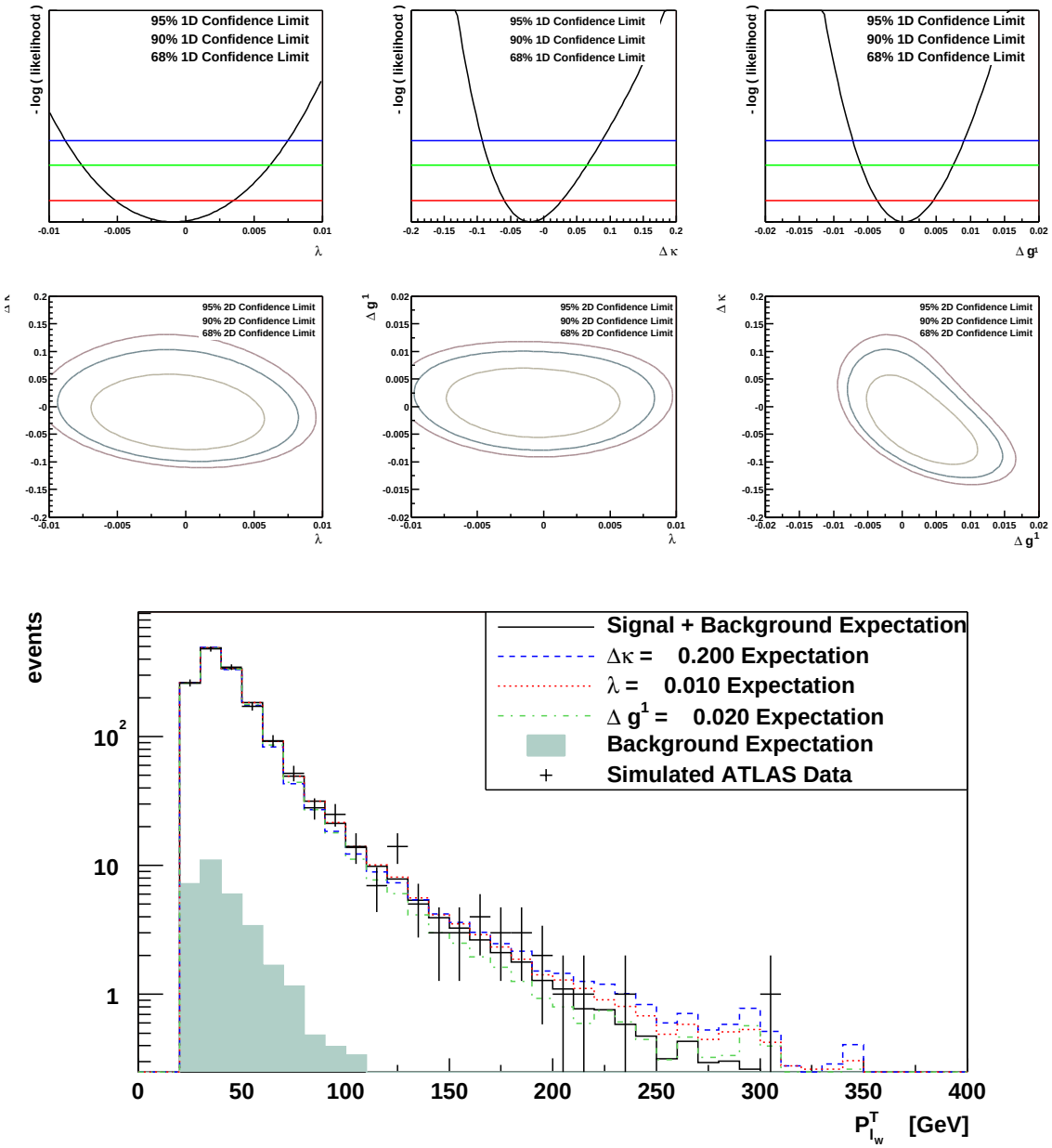

Figure C.2: The transverse momentum distribution of the charged lepton from the W decay in WZ production is shown (bottom), after applying the kinematic cuts described in Chapter 4. The points with error bars represent "mock" data for one ATLAS experiment with integrated luminosity of 30 fb^{-1}. This data has been simulated using the SM TGC parameters, and includes the background contributions. The lines are the reference distributions for several choices of the anomalous TGC parameters. The contribution of backgrounds to the reference distributions is shown as a shaded histogram, and does not depend on the anomalous TGC parameters. The one (top three plots) and two (middle three plots) parameter negative log likelihood curves are shown as a function of the λ_Z, $\Delta\kappa_Z$, and Δg_Z^1 parameters with the 68, 90, and 95% confidence limits indicated. These confidence limits correspond to the single experiment which has been simulated for this figure.

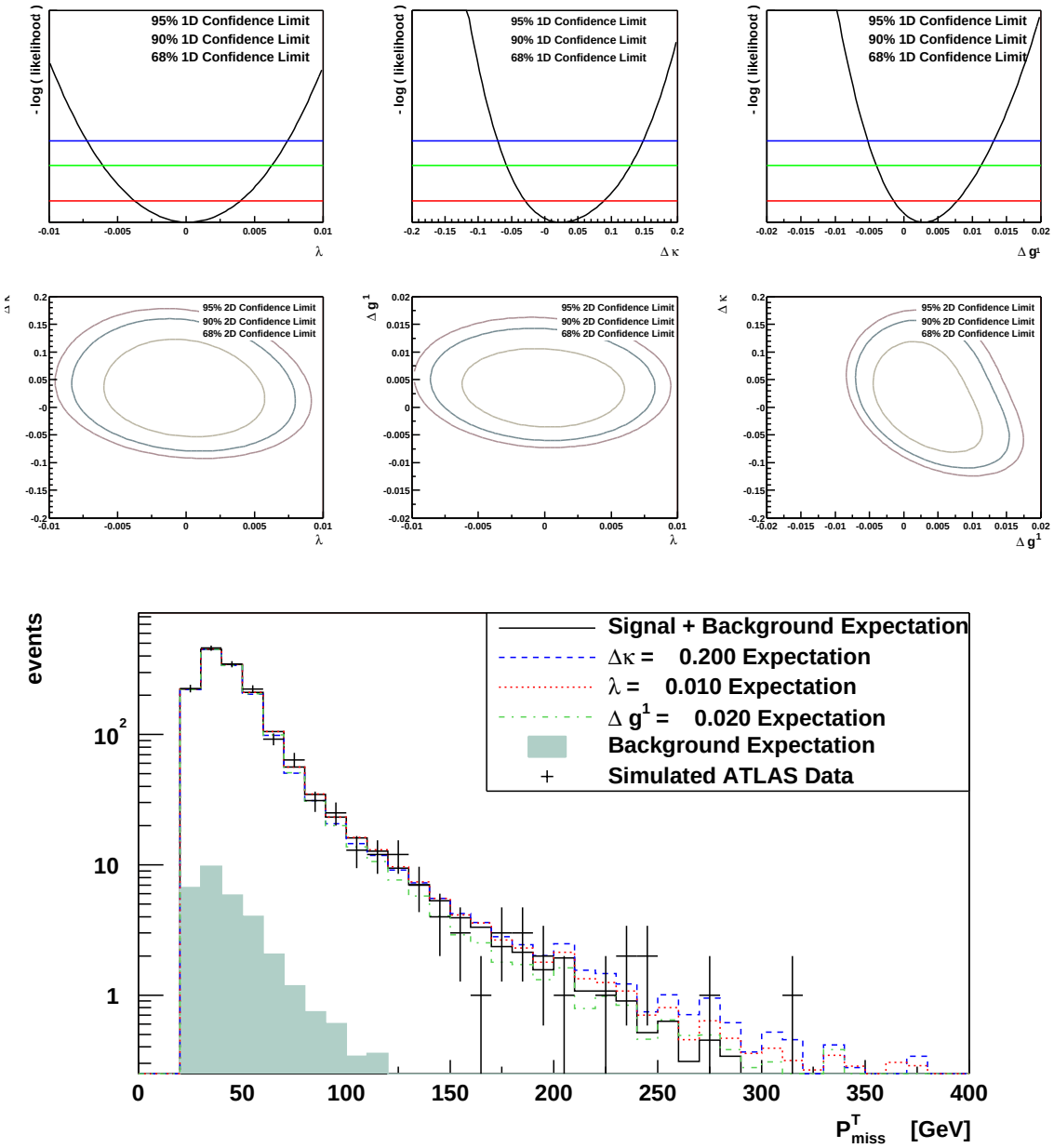

Figure C.3: The missing transverse momentum distribution in WZ production is shown (bottom), after applying the kinematic cuts described in Chapter 4. The points with error bars represent "mock" data for one ATLAS experiment with integrated luminosity of 30 fb^{-1}. This data has been simulated using the SM TGC parameters, and includes the background contributions. The lines are the reference distributions for several choices of the anomalous TGC parameters. The contribution of backgrounds to the reference distributions is shown as a shaded histogram, and does not depend on the anomalous TGC parameters. The one (top three plots) and two (middle three plots) parameter negative log likelihood curves are shown as a function of the λ_Z, $\Delta\kappa_Z$, and Δg_Z^1 parameters with the 68, 90, and 95% confidence limits indicated. These confidence limits correspond to the single experiment which has been simulated for this figure.

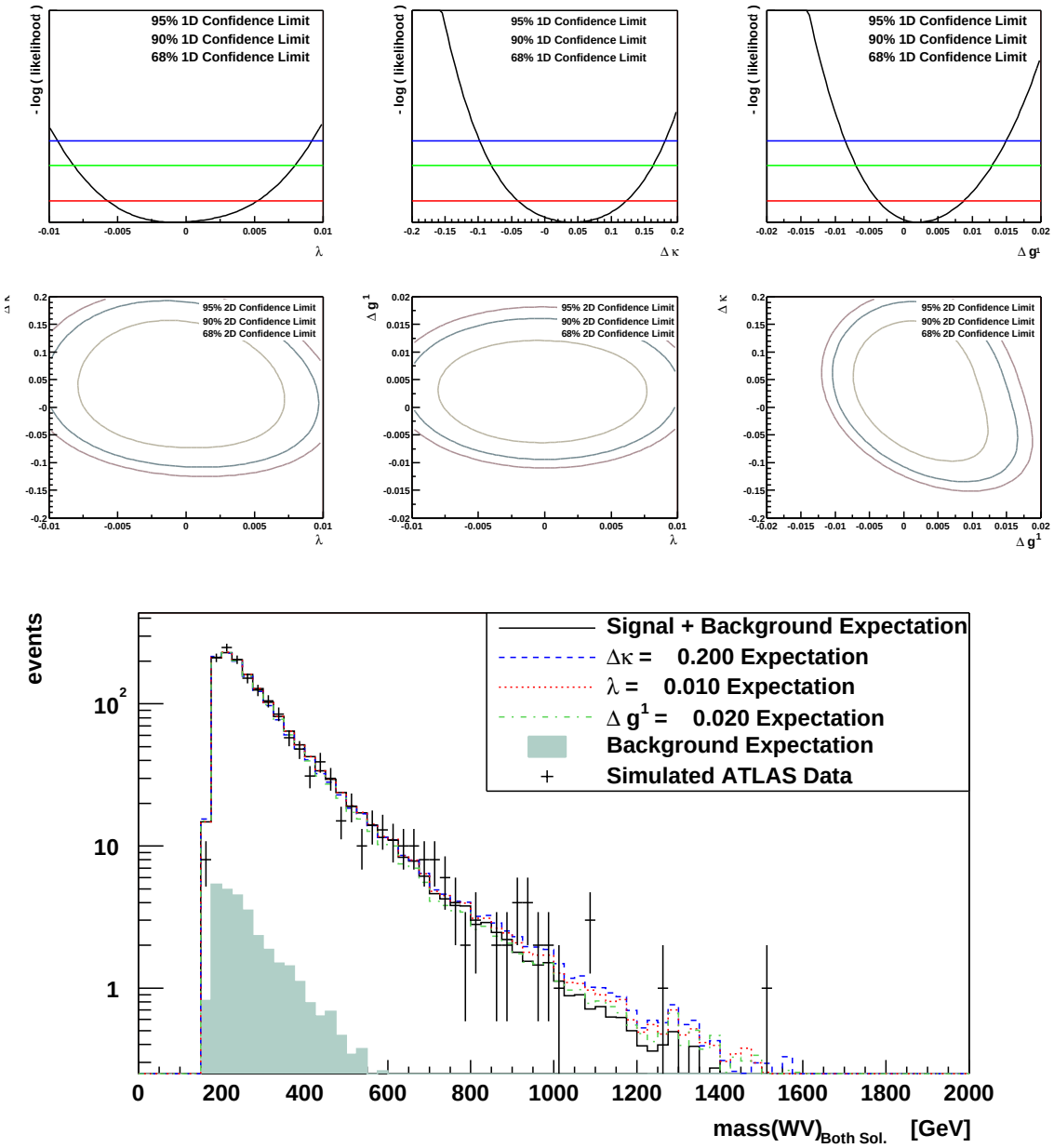

Figure C.4: The reconstructed diboson invariant mass (both solutions, Eq. 5.6) distribution in WZ production is shown (bottom), after applying the kinematic cuts described in Chapter 4. The points with error bars represent "mock" data for one ATLAS experiment with integrated luminosity of 30 fb^{-1}. This data has been simulated using the SM TGC parameters, and includes the background contributions. The lines are the reference distributions for several choices of the anomalous TGC parameters. The contribution of backgrounds to the reference distributions is shown as a shaded histogram, and does not depend on the anomalous TGC parameters. The one (top three plots) and two (middle three plots) parameter negative log likelihood curves are shown as a function of the λ_Z, $\Delta\kappa_Z$, and Δg_Z^1 parameters with the 68, 90, and 95% confidence limits indicated. These confidence limits correspond to the single experiment which has been simulated for this figure.

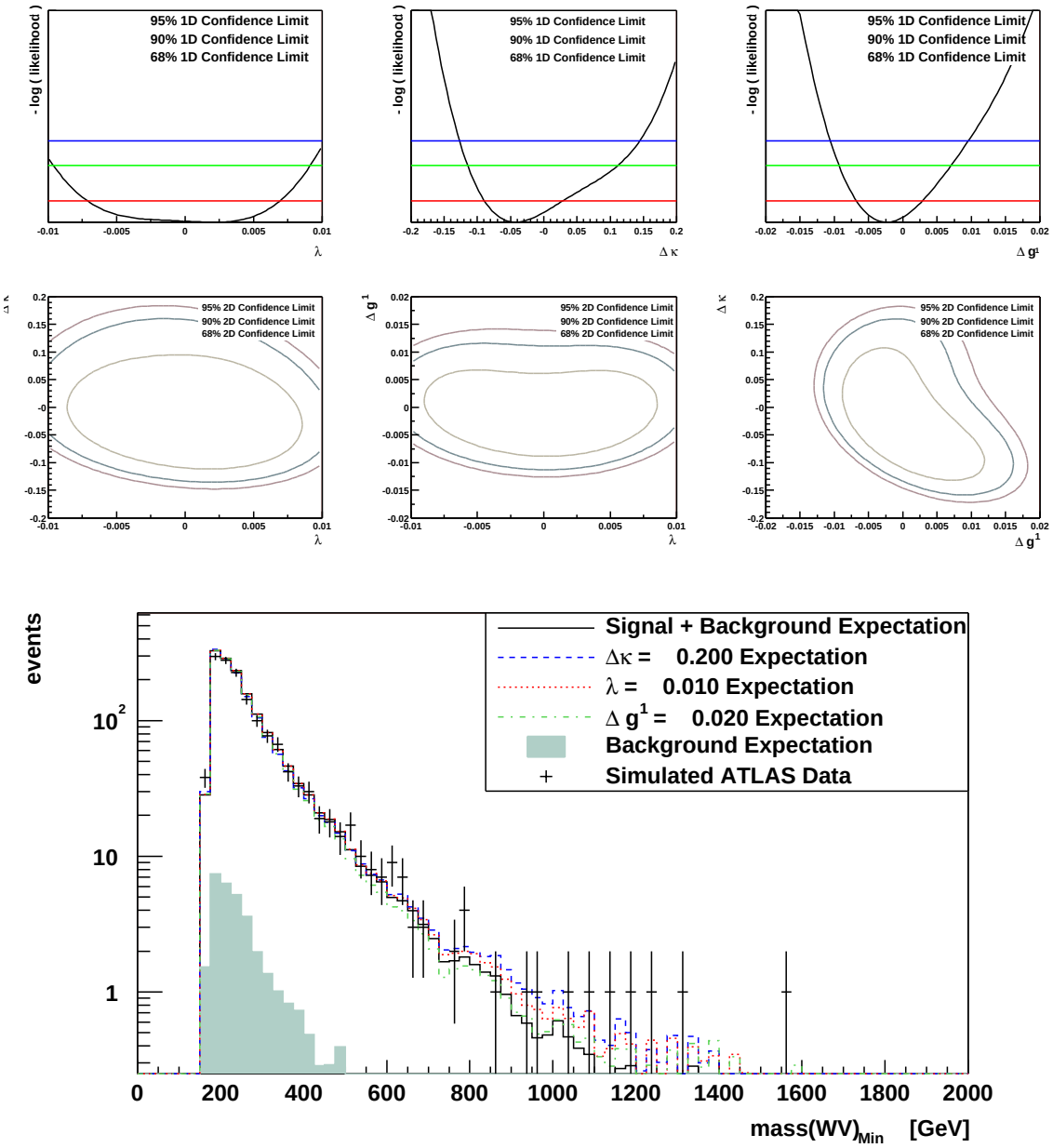

Figure C.5: The diboson invariant mass (minimum solution) distribution in WZ production is shown (bottom), after applying the kinematic cuts described in Chapter 4. The points with error bars represent "mock" data for one ATLAS experiment with integrated luminosity of 30 fb^{-1}. This data has been simulated using the SM TGC parameters, and includes the background contributions. The lines are the reference distributions for several choices of the anomalous TGC parameters. The contribution of backgrounds to the reference distributions is shown as a shaded histogram, and does not depend on the anomalous TGC parameters. The one (top three plots) and two (middle three plots) parameter negative log likelihood curves are shown as a function of the λ_Z, $\Delta\kappa_Z$, and Δg_Z^1 parameters with the 68, 90, and 95% confidence limits indicated. These confidence limits correspond to the single experiment which has been simulated for this figure.

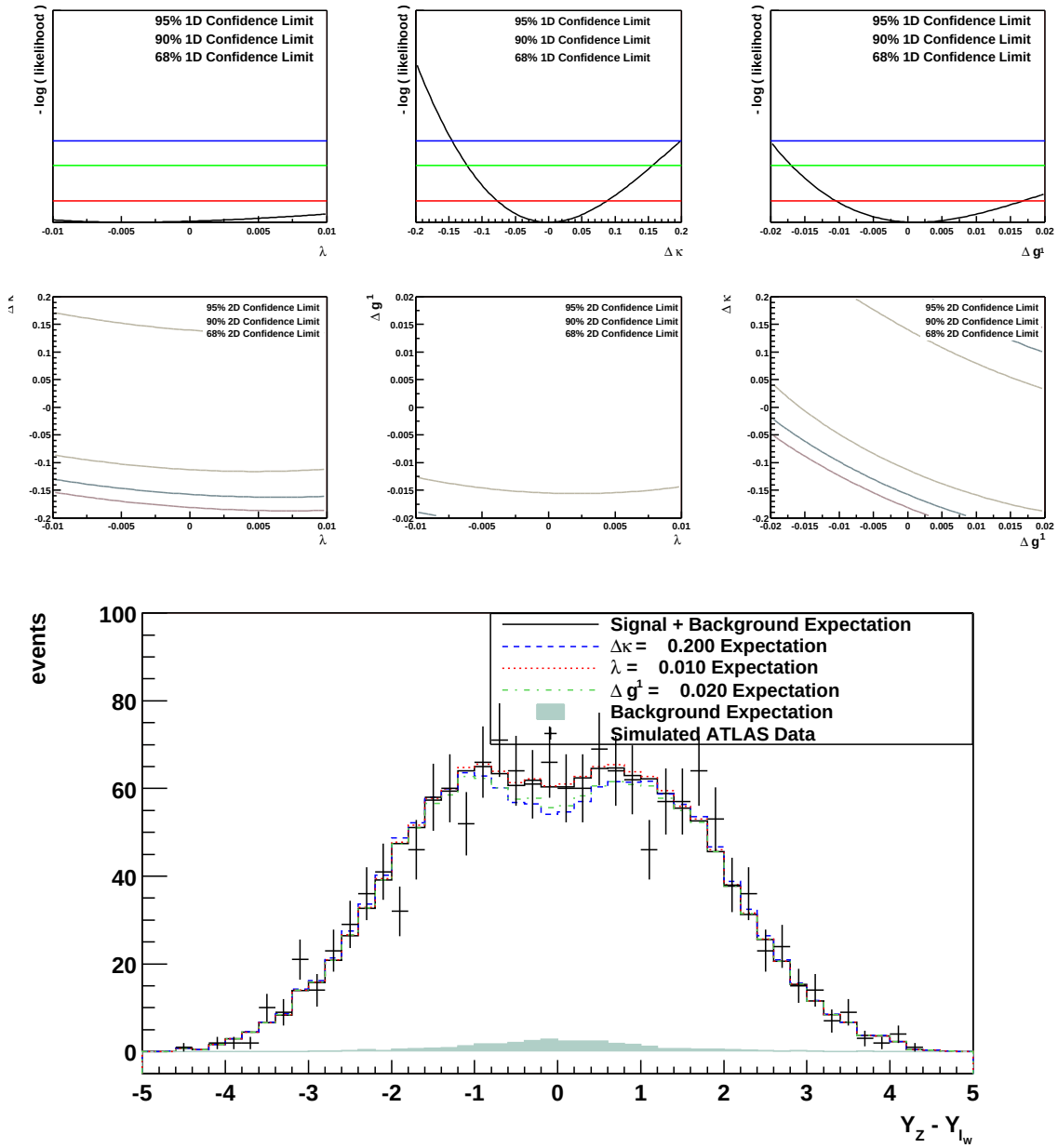

Figure C.6: The rapidity separation distribution of the Z^0 from the charged lepton arising in the $W^{\pm}$ decay in WZ production is shown (bottom), after applying the kinematic cuts described in Chapter 4. The points with error bars represent "mock" data for one ATLAS experiment with integrated luminosity of 30 fb^{-1}. This data has been simulated using the SM TGC parameters, and includes the background contributions. The lines are the reference distributions for several choices of the anomalous TGC parameters. The contribution of backgrounds to the reference distributions is shown as a shaded histogram, and does not depend on the anomalous TGC parameters. The one (top three plots) and two (middle three plots) parameter negative log likelihood curves are shown as a function of the λ_Z, $\Delta\kappa_Z$, and Δg_Z^1 parameters with the 68, 90, and 95% confidence limits indicated. These confidence limits correspond to the single experiment which has been simulated for this figure.

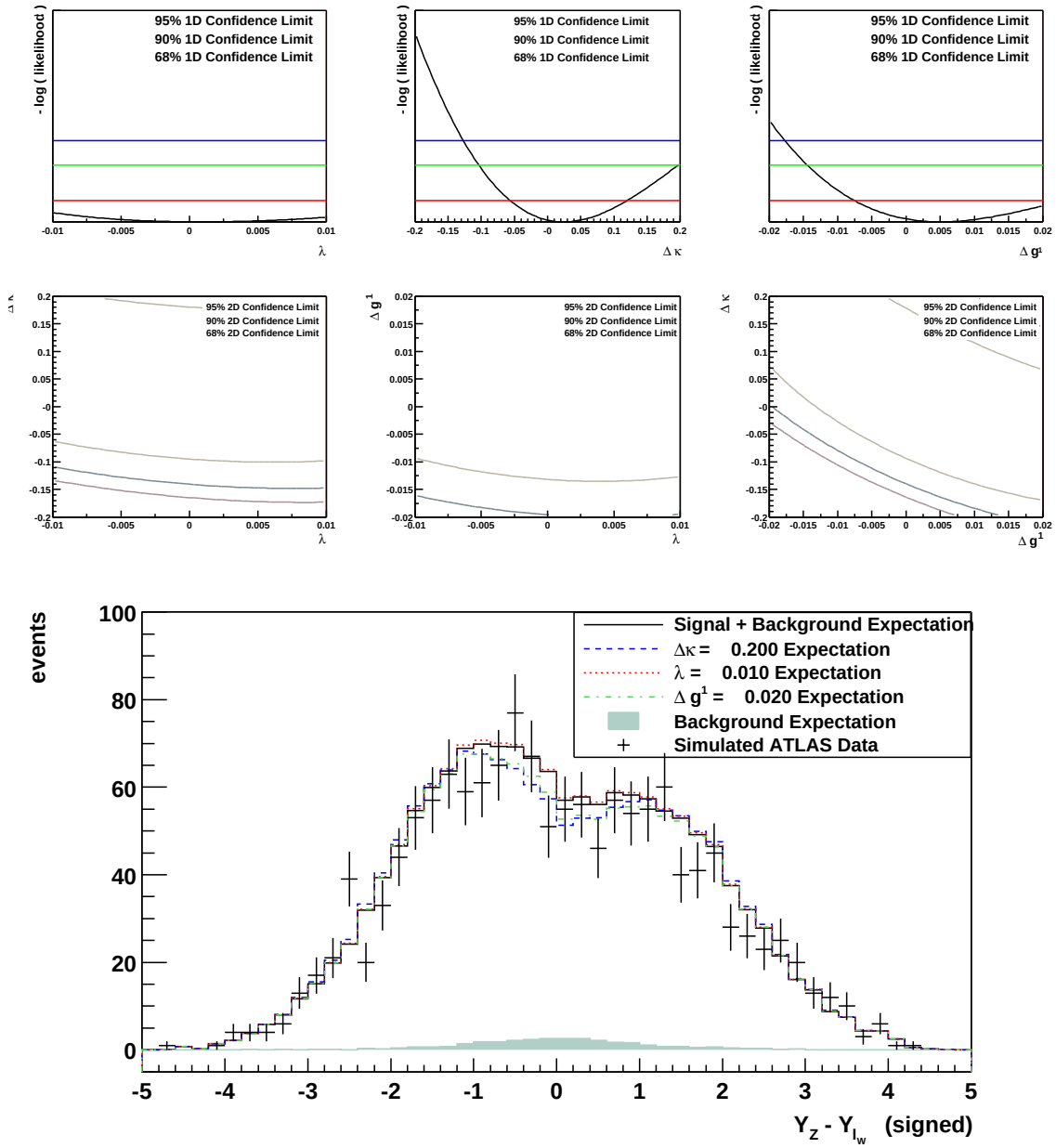

Figure C.7: The signed rapidity separation (Eq. 3.13) distribution of the Z^0 from the charged lepton arising in the $W^{\pm}$ decay in WZ production is shown (bottom), after applying the kinematic cuts described in Chapter 4. The points with error bars represent "mock" data for one ATLAS experiment with integrated luminosity of 30 fb^{-1}. This data has been simulated using the SM TGC parameters, and includes the background contributions. The lines are the reference distributions for several choices of the anomalous TGC parameters. The contribution of backgrounds to the reference distributions is shown as a shaded histogram, and does not depend on the anomalous TGC parameters. The one (top three plots) and two (middle three plots) parameter negative log likelihood curves are shown as a function of the λ_Z, $\Delta\kappa_Z$, and Δg_Z^1 parameters with the 68, 90, and 95% confidence limits indicated. These confidence limits correspond to the single experiment which has been simulated for this figure.

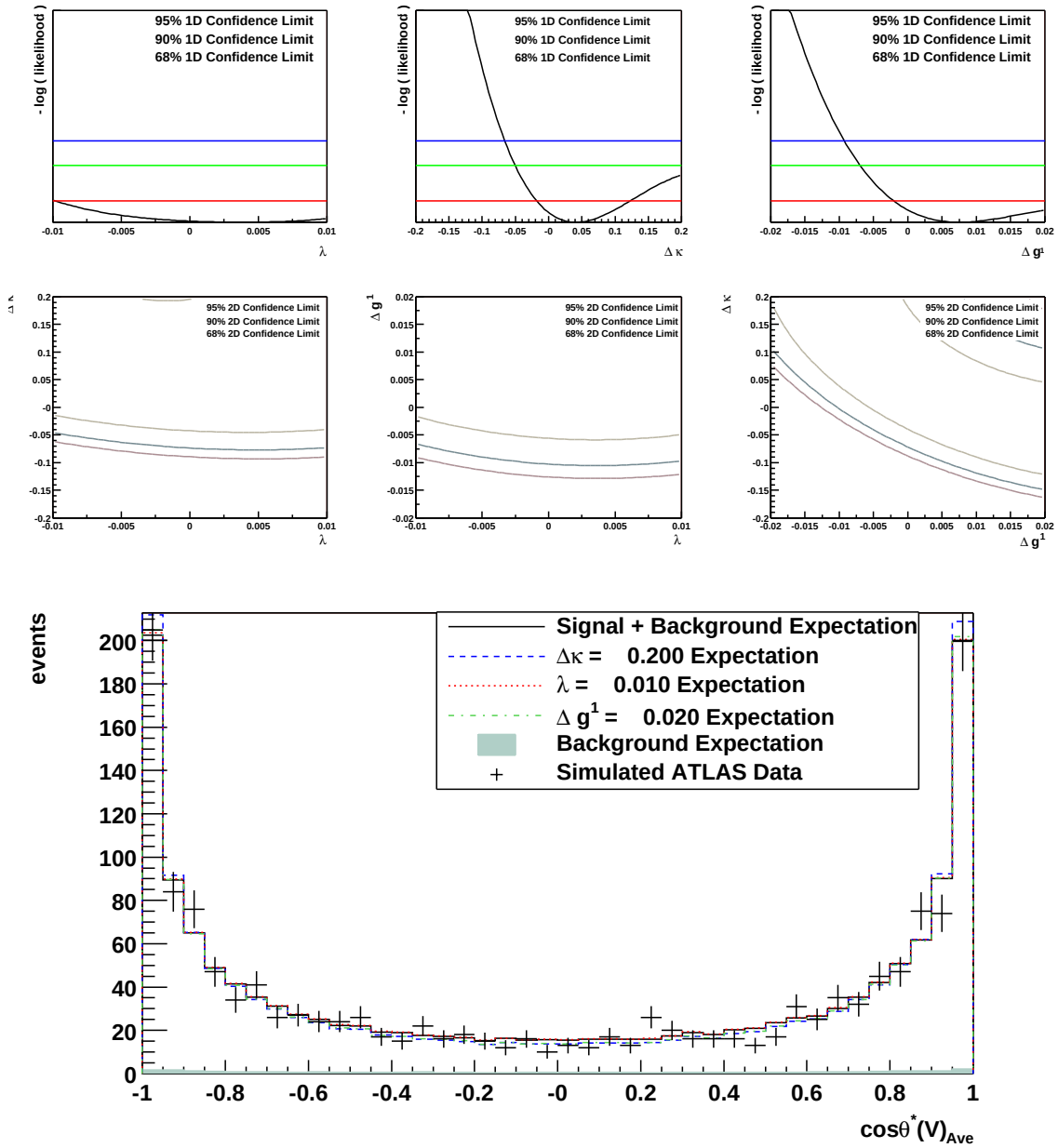

Figure C.8: The reconstructed center-of-mass frame Z^0 production angle (both solutions are included in the histogram) distribution in WZ production is shown (bottom), after applying the kinematic cuts described in Chapter 4. The points with error bars represent "mock" data for one ATLAS experiment with integrated luminosity of 30 fb^{-1}. This data has been simulated using the SM TGC parameters, and includes the background contributions. The lines are the reference distributions for several choices of the anomalous TGC parameters. The contribution of backgrounds to the reference distributions is shown as a shaded histogram, and does not depend on the anomalous TGC parameters. The one (top three plots) and two (middle three plots) parameter negative log likelihood curves are shown as a function of the λ_Z, $\Delta\kappa_Z$, and Δg_Z^1 parameters with the 68, 90, and 95% confidence limits indicated. These confidence limits correspond to the single experiment which has been simulated for this figure.

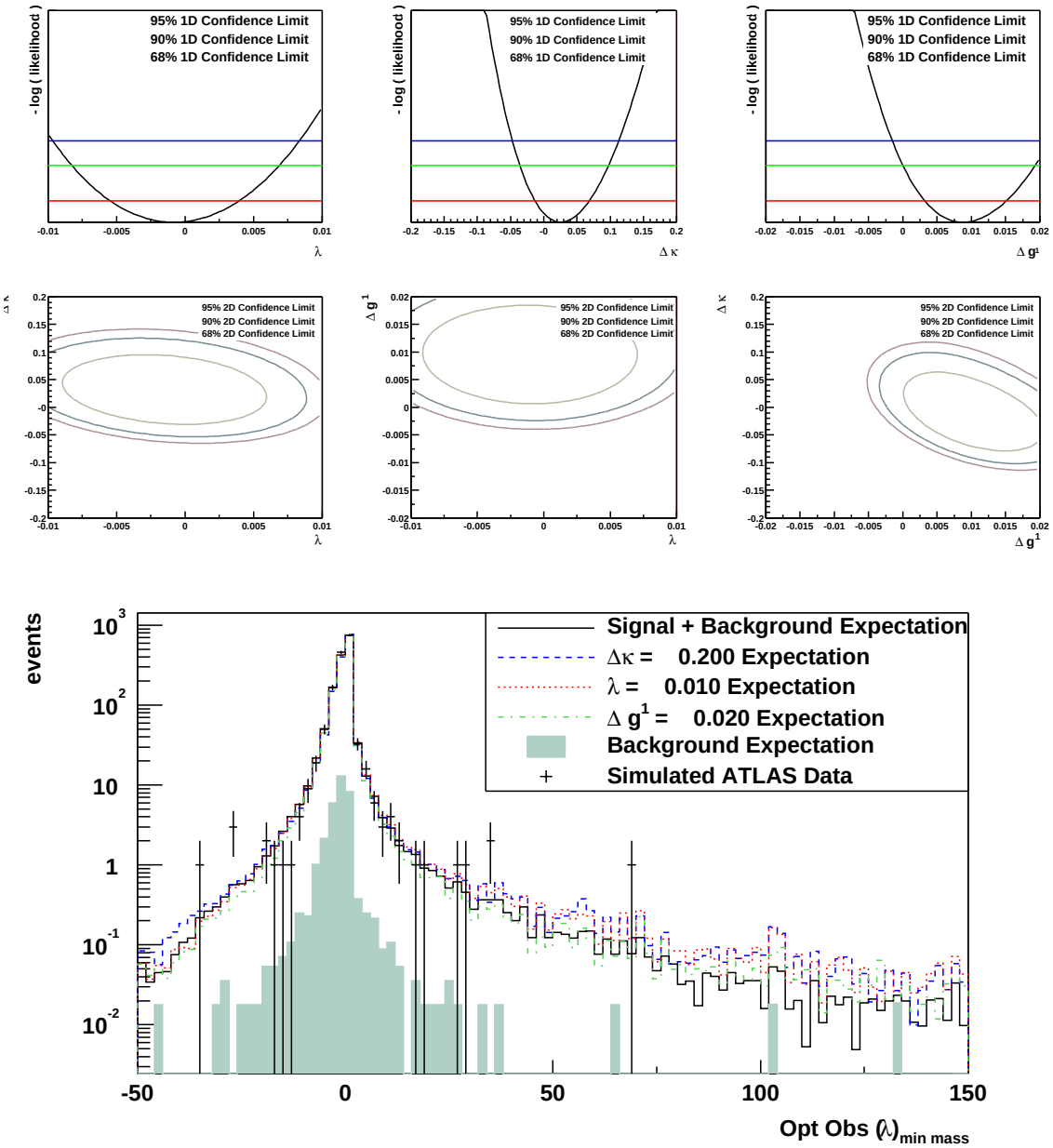

Figure C.9: The distribution of the λ_Z optimal observable in WZ production is shown (bottom), after applying the kinematic cuts described in Chapter 4. The points with error bars represent "mock" data for one ATLAS experiment with integrated luminosity of 30 fb^{-1}. This data has been simulated using the SM TGC parameters, and includes the background contributions. The lines are the reference distributions for several choices of the anomalous TGC parameters. The contribution of backgrounds to the reference distributions is shown as a shaded histogram, and does not depend on the anomalous TGC parameters. The one (top three plots) and two (middle three plots) parameter negative log likelihood curves are shown as a function of the λ_Z, $\Delta\kappa_Z$, and Δg_Z^1 parameters with the 68, 90, and 95% confidence limits indicated. These confidence limits correspond to the single experiment which has been simulated for this figure.

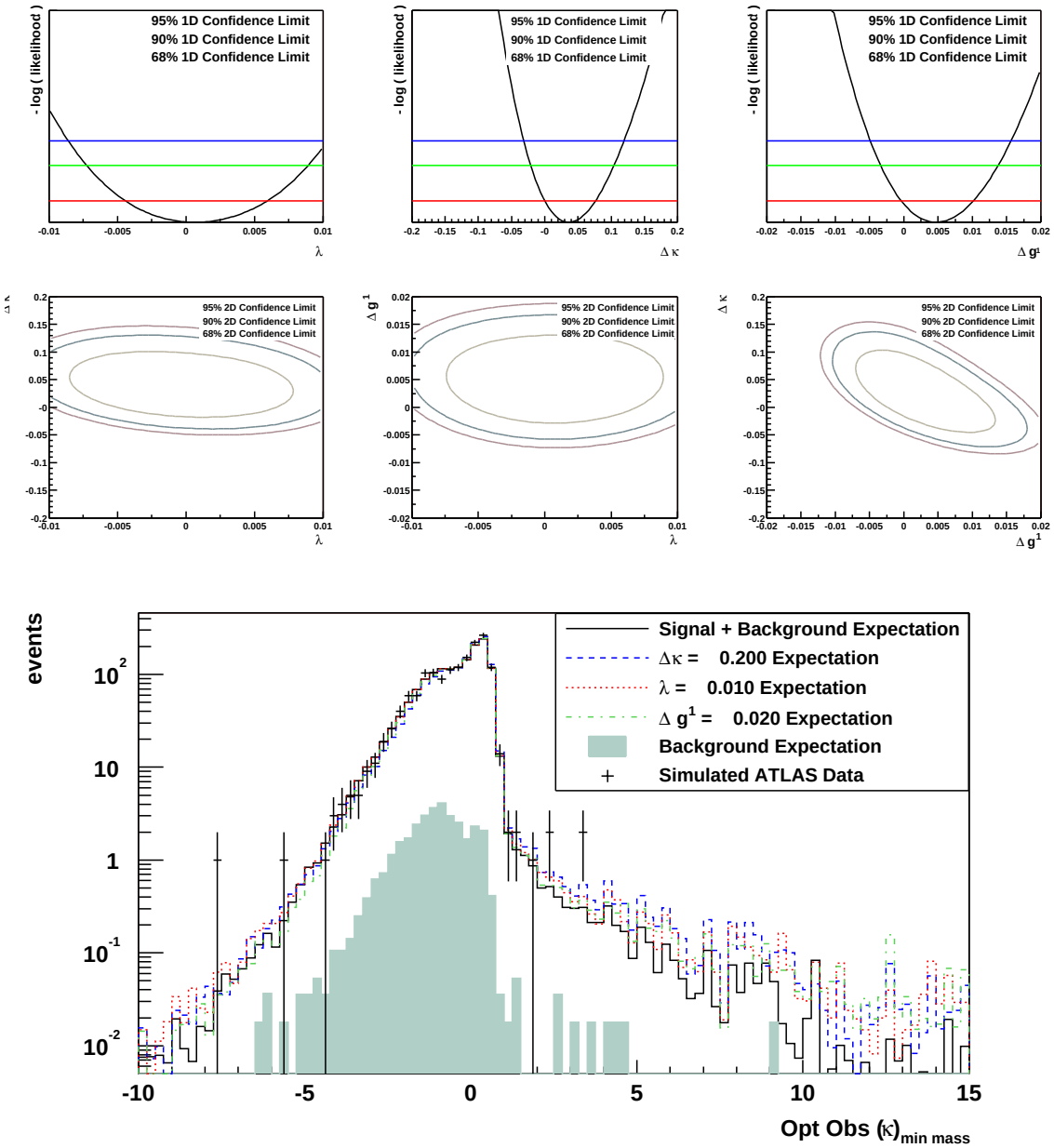

Figure C.10: The distribution of the $\Delta\kappa_Z$ optimal observable in WZ production is shown (bottom), after applying the kinematic cuts described in Chapter 4. The points with error bars represent "mock" data for one ATLAS experiment with integrated luminosity of 30 fb^{-1}. This data has been simulated using the SM TGC parameters, and includes the background contributions. The lines are the reference distributions for several choices of the anomalous TGC parameters. The contribution of backgrounds to the reference distributions is shown as a shaded histogram, and does not depend on the anomalous TGC parameters. The one (top three plots) and two (middle three plots) parameter negative log likelihood curves are shown as a function of the λ_Z, $\Delta\kappa_Z$, and Δg_Z^1 parameters with the 68, 90, and 95% confidence limits indicated. These confidence limits correspond to the single experiment which has been simulated for this figure.

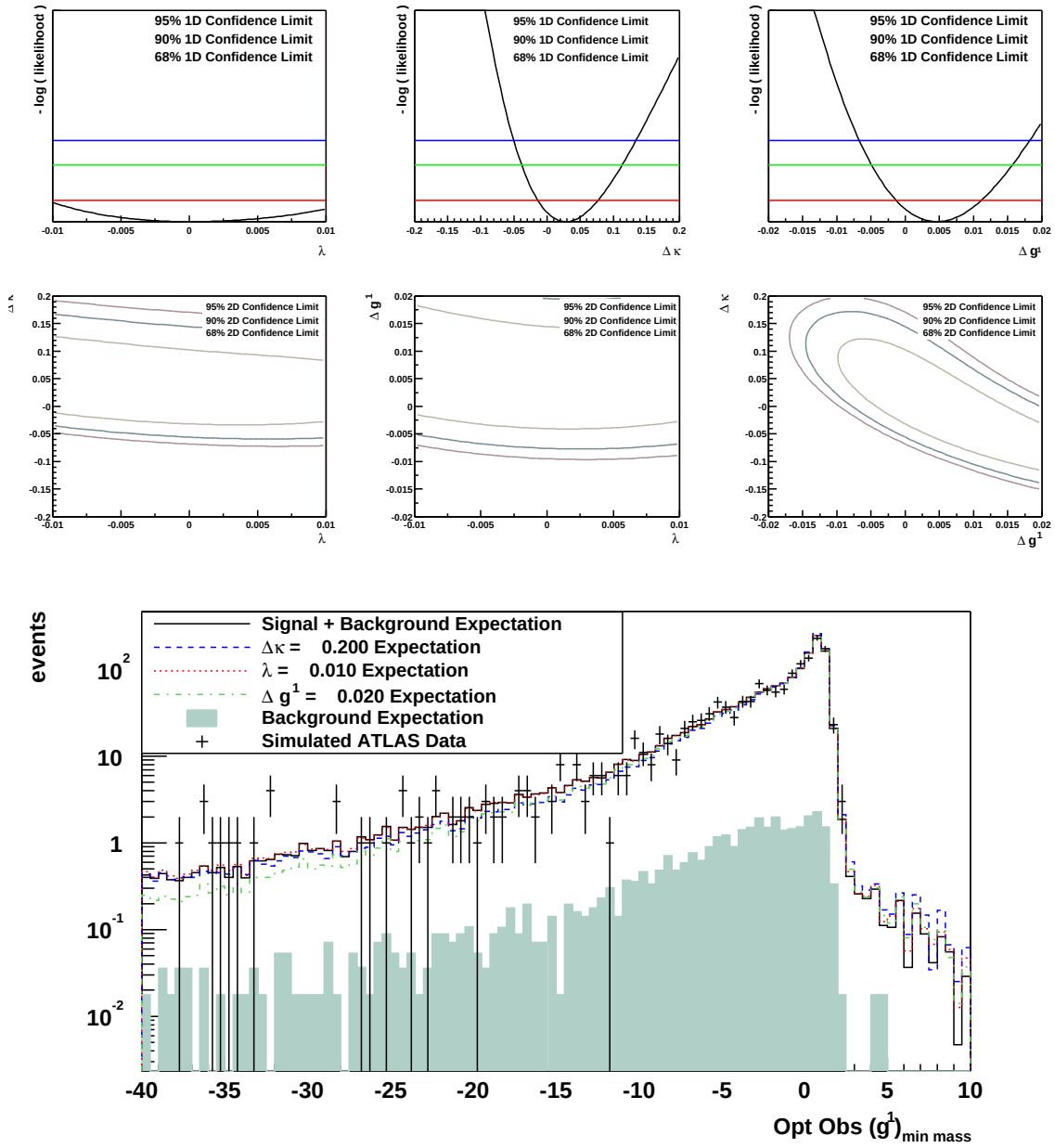

Figure C.11: The distribution of the Δg_Z^1 optimal observable in WZ production is shown (bottom), after applying the kinematic cuts described in Chapter 4. The points with error bars represent "mock" data for one ATLAS experiment with integrated luminosity of 30 fb^{-1}. This data has been simulated using the SM TGC parameters, and includes the background contributions. The lines are the reference distributions for several choices of the anomalous TGC parameters. The contribution of backgrounds to the reference distributions is shown as a shaded histogram, and does not depend on the anomalous TGC parameters. The one (top three plots) and two (middle three plots) parameter negative log likelihood curves are shown as a function of the λ_Z, $\Delta\kappa_Z$, and Δg_Z^1 parameters with the 68, 90, and 95% confidence limits indicated. These confidence limits correspond to the single experiment which has been simulated for this figure.

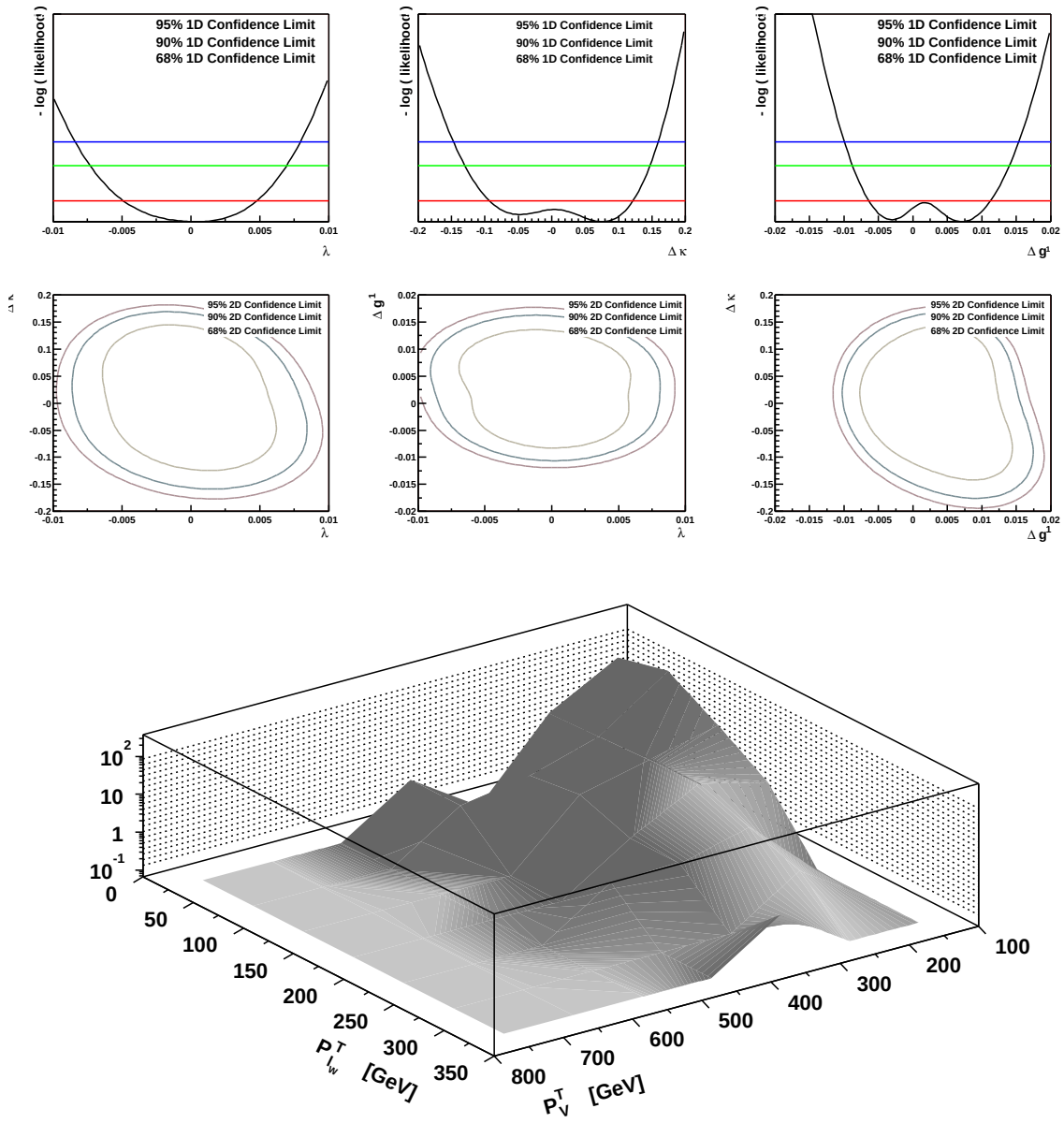

Figure C.12: The transverse momentum of the Z^0 versus the transverse momentum of the charged lepton arising in the $W^{\pm}$ decay distribution for WZ production is shown (bottom), after applying the kinematic cuts described in Chapter 4. Only the Standard Model reference histogram (including contributions from backgrounds) is shown. The one (top three plots) and two (middle three plots) parameter negative log likelihood curves are shown as a function of the λ_Z, $\Delta\kappa_Z$, and Δg_Z^1 parameters with the 68, 90, and 95% confidence limits indicated. These confidence limits correspond to the single experiment which has been simulated for this figure.

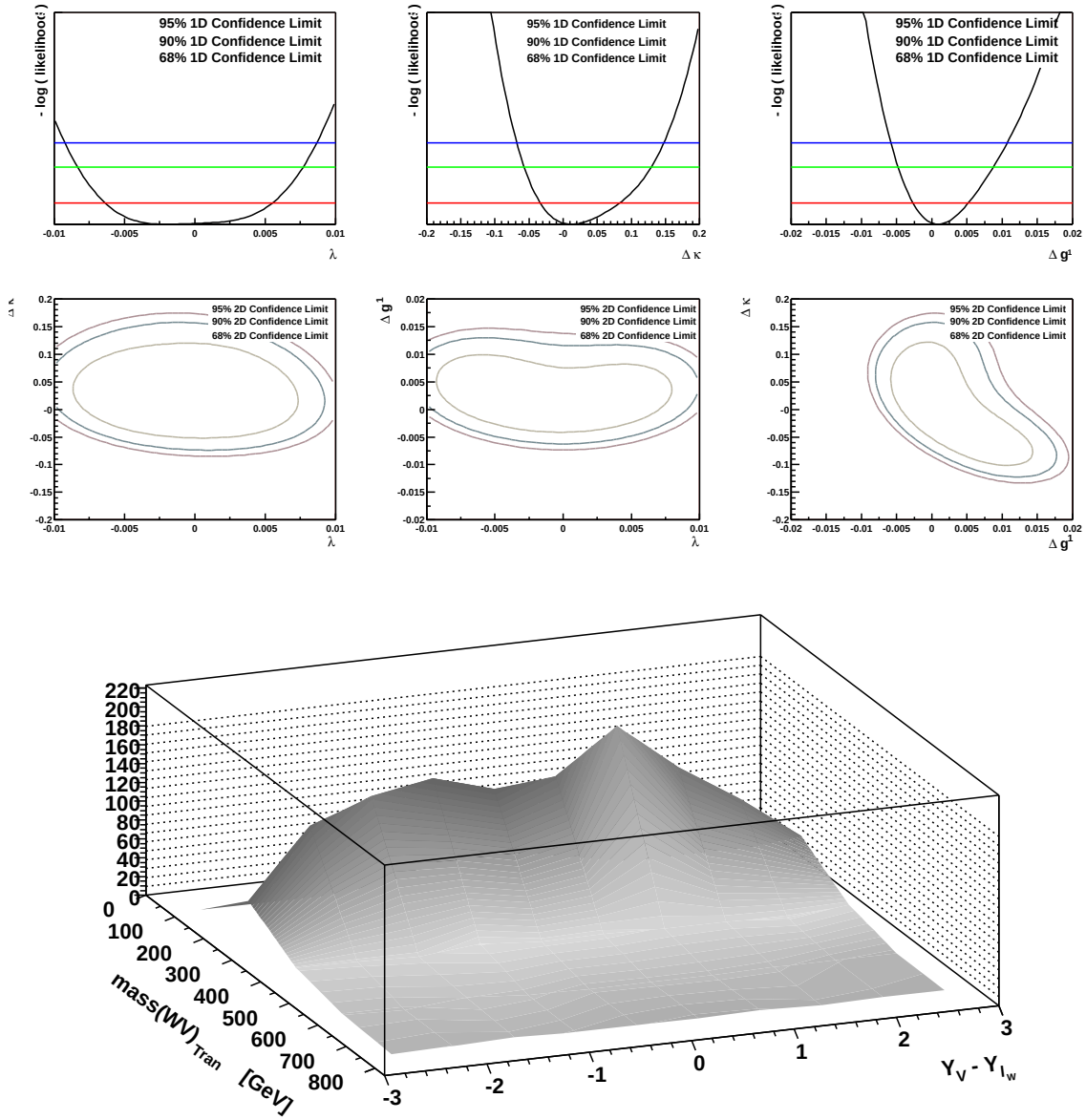

Figure C.13: The diboson transverse mass versus the rapidity separation of the Z^0 from the charged lepton arising in the $W^{\pm}$ decay distribution for WZ production is shown (bottom), after applying the kinematic cuts described in Chapter 4. Only the Standard Model reference histogram (including contributions from backgrounds) is shown. The one (top three plots) and two (middle three plots) parameter negative log likelihood curves are shown as a function of the λ_Z, $\Delta\kappa_Z$, and Δg_Z^1 parameters with the 68, 90, and 95% confidence limits indicated. These confidence limits correspond to the single experiment which has been simulated for this figure.

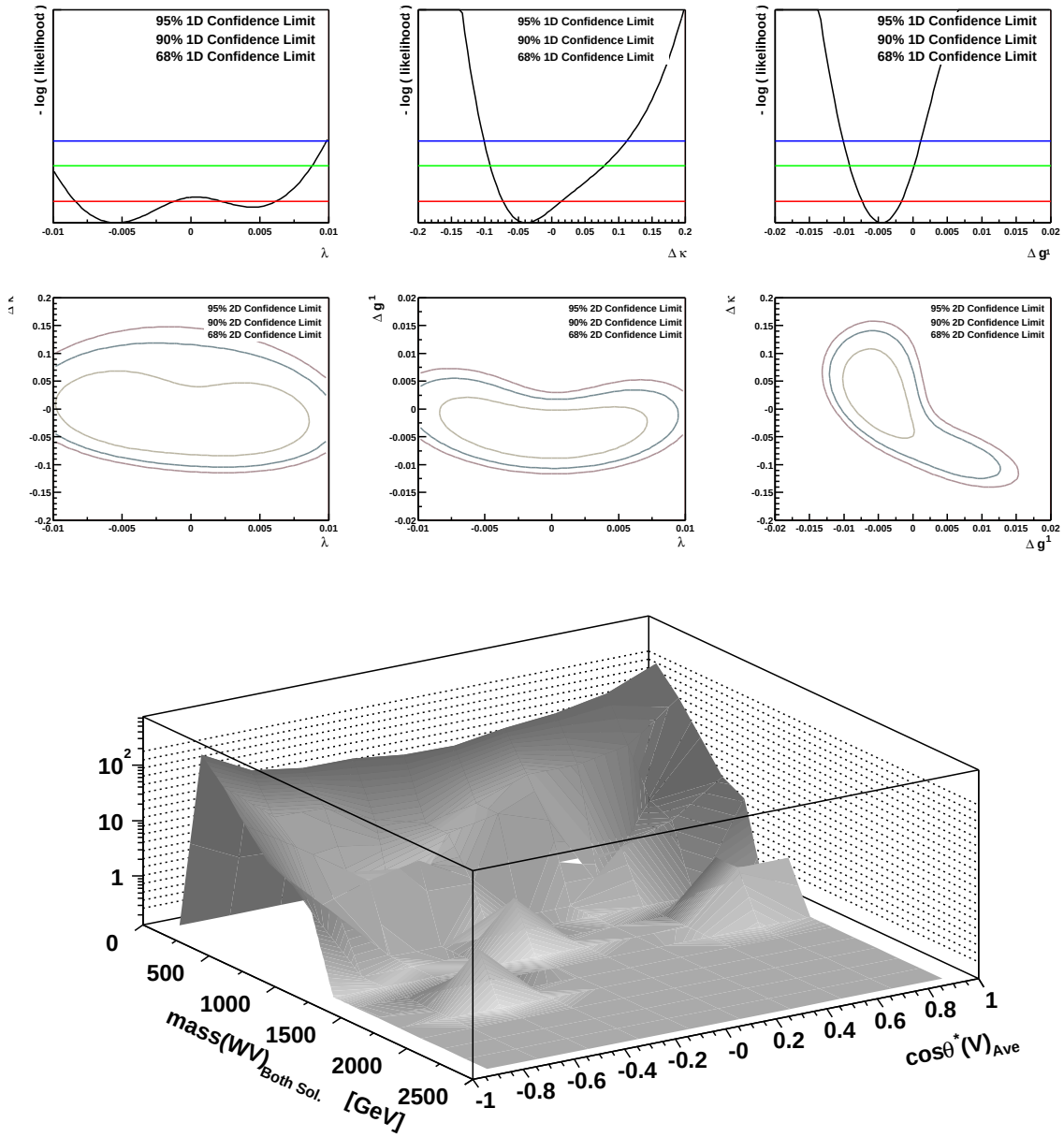

Figure C.14: The reconstructed diboson invariant mass (Eq. 5.6) versus the reconstructed center-of-mass frame Z^0 production angle (both solutions are included in the histogram) for WZ production is shown (bottom), after applying the kinematic cuts described in Chapter 4. Only the Standard Model reference histogram (including contributions from backgrounds) is shown. The one (top three plots) and two (middle three plots) parameter negative log likelihood curves are shown as a function of the λ_Z, $\Delta\kappa_Z$, and Δg_Z^1 parameters with the 68, 90, and 95% confidence limits indicated. These confidence limits correspond to the single experiment which has been simulated for this figure.